Iron in oxides, silicates and alloys under extreme pressure-temperature conditions

Von der Fakultät für Biologie, Chemie und Geowissenschaften
der Universität Bayreuth

zur Erlangung der Würde eines Doktors der Naturwissenschaften
- Dr. rer. nat. -

Genehmigte Dissertation
vorgelegt von

Konstantin Glazyrin
aus Tschita (Russland)

Bayreuth 2011

Vollständiger Abdruck der von der Fakultät für Chemie/Biologie/Geowissenschaften der Universität Bayreuth genehmigten Dissertation zur Erlangung des Grades eines Doktors der Naturwissenschaften (Dr. rer. nat.).

Prüfungsausschuß:

Prof. Dr. Hans Keppler, Universität Bayreuth   (Vorsitzender)

Prof. Dr. Leonid Dubrovinsky, Universität Bayreuth ,   (1. Gutachter)

Prof. Dr. Tomoo Katsura, Universität Bayreuth   (2. Gutachter)

Prof. Dr. Josef Breu, Universität Bayreuth

Tag der Einreichung: 18 August 2011
Tag der wissenschaftlichen Kolloquiums: 28 November 2011

Table of Contents

Acknowledgements

Summary

Iron and oxygen belong to the most abundant elements of Solar system, and the Fe-O system is considered to be one of the most important component of minerals and mineral assemblages. Pure iron is relevant for the cores of terrestrial planets, and different Fe-oxides are important for their mantle. Knowing the structural, elastic, electronic and magnetic properties of iron-bearing materials helps to constrain the structure of terrestrial planets in general, and processes occurring in the deep interior of planets in particular. For the current Ph. D. thesis we have selected four model minerals and studied the influence of high pressure on their physical properties.

I. Single crystal structure and spin state of ferric iron of magnesium silicate perovskite

There is a general agreement, that magnesium silicate perovskite (Pv) comprises around 80 vol% of the Earth's lower-mantle, making it by volume the most abundant mineral in our planet, and and there is no doubt that Pv in the mantle contains Fe and Al. However, the exact concentrations are unknown (Fiquet et al. 2008), as well as the effect of pressure on physical properties of Pv at conditions of Earth lower mantle. In our study we investigate Pv with one of the less explored substitution $Mg^{2+}_A+Si^{4+}_B \rightarrow Fe^{3+}_A+Al^{3+}_B$. Here we explore as a function of pressure and temperature the crystal structure of the material, the distribution of chemical elements between different crystallographic sites and the evolution the spin state of ferric iron, as one of crucial parameters determining electrical and radiative conductivity of the Earth's lower mantle (Xu et al. 1998, Goncharov et al. 2008).

We perform single-crystal x-ray diffraction on magnesium silicate perovskite with the composition $Mg_{0.63}Fe_{0.37}Si_{0.63}Al_{0.37}O_3$ (MgFeAlPv) at a beamline ID09a, ESRF, using a combination of *in-situ* diamond anvil cell technique and laser heating in order to simulate the extreme conditions of the Earth's lower mantle. This study is essential in order to constrain the elastic behavior of a candidate lower mantle mineral and explore previous theoretical predictions and experimental observations that had lead to contradictory conclusions. We provide a complete description of the behavior of MgFeAlPv in terms of crystal structure and ferric iron occupying its dodecahedral (A-)site. In contrast to Jackson et al. (2005), we observe no spin transition of ferric iron at A-site, confirming theoretical predictions (Zhang and Oganov 2006, Stackhouse et al. 2007) and recent experimental observations (Catalli et al. 2010). However, even upon heating MgFeAlPv samples to 1800 K at ~78 GPa we see no indication of a spin crossover or a pressure/temperature induced redistribution of ferric iron and aluminum between the different crystallographic sites as suggested previously by Catalli et al (2010).

Fitting our data with a third order Birch-Murnaghan equation of states we obtain the following parameters: bulk modulus $K_0=233\,(4)\,GPa$, its pressure derivative $K_0'=4.1(0.1)$, and the zero pressure volume at room temperature $V_0=169.7(3)\,Å^3$. We combine these data with high pressure-high temperature measurements to obtain a thermal equation of state using the formulation of Saxena et al. (1999).

We pay special attention to the pressure-dependence of crystal structure and individual

crystallographic sites of magnesium silicate perovskite, to the information that was scarce in the literature published previous to the current study. In particular, comparing our data with data for pure $MgSiO_3$ we show that the dodecahedral A-site of MgFeAlPv, occupied by ferric iron and magnesium, is much more compressible than the octahedral site, occupied by aluminum and silicon.

II. Compression induced metallization of magnetite below 25 GPa

As a model Fe-O system, magnetite is a mixed valence iron oxide incorporating both ferric and ferrous iron. Being essential part of some sedimentary (banded iron formations) and igneous rocks, magnetite can be subjected to high pressure in natural systems, for instance, during subduction of oceanic crust (Dobson and Brodholt 2005), or during serpentinization (metamorphic reaction). The ferrimagnetic nature of magnetite makes it one of the strongest magnetic minerals, due to the interaction of the mixed valence iron ions and relatively high Néel temperature. However, intrinsic magnetism also affects the complex phase diagram of magnetite, and in order to evaluate properties of magnetite, for instance, during its formation in the serpentinization process, large parts of the phase diagram need to be explored. At this point, due to the lack of experimental observations at high pressure, one can find contradicting hypotheses in the literature proposing an inverse to normal spinel transition (Rozenberg et al. 2007), or an iron spin state transition (Ding et al. 2008). It is worth noting that electrical and thermal conductivity and magnetic properties of magnetite should change significantly in case one of these models is correct.

In order to shed light on the complex physical properties of magnetite under compression we conducted a combined single crystal x-ray diffraction and Mössbauer spectroscopy at pressures below 25 GPa. In contrast to powder diffraction study reported in literature (Rozenberg et al. 2007), we find no evidence for the transition from inverse to normal spinel in magnetite. Analyzing the collected Mössbauer data, we show that a high spin – intermediate spin transition cannot occur in magnetite in the pressure range of 10-20 GPa, and finally, based on a careful analysis of the data and results reported in the literature (Klotz et al. 2008, Baudelet et al. 2010), we provide a model consistently describing the behavior of electronic and magnetic properties of magnetite in terms of a gradual charge delocalization induced by pressure. We show experimental evidence, that although at ambient conditions electrical conductivity of magnetite are dominated by $t_{2g\downarrow}$ minority band (Dedkov et al. 2002), compression widens majority band ($t_{2g\uparrow}$) and changes electron species dominating in conduction band from spin down to spin up at 15 GPa (change of charge carriers spin polarization).

III. Intrinsic defect structure of wüstite and its effect on high-pressure low temperature phase diagram

Our study of wüstite (Fe_xO) is focused on the high pressure – low temperature phase diagram of the Fe-end member in the (Mg,Fe)O system. Unlike magnetite, where ferric iron is an essential component occupying octahedral and tetrahedral crystallographic sites, the crystal structure of wüstite is formed by a framework of ferrous iron (octahedral positions), and ferric iron occupies interstitial tetrahedral sites in the form of defects (Battle and Cheetham 1979). Individual defects form clusters (long-range order) and are at origin of superlattice x-ray diffraction lines or spots measured in Fe_xO. Here we show that the ferric iron defects have a strong influence on the low temperature phase diagram of wüstite.

Summary

We perform high resolution neutron diffraction experiments in order to investigate the low temperature phase diagram of $Fe_{0.925}O$ and $Fe_{0.94}O$. By tracking the variation of the lattice parameter ratio (c/a) and variation of diffraction line intensities, we determine the critical temperatures of antiferromagnetic ordering (the Néel temperature T_N) and structural transitions (T_S) of the two compounds. Contrary to the general hypothesis, suggesting that the transition from cubic to rhombohedral structure is a result of magnetostriction, induced by the magnetic transition (Kanamori 1957), we report divergence of T_N and T_S as a function of pressure. As we observe no obvious correlation between magnetic and structural degrees of freedom, we suggest the presence of another subtle mechanism pushing the structural transition below the magnetic one by softening effects of magnetic interaction between the ferrous ions. Knowing that $Fe_{0.925}O$ and $Fe_{0.94}O$ have different concentrations of defect clusters formed by long range ordering of octahedral vacancies and interstitial tetrahedral sites (Akimitsu et al. 1983), we argue that a modification of the defect structure in wüstite can be invoked explaining the drastically different response of $Fe_{0.925}O$ and $Fe_{0.94}O$ to compression. We see the difference in T_N and T_S as an indicator of pressure effects on the intrinsic defect structure and detect an order-disorder transition of defect structure in $Fe_{0.925}O$, similar to the one reported in ambient temperature experiments (Ding et al. 2005a). Rapid decompression from a disordered state of defect structure ($Fe_{0.925}O$, ~8GPa) leads to a strong drop of T_S (>50 K) relative to pristine material with a similar composition ($Fe_{0.92}O$, Kantor et al. 2005). We argue that during rapid decompression a new defect structure is formed, which consists of ordered defect clusters. This ordering is different from ordering of defects of the as-prepared material. With that we show that although ferric iron is a minor structural component of wüstite, it is an essential component of defect structures and induces profound effects on the low temperature phase diagram of wüstite.

IV. Evidence of topological electronic transition in *hcp* phase of Fe and $Fe_{0.9}Ni_{0.1}$

As pointed out above, metallic iron and iron-nickel alloys with a small amount of Ni are the primary constituents of the cores of terrestrial planets. The central pressure of these planets range from ~40 GPa for Mars to ~360 GPa for the Earth, with the possibility of solid inner cores for both planets. The question of phase stability and physical properties of Fe and Fe-Ni at these conditions are therefore critical for our understanding of their nature. Possible crystal phases of iron and Fe-Ni alloys at high pressure are *bcc*, *fcc*, and *hcp*, with *hcp* thought to be the stable phase at least for the Earth's core.

For Fe and $Fe_{0.9}Ni_{0.1}$ as model compositions, we investigate effect of pressure (P) on the elastic and electronic properties of their *hcp* phases below 70 GPa. After analyzing literature data (Mao et al. 2001, Crowhurst et al. 2005), we find that the Debye sound velocity (V_D) shows a softening at ~40-50 GPa. Using nuclear inelastic x-ray scattering we confirm the presence of this softening in the *hcp* phase of $Fe_{0.9}Ni_{0.1}$, and explore this anomaly in a joint experimental (x-ray diffraction, Mössbauer spectroscopy) and theoretical study.

After processing our experimental data, we report a gradual decrease in the ratio of the *hcp* lattice parameters c/a for Fe in the pressure range below 45-50 GPa, and a non-linear behavior of Mössbauer isomer shift for *hcp* phases of pure Fe and $Fe_{0.9}Ni_{0.1}$, suggesting an isostructural transition in these phases.

Summary

We investigate paramagnetic *hcp* iron under compression by employing state-of-art calculations (LDA+DMFT) and including many-body correlation effects. Based on the results of the calculations, we predict an electronic topological transition (ETT). After comparing data on materials with already known ETT (Varlamov et al. 1989) with our observations and theoretical predictions, we conclude that results obtained from the three independent experimental measurements can be explained in the framework of an ETT.

V. Portable laser heating for high pressure experiments

The development of a portable laser heating system was a necessary requirement for our work done on minerals at conditions of Earth's lower mantle in general (Dubrovinsky et al. 2010a, Narygina et al. 2011, Potapkin et al. 2011), and for the study of magnesium silicate perovskite containing iron and aluminum in particular (Section I). The main advantages of the system developed are compactness, versatility for different *in-house* and synchrotron based techniques, including high pressure measurements of resistivity, Raman spectroscopy, energy and time-resolved Mössbauer spectroscopy, powder and single crystal x-ray diffraction, nuclear inelastic x-ray scattering, and x-ray absorption. These advantages, the low times of assembly, stable and homogeneous conditions for heating, *in-situ* measurement of sample temperature, as well as the direct visual control over the heating area distinguish our system from similar, but bulkier devices (Boehler et al. 2009).

Zusammenfassung

Eisen und Sauerstoff zählen zu den am häufigsten verbreiteten Elementen im Sonnensystem; das Fe-O-System gilt als einer der wichtigsten Bausteine von Mineralen und Mineralaggregaten. Reines Eisen ist von zentraler Bedeutung für die Kerne erdähnlicher Planeten, und verschiedene Fe-Oxide für deren Silikathülle (Mantel und Kruste). Eine Charakterisierung ihrer Struktur, ihrer Elastizität, sowie ihrer elektronischen und magnetischen Eigenschaften sind deshalb wichtig, um deren innere Struktur, sowie Prozesse in ihrem Innern zu bestimmen. In der vorliegenden Dissertation werden vier Modell-Minerale untersucht, um den Einfluss von hohem Druck und hoher Temperatur auf deren Eigenschaften zu charakterisieren.

I. Einkristall-Struktur und Spin-Zustand von dreiwertigem Eisen in Magnesium-Silikat-Perowskit

Es besteht allgemein Einvernehmen darüber, dass der untere Erdmantel zu ca. 80 vol% aus Magnesium-Silikat-Perowskit (Pv) besteht, der damit das häufigste Mineral in unserem Planeten darstellt. Zweifellos müssen Fe und Al in diesem Pv gelöst sein, deren exakte Gehalte sind jedoch nicht bekannt (Fiquet et al. 2008). Genauso wenig ist Druckabhängigkeit der Eigenschaften des Pv mit Fe-Al-Anteil charakterisiert. In der vorliegenden Studie widmen wir uns Proben mit der bisher wenig untersuchten Substitution $Fe^{3+}_A + Al^{3+}_B \rightarrow Mg^{2+}_A + Si^{4+}_B$. Dabei untersuchen wir in Abhängigkeit von Druck und Temperatur die Kristallstruktur des Minerals und die Verteilung chemischer Elemente zwischen verschiedenen kristallographischen Gitterplätzen. Des Weiteren stehen die Entwicklung des Spin-

Zustands von dreiwertigem Eisen als einem der wesentlichen Parameter zur Bestimmung der elektrischen Leitfähigkeit und der Strahlungskomponente der Wärmeleitfähigkeit im unteren Erdmantel (Xu et al. 1998, Goncharov et al. 2008) im Vordergrund.

An der Strahllinie ID09a am ESRF/Grenoble werden Pv-Einkristalle mit der Zusammensetzung $Mg_{0.63}Fe_{0.37}Si_{0.63}Al_{0.37}O_3$ (MgFeAlPv) durch Röntgenbeugung untersucht. Dabei kommt eine Kombination aus in-situ-Diamantstempelzellen-Technik mit Laserheizung zum Einsatz, mit der sich die extreme Bedingungen des unteren Erdmantels simulieren lassen. Diese Messungen sind für die Bestimmung der Elastizität eines Modell-Minerals des unteren Erdmantels von großer Bedeutung; mit ihrer Hilfe werden unterschiedliche, stellenweise widersprüchliche Beobachtungen und Interpretationen aus der Literatur untersucht. Wir präsentieren eine vollständige Beschreibung der Kristallstruktur von MgFeAlPv, sowie von Fe^{3+} auf dem 12-fach koordinierten Gitterplatz (A-Platz). Im Gegensatz zu Jackson et al. (2005) erkennen wir keinen Übergang im Spinzustand des dreiwertigen Eisens, was Berechnungen (Zhang and Oganov 2006, Stackhouse et al. 2007) sowie neuere Experimenten (Catalli et al. 2010) bestätigt. Allerdings sind auch für uns, auch nach Aufheizen der MgFeAlPv-Proben auf 1800 K und bei Drücken von ~78 GPa weder ein Übergang im Spinzustand noch eine druck-/temperaturabhängige Umverteilung von dreiwertigem Eisen und Aluminiums zwischen verschiedenen kristallographischen Plätze erkennbar, wie von Catalli et al. (2010) vorgeschlagen.

Aus unseren Daten ergibt sich eine Birch-Murnaghan-Zustandsgleichung dritter Ordnung mit folgenden Parametern: ein Kompressionsmodul von $K_0=233\ (4)$ GPa, seine Ableitung nach Druck von $K_0'=4.1(0.1)$, und ein Gleigewichtsvolumen bei Raumtemperatur von $V_0=169.7(3)\ Å^3$. Wir kombinieren die Daten bei Raumtemperatur mit solchen bei hohem Druck und hoher Temperatur, um eine vollständige Zustandsgleichung in Abhängigkeit von Druck und Temperatur zu erhalten, die auf der Formulierung von Saxena et al. (1999) basiert.

Das Ziel der Untersuchungen ist es, neue Informationen über Veränderungen in der Kristallstruktur und einzelnen Kristall-Gitterplätze in Magnesium-Silicat-Perowskit unter Druck zu erlangen, die in der Literatur bisher kaum verfügbar sind. Insbesondere können wir in einem Vergleich unserer Daten mit denen für reines $MgSiO_3$ zeigen, dass Kristalle mit dreiwertigem Eisen und Magnesium auf dem A-Platz im Gitter deutlich kompressibler sind als jene mit Aluminium und Silizium auf den Oktaederplätzen.

II. Kompressionsbedingte Metallisierung von Magnetit unterhalb von 25 GPa

Magnetit ist ein Eisenoxid mit gemischten Valenzen (Fe^{2+} und Fe^{3+}), und damit ein Modell-Mineral im Fe-O System. Als wesentlicher Bestandteil sedimentärer (Bändereisenerze BIF) und magmatischer Gesteine, kann Magnetit in natürlicher Umgebung hohem Druck ausgesetzt sein, zum Beispiel bei der Subduktion ozeanischer Kruste (Dobson and Brodholt 2005) oder während Serpentinisierung (eine metamorphe Reaktion). Magnetit stellt aufgrund seiner ferrimagnetischen Eigenschaften, die auf Wechselwirkungen von Fe mit unterschiedlicher Valenz sowie einer relativ hohen Néel-Temperatur eines der stärksten magnetischen Minerale dar. Der Magnetismus von Magnetit

bedingt auch sein komplexes Phasendiagramm, und für eine Abschätzung seiner Eigenschaften, zum Beispiel während seiner Bildung durch Serpentinisierung, müssen große Bereiche des Phasendiagramms untersucht werden. Aufgrund fehlender Erkenntnisse aus Hochdruck-Experimenten finden sich im Moment verschiedene widersprüchliche Hypothesen in der Literatur, die einen Phasenübergang von inversen bis normalen vorschlagen (Rozenberg et al. 2007) oder auch einen Zustandswechsel des Magnetismus (Ding et al. 2008). Aufgrund solcher Übergänge sollten elektrische und thermische Leitfähigkeit sowie Magnetismus von Magnetit im großen Maßstab verändert werden.

Um die komplexen physikalischen Eigenschaften von Magnetit bei Kompression zu bestimmen, kobinieren wir Einkristall-Röntgenbeugung mit Mössbauer-Spektroskopie für Magnetit bei Drücken bis 25 GPa. Im Gegensatz zu Ergebnissen mit Röntgenbeugung an Pulvern (Rozenberg et al. 2007), können wir keinen Hinweise auf einenn Phasenübergang von inversem zu normalem Spinel finden. Ähnlich zeigt die Auswertung unserer Mössbauer-Untersuchungen, dass ein Übergang von einem high spin zu intermediate spin Zustand in Magnetit zwischen 10-20 GPa nicht auftreten kann. Basierend auf der sorgfältigen Analyse von in der Literatur veröffentlichten Daten und Ergebnissen (Klotz et al. 2008, Baudelet et al. 2010) stellen wir ein widerspruchsfreies Modell vor, das die elektronischen und magnetischen Eigenschaften von Magnetit im Rahmen einer Ladungs-Delokalisierung unter hohem Druck erklärt. Darüber hinaus zeigen wir mit Experimenten, dass eine Änderung der elektrischen Leitfähigkeit von Magnetit durch Änderungen in der elektronischen Bandstruktur erklärt werden kann: Bei Raumbedingungen wird die elektrische Leitfähigkeit vom $t_{2g\downarrow}$ spin minority Band (spin down, Dedkov et al. 2002) bestimmt, unter hohem Druck weitet sich jedoch das $t_{2g\uparrow}$ spin majority Band und spin up Elektronen dominieren die elektrische Leitfähigkeit bei 15 GPa.

III. Intrinsische Defektstruktur des Wüstit und ihr Einfluss auf das Hochdruck/Niedrigtemperatur-Phasendiagramm

Unsere Untersuchungen an Wüstit (Fe_xO) verfolgen das Ziel das Phasendiagramm bei hohem Druck und niedriger Temperatur des Fe-Endglieds im (Mg,Fe)O-System zu bestimmen. Anders als in Magnetit, wo dreiwertiges Eisen als wesentliche Komponente kristallographische Oktaeder- und Tetraeder-Stellen besetzt, ist das Kristallgitter von Wüstit durch ein Gerüst aus zweiwertigem Eisen (in den Oktaeder-Positionen) aufgebaut; dreiwertiges Eisen besetzt in Form von Defekt-Stellen tetraedrische Zwischengitterplätze (Battle and Cheetham 1979). Einzelne Leerstellen formen Cluster und durch deren Ordnung ergeben sich Übergitter-Reflektionen in Röntgenbeugung in der Form von Linien oder Punkten. In der vorliegenden Untersuchung zeigen wir, dass Defektstellen aus dreiwertigem Eisen ein starken Einfluss auf das Phasendiagramm von Wüstit bei niedriger Temperatur haben.

Wir untersuchen das Phasendiagramm von nicht-stoichiometrischem Wüstit in der Zusammensetzung $Fe_{0.925}O$ and $Fe_{0.94}O$ bei niedrigen Temperaturen mit Hilfe von hochauflösender Neutronenbeugung. Änderungen im Verhältnis der Gitterparameter (c/a) sowie der Intensität der Beugungslinien ermöglichen es uns, kritische Temperaturen für die magnetischen (T_N) und strukturellen (T_S) Übergänge der Mineralien zu bestimmen. Nach einer gängigen Hypothese wird der Übergang von einer kubischen in eine rhomboedrische Struktur durch Magnetostriktion in Folge des magnetischen Übergangs hervorgerufen (Kanamori 1957). Im Gegensatz zu dieser Annahme stellen wir eine Divergenz von T_N und T_S bei hohem Druck fest. Da keine offensichtliche Korrelation zwischen

magnetischen und strukturellen Freiheitsgraden vorliegt, schlagen wir einen subtilen Mechanismus vor, der Strukturübergang unter den magnetischen Übergang drückt und durch eine Schwächung der magnetischen Wechselwirkungen zwischen den Fe^{2+} Ionen hervorgerufen wird. Es ist bekannt, dass $Fe_{0.925}O$ und $Fe_{0.94}O$ unterschiedliche Konzentrationen an Fehlstellen-Clustern aufweisen, die durch Fernordnung der Oktaeder-Leerstellen und Zwischengitterplätze an den Tetraeder-Stellen charakterisiert ist (Akimitsu et al. 1983). Die Änderungen in Defektstruktur der Minerale können die drastisch unterschiedliche Reaktion von $Fe_{0.925}O$ und $Fe_{0.94}O$ bei einer Komprimierung erklären. Wir sehen die Unterschiede in T_N und T_S als einen Hinweis auf Druckeffekte auf die intrinsische Defektstruktur an und erkennen einen Übergang von Ordnung zu Fehlordnung in $Fe_{0.925}O$, so wie Ding et al. (2005a) dies unter Umgebungsbedingungen berichten. Eine schnelle Dekompression aus dem Fehlordnungszustand von $Fe_{0.925}O$ (~8GPa) führt zu einem T_S-Wert, der um mehr als 50 K unter den T_S-Wert, der für $Fe_{0.92}O$ unter Raumdruck bestimmt wurde (Kantor et al. 2005). Wir glauben, dass sich aufgrund der schnellen Dekompression eine neue Defektstruktur bildet, die aus geordneten Fehlstellen-Clustern besteht. Diese Ordnung unterscheidet sich von der Fehlstellenordnung in ursprünglich Material. Damit stellen wir fest, dass dreiwertiges Eisen eine wesentliche Komponente der Defektstruktur in Wüstit darstellt und bei niedrigen Temperaturen einen starken Einfluss auf das Phasendiagramm hat, trotz des relativ niedrigen Gehalts von Fe^{3+}.

I V. Indizien auf topologische Elektronenübergänge in der hcp-Phase von Fe und $Fe_{0.9}Ni_{0.1}$

Wie oben ausgeführt, bestimmen Eisen und Eisen-Nickel-Legierungen (mit einem geringen Ni-Anteil) die Zusammensetzung in den Kernen erdähnlicher Planeten. Der Druck am Mittelpunkt solcher Planeten bewegt sich im Bereich von ~40 GPa für Mars und ~360 GPa für die Erde, mit der Möglichkeit, dass sich für beide Planeten ein fester innerer Kern gebildet hat. Die stabile Phase und physikalische Eigenschaften von Eisen und Fe-Ni unter solchem Druck sind daher von zentraler Wichtigkeit für das Verständnis von planetaren Kernen. Mögliche Kristallstrukturen, die bei hohem Druck stabil sind, sind *bcc*, *fcc*, und *hcp*, wobei *hcp* wohl die stabile Phase im inneren Erdkern ist.

Für reines Eisen und $Fe_{0.9}Ni_{0.1}$ als Modellzusammensetzungen untersuchen wir den Druckeffekt auf das elastische und elektronische Verhalten der *hcp*-Phase unterhalb von 70 GPa. Eine Auswertung der Literatur (Mao et al. 2001, Crowhurst et al. 2005) ergibt, dass für Eisen eine Anomalie in der Debye-Schallwellengeschwindigkeit (V_D) im Bereich 40-50 GPa vorliegt. Mit Hilfe von nuklearer inelastischer Röntgenstreuung finden wir für die *hcp*-Phase in $Fe_{0.9}Ni_{0.1}$ eine ähnliche Anomalie, und untersuchen diese mit Hilfe von Röntgenbeugung und Mössbauer-Spektroskopie im Detail.

Nach Auswertung der experimentellen Daten stellen wir eine Abnahme des Verhältnis der Gitterparameter *c/a* für Eisen im Druckbereich unterhalb von 45-50 GPa fest, sowie eine nicht-lineares Verhalten der Isomerverschiebung in Mössbauer-Experimenten, was einen iso-strukturellen Phasen-Übergang in diesen Phasen nahelegt.

Mit Hilfe von Elektronenstruktur-Berechnungen, unter Berücksichtigung von Vielkörper-Korrelationseffekten (LDA+DMFT), haben wir paramagnetisches *hcp*-Eisen unter Druck untersucht. Die Berechnungen sagen einen Übergang in der Elektronen-Topologie (ETT) voraus. Nach einem Vergleich von Daten an Materialien mit bekannter ETT (Varlamov et al. 1989) mit unseren

Beobachtungen und theoretischen Vorhersagen, ziehen wir den Schluss, dass sich die verschiedenen, voneinander unabhängigen, experimentellen Beobachtungen durch eine ETT erklären lassen.

V. Tragbares Laser-Heizsystem für Hochdruck-Experimente

Die Entwicklung eines tragbaren Laser-Heizsystems wurde im Rahmen unserer Arbeiten über Materialien des unteren Erdmantels (Dubrovinsky et al. 2010a, Narygina et al. 2011, Potapkin et al. 2011) vorangetrieben. Im Zusammenhang mit dieser Disseretation war es im Besonderen für die Untersuchungen des MgFeAlPv (Abschnitt I) unter hohem Druck und hoher Temperatur notwendig. Der Hauptvorteil des entwickelten Systems liegt in seiner Kompaktheit, der Verwendungsmöglichkeit für Experimente sowohl im Labor als auch am Sychrotron. Zu den Messverfahren, die zusammen mit der Laserheizung unter hohem Druck durchgeführt werden könne, zählen Messungen des elektrischen Wiederstands, Raman-Spektroskopie, energie- und zeitaufgelöste Mössbauer-Spektroskopie, Pulver- und Einkristall-Röntgendiffraktometrie, inelastische Kernstreuung sowie Röntgenabsorptionsmessungen. Geringe Montagezeiten, vielseitige Einsatzmöglichkeiten, stabile und homogene Heizbarkeit, in-situ-Bestimmungen der Probentemperatur bei gleichzeitiger visueller Kontrolle der beheizten Fläche heben unser System von ähnlichen, jedoch größeren Heizsystemen (Boehler et al. 2009) ab.

1. Introduction

1.1. Origin and structure of Earth and terrestrial planets

Our knowledge of the surrounding world has greatly improved from the ancient times. It is generally accepted that our planet Earth is one of the eight planets taking an elliptical orbit around the Sun – the center of our Solar system.

The Solar System was formed around 4.568 billion years ago (Bouvier and Wadhwa 2010) as a result of the nebula (giant atomic/molecular cloud) collapse. Conservation of the angular moment made the cloud rotate faster pushing mass to the center of the rotation. At the same time, the collapse of the nebula released enormous amounts of energy which was absorbed by the cloud material due to its high radiative opacity. Thus the early stages of the our Solar system were extremely hot. The densest part of the compressing cloud became our Sun and the Solar system planets were formed later.

At the first stage, radiative cooling of the nebula material led to the precipitation of highly refractory compounds - materials with high melting temperature (1850-1400K)(Lewis 2004). These were lithophile (rock loving, Ca/Al oxides and silicates) and siderophile compounds (free metals - W, Ir, Os, Fe, Ni, Co). Due to reducing conditions of the process, metals like Fe were condensing in pure or alloy form (Fe-Ni). Major condensation of Mg, Si is considered to happen at 1400-1250K with formation of forsterite ($Mg_2SiO_4 \sim 1400$ K), and enstatite ($MgSiO_3$) at slightly lower temperatures (1100 K). Atomic sodium and potassium could remain in vapor phase until the completion of the enstatite formation. At temperatures 1250-650 K, Na and K in form of vapor were reacting with Al bearing minerals producing alkali aluminosilicates. Upon further cooling (680-600 K), the first and one of the most important sulfides FeS was formed. Finally at even lower temperatures, cooling of gases containing highly volatile elements (C, H, O, N) led to their condensation (Palme and Jones 2003). First, O an OH components were incorporated into forming minerals, then ammonium salts were formed, followed by condensation of different ices. The lightest elements in form of H_2 and He evaded condensation or solidification maintaining gaseous form.

Although, the earliest stages of the Solar system formation are not well understood, it is likely that dust particles and constantly condensing material could build up meter to kilometer sized bodies in presence of the nebula as a result of turbulence and gravitational instabilities (Goodman 2000). According to the widely accepted planetesimal theory (Lewis 2004), the accretion process continued after dissipation of the nebula with smaller objects devoured by larger bodies, and with the latter constantly increasing their mass and gravitational influence. Massive bodies were absorbing smaller, at the same time decreasing their own orbital eccentricity and inclination. After certain period of time, most of the nebula material was consumed by larger planetary embryos and the last stage of planet formation, also called 'oligarchic growth', is considered to be the slowest and the most spectacular, including giant collisions of Mars/Moon size objects (Agnor 1999). Energy released in such massive impacts together with energy provided by radioactive decay of isotopes was sufficient to melt some of the protoplanets (partially or completely) leading to their differentiation (Tonks 1992, Rubie et al. 2007).

The differentiation of the terrestrial planets originates in density difference between the silicates

and metal phases and manifests in the depletion of mantle with siderophile elements relative to the original abundances (Solar system or chondric). According to the modern planetary core formation theories, diapirs formed by dense siderophile elements (Fe, Ni, Co, Pt, Pd, Au) were sinking through magma ocean or the partially molten mantle. Discrepancies between the predicted and observed concentrations of the siderophile elements in Earth's minerals representing crust and upper mantle gave birth to additional hypotheses, namely, metal-silicate equilibration at high pressure and temperature at the base of magma ocean (Murthy 1991), the 'late -veneer' hypothesis describing addition of material to the Earth's lithosphere by meteor/asteroid bombardment (Kimura et al. 1974, Morgan 1986), and inefficient core formation with small quantity of iron trapped in the mantle during core formation (Jones and Drake 1986).

Although each of the terrestrial planets (Mercury, Venus, Earth, Mars) has gone through its own peculiar stages of evolution, it is believed that the processes of metal core formation, its differentiation from silicate mantle, and complex crystallization of the magma ocean (Labrosse et al. 2007, Solomatov 2007) are common mechanisms. Undoubtedly, from all of the terrestrial planets the Earth has been studied the most. Direct access to the invaluable information on the structure of the Earth comes from the measurements of seismic sound velocities, which combined with advances in high pressure experimental research provide necessary information to constrain, to certain extent, Earth's interiors and compositions of the silicate mantle and the core (Figure 1.1).
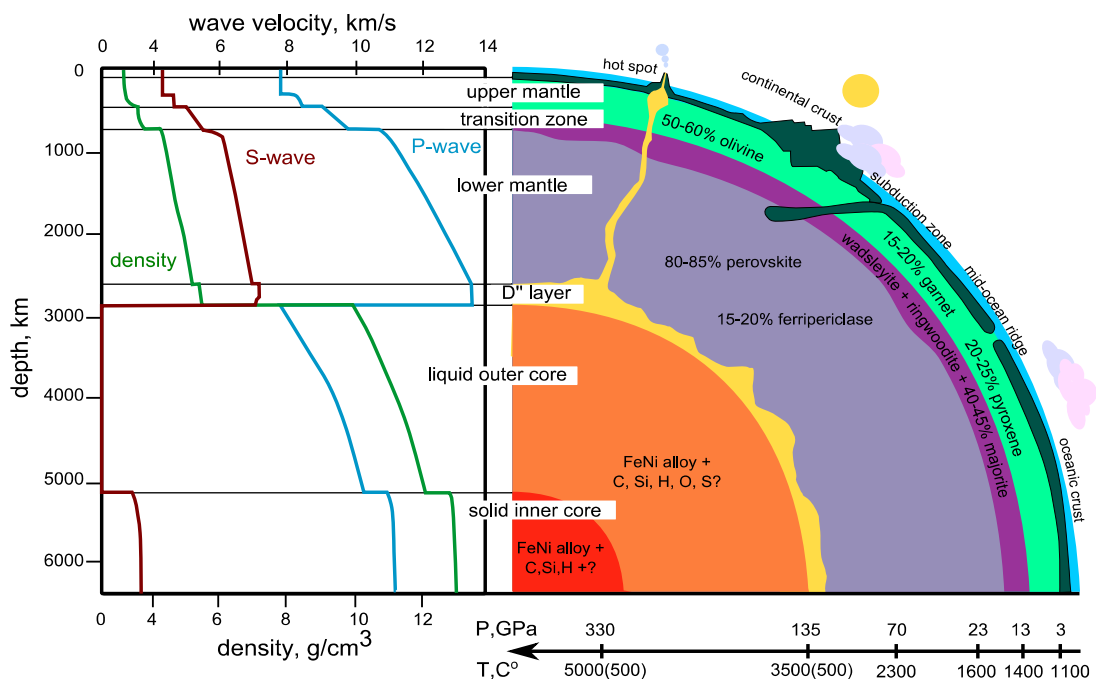
Figure 1.1:

Representation of the Earth's inner structure together with density and seismic sound velocity profiles after Dziewonski and Anderson (1981). The ratio of the major upper/lower mantle minerals are given in volume fractions (Stixrude and Lithgow-Bertelloni 2005a, 2005b)

The bulk chemical composition of the Earth and other terrestrial planets is tightly bound to the Solar nebula composition, and to composition of planetosimals consumed during the accretion process. More than 99.8 wt.% of the Solar system is concentrated in the Sun (Woolfson 2000), and its composition represents the nebula ancestor or the Solar system abundances. Additional evidences come from the meteorite studies. The elemental abundances of the most chemically primitive carbonaceous chondrite C1 type meteorites (with exception of highly volatile elements) are close to that of the Sun (McSween and Huss 2010). This observation supports the idea of the homogeneity of the solar nebula predicting similarities and regular correlations of terrestrial planet compositions/mineral assemblages. By knowing the principal structure of the Earth (Figure 1.1) and using a number of additional arguments, it is possible to constrain roughly the composition of the bulk silicate Earth (BSE) differentiated from the core (Table 1.1.1).

It is generally accepted that the solid inner core and the liquid outer core of the Earth are composed from dense iron-nickel alloy. However, the outer core has a density deficit of 6-10% compared with the pure liquid iron at the same conditions (Birch 1952, Nimmo 2007). The density deficit of the outer core and the smaller density deficit of the inner core (Jephcoat and Olson 1987) are believed to be an effect of alloying by a light element. Carbon, oxygen, hydrogen, sulfur and silicon are considered as the most probable candidates. Analysis of data provided by NASA space missions shows that incorporation of a light element to the material of a planetary metallic core is a common feature of the terrestrial planets (Goettel 1988, Urakawa et al. 2004). For instance, the core of the Mars may contain as much as ~14 wt % of sulfur. Although there is not enough information on the planet Venus, it is reasonable to assume that amount of sulfur as volatile element in the cores of the terrestrial planets increases proportionate to planetary orbital radii in the Solar system. Taking into account that even Mercury may have non negligible amount of the sulfur in the core (Sohl and Schubert 2007), one comes to conclusion that sulfur could be an essential component of Venus planetary core.

Table 1.1.1:

Major elements composition of the BSE according to different estimates (wt.%)

	A	**B**	**C**	**D**	**E**	**F**	**G**	**H**
MgO	38.1	38.3	36.8	35.5	37.8	37.8	37.8	36.3
Al_2O_3	3.3	4.0	4.1	4.8	4.1	4.4	4.1	4.7
SiO_2	45.1	45.1	45.6	46.2	46.0	45.0	46.1	45.6
CaO	3.1	3.5	3.5	4.4	3.2	3.5	3.2	3.8
FeO^t	8.0	7.8	7.5	7.7	7.5	8.1	7.5	8.2
Total:	97.6	98.7	97.5	98.6	98.6	98.8	98.7	98.6

A - (Ringwood 1979) B - (Jagoutz et al. 1979); C - (Wänke et al. 1984); D - (Palme and Nickel 1985); E - (Hart and Zindler 1986); F - (McDonough and Sun 1995); G - (Allègre et al. 1995); H - (O'Neill and Palme 2000); FeO^t – All Fe as FeO

All in all, the interiors of the Earth and the terrestrial planets are strongly differentiated, and basically consist of the core, the silicate mantle and the crust. The cores of the terrestrial planets are metallic and average densities of terrestrial planets are higher compared with the giant planets of the outer Solar system. Due to the lack of direct experimental observations focused on the deep interiors of the Mars, Mercury, and Venus it is hard to constrain their composition or inner structure (Riner et al. 2008). However, it is possible that some of them, for instance the Mercury, have less complex structures than the structure of the Earth, which has its own fascinating path of evolution. According to the seismological model of the Earth, it has seven separate regions, namely, the crust, upper mantle, transitional zone, lower mantle, D" layer, the liquid outer and the solid inner core. The transitional zone and the D" layer are believed the most peculiar features of the Earth interior.

1.2. Mineral assemblage of the Earth's mantle.

The widely accepted and successful 'pyrolite' model (Ringwood 1962) states that olivine $(Mg,Fe)_2SiO_4$ is the major component of the upper mantle (Figure 1.2). The stability of this mineral strongly depends on pressure-temperature conditions of the environment, and at 14 GPa (410 km depth)
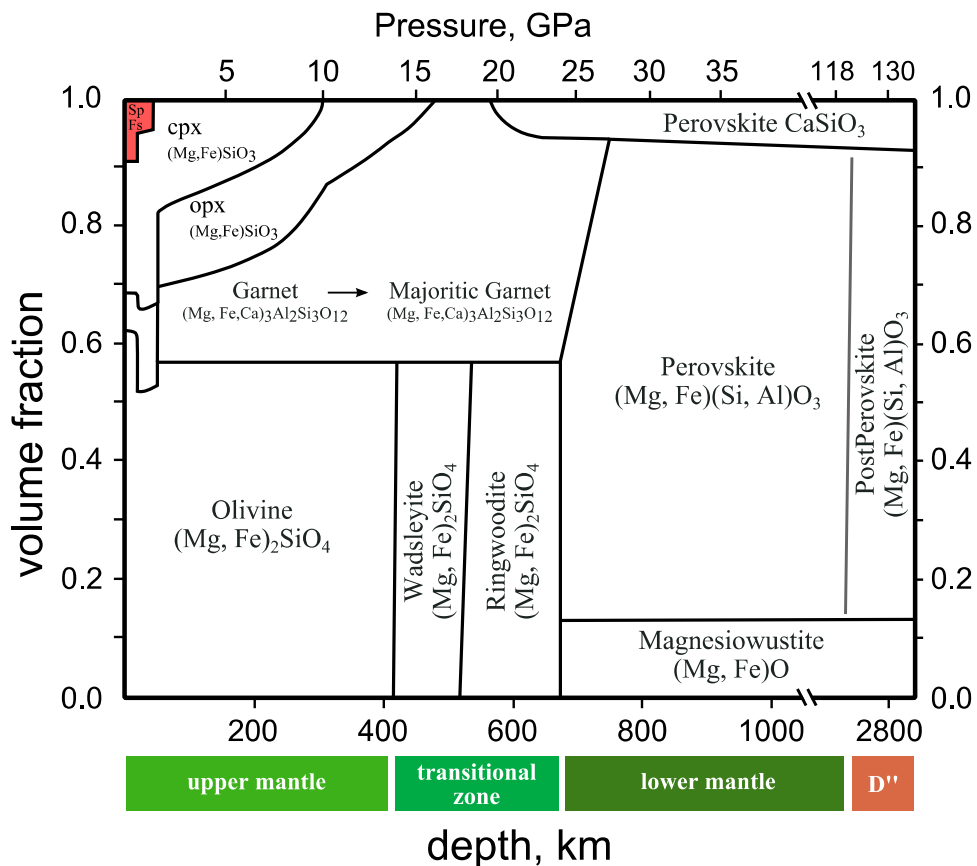
Figure 1.2:

Mineral volume fractions of the upper and the lower mantle. Opx, cpx, Sp, Fs indicate orthopyroxene, clinopyroxene, spinel and feldspar components, respectively. Modified after Frost 2008.

12

it undergoes a transition to a high pressure polymorph, namely β-phase or wadsleyite. However, the stability field of wadsleyite is limited as well, and in turn it transforms to the ringwoodite at 17 GPa (500-550 km depth), which later (660 km depth) disproportionates into ferropericlase (Mg,Fe)O and perovskite $(Mg,Fe)SiO_3$ phases. Here and below we use Fp and MgPv notations to indicate the ferropericlase and magnesium silicate perovskite phases, respectively. The transitions olivine→wadsleyite and ringwoodite→Fp+MgPv underline a beginning and an end of the transition zone, respectively separating the upper and the lower mantle. Variable, finite thickness of this zone at different regions of the Earth determined in seismologic studies is explained by strong influence of the temperature-pressure conditions on Clapeyron slope of the transitions (Bina and Helffrich 1994, Frost 2008). For instance, the transition zone should be thicker in a region of a subducting crust and thinner in the vicinity of a hot plum.

As shown in Figure 1.2, circa 40 vol% of the upper mantle is comprised from orthopyroxene, clinopyroxene, garnet phases including a small percent of feldspar and spinel. The volume fraction of these materials changes with depth, and feldspar, spinel and pyroxene dissolve within the garnet phase dominating at greater pressures (Moore and Gurney 1985). Garnet absorbs most of the pyroxene components with exclusion of Ca, which prefers to exsolve in form of $CaSiO_3$ perovskite (CaPv) at 18 GPa (Frost 2008). This phase is considered to be stable up to the core mantle boundary (CMB). Deep in the Earth's interiors, close to the transitional zone-lower mantle boundary (23-26 GPa or 660-670 km depth), garnet, similar to ringwoodite, undergoes a structural transition into the magnesium silicate perovskite phase. In first approximation, in absence of strong pressure-temperature gradients, average distribution of the Fe, Al elements in MgPv formed from ringwoodite and garnet should be the similar due to equilibration processes averaging the composition of the lower mantle.

Volume fractions of the lower mantle minerals are not well constrained as well as their Fe and Al content (Fiquet et al. 2008). Although, the exact proportions are unknown, it is clear that the MgPv is the most abundant lower mantle mineral, followed by Fp, and finally by CaPv. For instance, the 'pyrolitic' model suggests the following molar fractions of these minerals: 32.9% (Fp), 61.8% (MgPv) and 5.3% (CaPv) (Jackson and Ridgen 2000).

The deepest part of the lower mantle is the D'' layer (Figure 1.1). It spans up to 350 km (115-135 GPa) above the CMB and has 5-20 km thick patches characterized by ultra low seismic sound velocity anomaly - ULV (Thorne and Garnero 2004). For some of these D'' regions the corresponding seismic wave velocities are reduced by ~30%. The enigma of the D'' layer was partly resolved by a discovery of a postperovskite (PPv) phase. At conditions similar to the conditions of the D'', MgPv (Pnma space group) undergoes a transition to a postperovskite phase (Pnmn) (Murakami et al. 2004). In addition, there are evidences suggesting that composition of D'' is heterogeneous and probably represents different phase assemblages (Lay et al. 2008). The possible scenario include formation of metal bearing layers (Manga and Jeanloz 1996), iron rich PPv phase (Mao et al. 2004), partial melting (Williams et al. 1998, Labrosse et al. 2007, Mosenfelder et al. 2009), and finally iron rich Fp phase (Wicks et al. 2010).

1.3. The core material of terrestrial planets

The common feature of the terrestrial planets is the separation of the silicate mantle and the

denser metallic core. After taking into the solar system abundances of the elements, one can constrain principal material of the Earth's core - Fe-Ni alloy bearing is ~5-15% of Ni as estimated from the geochemical models (McDonough and Sun 1995, Dubrovinsky et al. 2010b). In case of the Earth, seismologic studies provide unambiguous evidences that the outer core is liquid, as it has no shear seismic wave response. The Earth's inner core is solid. The Earth's mantle extracts heat from the system comprised from inner-outer cores, promoting crystallization and growth of the inner core. This process drives convection of the liquid iron in the outer core (Nimmo and Alfè 2007), and is considered as one of the reasons for geodynamo of the Earth and Mercury, which is the source of their planetary magnetic fields.

Early shock wave experiments have shown that the Earth's outer and the inner cores are too light to consist of pure iron (Birch 1952, Jephcoat and Olson 1987), with C, O, H, S, and Si named as the candidate alloying elements. The Earth is not the only terrestrial planet having a light element in its core. Sulfur is considered to be the most plausible candidate for the Mars and Mercury cores (Urakawa et al. 2004, Sohl and Schubert 2007, Zuber et al. 2007). Recent advances in high pressure research and new data on the terrestrial planets stimulated great number of studies of the iron based alloys with or without addition of a light element. Making a long story short, there are three possible candidate
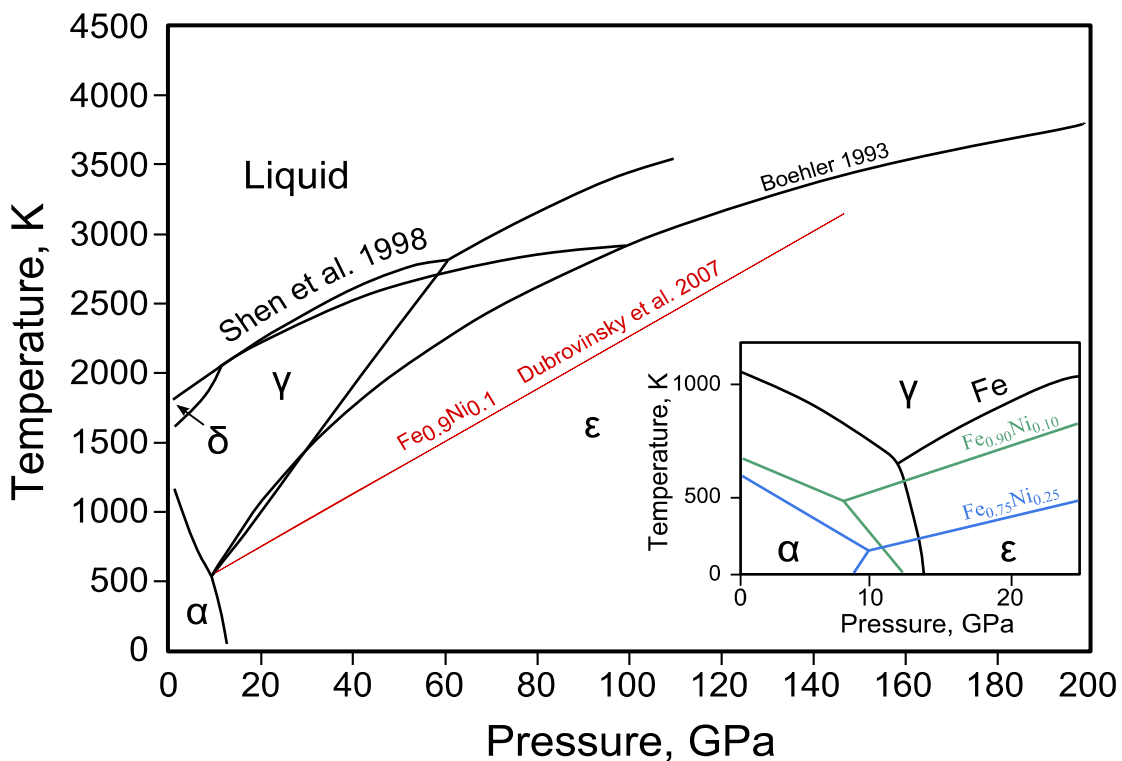
Figure 1.3:

Phase diagram of pure iron compiled from static experiments results. The red line represent *fcc-hcp* phase boundary for the $Fe_{0.9}Ni_{0.1}$ alloy. Inset shows the effect of nickel incorporation on the stability field of the iron ambient and high pressure polymorphs (α,δ-*bcc*, γ-*fcc*, ε-*hcp*). Modified after (Huang et al. 1988, Boehler 1993, Shen et al. 1998, Dubrovinsky et al. 2007).

structures of iron or iron-nickel alloy for the cores of the Earth and other terrestrial planets . They are body centered cubic (*bcc*), face centered cubic (*fcc*), and hexagonal close packed (*hcp*). Addition of a light element can result in formation of solid solutions (Lin et al. 2003a), or in a mixture of different phases (Urakawa et al. 2004, Ono and Kikegawa 2006). There are certain nuances, for example, some light elements can inhibiting dissolution of the other, and partitioning of the light elements between the solid and the liquid cores is different for different elements. One of the state-of-art models predicts 8% silicon/sulfur content for the Earth's inner core and 8-10% silicon/sulfur plus 8-13% oxygen for the Earth's outer core (Nimmo and Alfè 2007).

According to the preliminary Earth reference model (PREM), the Earth's core lies ~2900 km deep from the ocean level with corresponding pressure range 136 to 364 GPa at the CMB and in the center of the Earth, respectively (Dziewonski and Anderson 1981). The terrestrial planets have smaller sizes and masses compared to the Earth. It is reasonable to assume that pressures of their interiors are smaller, reaching, for instance, depending on the model composition of the Mars core ~40-47 GPa (Urakawa et al. 2004).

2.   Motivation

Iron is the principle element of the Earth's lower mantle and the core.

The cosmic abundance of the iron is very high, due to the extreme stability of the ^{56}Fe produced by nucleosynthesis in stars (Truran and Heger 2005). After H, He, O, C, N, Ne, Mg, and Si, iron is the ninth most abundant element of the Solar system (molar abundances relative to Si) (Cameron 1973), and forming alloy with Ni it contributes up to 32 wt.% to the mass of our planet (Morgan and Anders 1980). Iron has proved to be one of the most important material for the human civilization evolution and is widely used in different forms.

The Earth's or terrestrial planets cores are the largest planetary reservoirs of iron. Although, properties of pure iron or iron-nickel alloy at ambient or under extreme conditions of planetary interiors have being studied for decades, simple material like iron does not stop to surprise us. Heat transport from the Earth's inner core drives convection of liquid iron in the outer core generating geodynamo. The latter is the source of planetary magnetic field, and its dynamics is still a challenge for geophysicists. Away from the extreme hot conditions, there is no simple explanation of high pressure induced superconductivity of the iron at extremely low temperatures (Shimizu et al. 2001).

The lower mantle is by volume the largest entity of the Earth. It is believed that lower mantle minerals incorporate in average 10 mol.% of the iron in form of Fe^{2+} or Fe^{3+} (Sturhahn et al. 2005), however, in certain cases, for instance in D" layer (Labrosse et al. 2007, Wicks et al. 2010), the amount of iron could reach 42 mol.% (Fp). Determining properties of materials composing the lower mantle, namely magnesium silicate perovskite (MgPv), calcium silicate perovskite (CaPv), magnesium ferropericlase (Fp) is crucial for our understanding of the Earth, its evolution and its current state. Taking into account that thermal, electrical conductivity and elastic properties of the lower mantle strongly depend on its oxidation state and electronic properties of iron (Xu et al. 1998, Lin et al. 2005a, Keppler et al. 2008), and that iron containing minerals such as MgPv and Fp build up the most of the

15

lower mantle, iron is its the most important transitional element of the Earth.

The Earth has been studied the most from the all of the Solar system terrestrial planets. However, meteorites studies and information available from space exploration missions suggest that FeO mantle component increases in series from Mercury to Mars, with the Mars mantle being more enriched in FeO component, than the Earth (Dreibus and Wanke 1987, Bertka and Fei 1998). Although, there is no clear data on the Mars structure and layering, it is assumed that MgPv and Fp materials are present in its mantle and should be enriched with iron.

In conclusion, understanding the properties of iron in different environments, the intrinsic element of lower mantle (oxides) and core of terrestrial planets (pure iron and iron alloys) is essential for the understanding, constraining and ultimately reliable modeling of the processes taking place in planetary interiors.

2.1. **Pure iron and iron-nickel alloy.**

As mentioned before, the principal crystal structures of iron and iron-nickel alloys with small nickel content are *bcc* (α, δ), *fcc* (γ), and *hcp* (ε) Figure 2.1. All of them are candidate structures for the core material of the Earth. At ambient conditions, application of high pressure (13-15 GPa) transforms magnetic *bcc* phase to a more dense polymorph – the *hcp* phase (Jamieson and Lawson 1962, Cort et al. 1982). The magnetic state of the latter is still under intense debate. At ambient conditions the *hcp* phase is considered to be stable at least to the pressures of the Earth inner core (Mao et al. 1990). At high temperatures the *fcc* phase takes over, however its stability field is limited to certain pressures.

Nickel and iron form complete solid solutions. Several studies have shown that addition of Ni increases the stability field of the *fcc* phase (Lin et al. 2002b), decreasing the *bcc* phase stability field to lower pressures. The compressional behavior of Fe and $Fe_{0.8}Ni_{0.2}$ *hcp* phases was reported previously
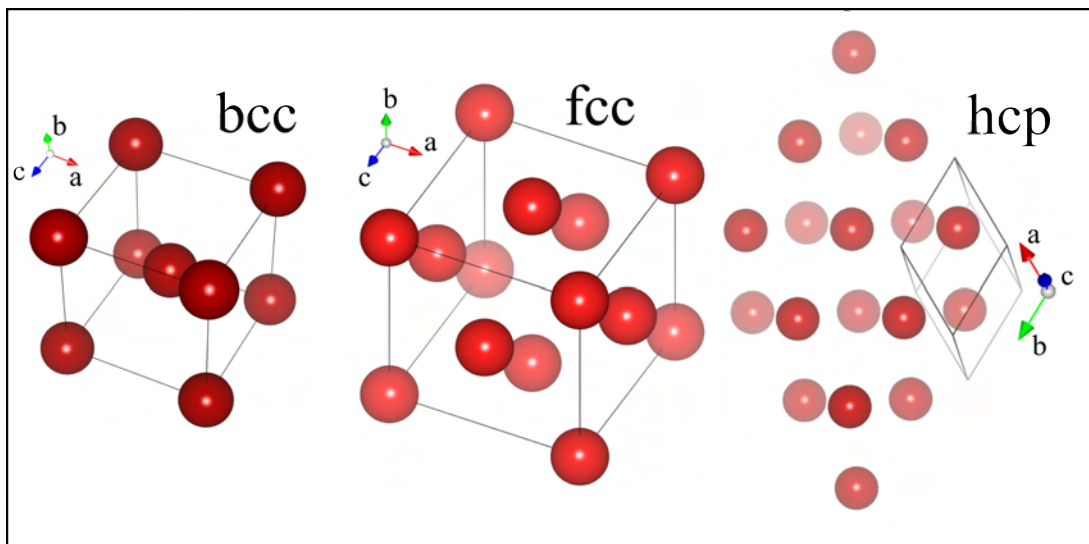
Figure 2.1:
A graphical representation of iron polymorph structures. Shown from left to right: *bcc*, *fcc*, *hcp*.
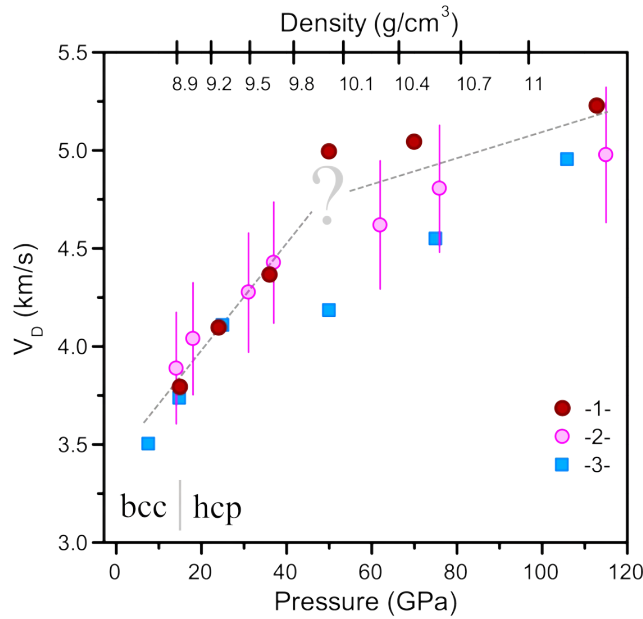
Figure 2.2:

Debye sound velocities for pure Fe measured in (-1-) inelastic nuclear resonant scattering experiment (NIS)(Mao et al. 2001), (-2-) impulsive stimulated light scattering measurements (Crowhurst et al. 2005). The blue symbols (-3-) correspond to $Fe_{0.92}Ni_{0.08}$ data points measured by NIS (Lin et al. 2003a). All points were measured at ambient temperature in static compression experiments. Dashed lines are the eye guides.

and was found to be the same withing error bars at 300 K (Mao et al. 1990). Parameters extracted from this study after fitting the 3rd order Birch-Murnaghan equation of states are *V_0=6.73(1) cm³·mol⁻¹, K_0 =165(4) GPa*, and *K'_0=5.33(9)*, and *V_0=6.737(5) cm³·mol⁻¹, K_0=172(2) GPa*, and *K'_0=4.95(9)* for pure iron and the iron-nickel alloy respectively, where *V_0* is the ambient pressure volume, K_0 is the bulk modulus and K'_0 is the bulk modulus pressure derivative.

Recent advances of high pressure and synchrotron radiation techniques allow measuring sound velocities and density of iron (Mao et al. 2001, Lin et al. 2003b, Crowhurst et al. 2005). Compilation of data measured by two different methods on pure iron and iron-nickel alloy are shown in Figure 2.2.

As mentioned above, both pure Fe and Fe-Ni alloys undergo the *bcc* to *hcp* phase transition at relatively low pressures (~16 GPa in hydrostatic pressure medium) (Mathon et al. 2004). Although, there is no evidence that crystal structure of *hcp* phase changes upon compression to 300 GPa (Mao et al. 1990), one can observe a clear softening of Debye or mean sound velocity at 50-60 GPa.

This subtle, but fascinating feature, observed for pure iron and iron-nickel alloy, has attracted our attention and we performed a joint experimental/theoretical study probing behavior of iron in pressure region close to the observed anomaly. The detailed description of experiments, their interpretation and comparison with a computed state-of-art theoretical model is given below (Section 5.4). Here we give a short overview of aims pursued and possible implications.

Due to the high discrepancy of data points at 40-60 GPa reported previously for pure iron and

iron-nickel alloy, we investigated behavior of $Fe_{0.9}Ni_{0.1}$ Debye velocities (V_D) at pressures below 62 GPa. Under an assumption that pressure induces an unknown isomorphic electronic transition in *hcp* phases of Fe and Fe-Ni alloy, and taking into account a discussion of *hcp* phase magnetic state (Cort et al. 1982, Steinle-Neumann et al. 1999a), we employed treatment similar to the one reported for another iron alloy- Fe_3C (Lin et al. 2004). We conducted a high pressure x-ray diffraction study probing evolution of *hcp c/a* lattice constants ratio as an sensitive indicator for electronic/magnetic transitions. In addition, we probed electronic and magnetic properties of *hcp* phases of pure Fe and $Fe_{0.9}Ni_{0.1}$ by means of Mössbauer spectroscopy. Finally, we compared our data with predictions of a theoretical study, conducted separately.

Knowing little how the suggested transition Clapeyron slope behaves as a function of pressure, we find it hard to discuss implications for the terrestrial planets, and a possibility to find such transition in nature. The recent estimations of pressures relevant for the Mars core give the upper limit ~47 GPa, which is close to the pressures of the observed V_D softening . The pressures at the core-mantle boundary (CMB) for the planet Venus are predicted to be a little lower than Earth's CMB ~100 GPa (Fegley 2007).

2.2. Crystal chemistry and spin state of iron in Earth's lower mantle minerals – magnesium silicate perovskite and magnesium ferropericlase.

Ferropericlase (Fp) and magnesium silicate perovskite (MgPv) are comprising the major part of the Earth's lower mantle. Formed as a result of a disproportion from olivine and garnet, both minerals contain non negligible amount of iron in form of Fe^{2+} and Fe^{3+}.

In contrast to Al-free or Al-containing MgPv, which are expected to have 30% or 50% of iron in Fe^{3+} state, respectively (McCammon 2005), Fp or $Mg_{1-x}Fe_xO$ is almost pure Fe^{2+} mineral. The incorporation of Fe^{3+} to the structure of the Fp is possible by formation of point defects, however is considered to be negligible, in contrast to its end member composition Fe_xO (x=0.89-0.95).

Average content of iron in Fp should vary proportionally to amount of FeO expected for a planetary silicate mantle, which changes from one terrestrial planet to another increasing in series from the Mercury to the Mars. The average composition of Fp in the Earth's lower mantle is considered to be around ~10 mol%. Due to the unique evolution of the Earth, the very bottom of the lower mantle can be enriched in iron (Labrosse et al. 2007, Wicks et al. 2010).

End member compositions of Fp (MgO, FeO) form complete solid solutions. The crystal structure of material with the ideal (x=0,1) or mixed composition is cubic. At ambient temperature application of pressure tends to change magnetic state of iron rich compounds (x>0.5) (Kantor et al. 2004), and then, at higher pressures, transforms cubic crystal structure of Fp (x>0.5) to rhombohedral structure (Jacobsen et al. 2005, Fei et al. 2007a). It is worth to note, that there is no plausible explanation describing nature of divergence between the onsets of magnetic and structural transitions observed at ambient temperature static compression experiments for Fp (x>0.5). The basic phase diagram compiled from different resources is shown in Figure 2.3.
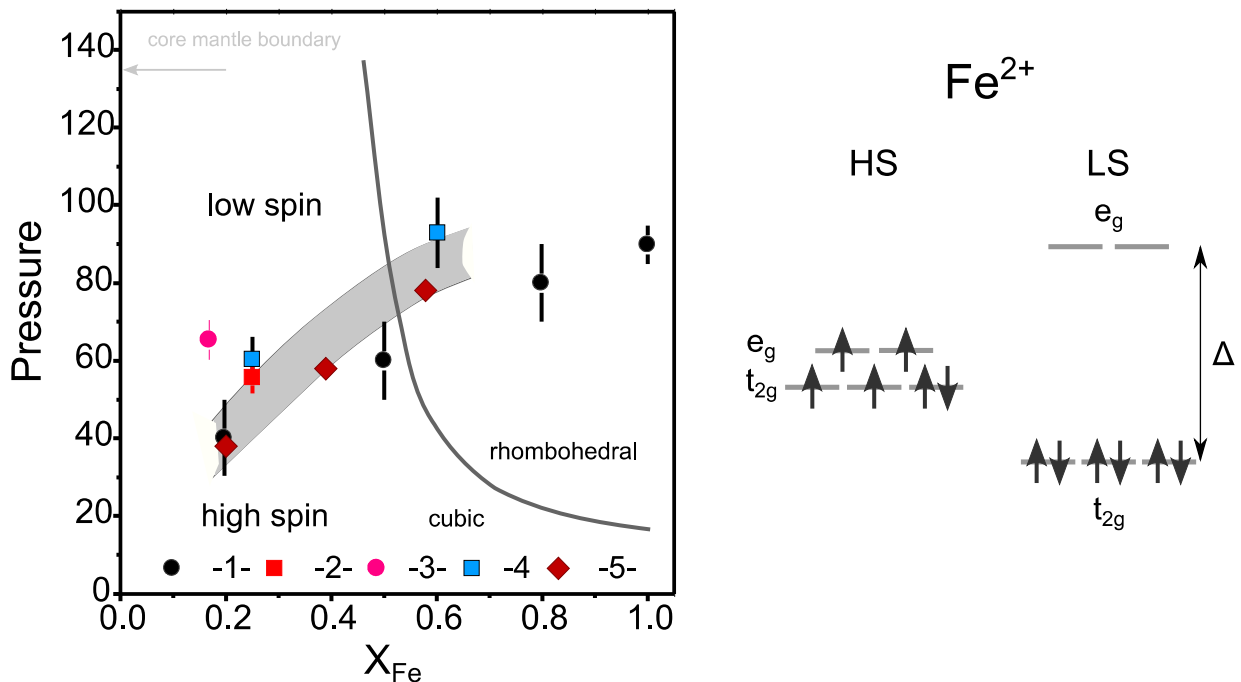
Figure 2.3:

(left) Phase diagram of $Mg_{1-x}Fe_xO$ for pressures relevant to the condition of the mantle (-1-) (Speziale 2005), (-2-) (Lin et al. 2006), (-3-) (Badro et al. 2003), (-4-) (Lin et al. 2005a), (-5-) (Fei et al. 2007a). (right) a basic diagram depicting high spin (HS) and low spin (LS) electronic configurations for Fe^{2+} ion in octahedral environment. Symbol Δ is used to show energy splitting of *3d* orbitals.

The most fascinating effect induced by compression in Fp is a spin crossover of Fe^{2+} ions, which is manifested through changes of electron charge distribution between t_{2g} or e_g electronic orbitals. Each of these orbitals has its own symmetry and energy, depending on the local environment. For example, t_{2g} and e_g *3d* orbitals are degenerate (have same energy) in case of a free atom/ion. Electrons of a free ion restrained by a crystal lattice experience interaction with electrons of neighboring atoms, and t_{2g}/e_g degeneracy is lifted by energy splitting of electronic orbitals (Burns 2005). This splitting affects distribution of charge at different orbitals and the total spin of ion. At certain conditions, a high spin (HS, S=2), an intermediate spin (IS, S=1) or even a low spin (S=0) electronic configuration may occur in nature (Dickson and Berry 2005). In case of Fe^{2+} in Fp, the low spin configuration becomes stable at ~40 GPa, depending on the composition (Figure 2.3). In low spin state Fe^{2+} has lower volume, and, consequently, unit cell volume of Fp decreases upon HS-LS transition changing elastic properties of Fp (Fei et al. 2007a). It was initially suggested, that pressure induced HS-LS crossover should affect other elastic properties of Fp, for example, sound wave propagation. However, a recent study have shown this suggestion to be wrong (Antonangeli et al. 2011). Still, the HS-LS transition in Fp is very important for the lower mantle, since it may modify partitioning of iron in lower mantle as was proposed in a multianvil study of material with 'pyrolite' model composition (Irifune et al. 2009).
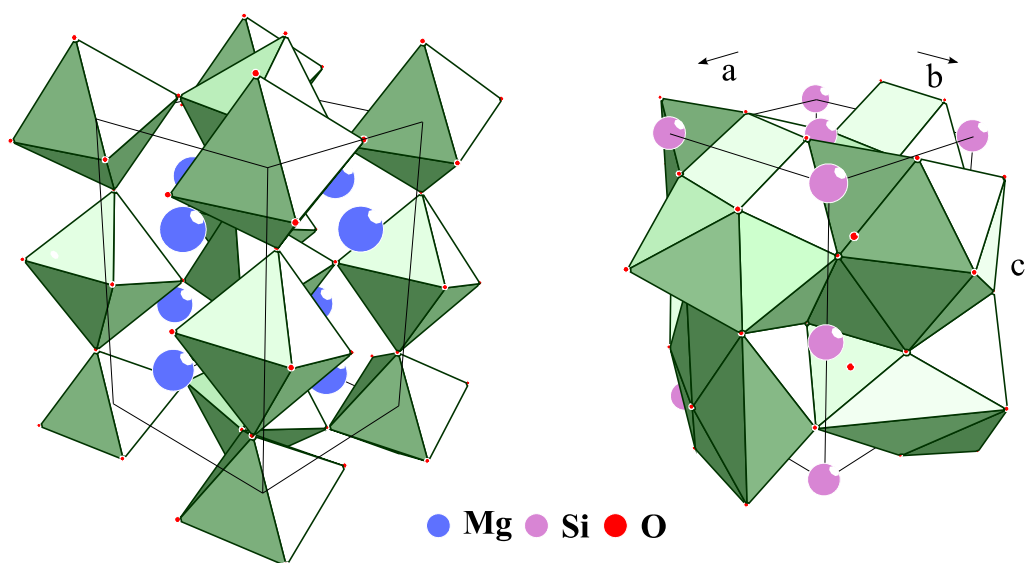
Figure 2.4:

Crystal structure of $MgSiO_3$ perovskite featuring two crystallographic sites, namely B- octahedral, occupied by Si (left), and A- dodecahedral or 8-12 site, occupied by Mg (right).

Crystal structure of pure $MgSiO_3$ can be described in terms of SiO_6 octahedra (B-sites) forming a 3D network and dodecahedra (A-sites) occupied by Mg ions (Figure 2.4). For real compositions representing planetary mantles, it is assumed that MgPv incorporate non negligible amounts of Al, and most importantly, Fe in Fe^{2+} or Fe^{3+} valence states.

Crystal chemistry of MgPv forces ferrous ions to occupy exclusively A-sites, most probably due to symmetry or size constraints. Ferric iron ions are smaller, and they can substitute both Mg and Si and take over A- or B- sites respectively. Valence number of magnesium ions is equal to two, thus Fe^{2+} ions can replace them in one to one ratio. Experiments demonstrated that Fe^{3+} can enter MgPv lattice through double substitution mechanisms, namely $Mg^{2+}_A+Si^{4+}_B{\rightarrow}Fe^{3+}_A+Fe^{3+}_B$ (SFE), and $Mg^{2+}_A+Si^{4+}_B{\rightarrow}Fe^{3+}_A+Al^{3+}_B$ (SAL), where A and B subscripts indicate the corresponding MgPv crystallographic sites.

Although valence states of Fe in MgPv remain unchanged with pressure (Jackson et al. 2005), it is possible that compression may modify Fe^{2+} and Fe^{3+} spin states promoting transitions to intermediate or low spin states. Indeed stress applied on crystal lattice of MgPv should increase crystal field splitting of *3d* orbitals of iron occupying A- or B- sites and may result in spin transition. At this point, however, there is a strong contradiction between theoretical predictions and experimental observations. For example, theoretical studies fail to predict intermediate spin state (Zhang and Oganov 2006, Stackhouse et al. 2007) for Fe^{2+}_A observed experimentally (McCammon et al. 2008). In addition, it has been recently shown that Fe^{3+} occupying octahedral B-sites undergo HS-LS transition at relatively high pressures (48-63 GPa)(Catalli et al. 2010). However, most theoretical studies assign the LS spin state to Fe^{3+} occupying B-sites for all pressures, including ambient.

The concept of the spin crossover in lower mantle minerals is very important for our understanding of the Earth's lower mantle. First, it has been shown that partitioning of iron between

MgPv and Fp changes at ~40 GPa (Irifune et al. 2009). The authors argue that redistribution of Fe^{2+} ions between MgPv and Fp phases coincide with of the HS-LS transition in Fp. However this may be also a result of the following process. Ferrous ions in MgPv undergo HS-IS transition at the same pressures, and it could be energetically more favorable for Fe^{2+} ion to be in LS state in Fp than in IS in MgPv. As was shown in the study of Irifine et al., only Fe^{2+} leaves crystal lattice of MgPv in favor of Fp, and Fe^{3+} content coupled with Al^{3+} remains almost unaffected. Considering electron hopping between Fe^{2+} and Fe^{3+} iron ions as the most effective conducting mechanism of MgPv, any change of iron partitioning between Fp and MgPv should affect electrical conductivity of the lower mantle, as well as elastic properties.

Most of the studies present in literature are focused on MgPv enriched with Fe^{2+} or Fe^{3+} incorporated through SFE substitution mechanisms. At the same time there are few studies on ferric iron introduced into MgPv lattice through SAL substitution. However, the latter case is important as well.

Ferric iron and aluminum incorporated into MgPv through SAL substitution occupy A-sites and B-sites, respectively. Theoretical studies predict no spin transitions of ferric iron occupying A-site at pressures below CMB (Hsu et al. 2011). However, pressure may induce redistribution of the Al^{3+} and Fe^{3+} between different crystallographic sites through ferric iron HS-LS spin transition (Catalli et al. 2010). Catalli et al. (2010) used reasoning similar to Irifune et al. (2009), and argued, that it may be energetically favorable for Fe^{3+}_A to exchange its position with Al^{3+}_B at high pressure and high temperature conditions. They suggested that such redistribution should happen above 48-63 GPa, and that $Fe^{3+}_A \rightarrow Fe^{3+}_B$ would have to change its spin state to LS. The implications are as follows. The transition proposed by Catalli et al. should affect elastic properties of MgPv because ferric iron is less compressible in LS state and has smaller radius. Thus the predicted redistribution of Al^{3+} and Fe^{3+} between different crystallographic sites will affect compressibility of MgPv unit cell in general and compressibility of different crystallographic sites in particular. Modification of elastic properties should change acoustic properties of MgPv. Finally, following similar lines of reasoning as above, electrical conductivity of MgPv material should be affected as upon Fe-Al redistribution in structure of MgPv charge hopping path and distances will change.

The importance of this effect for the properties of material, which is considered as the most abundant in the Earth's lower mantle inspired our single crystal x-ray diffraction study of MgPv with model composition $Mg_{0.63}Fe_{0.37}Si_{0.63}Al_{0.37}O_3$. The aims of the study were to explore elastic properties of the MgPv material at conditions similar to conditions of lower mantle and to test prediction of Fe/Al redistribution. In light of recent controversial experimental reports we employed single crystal x-ray diffraction as a tool capable to detect spin crossover (Fei et al. 2007b). The advantage of our single crystal x-ray diffraction with *in-situ* laser heating approach is its sensitivity to slightest changes of a crystal structure at ambient temperature as well as at temperatures close to the condition of the lower mantle. Laser heating was also employed to anneal material and release strain created by compression. The results of the study are presented below (Section 5.1).

2.3. Portable laser heating system as a new tool to emulate conditions of the lower mantle.

In order to have comprehensive understanding of the processes taking place in the depths of the our planet, we need to obtain reliable experimental evidence. Emulating conditions of the lower mantle requires use of different complicated high pressure equipment (discussed in Chapter 3). Generation of high pressure in diamond anvil cells has proven to be the most useful technique, as it covers the whole range of pressures relevant for the Earth's lower mantle and even core. However, high pressure investigations of magnesium silicate perovskite and ferropericlase require generation of high temperature, as temperature can modify critical pressures of structural, electronic transitions or any other properties, as was shown for (MgFe)O (Sturhahn et al. 2005, Komabayashi et al. 2010). The ultimate goal of geophysics is to study lower mantle minerals at conditions similar to natural, namely, high pressure-high temperature conditions.

Generation of high temperatures, similar to temperatures of the lower mantle is a challenging task. Due to diamond anvils oxidation, it is not possible to heat diamond anvil cells above 1000 K with external resistive heaters. Another technique - laser heating is available only at few scientific stations, even at large scale synchrotron facilities. However, on the one hand, the setups available to users are too cumbersome and do not allow to use full power of *in-situ* analysis, as impose restrictions for moving diamond anvil cells during the collection (European Synchrotron Radiation Facility (ESRF), Advanced Photon Source (APS), Super Photon ring (Spring-8) synchrotron facilities). It is worth mentioning that only few beamlines in the whole world allow homogeneous heating of the sample during data collection, but still, single-crystal x-ray diffraction could not be done on any of them. And of course, many facilities have no equipment for laser heating at all.

Having no alternatives of on-site available laser heating at beamlines of ESRF (ID09a – single crystal x-ray diffraction, ID18 - nuclear inelastic scattering, ID24 – x-ray absorption), and for extensive use in high pressure studies of materials relevant for the Earth's lower mantle, for example magnesium silicate perovskite (see sections 4.1, 5.1), we developed a unique portable laser heating system. We describe the system in detail in Section 5.5.

2.4. Electronic properties of minerals under high pressure – magnetite as a model system

It is in the nature of transitional elements that compression may transform properties of material by modifying their electronic and magnetic properties, and iron is a good example. For instance, magnetism of pure *bcc* iron is strongly suppressed by compression which forces a transition to the non ferromagnetic *hcp* phase (Iota et al. 2007). Of course effect of pressure varies from material to material, and a problem of iron oxide – magnetite is one of the most challenging.
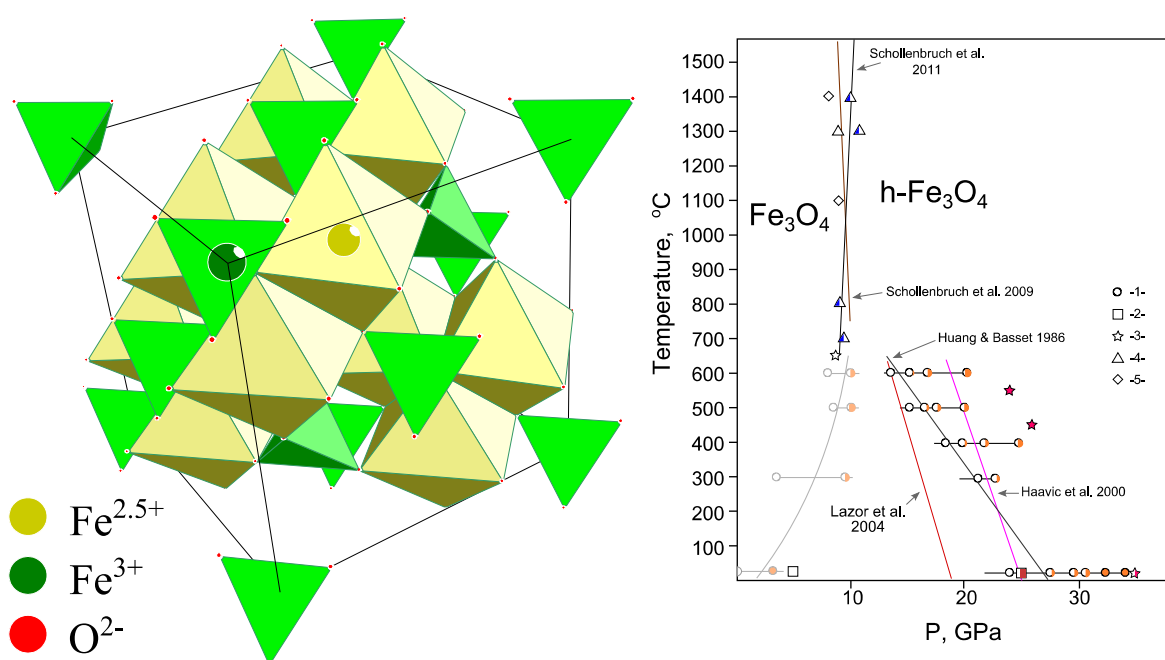
Figure 2.5:
Crystal structure of magnetite at ambient conditions (left) together with magnetite's high-pressure phase diagram modified after Schollenbruch et al. 2011 (right). Lines and symbols represent experimental points reported in (1)(Huang and Bassett 1986), (2)(Mao et al. 1974), (3) (Fei et al. 1999), (4) (Schollenbruch et al. 2011), and (5) (Schollenbruch et al. 2009). Symbol filling reflects the degree of transformation into high pressure polymorph (h-Fe₃O₄). We use grey shading to feature the reverse transition on decompression.

Being one of the oldest known magnetic materials, mixed valence iron oxide Fe_3O_4- magnetite has been studied for centuries leading to discovery of many unusual, puzzling and useful features. Among these are the low temperature Verwey transition (Verwey 1939) and half metallic state of magnetite (Dedkov et al. 2002). At ambient conditions, magnetite has inverse spinel structure (see Figure 2.5), generally described as $Fe^{3+}_T Fe^{2+}_O Fe^{3+}_O O_4$. Here we use T and O subscript symbols as indicators of respectively tetrahedral (T-) and octahedral (O-) sites. Magnetite is an antiferromagnet with an uncompensated magnetic moment and relatively high Néel temperature (858 K). Magnetic moments of iron at O-sites are aligned in [111] direction - opposite to magnetic moments of T-sites (total spin $4\uparrow=4\uparrow(Fe^{2+}_O)+5\uparrow(Fe^{3+}_O)-5\uparrow(Fe^{3+}_T)$). Volumes of the T- and O- sites are defined by a single parameter – the oxygen fractional unit cell coordination (*u*).

For geoscience, magnetite is more than a mineral. It is a valuable tool to study paleomagnetism, and is used as a thermobarometer for investigations of granitic rocks. At higher pressures magnetite can be found in nature as a product of mantle serpentinization (Blakely et al. 2005) or as major component of subducting iron banded formations (Dobson and Brodholt 2005). Incorporating considerable amount of iron, even at ambient conditions magnetite is a good example of material with strong correlation between electronic, magnetic and structural degrees of freedom. As can be seen from Figure 2.5, the high pressure phase diagram of magnetite is strongly influenced by the mineral's magnetic state, with Néel point separating high and ambient temperature regions at temperatures around 860 K.

Compression can induce significant modifications of magnetite's structure. The structure the mineral is transformed to a high pressure polymorph by application of pressures above 21-25GPa (Mao et al. 1974, Huang and Bassett 1986). Structure of the high pressure phase (h-Fe_3O_4) has been intensively investigated, however, no consensus has been reached (Mao et al. 1974, Fei et al. 1999, Haavik et al. 2000, Dubrovinsky et al. 2003, Schollenbruch et al. 2011). In addition to an unknown crystal structure of h-Fe_3O_4, behavior of the mineral in pressure region from 5 to 20 GPa is another higly debated topic. Numerous observations coming from Mössbauer absorption, x-ray powder diffraction, electrical resistivity and x-ray magnetic circular dichroism (XMCD) experiments have revealed unknown effects at 6, 10, 16 GPa giving birth to several mutually exclusive hypotheses (Rozenberg et al. 2007, Ovsyannikov et al. 2008, Ding et al. 2008). One of the most recent models suggests a transition from the inverse to the normal spinel structure (Rozenberg et al. 2007), and another suggests a transition of Fe^{2+} ions occupying octahedral sites from the high spin state to the intermediate spin state (Ding et al. 2008).

According to the model suggesting a transition from the inverse to the normal spinel structure (IS-NS), there is a change of electronic charge distribution at pressures above 8-10 GPa. Basically, application of pressure modifies spinel structure of magnetite resulting in Fe^{2+} ions occupying exclusively T-sites and Fe^{3+} ions occupying exclusively O-sites. This hypothesis is based on results from powder diffraction study (Rozenberg et al. 2007) which reported anomalous change of *u* parameter and, respectively, anomalies of volume ratio between T- and O- sites as a function of pressure.

The principal points of the second model promoting the high spin-intermediate spin (HS-IS) crossover are as follows (Ding et al. 2008). At ambient conditions Fe^{2+} occupying O-site are in the high spin state. However, authors suggest that Fe^{2+}_O ions change their spin state to the intermediate at 12-16 GPa.

The fundamental importance of magnetite representing broader group of minerals with common inverse spinel structure and incorporating strongly interacting ferric and ferrous ions has motivated this study. It goes beyond simple test of the mutually exclusive models providing insight on magnetite as a part of serpentinized mantle (Blakely et al. 2005) and as a part of iron banded formations in subducting oceanic crust (Dobson and Brodholt 2005). We have performed a combined x-ray single crystal diffraction and Mössbauer spectroscopy study to investigate complex physics of magnetite at pressures below 25 GPa. The single crystal x-ray diffraction study was a test for the IS-NS model. Having determined nuances of magnetite's crystal structure and its evolution with compression, we used this crystallographic model in order to fit collected Mössbauer absorption spectra and to constrain Mössbauer parameters and. The results and the analysis are reported in (Section 5.2).

2.5. Low temperature phase diagram of wüstite

Wüstite or Fe_xO is the end-member of the lower mantle mineral - ferropericlase (Fp). If compared with already mentioned iron-bearing oxide minerals important for the mantle, wüstite is the only compound which has an intrinsic ordered defect structure. Having close relationship to Fp phase, this monoxide was in focus of numerous studies, and its ambient temperature phase diagram (for selected compositions) is known very well (Pasternak et al. 1997, Ding et al. 2005a, Kantor et al. 2007, Fei et al.

2007b). However, the low temperature high pressure part of this phase diagram is almost unexplored.

At ambient conditions crystal structure of wüstite is cubic, rocksalt type. Being paramagnetic at ambient conditions, wüstite undergoes an antiferromagnetic transition at low temperatures (~200 K, depending on composition). Upon the transition magnetic moments of Fe^{2+} become aligned parallel to the [111] direction. Although knowing that temperature of the Néel transition strongly depends on composition of wüstite and consequently on its defect structure (Akimitsu et al. 1983), most of the previous high pressure studies have neglected the influence of this important parameter, which can modify properties of material and reveal new effects. For example, until recently it was believed that low temperature rhombohedral distortion of wüstite crystal lattice accompanying the antiferromagnetic transition is a result of magnetostriction (Kanamori 1957). This idea was proved to be wrong for $Fe_{0.92}O$ compound, with a structural (cubic to rhombohedral) transition shifted by ~40 degrees Kelvin below Néel temperature at 0 GPa (Kantor et al. 2005). We note that for $Fe_{0.94}O$ at 0 GPa the temperatures of the magnetic and structural transitions coincide. The divergence of critical temperatures for magnetic and structural transition in $Fe_{0.92}O$ was explained by a stabilization of an unknown cubic magnetic phase, similar to that observed at ambient temperature/high pressure experiments (Kantor et al. 2004, 2005), however a certain role of defect structure should not be excluded. In order to determine the effect of composition and intrinsic defect structure on the low temperature phase diagram of wüstite we conducted a high resolution neutron diffraction study probing two different compounds with similar type of defects but different concentration of them (Akimitsu et al. 1983), namely $Fe_{0.94}O$ and $Fe_{0.925}O$, at pressures up to 8 GPa. In particular, we tracked correlations between magnetic and crystal structures under pressure. The results of the study can be found below (Section 5.3).

3.   Experimental techniques

Generation of extreme high pressure-high temperature conditions

High pressure instrumentation is a logical extension of scientific tools developed for exploration of material properties. Being limited to ambient pressure experiments, scientists soon realized how to use pressure for advanced synthesis, analysis or modification of material properties. Moreover, modern high pressure instrumentation, including multi-anvil and piston cylinder apparatus, Paris-Edinburgh press, diamond anvil cell and etc. are invaluable tools for synthesis of materials with enhanced properties or substances metastable at ambient conditions. All of the mentioned techniques were developed and have been actively employed for geoscience related studies.

One can classify techniques of high pressure generation by different criteria: the upper pressure boundary, the highest achievable temperature, amount of sample, etc. For example, one can reach ~4 GPa using piston-cylinder setup, and ~28 GPa in multianvil apparatus used in combination with tungsten carbide cubes (used as pressure generating anvils)(Kubo 2000). State-of-art multianvil machines employing pricey cubes made from sintered diamond can generate pressures as high as 90 GPa (Zhai and Ito 2011), with a safe limit ~60-70 GPa (Yamazaki et al. 2010). However, the advanced techniques employing sintered diamond cubes can be used only at few places in the world. Some of most valued advantages of multianvil apparatus are relatively high pressure limits and large sample volume.

The main advantage of diamond anvil cells is possibility to step over the pressure limits of conventional multianvil apparatus and study material at higher pressures (>350 GPa, ≥5000 K) (Tateno et al. 2010). However, every achievement comes at a price, which is very small sample volume. Large part of the work presented below, excluding the neutron diffraction study of Fe_xO was done using diamond anvil cells (DACs). In the powder neutron diffraction study we used Paris-Edinburgh press. Both DAC and Paris-Edinburgh press high pressure generation techniques are described in the following sections.

It is clear, that Paris-Edinburgh press and DACs are just means to create high pressure conditions. A special section of this chapter is dedicated to *in-situ* methods used to investigate the mentioned materials, including x-ray diffraction, high resolution neutron powder diffraction, and Mössbauer absorption spectroscopy.

3.1.   Diamond anvil cells technique

The era of diamond anvil cells has begone in late 50s of the 20th century (Weir et al. 1959). However, the method has gained popularity only after a discovery of a reliable pressure standard (Forman et al. 1972). Since then, the technique has been evolving with constantly growing number of possible applications, including measurements of magnetic properties, resistivity, nuclear magnetic resonance, x-ray diffraction, x-ray absorption, optical spectroscopy (Chervin et al. 1995, Mito et al. 2001, Garg et al. 2004, Haase et al. 2009). The original bulky setup has changed, it has been miniaturized and adopted for different purposes.

Figure 3.1:

Schematic diagram of a four-pin modified Merril-Basset DAC. Diamonds fixed to metallic plates pressurize sample chamber. Four pins not shown in diagram improve stability of the cell.

Operation of diamond anvil cell is simple and can be described as follows. Application of force on two uni-axially aligned diamonds pressurizes sample chamber compressing a sample, a pressure transmitting medium and a pressure standard. The force can be applied in different ways, for example, tightening screws is the most popular one (Merrill and Bassett 1974). Basic diamond anvil cell (modified after Merrill-Basset design) is shown in Figure 3.1.

For in-house experiments, we used two types of DACs shown in Figure 3.2, the four pin modified Merrill-Basset cell and the piston-cylinder cell, developed in Bayerisches Geoinstitut (BGI). The typical dimensions of these cells are: diameter Ø50mm and height 40-45 mm.

The upper limit of pressure generated by diamonds depends on the design of diamonds and on diamonds culet size. The rule of thumb is: the smaller is diamonds culet size – the higher is the maximal pressure. For the works described below we employed diamonds with a culet diameter Ø250-300 μm.

Good mechanical stability of a DAC body, diamond backing plates, and gasket material are important in order to generate high pressure without breaking diamond anvils. Bodies of DAC, machined at BGI, are prepared from Republica or Nimonic alloys. Design of diamond backing plates usually depends on experimental technique and varies from a manufacturer to manufacturer. For BGI DACs we used hardened stainless steel plates. However, for single-crystal x-ray diffraction experiments, we employed Boehler-type diamonds and baking plates made from tungsten carbide (Boehler and De Hantsetters 2004). Gasket material was prepared by cutting rhenium metal bars into small plates (5·5·0.2 mm). Rhenium gaskets are less compressible than steel gaskets and allow to reach higher pressures without inducing extremely nonhydrostatic conditions. In addition, they contain no iron, and this is a very important criterion for ^{57}Fe Mössbauer absorption experiments.

Preparation of a DAC for experiments requires gluing diamonds to diamond backing plates (Figure 3.1), and installation of this assembly into the DAC body. Alignment of diamonds to a common

27
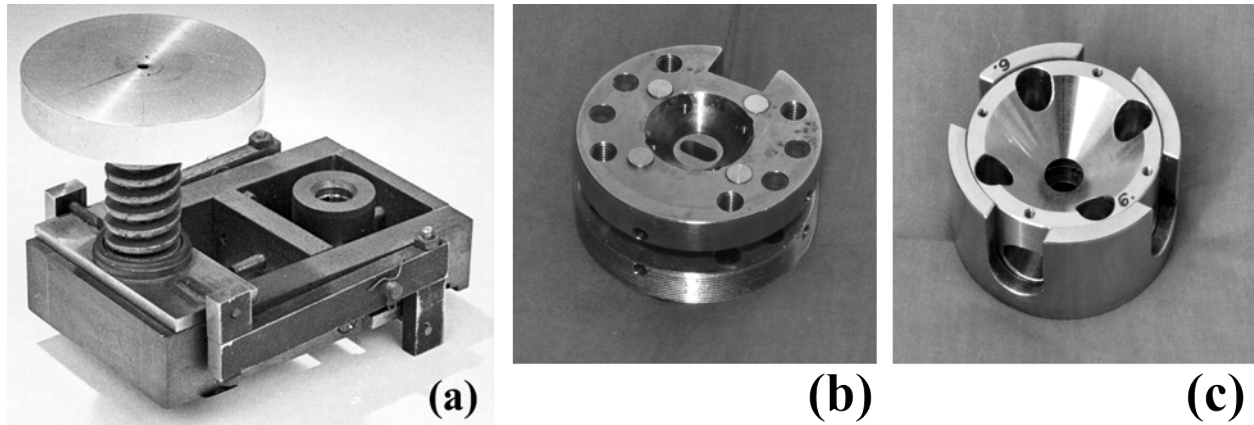
Figure 3.2:

Evolution of diamond anvil cells including (a) the first diamond anvil cell (Weir et al. 1959) and current designs (b) four pin modified Merril-Basset cell (c) piston-cylinder cell developed at Bayerisches Geoinstitut. The picture of the first DAC was retrieved from www.nist.gov

axis, perpendicular to a culet plane, is a crucial stage of the preparation. Tilt between diamonds culets is undesirable and can lead to destruction of diamond anvils at pressures lower than expected. Next, gasket material is preindented by diamonds to a desirable thickness, which is ~30-40 μm for diamond with culet size Ø250-300 μm. This step is followed by making a hole in the preindented gasket. The hole in the gasket serve as a sample chamber and, depending on a hole size, can be created at BGI by spark erosion, laser ablation, laser drilling and conventional drilling. The size hole should be around a half of the diamond culet size. Then, the whole setup including the DAC body with the installed and aligned diamonds, and the gasket is assembled together. Finally, sample material together with pressure standard, for example, ruby chips (Mao et al. 1986), gold, platinum, NaCl powders, etc. (Fei et al. 2007a) is loaded into the sample chamber of the gasket. Stress generated by diamonds is transmitted to a sample through a pressure medium.

If we exclude experiments where sample material plays a dual role, namely as a probe and a pressure transmitting medium, the choice of the pressure medium is very important. Each pressures transmitting medium has its own advantages or disadvantages, and hydrostaticity of a pressure medium is usually considered the most important criterion (Klotz et al. 2009). For experiments with DACs reported below we used the most hydrostatic pressure transmitting media (Ne or He), loaded into diamond anvil cells at 1-1.5 kbar by a gas loading system installed at BGI (Kurnosov et al. 2008).

3.1.1 Heating of samples loaded into diamond anvil cell.

In order to simulate particular processes relevant to the planetary mantles, application of high pressure is not enough, and generation of high temperature is a requirement. Some materials can be synthesized only at high pressure-high temperature (HP-HT) conditions, and for other materials their full phase diagram has to be explored, for example, in order to create convincing model of planetary interiors.

There are three common ways to heat samples loaded into diamond anvil cell. First of them is internal heating and involves heating of a sample by electrical current transmitted through the sample.

Although, one can reach quite high temperatures (≤2000K), the investigated material has to be metallic (Komabayashi et al. 2009).

In order to ensure homogeneous heating of any, even nonmetallic sample a whole-cell heating technique was developed (Dubrovinskaia and Dubrovinsky 2003). However, due to several limitations, including mechanical stability of DACs, and oxidation of diamond anvils, this technique should not be used above 1000 K - very moderate temperatures.

Combination of diamond anvil cell technique with the recent developments of solid state and CO_2 laser technology allows to bring laboratory samples, for instance *hcp* phase of iron (Tateno et al. 2010) to conditions similar to the extreme conditions of Earth's core (~300 GPa, 5000 K). Typical wavelengths of solid state and CO_2 lasers are 1064 nm and 10.6 μm, respectively. In general, heating by laser requires absorption of the laser beam by material, thus, at first glance, transparent materials should not be heated. This obstacle can be breached by using high power CO_2 lasers or by incorporating strong laser beam absorber on the surface of the heated sample or mixing it with sample material. Indeed, laser heating is very promising technique suffering from minor shortcomings such as non flexible temperature control.

We used laser heating for the study conducted on magnesium silicate perovskite, and some words should be said describing a procedure of temperature determination. Unlike, whole-cell heating technique employing thermocouples, temperature measurements of a sample loaded into diamond anvil cell are less obvious, as there is no direct access to the laser heated sample. Nevertheless, temperature can be monitored through diamond anvils, which are transparent for incoming (heating) and outgoing thermal radiation. In order to estimate temperature, most of high-pressure works (Bassett and Weathers 1986, Meng et al. 2006) collect thermal radiation coming from the heated spot on the sample, and than fit obtained spectra in the region of 500-800 nm to the Planck grey body radiation function. This function is defined as follows: $I(\lambda) = \frac{2 \cdot h \cdot c^2 \cdot \varepsilon(\lambda) \cdot \lambda^{-5}}{e^{h \cdot c / \lambda \cdot k \cdot T} - 1}$, where $I(\lambda)$ is spectral intensity, λ is wavelength, $\varepsilon(\lambda)$ is emissivity, T is the temperature; and c, h, k are respectively – the speed of light, the Planck constant and the Boltzmann constant. Strictly speaking, emissivity is a function of wavelength, surface roughness, absorption, etc., however it is usually considered as constant in real high pressure laser heating experiments (Sweeney and Heinz 1993).

In rare cases, temperature of the heated sample can be estimated directly from experimental data, for example when measuring nuclear resonant inelastic x-ray scattering absorption (Chumakov and Sturhahn 1999).

3.1.2 Paris-Edinburgh press

There is no doubt that constant development of equipment at synchrotron facilities, including creation of brighter x-ray sources allows to study various properties of materials under high pressure. One can find numerous x-ray diffraction, x-ray absorption, x-ray inelastic studies performed on samples loaded into DACs. However there are not many techniques allowing simultaneous evaluation of crystal structure and magnetic properties at extreme conditions. One of them is synchrotron nuclear forward scattering (Hastings et al. 1991), which allows *in-situ* probing magnetic properties of materials
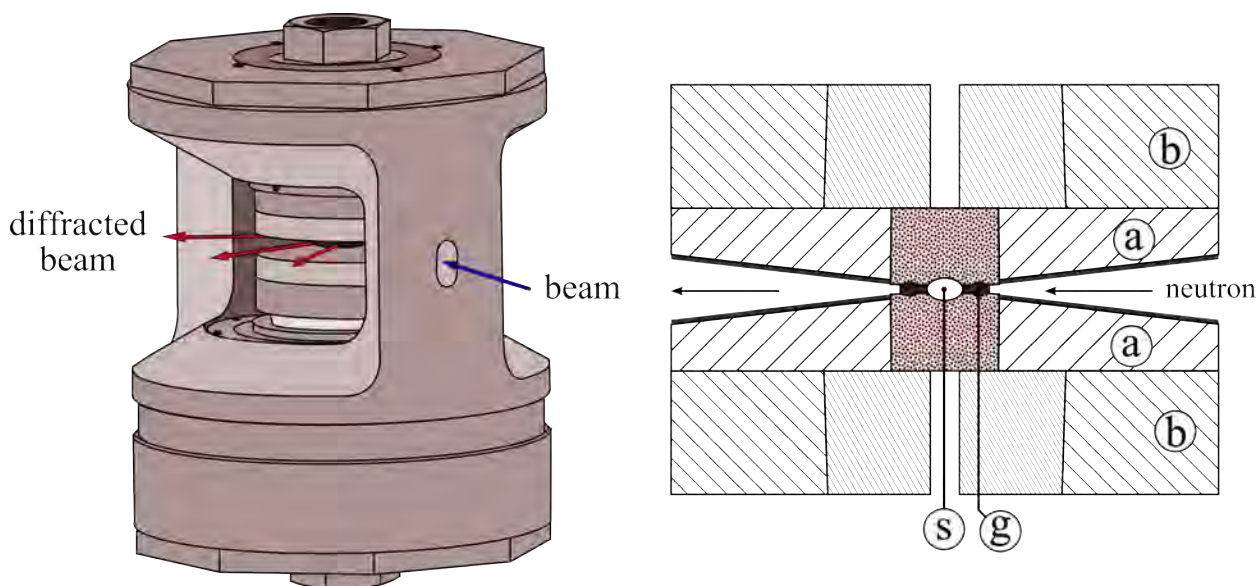
Figure 3.3:

Paris-Edinburgh press and its cross section - enlarged and featuring (a) anvils, (b) backing seats, (s) sample chamber, (g) TiZr gasket. Bold lines indicate cadmium shielding (Klotz et al. 2005).

containing a Mössbauer isotope and provides access to a crystal structure by means of x-ray diffraction (^{57}Fe resonant wavelength - 0.861 Å). However, if a simultaneous observation of magnetic and crystal structures is desired at high pressure, then neutron diffraction is the right tool.

Cross section of neutron scattering is different from x-ray scattering, and minimal amount of material required for neutron diffraction experiment is much higher than amount usually used in diamond anvil cell experiments. First designs of high pressure apparatus used for neutron scattering were limited to 3 GPa, and invention of Paris-Edinburgh press (Besson et al. 1992), shown in Figure 3.3, expanded pressure range accessible for neutron experiments up to 17 GPa (Morard et al. 2007). Although, this pressure is not high, compared with pressure range accessible with DAC technique, there are certain advantages of using Paris-Edinburgh press, including high 2θ range accessible for neutron diffraction (~140°)(Klotz et al. 2005).

Compression of material in Paris-Edinburgh press is achieved by a small hydraulic press which transmits stress upon anvils made from tungsten carbide or other hard materials. Anvils by-turn compress gasket loaded with a sample and with a pressure transmitting medium.

In order to create quasi-hydrostatic conditions, liquid or even gaseous pressure transmitting media are used (Bocian et al. 2010), with 4:1 methanol – ethanol mixture being one of the most popular transmitting media, as pressures created by Paris-Edinburgh press are not very high. Another widely used pressure transmitting medium is NaCl, which plays two roles in high-pressure experiments: as a pressure transmitting medium and as a pressure standard.

3.2. *In-situ* analysis

Experimental data shown and discussed below was obtained *in-situ* by means of single crystal x-ray diffraction, neutron powder diffraction, and Mössbauer spectroscopy. Each of these techniques is

described in a separate chapter below. In addition to these methods, characterization of prepared samples required use of microprobe analysis (Jeol JXA-8200 electron microprobe), powder x-ray diffraction (Phillips X'pert, equipped with Co x-ray tube), and equipment to measure magnetic properties (SQUID magnetometer MPMS-XL 5).

3.2.1 Single crystal and powder x-ray diffraction

Soon after the discovery of x-rays by Wilhelm Conrad Röntgen (Röntgen 1895), Max von Laue showed that x-rays can be diffracted by crystals (Friedrich et al. 1912). His work, together with a pioneering work of William Laurence Bragg (Bragg 1913) demostrating that diffraction of x-rays can be used to evaluate 3D ordering of atoms or ions in solid crystalline media, form a basis of modern characterization of materials using x-ray diffraction (XRD).

The primary aim of x-ray single crystal or powder diffraction is to measure a unit cell – the elemental building block of crystalline materials, and to characterize each of these blocks in terms of space occupancy by different atoms, their thermal motion, etc. These powerful techniques are widely used for ambient or high pressure experiments.

As was mentioned above, the DAC technique, which allows generating impressively high pressures has a small drawback – a restriction imposed by tight sample chamber and small amount of sample material. Like many other scientific methods, x-ray diffraction is also amount sensitive technique. In order to obtain signal of acceptable quality, to overcome geometrical restrictions of DACs, and minimize an effect of x-ray beam absorption by diamond anvils, DAC diffraction experiments are usually conducted in transmitting geometry (2D diffraction) employing a sensitive, high resolution CCD detector and a high brilliance x-ray source (a rotating anode or a synchrotron source).

Single crystal diffraction equipment available in-house at BGI is comprised from Oxford Diffraction Xcalibur 2 (kappa geometry, Sapphire 2 CCD), Huber machine (four circle geometry, "quartz & silice" point detector). These devices are equipped with Mo x-ray tubes (wavelength $\lambda_{Mo\,K\alpha1}$=0.7108) and allow measuring single crystalline material up to ~10 GPa, depending on scattering of the material. In order to go to higher pressures, smaller amount of material is required, however this amount is below the detection limit of the in-house equipment.

Due to gradually increasing demand from high pressure scientific community, most of the modern large scale synchrotron facilities have beamlines specialized in high pressure experiments. X-ray diffraction beamlines, such as ID09a, ID27 belonging to the European Synchrotron Radiation Facility (ESRF) or GSECARS beamline of Advanced Photon Source (APS) allow measuring samples of smaller sizes compared to the BGI in-house equipment. In Table 3.2.1, we show data comparing synchrotron equipment with the BGI machines.

Most of experimental data discussed in Chapter 5 was obtained in ID09a (ESRF) and APS (GSECARS). We conducted preliminary analysis and selection of single crystalline samples using Oxford Diffraction Xcalibur 2 system installed at BGI. Powder diffraction images collected in-house, at ESRF or at APS were transformed to 1D patterns using Fit2D software (Hammersley 1997, 1998) and subsequently analyzed with Fullprof or GSAS Rietveld refinement programs

Table 3.2.1:

Characteristic data for selected high-pressure beamlines and BGI in-house equipment

	λ (Å)	f.s. (μm^2)	2θ range (deg.)	Detector
ID27 (ESRF), France	0.3738	10·9	2-19	MAR345
ID09a (ESRF), France	0.4149	10·10	2-30	MAR555
GSECARS (APS), USA	0.3344	5·5	2-22	MAR345
BL10XU (Spring-8), Japan	0.4125	10·10	2-22	Rigaku R-AXIS IV
x-ray diffractometer with Mo anode (BGI)	0.7108	40·40	0-35	SMART APEX 4K CCD
Oxford Diffraction Xcalibur 2 (BGI)	0.7108	100·100	2-30	Oxford Diff. Sapphire 2 CCD

f.s. - full width at half maximum of x-ray beam focal spot

(Rodríguez-Carvajal 1993, Larson and Von Dreele 2000). X-ray diffraction intensities obtained from single crystal experiments were extracted from diffraction patterns using Oxford diffraction Crysalis program (Crysalis RED 2006) and further analyzed in JANA2006 or SHELX software (Petricek et al. 2006, Sheldrick 2008). Additional information can be found below.

In order to obtain best quality of single-crystal diffraction data, we used diamonds and diamond anvil cells of special disign characterized by high opening angle 60-80° (Boehler and De Hantsetters 2004). In addition to diamond anvil cells produced by BGI, we also used membrane DACs for experiments conducted at ESRF (Chervin et al. 1995).

3.2.2 Neutron diffraction

In contrast to x-ray diffraction where x-ray phonons are scattered by electrons, neutrons are scattered by nuclei of matter. Comparing x-ray and neutron diffraction, advantage of using neutrons becomes apparent while probing dynamic properties of material or while probing magnetic properties. Our project on wüstite, described below, required simultaneous measurement of magnetic and crystal structures.

The experiments were conducted at D20 beamline, Institut Laue-Langevin (ILL). Setup, shown in Figure 3.4, is two axis diffractometer with first stage containing four monochromators installed on carousel. Different monochromators allow users to choose between high resolution and high flux options, with highest resolution $\Delta d/d \approx 2 \cdot 10^{-3}$. Second stage of setup consists of a sample chamber and a microstrip detector built based on 'microstrip' gas chamber design (Oed 1988). Curved linear detector consists of 1536 detection cells and cover 2θ range equal to 153.6°. In order to suppress unwanted scattering from sample environment 372 vertical collimation blades are installed between sample chamber and the detector. Additional information can be found in the current review of the instrument (Hansen et al. 2008).
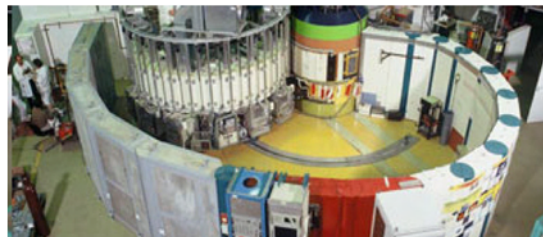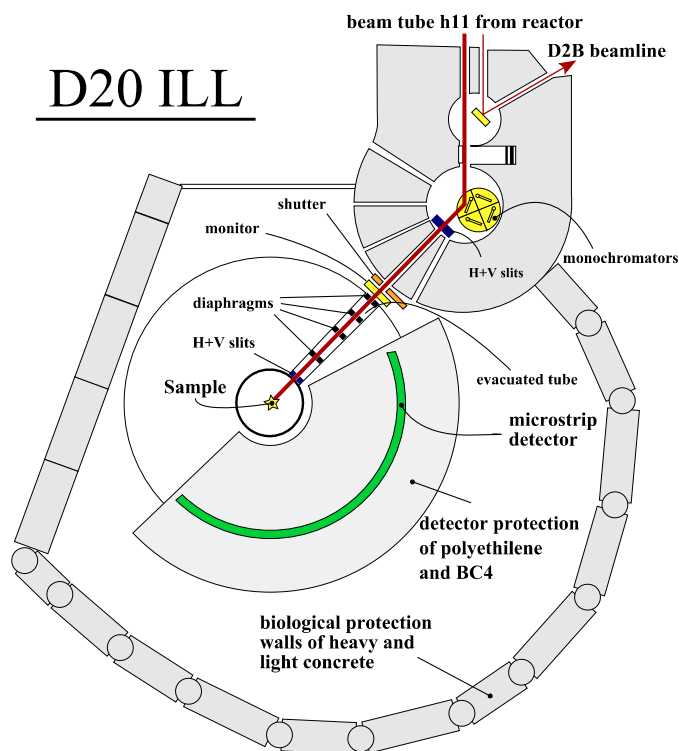
D20 ILL

Figure 3.4:

Schematic view from the top on the beamline D20, ILL (Hansen et al. 2008). The picture of the real instrument was downloaded from www.ill.fr and is shown above.

3.2.3 Mössbauer spectroscopy

Mössbauer spectroscopy is based on observation that nuclei of a solid can emit and absorb x-rays without recoil (Mössbauer 1958). The probability of recoilless scattering depends on temperature and energy of incident radiation. Mössbauer absorption is the resonant effect and can be observed only at certain wavelength and for selected isotopes with low lying excited states, such as ^{57}Fe, ^{119}Sn, ^{191}Ir, etc.

Absorption spectra can be obtained by conducting energy scans in the vicinity of resonance by moving a radioactive source relative to a fixed sample in constant velocity or constant acceleration mode. Due to hyperfine interactions between atoms and electrons in general and between electrons and nuclei of the solid in particular, various features of a spectrum can be observed. The well established theory of the Mössbauer effect helps to describe excitation of Mössbauer isotope nuclei to different energy levels in terms of Mössbauer parameters (Figure 3.5), namely hyperfine magnetic splitting (HMF), quadrupole splitting (QS), isomer shift (IS), and second order Doppler effect (Gonser 1975, Dickson and Berry 2005).

Hyperfine magnetic splitting is a characteristic feature of magnetically ordered materials, quadrupole splitting is another parameter describing different valence or lattice induced effects. For example, value of quadrupole splitting describes splitting between energies of different *3d* orbitals in iron containing minerals. Mössbauer isomer shift depends by definition on charge density of *s* electrons on a nucleus, however, due to interaction between *s, p,* and *d* electrons this parameter is also sensitive to a valence state of Mössbauer isotope. Mössbauer technique is very efficient probe of various electronic and magnetic properties of solid state materials.

(a)   **(b)**
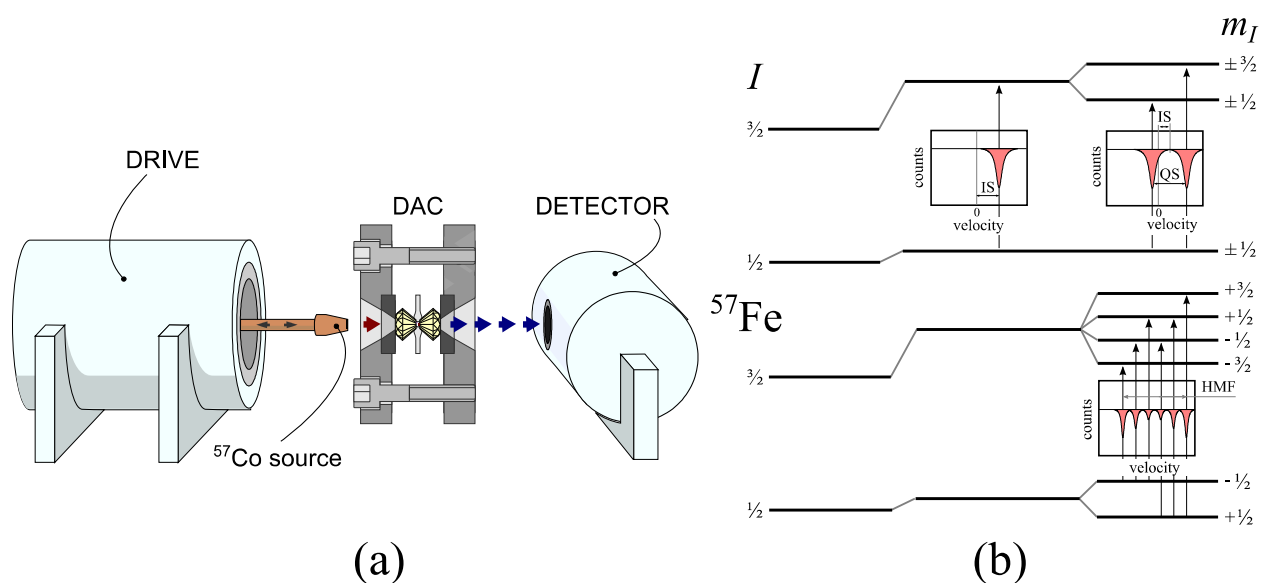
Figure 3.5:

Schematic drawing of (a) a typical BGI high pressure Mössbauer experiment and (b) a diagram describing energy levels splitting of nuclei(^{57}Fe) in terms of hyperfine interactions (IS, QS, HMF without QS), showing their manifestation in absorption spectra (Gonser 1975, Dickson and Berry 2005). Symbols I and m_I correspond to nuclear spin and magnetic quantum number, respectively

For all experiments described in Chapter 5, we employed in-house ^{57}Fe Mössbauer spectroscopy equipment. Typical setup for a high pressure Mössbauer experiment is shown in Figure 3.5. It consists from a radioactive source mounted on drive, a DAC loaded with sample, and a detector. While the ^{57}Co source oscillates in constant acceleration mode, an absorption spectrum is collected on a scintillation detector tuned to a specific energy window corresponding to the ^{57}Fe Mössbauer resonant energy. For high pressure experiments we used small radioactive point sources (Ø0.5 mm). In order to decrease collection time we enriched sample material with ^{57}Fe isotope. Still, spectra were collected for 24-48 hours, depending on DAC loading and pressure and then fitted using NORMOS software package (Brand 1990).

4.   Scope of thesis

This chapter provides a summary of the results presented in Chapter 5 and is organized in the following way. Subsection 4.1 reports results on the single crystal diffraction study of $(MgFe)(SiAl)O_3$ incorporating substantial amount of Fe^{3+} iron at pressures up to 80 GPa and temperatures up to 1800 K. In order to generate high temperature for this and other high pressure diamond anvil experiments, conducted outside the scope of the thesis, we developed the portable laser heating system. As the current work is dedicated to the studies of material properties and not to technical aspects of high temperature generation for diamond anvil cells, we do not include description of the portable laser-heating system here (Chapter 4), however we provide necessary details in the Results section. In Section 4.2 we present a model consistently describing behavior of magnetite's electronic and magnetic properties at pressures below 25 GPa. Subsection 4.3 is devoted to the low temperature study of Fe_xO evaluating the role of its intrinsic ordered defect structure on its phase diagram. Finally, we present new results indicating a compression induced electronic topological transition in *hcp* phases of iron and iron-nickel alloy in Section 4.4.

Three of the five papers presented in Chapter 5 were written by me as a first author, and I have done considerable amount of the work by preparing, selecting, characterizing, measuring material and analyzing the results. Being the second author of the other two papers, I was an active participant of these projects and I have made significant scientific contribution by preparing sample material, sample environment, collecting and analyzing data as well as writing manuscript.

4.1.   Single crystal structure and spin state of ferric iron of magnesium silicate perovskite

Using high pressure single crystal x-ray diffraction at ambient and elevated temperatures, generated by *in-situ* laser heating, we conducte a study of Fe-Al bearing magnesium silicate perovskite (MgFeAlPv). The composition of the sample $(Mg_{0.63}Fe_{0.37})(Si_{0.63}Al_{0.37})O_3$, was determined in a combined microprobe, Mössbauer spectroscopy and x-ray single crystal diffraction study. We verify that iron ions occupy exclusively dodecahedral A-sites, leaving octahedral B-sites for Si and Al. The investigated material contain large amount of ferric iron ($Fe^{3+}/\Sigma Fe\sim93\%$) introduced into MgPv lattice by $Mg^{2+}_A+Si^{4+}_B\rightarrow Fe^{3+}_A+Al^{3+}_B$ (SAL) substitution mechanism. Additional information of the sample preparation and characterization can be found in Section 5.1.

In a high pressure diamond anvil experiment, we conduct a study of MgFeAlPv crystal structure and its variation under P-T conditions similar to the conditions of the Earth's lower mantle. In addition we use x-ray diffraction as a sensitive tool to detect changes of Fe^{3+} spin state and test contradicting experimental evidences reported in literature (Jackson et al. 2005, Catalli et al. 2010). Additionally, we investigate a hypothesis of Fe-Al redistribution between different crystallographic sites at high pressure-high temperature conditions, proposed by Catalli et al. (2010). The results are presented below.

Combining new data with results of previous study performed on same material (Dubrovinsky et al. 2010a), we derive a thermal high pressure equation of states. It is based on 3rd order Birch-Murnaghan equation of states but modified to include the effect of high temperatures
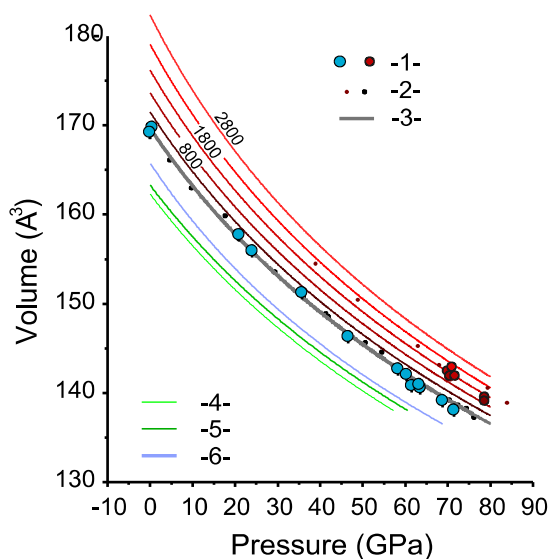
Figure 4.1:

Pressure dependencies of unit cell volume determined for Pv with different iron content (*x,* mole *%)*: (1) $x_{Fe/Al}$=0.37, current; (2) $x_{Fe/Al}$=0.37, same material (L. Dubrovinsky et al. 2010); (3) $x_{Fe/Al}$=0.37, equation of state at 300 K; (4) x_{Fe} =0.2 from (Catalli et al. 2010); (5) x_{Fe} =0.15 from (Lundin et al. 2008), (6) x_{Fe} =0 from (Lundin et al. 2008). Black/blue and red points represent ambient and high temperature points, respectively. Lines with different red shading were obtained after fitting data to thermal equation of states, and we show by numbers corresponding temperatures.

(Saxena et al. 1999). A full set of fitting parameters describing compressional behavior of the studied material is given in Section 5.1. Here we present a result of the fitting (Figure 4.1) and compare it with data reported in literature.

Before analyzing the effect of pressure on spin state of ferric iron incorporated into MgFeAlPv, we had to test the hypothesis proposed by Catalli et al. (2010) suggesting that high pressure high temperature treatment of magnesium silicate perovskite containing Fe and Al, has to result in a redistribution of Fe and Al between different crystallographic sites. We approach this complicated problem by conducting the experiment in the following way. First we collect data at room temperature (RT), high pressure and verify that compression itself has not induce any changes crystallographic sites occupancies of Fe or Al. After that, we collect data at high temperature (~78 GPa, 1800K), and finally we collect data just after the heating. The results are shown in Figure 4.2. We demonstrate that iron remains at A-site even after high temperature treatment.

After confirming that iron does not exchange crystallographic sites with aluminum at all conditions of the experiment, we address a problem of ferric iron spin state under pressure and controversies observed in different experiments (Jackson et al. 2005, Catalli et al. 2010). Most of the scientific techniques employed for high pressures experiments, with an exception of single crystal x-ray diffraction, do not allow unambiguous separation of contributions coming from ferric iron occupying B- or A-sites. First, we observe no anomalies of compressional behavior of materials unit cell volume. In addition, we investigate changes of volumes attributed to individual crystallographic sites under pressure. As can be seen in Figure 4.3, we observe no abrupt contraction of volumes belonging to A- or B- crystallographic sites which could be attributed to spin state crossover of ferric iron. Here we conclude that there is no a spin crossover for ferric iron ccupying A-site at all pressures of experiment.

36
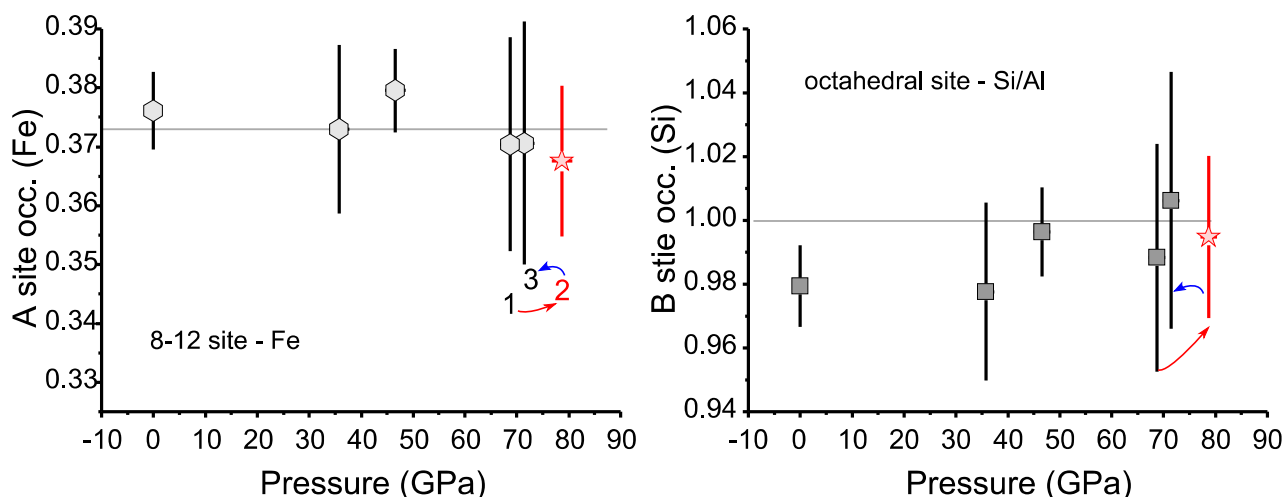
Figure 4.2:

Occupancies of Fe_A and Si_B sites as a function of pressure. Numbers and arrows serve as sequence markers: (1) before laser heating (2) during the heating at ~1800 K, (3) just after the heating. The grey lines show the occupancies of the sites determined with high accuracy at 0 GPa. We use pure Si to describe occupancies of Al^{3+}/Si^{4+} occupying B-sites due to similar (almost indistinguishable) x-ray scattering of these ions.
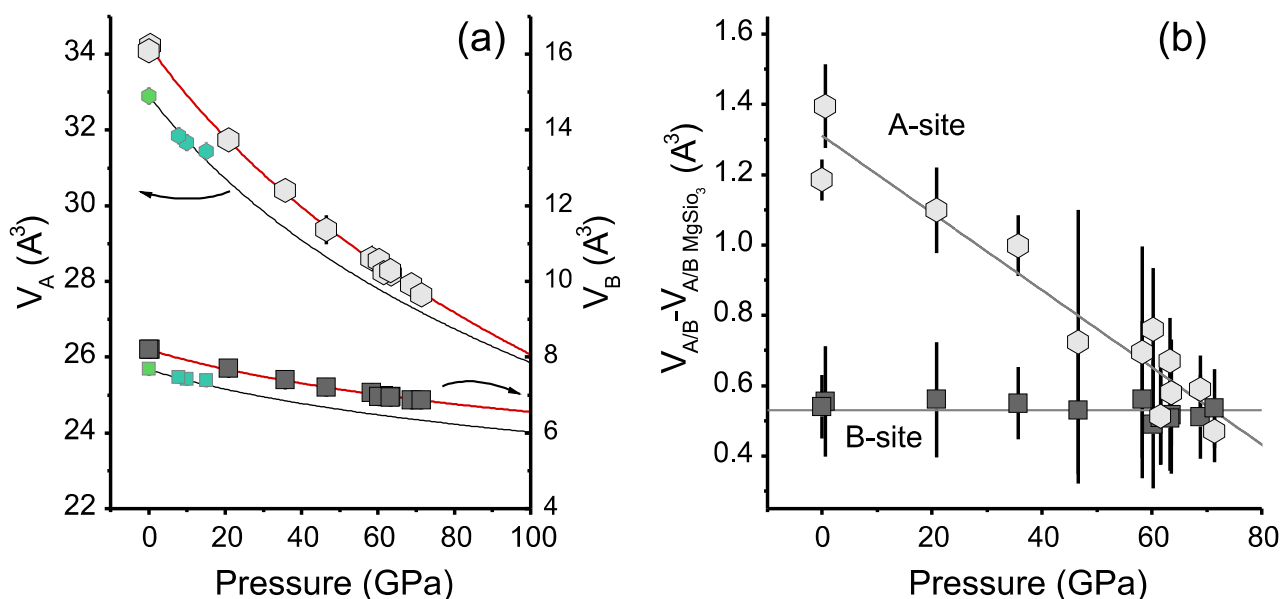
Figure 4.3:

(a) Volumes of individual crystallographic sites and their variation with pressure measured on MgFeAlPv (grey points). We show literature data for pure $MgSiO_3$ using green and light blue symbols (Horuichi et al. 1987, Sugahara et al. 2006). We obtain black lines in an assumption of non uniform compression of $MgSiO_3$ unit cell (Lundin et al. 2008) using crystallographic data measured at 0 GPa (Dobson and Jacobsen 2004). Using the same assumption and tracking compression of A- and B- sites of MgFeAlPv relative to pure $MgSiO_3$, shown in (b), we plot red lines. Grey lines in (b) represent linear fits.

Our study on crystal structure of the MgFeAlPv material revealed a number of additional pressure induced effects. For example, we see that A-site occupied by ferric iron and magnesium is clearly more compressible compared with B-site (with or without Al) or with compression of A-site of pure $MgSiO_3$. This is an important effect which should be considered in future analysis of geochemistry of silicate perovskites and in theoretical calculations for more accurate predictions.

4.2. Compression induced metallization of magnetite below 25 GPa

The combined single crystal x-ray diffraction and Mössbauer spectroscopy study described in detail in Section 5.2, is devoted to a long standing problem of magnetite's behavior at pressures below 25 GPa. In order to resolve strong contradiction between recently proposed models (see Section 2.3 for details), we determined effect of compression on crystal structure of Fe_3O_4. Based on the results of the single crystal study, we probe electronic and magnetic properties of magnetite by high pressure Mössbauer absorption experiments. Comparing our data with various data reported literature we propose a model consistently describing metallization of magnetite and the effects induced by compression.

The results obtained in the single-crystal x-ray diffraction experiment are shown in Figure 4.4. Our data on unit cell compression is in good agreement with powder diffraction results (Rozenberg et al. 2007), however we show that oxygen fractional coordinate u determined in our single-crystal diffraction behaves differently.
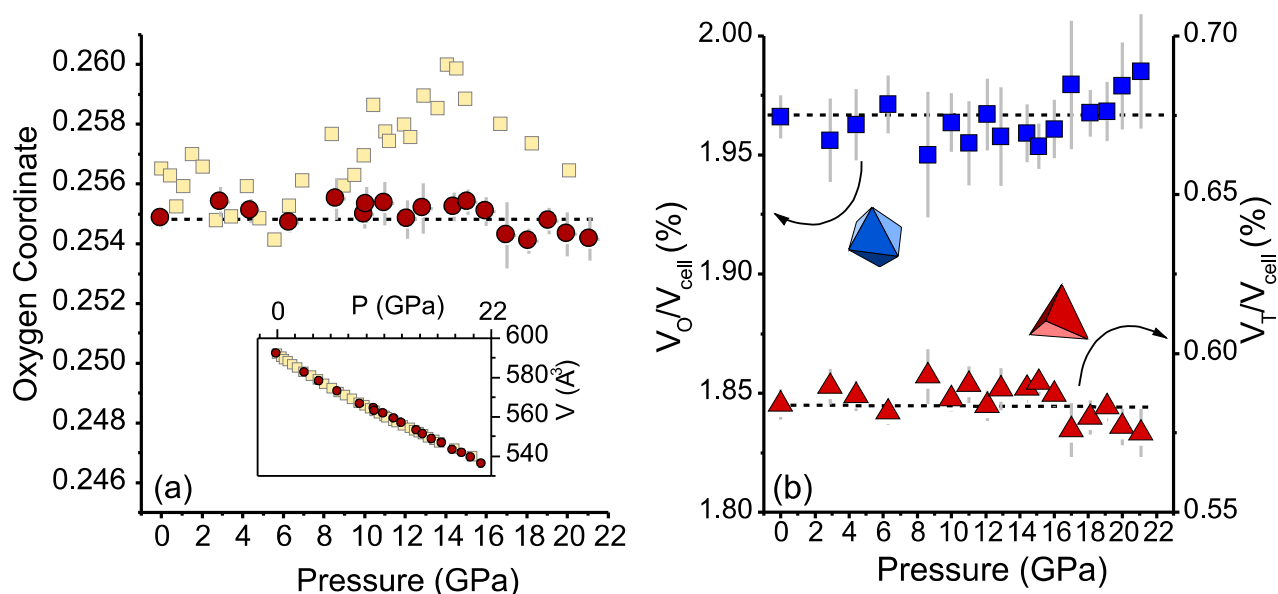
Figure 4.4:

Left - pressure dependencies of oxygen fractional coordinate u. We use red circles and yellow squares to compare out data and data from Rozenberg et al. 2007, respectively. Volumes of T- and O-site, normalized to unit cell volume, are shown in figure to the right. Blue squares and red triangles represent O- and T- sites respectively. Dashed lines are the eye guides.

Considering numerous shortcomings of high pressure powder diffraction studies, including evolution of texture, inter-grain strain and higher pressure gradients in sample chamber, we believe that our single crystal x-ray diffraction study provides more reliable information. After taking into account that volumes of tetrahedral T- and octahedral O-sites do not change under pressure Figure 4.4, we conclude that there is no electronic charge redistribution between different crystallographic sites in magnetite implying no transition from the inverse ($Fe^{3+}_T Fe^{2+}_O Fe^{3+}_O O_4$) to the normal spinel structure ($Fe^{2+}_T Fe^{3+}_O Fe^{3+}_O O_4$). Although, our data on compressional behavior of O-site does not support the model of Fe^{2+}_O spin state crossover, proposed by Ding et al 2008, we address this model in our high pressure Mössbauer absorption study.

At ambient conditions, Mössbauer absorption spectra of magnetite consists of two magnetic subspectra. One of them corresponds to Fe^{3+} occupying T-sites and another to $Fe^{2.5+}$ occupying O-sites. Although iron occupying O-sites has mixed valence state, mean lifetime of an excited Mössbauer nucleus ($\sim 10^{-7}$s) is much longer than charge hopping ($\sim 10^{-16}$s) between adjacent O-site Fe^{2+} and Fe^{3+}. Thus, these ions contribute to a single sub-spectrum. Fitting the collected spectra, we extract hyperfine magnetic field (HMF), quadrupole splitting (QS) and isomer shift (IS) Mössbauer parameters (Figure 4.5, and Section 5.2).

Analyzing pressure induced variation of the T-site absorption sub-spectrum, and variation of the corresponding derived values, namely isomer shift, and hyperfine magnetic splitting, we extract the following information. First, Mössbauer subspectrum for the T-site is always well resolved in the absorption spectra. Combining this observation together with negligible pressure dependence of T-site isomer shift, we conclude that T-site does not participate in charge transfer or electrical conductivity at all pressures of our study. Indeed, if considerable amount of Fe^{3+}_T would participate in charge transfer, the isomer shift of T-site would decrease reflecting lower interaction (`screening`) between *s*- and *d*-electrons.

According to our observations, hyperfine magnetic splitting of T-site decreases with pressure. Knowing that Fe^{3+}_T *3d* orbitals have spherical charge distribution, we argue that hyperfine magnetic splitting of T- site is directly proportional to the value of effective magnetic spin (Dickson and Berry 2005). Analyzing these observations and taking into account the localized nature of Fe^{3+}_T *3d* electrons, we come to a conclusion, that effective magnetic moment of Fe^{3+} at T-site is decreasing due to a weakening of the strongest magnetic interaction in the material, namely, the antiferromagnetic interaction between O- and T-sites.

As can be seen from Figure 4.5, the effect of compression is different for O- and T-crystallographic sites. Before we can proceed with description, how magnetic and electronic properties of O-site change with compression we need to clarify certain points. At ambient conditions magnetite is a half metal with high spin polarization of charge carriers formed by minority band $t_{2g\downarrow}$ electrons hopping in between O-sites (Dedkov et al. 2002). Upon compression, resistivity of magnetite gradually decreases (Morris and Williams 1997, Ovsyannikov et al. 2008) due to the ongoing delocalization of *3d* electrons.

39
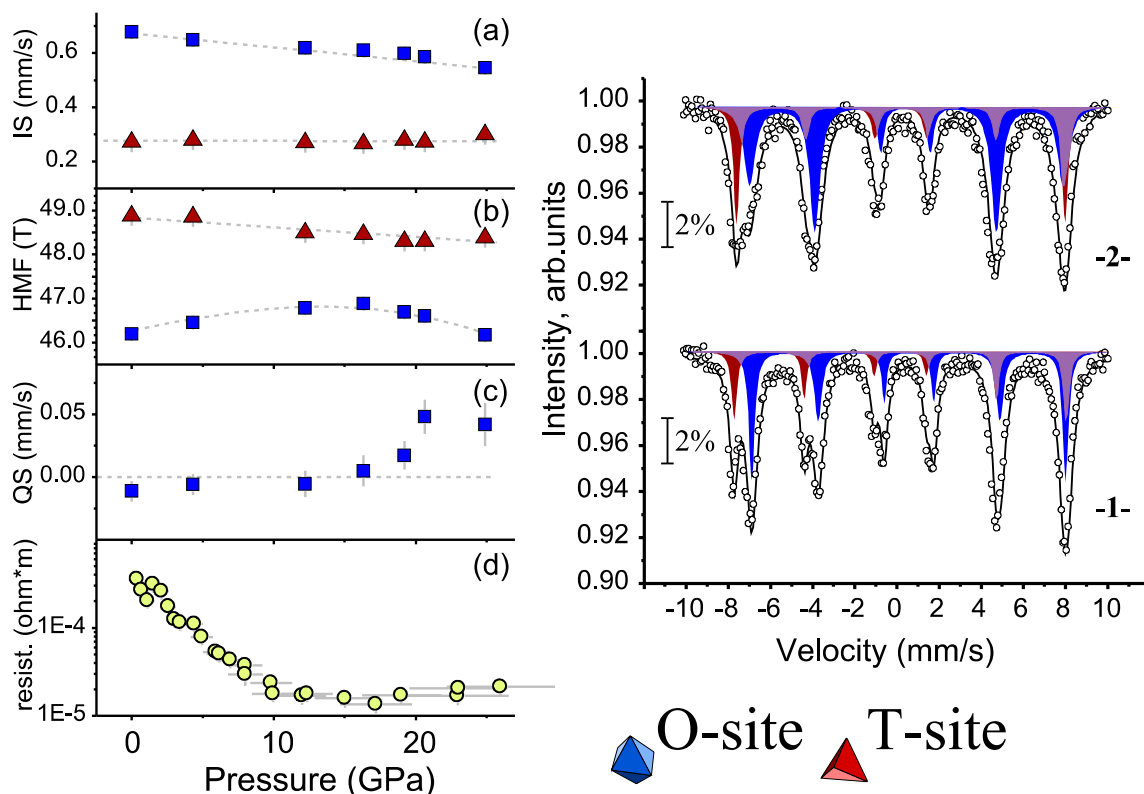
Figure 4.5:

Behavior of the O- and T- sites Mössbauer parameters as a function of pressure, namely (a) IS-isomer shift, (b) HMF-hyperfine magnetic field and (c) QS - quadrupole splitting are shown in the left part of the figure. The figure (d) is shown as reference and describes behavior of magnetite's resistivity under pressure (Morris & Williams 1997). Representative Mössbauer absorption spectra fit within transmission integral approach are shown to the right for (-1-) 0 GPa and (-2-) 20.7 GPa. The sub-spectra corresponding to O- and T-sites are shown in blue and in red, respectively. Dashed lines are guides for the eyes.

As was mentioned above, we show the evidence that T-sites do not participate in charge transfer at all pressures of our experiment. But following the process of continuous pressure induced metallization, the *3d* electrons of iron occupying O-sites become more and more delocalized and the corresponding values of O-site isomer shift gradually decrease.

After analyzing data, we reject the possibility of the Fe^{2+}_O HS-IS spin transition (Ding et al. 2008). Indeed, in case of a transition to the intermediate spin state, *3d* electron charge distribution of the Fe^{2+} ion will become more spherical. The corresponding values of the O-site isomer shift will be lower, as reported for the spin state transition of Fe^{2+} ions in magnesium ferripericlase (Lyubutin et al. 2010). Thus, either slope of the isomer shift or its value would change as a function of pressure upon the HS-IS transition.

At the first glance, hyperfine magnetic splitting of O-site should decrease proportionally to the degree of metallization. However, the curious two stage behavior of O-site hyperfine magnetic field

40

(HMF) can be explained only after analyzing different contributions.

Total hyperfine magnetic field for *3d* transitional elements is defined by an equation:

$$HMF = B_c + B_{orb} + B_{dip},$$

where B_c is contact interaction, B_{orb} is magnetic field generated by orbital motion of unpaired *3d* electrons, and B_{dip} is hyperfine interaction produced by dipolar field of *3d* electrons spin (Dickson and Berry 2005). In case of mixed valence state of iron occupying O-site, we could expect non-zero contribution of B_{dip} and B_{orb}. We have evidence that B_{dip} term is not, as the value for the quadrupole splitting at O-site is small at all pressures of our Mössbauer experiment (Figure 4.5). Based on the observation, that at ambient conditions magnetite's minority band ($t_{2g\downarrow}$) is responsible for its conductivity, we argue, that B_{orb} term should also be small. Indeed, $Fe^{3+}{}_O$ has the electronic configuration $3d^5$, with total orbital moment equal to zero, and $Fe^{2+}{}_O$ ion occupying O-site has the electronic configuration $3d^6$, particularly described as $2e_{g\uparrow}+3t_{2g\uparrow}+1t_{2g\downarrow}$ with $t_{2g\downarrow}$ partially delocalized. Due to the delocalization of $t_{2g\downarrow}$, the orbital moment of $Fe^{2.5+}{}_O$ at ambient conditions should have a very small value.

The contact interaction term (B_c) is usually considered as the major contribution to the total hyperfine magnetic field (Dickson and Berry 2005) and we show above that contribution of other terms should be small. According to the definition of the contact term, $B_c=k\cdot<S>$, where k is a parameter describing polarization of *s-* electrons, and $<S>$ is a value of effective magnetic spin. In order to resolve the mystery behind the unusual two stage behavior of O-site HMF we should track behavior of $k\cdot$ and $<S>$ as a function of pressure.

It was shown in a recent neutron powder diffraction study of magnetite (Klotz et al. 2008), that effective magnetic moments and correspondingly $<S>$ of Fe ions occupying T- and O-sites are decreasing with pressure. We argue that initial growth of HMF at O-site below ~15 GPa should be attributed to the polarization term k overcompensating the decreasing $<S>$. This way, B_C will increase together with total HMF of O-site.

Combining evidences together, we propose the following model. Considering Fe^{2+} ($3t_{2g\uparrow}+2e_{g\uparrow}$ $-1t_{2g\downarrow}$) and Fe^{3+} ($3t_{2g\uparrow}+2e_{g\uparrow}$) ions occupying O-site of magnetite, at ambient conditions $t_{2g\downarrow}$ (minority band) provides the major contribution to the bulk conductivity. Compression induces gradual delocalization of $t_{2g\downarrow}$ electrons. However, in order to explain corresponding decrease of the average magnetic moment observed at O-site upon compression, we suggest that pressure should also delocalize electrons from $t_{2g\uparrow}$ major band. Indeed, if delocalization affects only $t_{2g\downarrow}$ electrons then the average magnetic moment of O-site would increase ($3t_{2g\uparrow}+2e_{g\uparrow}-1t_{2g\downarrow}<3t_{2g\uparrow}+2e_{g\uparrow}$), and experiments show the opposite (Klotz et al. 2008). It is reasonable to assume that energy levels of $t_{2g\uparrow}$ electrons of iron at O-sites are degenerate, and we suggest that compression induces equal hybridization of these electrons. Due to a constant gradual delocalizaton of t_{2g} bands, interaction between *s-* and *3d-* electrons becomes weaker and manifests in lower values of O-site isomer shift and in higher values of k parameter contributing to the major component of HMF. At certain pressure, compression completely delocalizes $t_{2g\downarrow}$. Further application of pressure affects solely $t_{2g\uparrow}$ majority band delocalizing it more and more. At certain pressure, the magnetic moment of O-sites will suddenly decrease, because the effective number of spin-up (↑) electrons in the magnetite's conduction band will exceed the number of those with spin

41

down ($\downarrow$). A recent XMCD study by Baudelet et al. 2010 has shown that the net magnetization of magnetite starts to decrease at pressures higher than 15 GPa (Baudelet et al. 2010). Comparing the experimental observations, we conclude that at 15 GPa effective number of $t_{2g\uparrow}$ electrons in the conduction band approaches the number of $t_{2g\downarrow}$ electrons, and that at higher pressures we expect a change of charge carries polarization. Our study shows that, contrary to the idea of Baudelet et al. suggesting that majority band reaches Fermi level only at ~15 GPa, this band is always at the Fermi level, however its bandwidth is modified by pressure.

To conclude, using single-crystal x-ray diffraction and Mössbauer spectroscopy techniques we tested different models intensively discussed in literature, namely the models of HS-IS spin state transition(Ding et al. 2008) and the inverse spinel to normal spinel transition (Rozenberg et al. 2007). Our experimental data suggests that these hypothesis are wrong, and we propose a new model, consistent with data reported in literature. Here we describe all observed phenomena it terms of magnetite metallization under compression. Due to unique crystal chemistry of magnetite, iron occupying its tetrahedral sites does not participate in charge transfer at all pressures below 25 GPa, and charge carriers move through the the network of octahedral sites. We suggest that at pressures above 15 GPa the polarization of charge carriers changes, and majority band electrons dominate in conductivity band at higher pressures.

4.3. Intrinsic defect structure of wüstite and its effect on high-pressure low temperature phase diagram

We conduct a high resolution neutron powder diffraction study of wüstite in order to determine influence of composition and intrinsic defect structure on its low temperature phase diagram. We study two compositions ($Fe_{0.94}O$, $Fe_{0.925}O$) which have similar type but different concentration of defects in the following way (Akimitsu et al. 1983). Material together with pressure transmitting medium was loaded into Paris-Edinburgh press installed into a He flow cryostat. Neutron diffraction spectra were collected during cooling runs. Additional details on sample preparation, experimental setup and characterization of material can be found in Section 5.3. We analyze the collected diffraction patterns using Fullprof Rietveld refinement software (Rodríguez-Carvajal 1993). A representative diffraction pattern is shown in Figure 4.6.

Due to limited time allocated for our experiments at neutron facility (ILL, Grenoble, France), we organize compression sequence in the following way. For the sample with composition $Fe_{0.94}O$ we obtain data at 0, 4, 6.8 GPa, and for the composition $Fe_{0.925}O$ compressional sequence is different: 4.2, 8 and 0 GPa. For the $Fe_{0.925}O$ composition, the 0 GPa point is collected last as a test point to evaluate effect of rapid decompression on the properties of the material and its defect structure.

At ambient conditions Fe_xO has the cubic, rocksalt structure. Upon cooling, wüstite undergoes structural (cubic to rhombohedral) and antiferromagnetic transitions. Below the Néel temperature, magnetic moments of Fe^{2+} ions align parallel to [111] or [001] axis in cubic or hexagonal notation, respectively. Being interested in precise determination of critical temperatures for the structural (T_S) and the magnetic transition (T_N), we analyzed crystal structure of wüstite within hexagonal crystal structure model above and below the structural transition. We find that ratio of unit cell parameters *c/a* is very
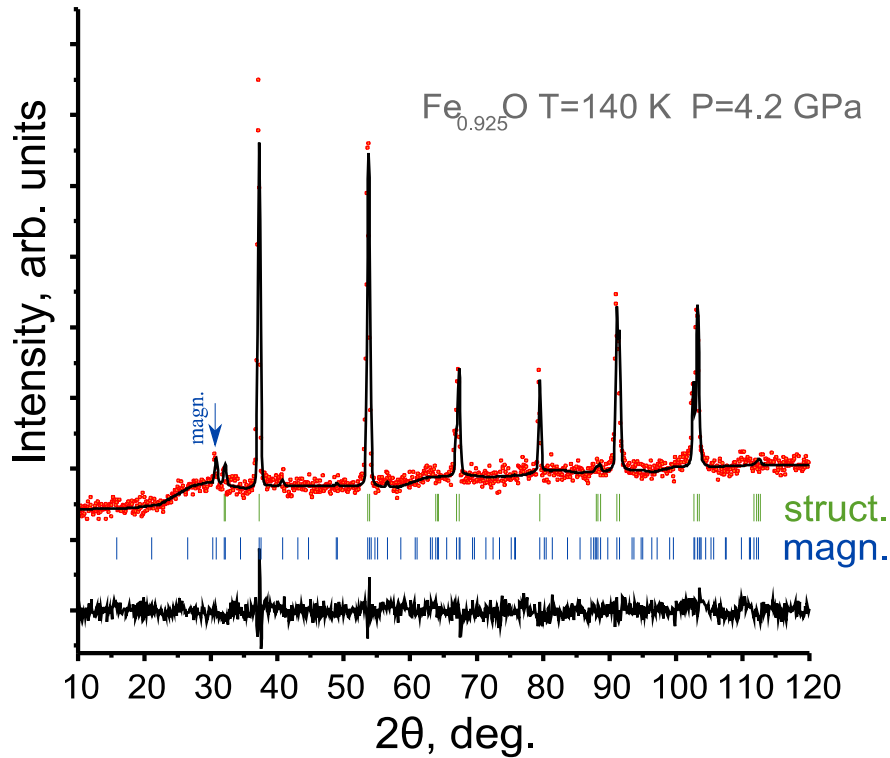
Figure 4.6:

The neutron powder diffraction pattern collected on $Fe_{0.925}O$ at 4.2 GPa, 140±5 K. Upper and lower ticks correspond to diffraction lines of crystal and magnetic structures, respectively. Blue arrow indicates the most intensive magnetic peak.
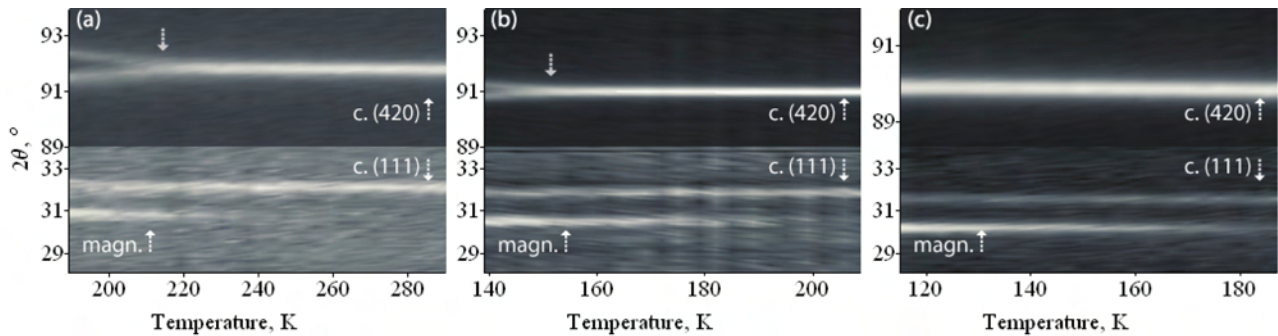
Figure 4.7:

Grey maps featuring selected 2θ ranges of $Fe_{0.925}O$ diffraction data collected at (a) 8GPa, (b) 4.2 GPa, (c) 0 GPa. We indicate the magnetic and structural (cubic notation) diffraction peaks. Structural transition manifesting through a splitting of the diffraction peak (high 2θ) is featured separately by arrows.

sensitive to the onset of crystal structure transition. By tracking evolution of this parameter as a function of pressure we determined T_S. We could not not estimate critical temperature of structural transition for $Fe_{0.925}O$ decompressed from 8 to 0 GPa by means of neutron diffraction, but our data suggests that it lies below 110 K, because we see no splitting of high 2θ diffraction lines or corresponding changes of *c/a* parameters at higher temperatures (Figure 4.7). Although we collected no data for $Fe_{0.925}O$ at 0 GPa, prior to the high pressure treatment, we argue that T_S value for $Fe_{0.925}O$ compound should be close to the value of 160±5 K reported for $Fe_{0.92}O$ (Kantor et al. 2005).

Critical temperatures corresponding to the onset of the antiferromagnetic transition and values of magnetic moment are determined by means of Fullprof. Graphical representation of the data showing evolution of structural parameters and values of magnetic moments can be found in Section 5.3.

Combining together data obtained for different critical temperatures, we plot low temperature phase diagram for both studied compounds (Figure 4.8).We observe divergence of T_N and T_S as a function of pressure, and it is clear that behavior of $Fe_{0.925}O$ and $Fe_{0.94}O$ at high pressure is different. Comparing our results with results reported for a similar antiferromagnetic compound MnO (Kantor et al. 2005), we find no correlation between values of magnetic moments and *c/a* ratio as the indicator for the rhombohedral distortion. This lead us to a conclusion that defect structure of material may play major role in the observed phenomena. Indeed both materials have similar defect structure, but different concentration of defects. The intrinsic defect structure of wüstite may influence properties of Fe_xO material stronger than expected, especially at high pressure.

It is known that defects of Fe_xO form clusters which influence the magnetic properties of the material and participate in the antiferromagnetic ordering (Battle and Cheetham 1979). We suggest that at low temperature and low pressure the material with larger defect concentration should adapt more easily to magnetic ordering and magnetostriction by distorting individual clusters while overall preserving the (long-range) cubic symmetry. On the other hand, the presence of defects introduces some distortion of the structure of "as-prepared" Fe_xO samples making them "less ideal" in comparison with stoichometric FeO. The effect of magnetostriction induced by magnetic interactions should be less pronounced and softened by the defect-containing structure. We suggest that the cubic magnetic phase should not exist in magnetically ordered Fe_xO in the absence of defects (i.e., for x = 1).

Compression modifies defect structure. It can be seen from the phase diagram (Figure 4.8), that application of pressure has different effect on compositions with different concentration of defects. In case of $Fe_{0.925}O$ characterized by higher concentration of defects, T_N and T_S almost coincide at 8 GPa. This observation can be explained within the framework of the Fe_xO defect structure order disorder transition (DDS) observed for $Fe_{0.93}O$ at ambient temperature and 14 GPa (Ding et al. 2005a). We argue that rapid decompression (quenching) from 8 to 0 GPa modifies defect structure of $Fe_{0.925}O$, and that by quenching we form a new ordered defect structure which is different from defect structure of the as-prepared material.

Previous studies have revealed two types of intrinsic defects, namely interstitial Fe^{3+} ions trapped in tetrahedral environment and surrounded by four octahedral vacations (Koch and Cohen 1969). These defects form clusters which in turn form super-lattice in the pristine material. We suggest that upon
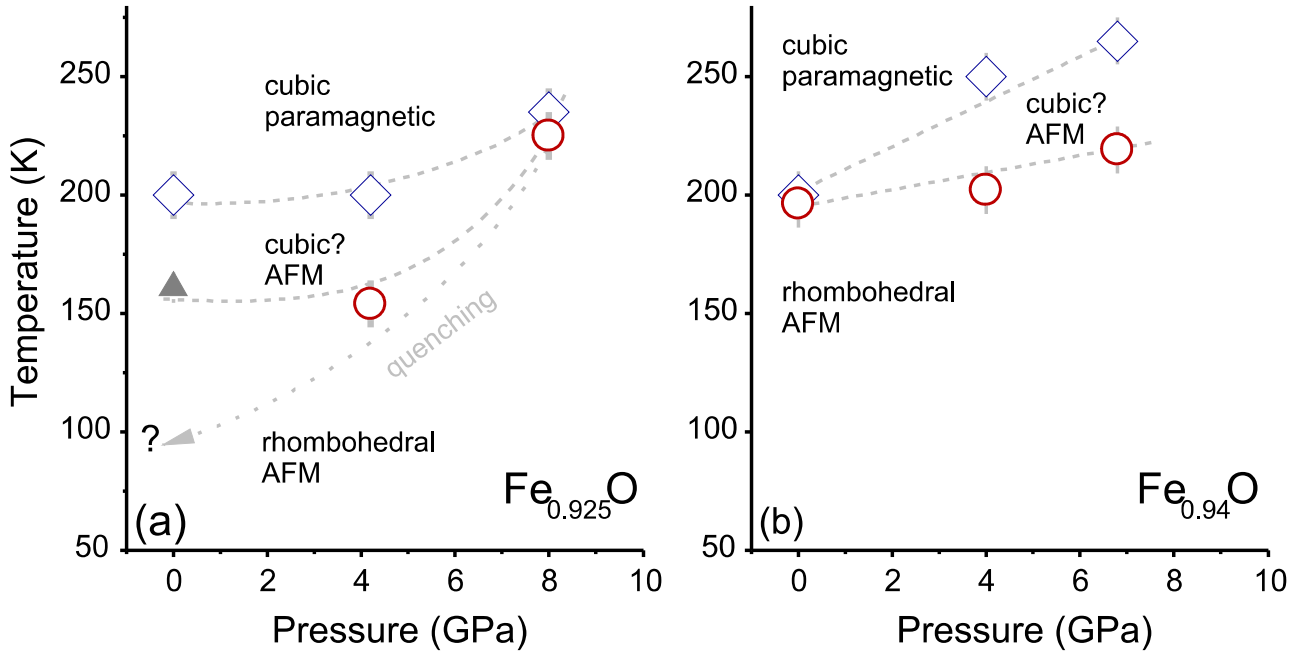
Figure 4.8:

Low temperature phase diagram for two compositions of wüstite: (a) $Fe_{0.925}O$, (b) $Fe_{0.94}O$. Circles and diamonds represent critical temperatures of the observed structural and magnetic transitions, respectively. We use grey triangle to indicate temperature of structural transition observed in neutron powder diffraction of $Fe_{0.92}O$ (Kantor et al. 2005). The dashed lines are guides for eyes, and dotted line represents quenching of $Fe_{0.925}O$ material from 8 to 0 GPa at low temperature.

reaching the pressure of DDS, the interstitial Fe^{3+} are "extruded" in random way from tetrahedral sites in favor of octahedral sites, so that the long range order formed by defect clusters is destroyed. However, in contrast to the study of Ding et al. 2005a, we report that DDS state is not stable at 0 GPa and low temperatures. We suggest, that upon decompression, some of displaced Fe^{3+} ions retake their previous positions forming new long range order. If the resulting defect structure would be the same as in pristine material (see Figure 4.8), then T_S of $Fe_{0.925}O$ would be very close to the T_S value reported for $Fe_{0.92}O$ compound (Kantor et al. 2005). But upon quenching of $Fe_{0.925}O$, T_S is shifted by more than 60 K below its value reported for $Fe_{0.92}O$. The data obtained in our study suggests that, in contrast to T_S, T_N is almost unaffected by rapid decompression, suggesting that Fe^{2+} ions, forming the framework for the crystal and magnetic lattice of the material do not participate in DDS.

In conclusion, we explore the low temperature part of wüstite phase diagram to 8 GPa. Having selected two model compositions with different concentration of defects, namely $Fe_{0.94}O$ and $Fe_{0.925}O$, we show that pressure induces and influences the divergence of critical temperatures for magnetic and structural transitions in different way. We suggest that the observed phenomena is strongly correlated with intrinsic defect structure of wüstite. Application of pressure modifies defect structure of wüstite influencing local environment of defects (ferric iron), temperature of structural transition and ultimately manifests through the order-disorder transition of defect structure. We report, that rapid decompression of $Fe_{0.925}O$ material from the DDS state results in formation of a new defect structure, different from DDS and the one of the as-prepared material.

4.4. Evidence of topological electronic transition in hcp phase of Fe and $Fe_{0.9}Ni_{0.1}$

As introduced in Section 2.1, our study of iron and iron-nickel alloy ($Fe_{0.9}Ni_{0.1}$) was initiated to unravel behavior of *hcp* phase of iron at pressures below 70 GPa, where the anomalous softening of Debye sound velocity (V_D) was observed for *hcp* phases of pure iron and iron, alloyed by small amount of nickel. Using x-ray powder diffraction, nuclear inelastic x-ray scattering (NIS), and Mössbauer spectroscopy we investigate various properties of Fe and $Fe_{0.9}Ni_{0.1}$ at ambient temperature. Details on the experimental setup, sample preparation and the treatment of data can be found in Section 5.4.

First, by means of nuclear inelastic x-ray scattering (NIS) we evaluate compression induced changes of Debye sound velocity in *hcp* $Fe_{0.9}Ni_{0.1}$ and compare our results with data reported for pure iron. Hexagonal closed packed phase of iron and $Fe_{0.9}Ni_{0.1}$ becomes stable above ~15 GPa with its stability field spanning up to 100 GPa and above (Dubrovinsky et al. 2007). Using static compression experiments, we measure a set of points at pressures below 62 GPa. We find our data in good agreement with previous results reported for pure iron (Figure 4.9), and we confirm our hypothesis of the Debye sound velocity softening at pressures between 40 and 60 GPa. Indeed, our data measured at 40-60 GPa reproduces data measured by Mao et al. 2001, and indicates that V_D asa function of pressure changes slope upon compression above 40-50 GPa.

Knowing that at 300 K *hcp* phase is stable up to the pressures of the Earth inner core (Dubrovinsky et al. 2007, Tateno et al. 2010), we considere that a previously unknown electronic transition is at origins of the observed softening at 40-60 GPa. Using Mössbauer spectroscopy as sensitive tool to probe electronic properties of material, we conduct a series of high pressure Mössbauer absorption experiments. We assume that an electronic transition manifesting in softening of V_D could affect crystal structure parameters, and in addition to the Mössbauer experiments we perform a high resolution synchrotron x-ray diffraction study of iron. Indeed, reviewing data available for other iron based alloys, we find an example of Fe_3C. Although there is no discontinuity of Fe_3C unit cell volume behavior under pressure, the variation of lattice parameters served as an indicator for the magnetic transition in Fe_3C (Lin et al. 2004).

We performed Mössbauer and x-ray diffraction experiments up to 60 GPa, and our data is shown in Figure 4.10. We observe nonlinear variation of *c/a* ration of *hcp* phase lattice parameters with compression, and although it is hard to single out the corresponding critical pressure, our experiments show correlation between softening of V_D and variation of *c/a hcp* phase lattice parameters ratio.We observe better resolved features by tracking evolution of Mössbauer parameters (central shift - CS) extracted from Fe and $Fe_{0.9}Ni_{0.1}$ absorption spectra. At 13-15 GPa the magnetic *bcc* phase of both compounds undergoes phase transition to paramagnetic *hcp* phase. If the *bcc* phase absorption spectra have six absorption lines, the spectra of the paramagnetic *hcp* phase has only one absorption minimum, center of which is related to the Mössbauer central shift. Central shift is very sensitive to structural or electronic transitions and, upon *bcc* to *hcp* structural transition it suddenly decreases. Further compression belowe 40 GPa decreases the *hcp* phase central shift gradually. At pressures below 40 GPa behavior of *hcp* Fe and $Fe_{0.9}Ni_{0.1}$ central shift can be explained by continuous delocalization of *3d*

46
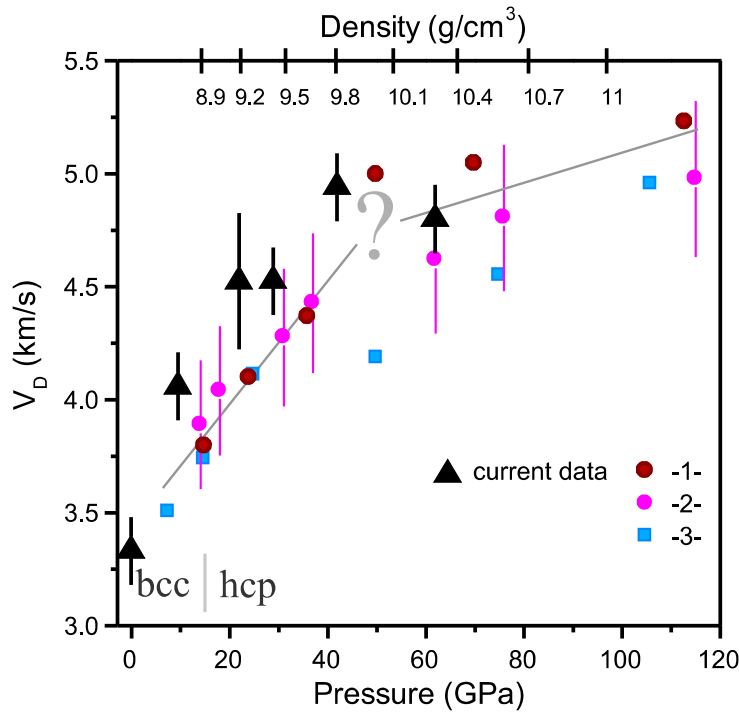
Figure 4.9:

Debye sound velocity for pure Fe and Fe-Ni alloys as a function of pressure. Black solid triangles indicate our $Fe_{0.9}Ni_{0.1}$ data. We compare it with data on pure Fe measured by (-1-) NIS (Mao et al. 2001), and (-2-) impulsive stimulated light scattering measurements (Crowhurst et al. 2005). The blue symbols (-3-) correspond to $Fe_{0.92}Ni_{0.08}$ data points measured by NIS (Lin et al. 2003b). Dashed lines are the eye guides.
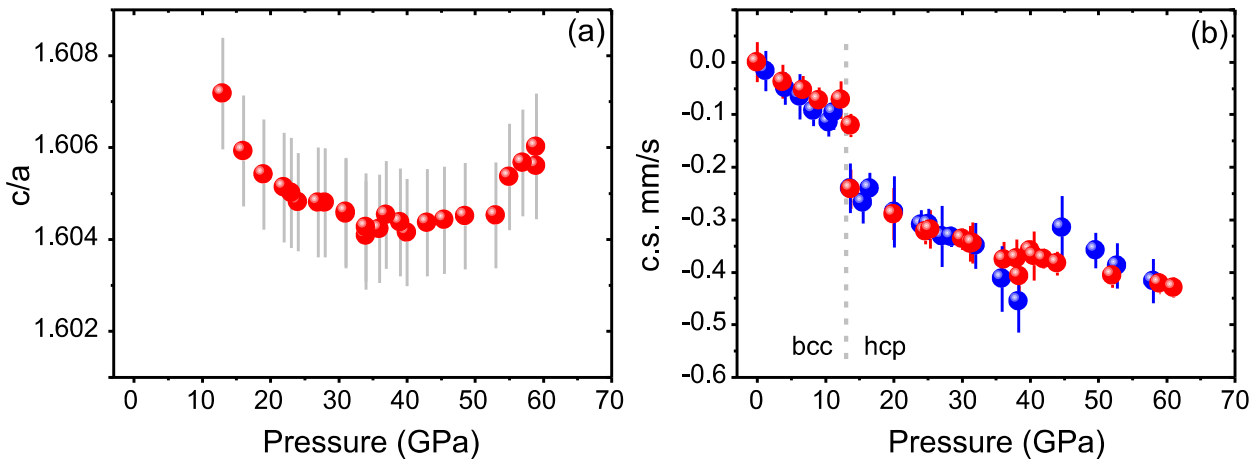
Figure 4.10:

Pressure induced variation of (a) *hcp* phase c/a lattice parameters ratio and (b) Mössbauer central shift determined for pure iron (red circles), and $Fe_{0.9}Ni_{0.1}$ (blue circles). Central shift of materials is given relative to iron. Dashed line indicates transition of *bcc* phases of iron and iron-nickel alloy to *hcp* phase.

electrons, and corresponding weakening of screening interaction between *s-* and *d-* electrons of iron. However, at pressures above 40 GPa we observe a jump of central shift and a change of central shift slope for both compounds.

By definition, Mössbauer central shift is comprised from two components, namely the isomer shift and the second order Doppler shift. First of them is directly connected with *s-* electron density on material nuclei and its interaction with *3d* electrons. The second can be attributed to mean atomic vibrations. Our data does not allow us to separate these two effects, however we approach this problem from another direction.

Summing up our results obtained from the NIS, x-ray diffraction, and Mössbauer experiments, we observe an unknown transition affecting electronic (through the central shift) and elastic properties (through the variation of *c/a,* softening of V_D). In order to determine the nature of this transition, we conducted a theoretical study employing full potential linear augmented plain wave (LAPW) band structure method with the dynamical mean-field theory (DMFT) treatment of the on-site Coulomb repulsion between Fe *3d* states (Aichhorn et al. 2009). The DMFT quantum impurity problem has been solved using the exact Continuous-time strong-coupling Quantum Monte-Carlo method (Werner et al. 2006). The advantage of the combined LDA+DMFT approach comes from the treatment of many body correlation effects in a nonperturbative and thermodynamically consistent way (Leonov et al. 2011). Within the framework we computed ***k***-resolved spectral functions for *hcp* phase iron at 15.4 and 69 GPa (Figure 4.11).

The most striking feature discovered in our study is pressure induced modification of *hcp* iron Fermi surface by formation of hole pockets at **Γ** and **L** points, indicated by arrows in Figure 4.11. The predicted evolution of ***k***-spectral function with pressure implies existence of electronic topological transition (ETT) of *hcp* iron Fermi surface below 69 GPa. Finally, we compare our predictions with experimental observations and come to the following conclusions.

We know that ETT is always accompanied by sound velocity softening (Varlamov et al. 1989), and that variation of *c/a* ratio in model hexagonal materials, for instance Cd-Mg alloys can induce ETT
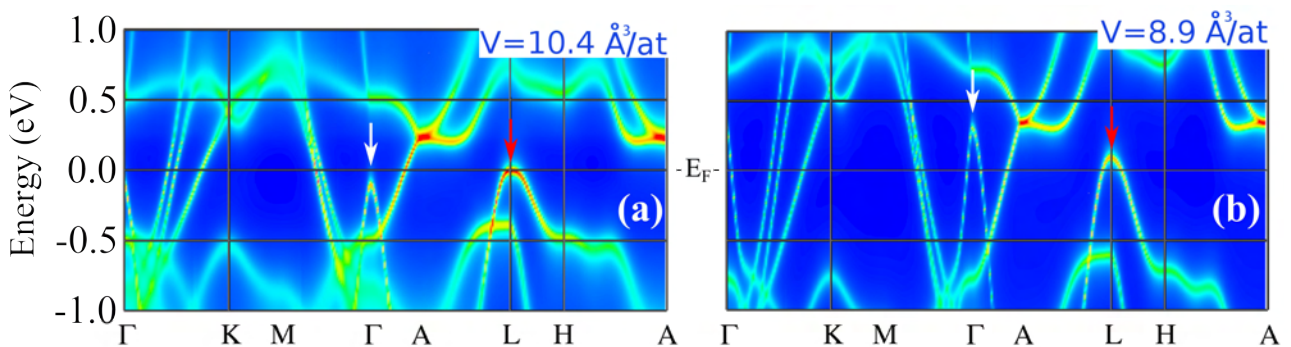
Figure 4.11:

The LDA+DMFT ***k***-resolved spectral function of *hcp* Fe at volumes of (a) 10.4 Å^3/at and (b) 8.9 Å^3/at corresponding to pressures of 15.4 and 69 GPa, respectively. Arrows indicate effect of pressure on the featured electronic bands in the vicinity of the Fermi surface.

transition. Considering behavior of the Fe or $Fe_{0.9}Ni_{0.1}$ *hcp* phases , we suggest that variation of *c/a* ratio with compression results in modification of materials Fermi surface. At certain pressure material undergoes ETT manifesting through a softening of Debye sound velocity. The results of our Mössbauer experimental study can be explained in framework of the ETT transition and support this idea.

Mössbauer parameter central shift (CS) is defined as a sum of two terms, namely isomer shift (IS) and second order Doppler shift (SOD). In turn, isomer or chemical shift is defined as a difference between *s*- electron densities on the nucleus in the absorber and in the radioactive source (Dickson and Berry 2005). Our study shows (see Section 5.4) that isomer shift of *hcp* phase should not be affected by ETT and should gradually decrease with compression. However, second order Doppler shift, which is proportional to the mean square velocity of the iron isotope in solid (Chen and Yang 2007), can be modified by ETT. Indeed, strong coupling between electronic and vibrational degrees of freedom usually observed at ETT (Varlamov et al. 1989) must affect oscillations of iron atoms in the *hcp* phase. We suggest that CS anomaly observed in our Mössbauer experiments at 40-45 GPa is a result of ETT, causing changes of iron atom vibrations and affecting value of SOD.

In conclusion, based on results of three independent experiments, including NIS, x-ray diffraction and Mössbauer spectroscopy we report a new isostructural transition in *hcp* phases of Fe and $Fe_{0.9}Ni_{0.1}$. Comparing our observation with results of the supplementary theoretical study, we argue that all observed anomalous phenomena can be described in the framework of electronic topological transition of *hcp* phases of iron and iron -nickel alloy induced by pressure at 40-45 GPa.

5.   Results

5.1.   Ferric iron in aluminum bearing magnesium silicate perovskite probed by single crystal x-ray diffraction.

K. Glazyrin[1], L. Dubrovinsky[1], T. Boffa Ballaran[1], A. Kurnosov[1], C. McCammon[1], D.J. Frost[1], M. Merlini[2], M. Hanfland[3]

[1]*Bayerisches Geoinstitut, Universität Bayreuth, Germany,* [2]*Università degli Studi di Milano, Milan, Italy,* [3]*European Synchrotron Radiation Facility, Grenoble Cedex, France*

5.1.1 Abstract

Comprehensive knowledge of iron and aluminum bearing magnesium silicate perovskite crystal structure and its evolution under pressure is vital to evaluate and interpret seismic data on the Earth lower mantle. In this study we investigate $Mg_{0.63}Fe_{0.37}Si_{0.63}Al_{0.37}O_3$ by means of single crystal x-ray diffraction at pressures up to 80 GPa and temperatures over 1800 K. After preparing material containing large amount of ferric iron we study effects of high pressure and high temperature conditions on its distribution in crystal structure. By tracking changes of unit cell volume, volumes of individual crystallographic sites and sites occupancies under high pressures and temperatures we found that (a) there is no spin state crossover of ferric iron occupying 8-12 crystallographic A-site in perovskite structure at pressures below 70 GPa, and (b) ferric iron avoids entering octahedral B-site at any conditions of our experiments. We also demonstrate that incorporation of ferric iron and aluminum significantly reduces compressibility of silicate perovskite ($K_{300 K}=233\pm4$ GPa, $K'=4.1\pm0.1$).

5.1.2 Introduction

Iron and aluminum bearing magnesium silicate perovskite $(Mg,Fe)(Si,Al)O_3$ (Pv) is considered the most abundant phase of the Earth's lower mantle. The physical properties of this material, including density, elasticity, electrical and heat-conductivity strongly depend on composition, specifically on the iron and aluminum content (~5-10 mole % for the lower mantle composition). For deep Earth geophysics and geochemistry the importance of iron affecting high-pressure high-temperature behavior of the Pv lies beyond a role of an ordinary impurity. The valence and spin state of iron in silicate perovskite and ferropericlase (Fp) is one of the important factors affecting sound velocity, rheology, elements partitioning, oxygen fugacity, and dynamics of Earth mantle (McCammon 2005, Lin et al. 2008, Irifune et al. 2009, Wicks et al. 2010).

The ideal cubic ABX_3 perovskite crystal structure with space group *Pm3m* consists of a three-dimensional network formed by corner connected octahedra (B-sites). The cavities between octahedra form the dodecahedral sites (A-sites). Lower mantle $(Mg,Fe)(Si,Al)O_3$ perovskite has a $GdFeO_3$ structure type, which is distorted from the ideal cubic symmetry by tilting of octahedral, and it has space group *Pbnm* (Horuichi et al. 1987)(Fig. 5.1.1). The large distorted 8- to 12-fold coordinated A-site in

orthorhombic perovskite can be occupied by Mg^{2+} or $Fe^{2+/3+}$ (Horuichi et al. 1987, McCammon et al. 1992); and the smaller and nearly ideal octahedral B-site (Fig. 5.1.1) may be occupied by Si^{4+}, Al^{3+} or Fe^{3+} cations. Here and below we will use the superscript at element's name to designate its valence state and the subscript to mark the site occupied. Addition of aluminum stabilizes Fe^{3+} in Pv and leads to higher values of $Fe^{3+}/\Sigma Fe$ ratio (~50-75%) (Lauterbach et al. 2000). It is generally accepted that special crystal chemistry of silicate perovskite is a reason explaining stability of ferric iron in Pv even under reducing conditions of the lower mantle (Lauterbach et al. 2000, McCammon 2005).

While implications of iron being in different valence and spin states for geophysically or geochemically important properties of Pv are still intensively debated, there is a general agreement that spin state crossover of ferrous iron has minor or even undetectable effect. In absence of reliable experimental results, the picture is not clear in case of Pv containing ferric iron. Magnesium silicate perovskite may have finite amount of ferric iron (Fe^{3+}) incorporated through different substitution mechanisms, for example, by charge coupling with Al^{3+}_B (FeAl coupling) or by coupling with Fe^{3+}_B (FeFe coupling). Considering Al-free Pv and Fe^{3+}_A, theoretical studies predict a HS-LS crossover (spin number S changes from 5/2 to 1/2) at 105-130 GPa (Stackhouse et al. 2007), and they estimate 60-150 GPa for pressures of Fe^{3+}_B spin crossover. In addition, it has been foretold that Fe^{3+}_B undergoes a HS-LS spin-state transition under compression (40-70 GPa), while the Fe^{3+}_A remains in the HS state (Hsu et al. 2011). The predicted spin-state crossover at Fe^{3+}_B should result in a noticeable volume reduction accompanied by a significant softening of bulk modulus, and, ultimately, it may be at origins of observed lower mantle seismic-velocity anomalies. In contrast to theoretical predictions, some nuclear forward scattering (NFS) data suggest that Fe^{3+}_A completes transition to LS state at 70 GPa (Jackson et al. 2005). The more recent combined x-ray powder diffraction, NFS, and x-ray emission spectroscopy (XES) study (Catalli et al. 2010) of pure ferric iron-magnesium Pv reports that LS population of the B site gradually increases above 40 GPa, with all Fe^{3+}_B being in LS state above 50-60 GPa. According to Catalli et al. (2010) Fe^{3+}_A remains in HS state below 136 GPa. This complicated and so far controversial picture of ferric iron behavior in silicate perovskite at high pressures may become even more complex if Al^{3+} is present as expected for Earth mantle compositions.
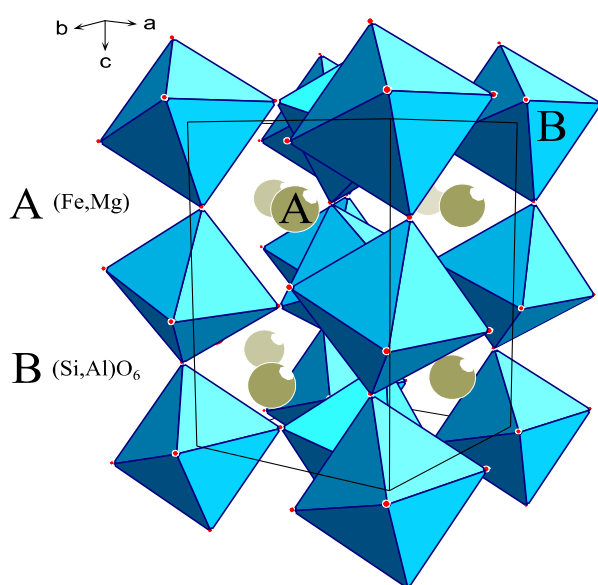
Fig. 5.1.1:

Representation of *Pbnm* structure of magnesium silicate perovskite. A and B letters represent different crystallographic sites.

Ferric iron in aluminum bearing magnesium silicate perovskite probed by single crystal x-ray diffraction.

In order to evaluate effect of ferric iron on structure and properties of silicate Pv at conditions of Earth lower mantle geotherm, we studied sample material $Mg_{0.63}Fe_{0.37}Si_{0.63}Al_{0.37}O_3$ Pv synthesized in multi-anvil apparatus at 25 GPa and 1300 K (see Experimental Methods for details). According to results of Mössbauer spectroscopy study conducted on the sample, the material contains almost all iron in the form of Fe^{3+} ($Fe^{3+}/\Sigma Fe = 0.93\pm0.3$). Based on information obtained from a comprehensive single crystal diffraction collected at ambient conditions, we verified that all iron incorporated into A-site. Among a few methods suitable for investigations of structural, valence, and electronic state of iron in silicate perovskite single crystal x-ray diffraction and energy-domain (conventional) Mössbauer spectroscopy are probably the most reliable and precise techniques of choice, but they are rarely employed together for studies of materials at conditions of the Earth's lower mantle. Using single crystal x-ray diffraction data collected at pressures over 70 GPa and temperatures over 1800 K (see Methods for additional details), we conducted a full structural refinement of Pv accompanied by a Mössbauer spectroscopy study, published elsewhere (Potapkin et al. 2011).

5.1.3 Experimental Methods

The perovskite sample was synthesized from a ground mixture of oxides and hydroxides (13.6% Al_2O_3, 21.6% Fe_2O_3, 33% SiO_2, 31.8% $Mg(OH)_2$ wt%) with a bulk composition similar to that used in experiments on mid-ocean ridge basalt compositions. The prepared mixture was welded in platinum capsule and together with $W_{97}Re_3$-$W_{75}Re_{25}$ thermocouple and $LaCrO_3$ furnace was put into octahedral multianvil pressure assembly. The assembly was compressed in multianvil press to approximately 25 GPa and then heated to 1300 °C for 30 minutes. The run products comprised magnesium silicate perovskite coexisting with quenched crystallized melt and small (<10 μm) crystals of an Al-rich hydrous phase. The composition of the several perovskite crystals was probed by microprobe analysis giving the following result in wt%: 16.4 (3)% Al_2O_3, 26.1 (4)% FeO, 33.6 (5)% SiO_2, 21.6 (3)% MgO. Additionally, we determined the $Fe^{3+}/\Sigma Fe$ ratio (0.93±0.3) using Mössbauer spectroscopy on a powdered sample from the same experimental charge. The data on the crystallographic sites occupancy for iron and other elements derived from ambient condition single crystal diffraction experiments provided unambiguous evidence that ferric and ferrous iron ions occupy exclusively the A-sites.

Small single crystalline pieces of the prepared material (~10·15·5μm) together with ruby chips (pressure marker) were loaded into sample chambers of Chervin type membrane diamond anvil cells (DAC) available at ESRF (Chervin et al. 1995). The sample chamber was prepared by drilling a hole in preindented rhenium gasket, and prior to compression was filled with the quasihydrostatic pressure medium – Ne, which was also used as independent ambient and high-temperature pressure standard (Fei et al. 2007a).

For single crystal x-ray diffraction experiment we used MAR555 flat panel detector installed at beamline ID09a, ESRF, Grenoble, France. The x-ray wavelength was 0.415 Å. At ambient temperature the data was collected during ω rotation scans ±30º with 0.5º step. Due to strict space restrictions imposed by beamline, the limits of the ω rotation scans collected at high temperature were lower (-28º→20º). However, in order to improve the number of diffraction spots (observations) from the sample and, respectively, the quality of the data, we collected diffraction at high temperatures in two different sample orientations by rotating DAC by 90º along the x-ray beam propagation axis. The

collected 2D diffraction images were first analyzed by Oxford Diffraction Crysalis software (Crysalis RED 2006) with consequent refinement of integrated intensities in SHELXL-97, WinGX version (Farrugia 1999, Sheldrick 2008). Volumes of specific crystallographic sites were determined using Mathematica software (Wolfram Research, Inc. 2008) by splitting corresponding polyhedrons into tetrahedral components and summing volumes of the latter.

In order to create high temperature conditions, we used an enhanced version of portable laser setup described previously and adjusted for the requirements of ID09a (Dubrovinsky et al. 2009, 2010a). The setup consist of the SPI laser system (SPI100, wavelength 1064 nm, 100 W) coupled by optical fiber with UniHead system, which allows simultaneous visual observation of the sample, laser heating and evaluation of temperature. In order to ensure homogeneous heating of the small single crystal samples, a laser spot with a diameter of about 50 μm was used. In order to guarantee homogeneous heating we flattened a laser beam power profile by means of a special optical device (π-shaper) mounted on the UniHead. Thermal radiation coming from the heated sample was collected by Ocean Optics QE65000 spectrometer, with fitting the resulting spectra by Planck's radiation function (Bassett and Weathers 1986). The laser heating was conducted in continuous laser operation mode.

5.1.4 Results and Discussion

The pressure-volume-temperature curves are shown in Fig. 5.1.2. Using 3rd order Birch–Murnaghan equation of state (EOS) and fixing the ambient conditions volume $V_{300\,K,0} = 169.7(2)\,Å^3$ to value measured with high precision at ambient conditions we have derived the bulk modulus $K_{300K,0} = 233(4)\,GPa$ and its pressure derivative $K' = 4.1(0.1)$. These values are in good agreement with our previous study (Dubrovinsky et al. 2010a). The lower value of bulk modulus we found and reported by Catalli et al. (2010) compared with pure $MgSiO_3$ Pv (Lundin et al. 2008) indicate that incorporation of larger amount of ferric iron to the silicate Pv irrespective of the crystallographic site leads to higher compressibility.

Combining our data and data from Dubrovinsky et al. (2010) measured on the same material, we provide a generalized model describing behavior of our material at ambient and elevated temperatures using a modified version of 3rd order Birch-Murnaghan equation of states:

$$P = \frac{3}{2} \cdot K_{T,0} \left[\left(\frac{V_{T,0}}{V} \right)^{7/3} + \left(\frac{V_{T,0}}{V} \right)^{5/3} \right] \cdot \left[1 + \frac{3}{4} \cdot (K'_{T,0} - 4) \cdot \left(\left(\frac{V_{T,0}}{V} \right)^{2/3} - 1 \right) \right] , (1)$$

where $K_{T,0}$, $K'_{T,0}$, P, and $V_{T,0}$ represent ambient pressure bulk modulus, its pressure derivative, applied pressure and volume of material. We expressed the former and the latter terms through the following relations (Saxena et al. 1999):

$$V_{T,0} = V_0 \cdot e^{a_1 \cdot (T - T_0) + 0.5 \cdot a_2 \cdot (T^2 - T_0^2)}, \ K_{T,0} = \frac{1}{b_1 + b_2 \cdot T + b_3 \cdot T^2} , (2)$$

where a_1, a_2, b_1, b_2, and b_3 are the fitting parameters; T_0 and T are used as a reference temperature (300 K) and a temperature of sample, respectively. After fitting the full set of data we obtain the following
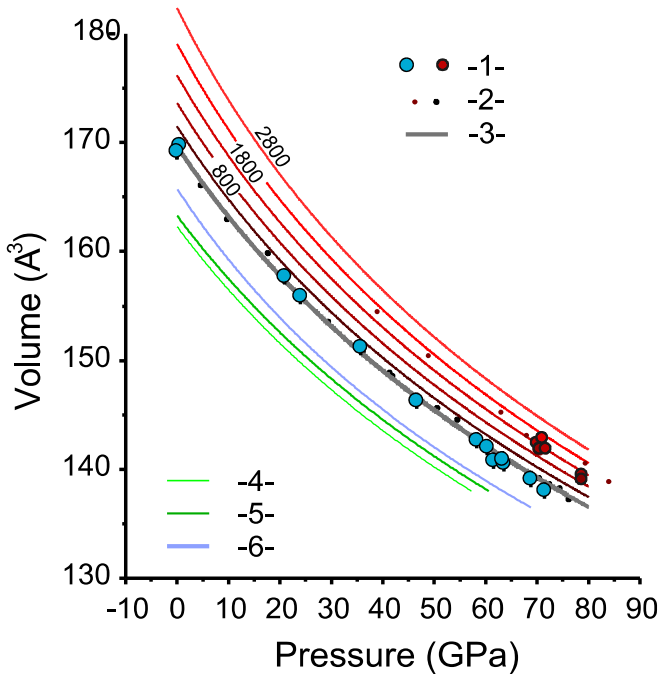
Fig. 5.1.2:

Pressure dependencies of unit cell volume determined for Pv with different iron content (*x,* mole %): (1) $x_{Fe/Al}$=0.37, current; (2) $x_{Fe/Al}$=0.37, same material (L. Dubrovinsky et al. 2010); (3) $x_{Fe/Al}$ =0.37, equation of state at 300 K; (4) x_{Fe} =0.2 from (Catalli et al. 2010); (5) x_{Fe} =0.15 from (Lundin et al. 2008), (6) x_{Fe} =0 from (Lundin et al. 2008). Black/blue and red points represent ambient and high temperature points, respectively. Lines with different red shading were obtained after fitting data to thermal equation of states, and we show by numbers corresponding temperatures.

values: a_1= 1.721·10⁻⁵; a_2=7.5·10⁻⁹; b_1=4.201·10⁻³; b_2=-7.69·10⁻⁹;b_3=192.06·10⁻¹². The $K'_{T,0}$ assumed to be temperature independent.

In addition to testing bulk elastic properties, single crystal x-ray diffraction allows direct probing of electronic density at corresponding crystallographic sites in silicate perovskite, and thus we can differentiate signal coming from Fe^{3+} occupying A- or B-sites. Additionally, we address a long standing problem of $Fe^{3+}_{A/B}$ spin state. By choosing single crystal over powder x-ray diffraction, we can avoid a few complications (powder texture evolution, strains due to grain-grain interactions), and we can detect complex processes promoted by compression, for instance, the redistribution of elements $Fe^{3+\ (HS)}_A+Al^{3+}_B \rightarrow Fe^{3+(LS)}_B+Al^{3+}_A$ suggested by Catalli et al. (2010). Applying reasoning similar to one reported by Irifune et al. (2009), Catalli et al. (2010) suggested that it is energetically more favorable for ferric iron to exchange crystallographic sites from A- to B- at pressures above 60 GPa, to be more precise, at pressures above HS-LS crossover, reported for Fe^{3+}_B by the same group.

Thus, before we can address the important topic of ferric iron spin state in Pv at conditions of the lower mantle, we have to know precisely what kind of elements occupy the various crystallographic sites of Pv and test problem of Fe and Al redistribution after high pressure, high temperature treatment raised by Catalli et al (2010). The data for the test was collected at pressures around 70 GPa in several sets, namely before, during and after laser heating at 1700-1800 K. At each P-T point we have collected 100-110 unique reflections, and we report values of R_1 below 6 %. Defined as $R_1=\Sigma ||F_O|-|F_C||/\Sigma |F_O|$, this value measures discrepancy between a model (calculated intensity F_C) and observations (observed intensity F_O). In this crystal structure refinement we did not distinguish Si or Al in B, and determined occupancy of Si_B/Al_B and Fe_A as the last step of refinement, by fixing of occupancies of other elements to values measured in the ambient conditions study (see table in Appendix 1). Fig. 5.1.3 shows that
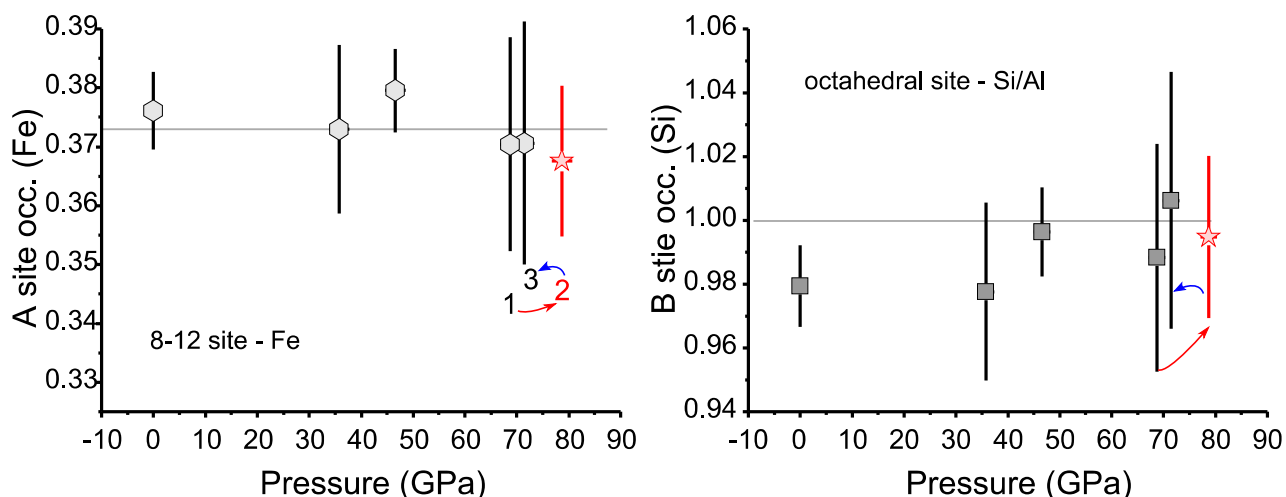
Fig. 5.1.3:

Occupancies of Fe_A and Si_B sites as a function of pressure. Numbers and arrows serve as sequence markers: (1) before laser heating (2) during the heating at ~1800 K, (3) just after the heating. The dashed lines show the occupancies of sites determined with high accuracy at 0 GPa. We used pure Si to describe occupancies of Al^{3+}/Si^{4+} attributed to B-sites due to similar (almost indistinguishable) x-ray scattering of these ions.

pressure-temperature treatment does not affect distribution of iron between A and B sites within accuracy of our measurements, and we conclude that $Fe_A \leftrightarrow Al_B$ redistribution is not relevant for silicate perovskite at conditions, close to conditions of the middle of the Earth lower mantle (78 GPa, 1800 K).

Knowing that all iron in our samples occupies exclusively A-sites at all pressures, and having large concentration of iron in the material, we were expecting to detect HS-LS transition of ferric iron with high sensitivity. As was motioned above we did not observes anomalies of unit cell volume contraction with pressure. We also investigated variation of A- and B-site partial volumes with pressure (Fig. 5.1.4). Since we determined, that ferric iron is in A-sites at all pressures of our study, the volume of A-sites should be modified most in case of HS-LS state crossover. Note, that due to very low amount of Fe^{2+}_A in our material, we do not expect to detect any profound change of volume due to HS-IS transition reported earlier (Lin et al. 2008, McCammon et al. 2008). We do not observed any abrupt changes or anomalies in compressibility of individual polyhedral volumes and conclude that there are no spin crossover in Fe^{3+}_A up to at least 80 GPa (Fig. 5.1.4). Considering temperature effects, A-site volume at constant pressure will also increase, thus making probability of HS-LS transition at A-site even lower. The same lines of arguments also suggest that effect of high temperature should shift possible spin state crossover of Fe^{3+}_A to higher pressures.

In order to extract additional information, we compare our data with data for reference material – pure $MgSiO_3$ (MgPv). Although, to our knowledge there is no precise data on crystal structure of the latter at pressures above 15 GPa, we create a non uniform compression model with known variation of lattice parameters (Lundin, Catalli, и др. 2008), however using unit cell coordinates accurately determined at ambient conditions (Dobson & Jacobsen 2004) in order to evaluate effect of pressure on the individual crystallographic sites (black line Fig. 5.1.4).
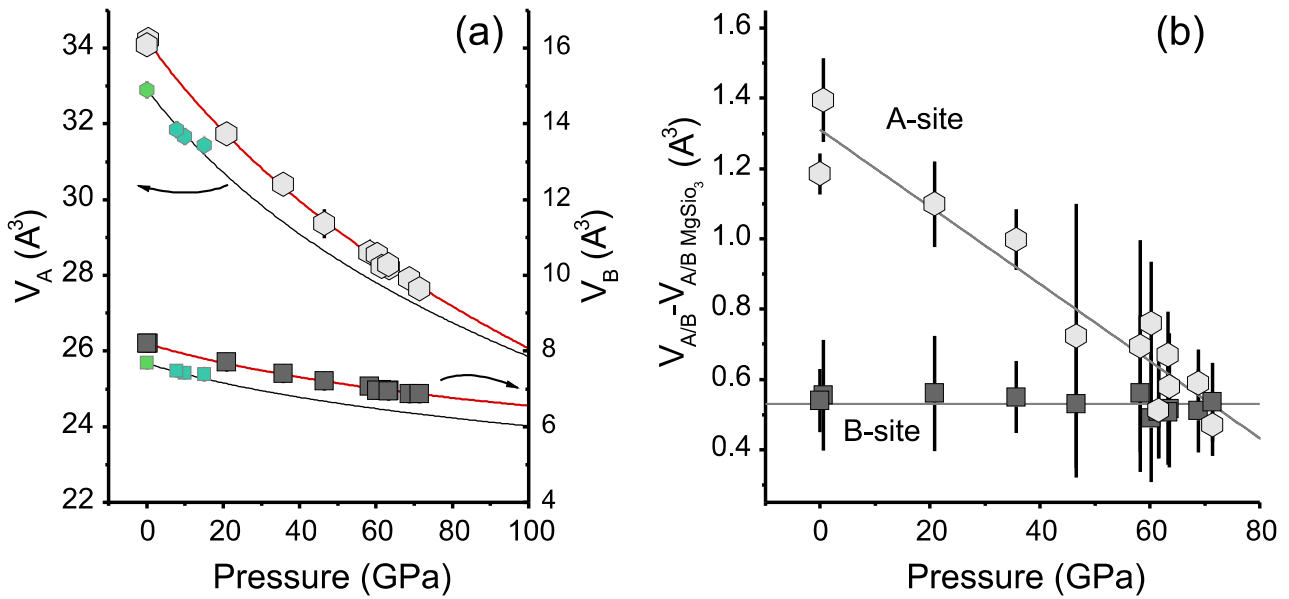
Fig. 5.1.4:

(a) Volumes of individual atomic polyhedra of A and B crystallographic sites and their variation with pressure measured on silicate perovskite $Mg_{0.63}Fe_{0.37}Si_{0.63}Al_{0.37}O_3$ (grey points). We show literature data for pure $MgSiO_3$ using green and light blue symbols (Horuichi et al. 1987, Sugahara et al. 2006). Black lines obtained in an assumption of non uniform compression employing available data (Dobson and Jacobsen 2004, Lundin et al. 2008). Using the same approach and tracking compression of A- and B- sites of our material relative to pure $MgSiO_3$ shown in (b), we plot red lines. Grey dashed lines in (b) represent linear fits.

Comparing observations for pure phase and phase with large amount of Fe/Al, we find that B- site is clearly less compressible than A-site (Fig. 5.1.4), and that Si_B/Al_B forming the octahedral framework are much less compressible than Fe_A. This is an important fact which should be considered in the theoretical calculations and predictions of the HS-LS transition of iron bearing Pv material.

To conclude, we conducted a high pressure single crystal diffraction study of magnesium silicate perovskite $Mg_{0.63}Fe_{0.37}Si_{0.63}Al_{0.37}O_3$ in order to investigate evolution of crystal structure with compression. We provided the equation of states for high temperature/high pressure conditions. After analyzing data collected at 70 GPa at ambient and elevated temperatures, we tested hypothesis of Catalli et al. (2010) and Hsu et al. (2011) and demonstrated that there is no redistribution of ferric iron and aluminum between different crystallographic sites after the high pressure or the combined high pressure/high temperature treatment. We demonstrated that although the effect of compression is clearly stronger for A-sites, there are no evidences for a spin state crossover of ferric iron Fe^{3+}_A up to at least 70 GPa. We suggest that high temperature expansion will suppress the predicted ferric iron spin state crossover to even higher pressures, thus diminishing a probability of any related anomalies of elastic, conductive, heat transport properties to the deeper regions of the lower mantle.

56

5.1.5 Appendix 1

Table.1 Lattice and unit cell parameters of MgFeAlPv determined in diamond anvil cell experiment, as a function of pressure and temperature

P, GPa	T, K	R1,%	A, Å	B, Å	C, Å	V, Å³	Unit cell coordinates x, y, z	occ.*
0.001$^\Delta$	300	3.85	4.8110(4)	5.0007(3)	7.0293(3)	169.11(1)	Si/Al: 0.5000, 0.0000, 0.5000 Mg/Fe: 0.5157(1), 0.5595(1), 0.2500 O1: 0.1140(4), 0.0446(4), 0.2500 O2: 0.1920(3), 0.1971(3), 0.5586(2)	
0.001	300	4.5	4.8121(2)	5.0011(2)	7.0308(10)	169.20(3)	Si/Al: 0.5000, 0.0000, 0.5000 Mg/Fe: 0.5159(2), 0.5601(2), 0.2500 O1: 0.1129(6), 0.4555(6), 0.2500 O2: 0.1922(4), 0.1978(5), 0.5587(5)	Fe 0.3762(66) Si 0.9794(129)
0.5	300	5.1	4.8222(4)	5.0101(2)	7.0275(5)	169.78(2)	Si/Al: 0.5000, 0.0000, 0.5000 Mg/Fe: 0.5154(4), 0.5593(4), 0.2500 O1: 0.1127(12), 0.4575(10), 0.2500 O2: 0.1928(8), 0.1981(8), 0.5574(5)	
20.9(1)	300	7.3	4.6996(3)	4.9080(2)	6.8386(3)	157.74(1)	Si/Al: 0.5000, 0.0000, 0.5000 Mg/Fe: 0.5161(4), 0.5639(6), 0.2500 O1: 0.1168(14), 0.4579(13), 0.2500 O2: 0.1898(8), 0.1966(10), 0.5589(6)	
35.7(2)	300	4.4	4.6278(3)	4.8529(4)	6.7335(18)	151.22(4)	Si/Al: 0.5000, 0.0000, 0.5000 Mg/Fe: 0.5187(2), 0.5675(3), 0.2500 O1: 0.1148(8), 0.4585(7), 0.2500 O2: 0.1866(6), 0.1942(5), 0.5588(8)	Fe 0.3730(143) Si 0.9777(280)
46.6(1)	300	5.2	4.5689(6)	4.8184(4)	6.6440(90)	146.27(20)	Si/Al: 0.5000, 0.0000, 0.5000 Mg/Fe: 0.5193(5), 0.5697(6), 0.2500 O1: 0.1157(15), 0.4601(12), 0.2500 O2: 0.1872(11), 0.1938(9), 0.5623(21)	Fe 0.3796(71) Si 0.9964(141)
57.4(2)	300	8.5	4.5282(1)	4.7785(7)	6.6002(15)	142.81(4)	Si/Al: 0.5000, 0.0000, 0.5000 Mg/Fe: 0.5186(7), 0.5687(8), 0.2500 O1: 0.1156(26), 0.4522(17), 0.2500 O2: 0.1871(17), 0.1934(13), 0.5590(10)	
58.3(2)	300	7.3	4.5330(20)	4.7807(16)	6.5830(30)	142.66(10)	Si/Al: 0.5000, 0.0000, 0.5000 Mg/Fe: 0.5195(7), 0.5688(8), 0.2500 O1: 0.1186(20), 0.4590(18), 0.2500 O2: 0.1824(13), 0.1915(13), 0.5601(8)	
60.3(2)	300	8.6	4.5179(10)	4.7730(5)	6.5884(11)	142.07(4)	Si/Al: 0.5000, 0.0000, 0.5000 Mg/Fe: 0.5200(6), 0.5716(8), 0.2500 O1: 0.1168(18), 0.4555(14), 0.2500 O2: 0.1849(11), 0.1953(10), 0.5582(7)	

Ferric iron in aluminum bearing magnesium silicate perovskite probed by single crystal x-ray diffraction.

P, GPa	T, K	R1,%	A, Å	B, Å	C, Å	V, Å³	Unit cell coordinates x, y, z	occ.*
61.5(2)	300	5.0	4.5099(5)	4.7606(6)	6.5580(30)	140.80(7)	Si/Al: 0.5000, 0.0000, 0.5000 Mg/Fe: 0.5204(3), 0.5715(4), 0.2500 O1: 0.1177(11), 0.4596(10), 0.2500 O2: 0.1840(8), 0.1919(6), 0.5614(10)	
63.3(1)	300	5.4	4.5038(2)	4.7632(3)	6.5697(14)	140.94(3)	Si/Al: 0.5000, 0.0000, 0.5000 Mg/Fe: 0.5201(4), 0.5728(4), 0.2500 O1: 0.1169(13), 0.4602(10), 0.2500 O2: 0.1860(10), 0.1928(7), 0.5607(11)	
68.8(2)	300	5.7	4.4817(3)	4.7478(4)	6.5391(17)	139.14(4)	Si/Al: 0.5000, 0.0000, 0.5000 Mg/Fe: 0.5214(3), 0.5733(4), 0.2500 O1: 0.1179(11), 0.4597(8), 0.2500 O2: 0.1844(8), 0.1922(6), 0.5609(9)	Fe 0.3704(182) Si 0.9883(357)
70.5(5)	300	10.1	4.5183(3)	4.7641(3)	6.5863(18)	141.77(4)	Si/Al: 0.5000, 0.0000, 0.5000 Mg/Fe: 0.5179(6), 0.5693(9), 0.2500 O1: 0.1155(22), 0.4593(21), 0.2500 O2: 0.1866(13), 0.1928(13), 0.5648(29)	
71.4(2)	300	4.8	4.4722(2)	4.7341(3)	6.5211(17)	138.06(4)	Si/Al: 0.5000, 0.0000, 0.5000 Mg/Fe: 0.5209(3), 0.5735(4), 0.2500 O1: 0.1193(11), 0.4594(9), 0.2500 O2: 0.1831(7), 0.1923(6), 0.5634(7)	Fe 0.3707(207) Si 1.0063(403)
71.8(5)	1750(50)	7.3	4.5194(7)	4.7653(7)	6.5860(50)	141.84(11)	Si/Al: 0.5000, 0.0000, 0.5000 Mg/Fe: 0.5180(5), 0.5699(7), 0.2500 O1: 0.1146(18), 0.4568(16), 0.2500 O2: 0.1870(11), 0.1937(12), 0.5636(19)	
71.8(2)	1800(150)	9.2	4.5183(5)	4.7638(6)	6.5910(40)	141.87(9)	Si/Al: 0.5000, 0.0000, 0.5000 Mg/Fe: 0.5180(6), 0.5703(8), 0.2500 O1: 0.1169(20), 0.4585(19), 0.2500 O2: 0.1857(12), 0.1923(12), 0.5639(26)	
78.2(5)	1700(50)	6.2	4.4932(3)	4.7479(3)	6.5400(20)	139.52(4)	Si/Al: 0.5000, 0.0000, 0.5000 Mg/Fe: 0.5204(5), 0.5701(6), 0.2500 O1: 0.1191(18), 0.4602(14), 0.2500 O2: 0.1847(13), 0.1922(9), 0.5626(14)	
78.7(5)	1700(50)	6.6	4.4910(6)	4.7452(6)	6.5460(40)	139.50(9)	Si/Al: 0.5000, 0.0000, 0.5000 Mg/Fe: 0.5190(6), 0.5691(6), 0.2500 O1: 0.1219(23), 0.4571(17), 0.2500 O2: 0.1855(15), 0.1929(12), 0.5631(18)	Fe 0.3676(128) Si 0.9948(254)

All values given in this table were measured on material loaded into DAC, unless stated otherwise. P and T show pressure and temperature conditions of experiments. A, B, C, and V correspond to the $Mg_{0.63}Fe_{0.37}Si_{0.63}Al_{0.37}O_3$ unit cell dimensions and volume, respectively. R1 is defined as $R_1 = \Sigma||F_O|-|F_C||/\Sigma|F_O|$, where $|F_O|$ and $|F_C|$ are the observed and calculated intensities, respectively.

*occ. - occupancies of Fe and Si at A-, and B- sites determined in special refinements while testing hypothesis of Fe/Al redistribution (Catalli et al. 2010). See main text for the details.

Δ - values determined at ambient conditions using four circle Oxford X'calibur diffractometer. R1 value is given for 394 diffraction intensities with $F_O > 4\sigma_{Fo}$, where we use σ_{Fo} to indicate value of standard deviation. In this run sample material was measured in air prior to its loading into DAC.

5.2. Effect of high pressure on crystal structure and electronic properties of magnetite below 25 GPa.

K. Glazyrin[1], C. McCammon[1], L. Dubrovinsky[1], M. Merlini[2], K. Schollenbruch[3], A. Woodland[3], M. Hanfland[4]

[1]*Bayerisches Geoinstitut, Universität Bayreuth, Germany,* [2]*Università degli Studi di Milano, Milan, Italy,* [3]*Institut für Geowissenschaften, Universität Frankfurt, Frankfurt, Germany,* [4]*European Synchrotron Radiation Facility, Grenoble Cedex, France*

5.2.1 Abstract

We report results from high pressure single crystal x-ray diffraction and Mössbauer absorption experiments on magnetite. Based on high quality diffraction data we have obtained accurate information on the crystal structure of magnetite below 25 GPa, which enables an unambiguous interpretation of the Mössbauer data using constrained area ratios and a full transmission integral fit that avoids area distortion due to thickness effects. Based on our analysis, all aspects of the electronic and magnetic properties of magnetite reported previously below 25 GPa at ambient temperature can be explained solely by enhanced delocalization of *3d* electrons of iron atoms. For instance, we present evidence that compression induced metallization changes the sign of the charge carrier spin polarization at 15 GPa.

5.2.2 Introduction

Magnetite is one of the most fascinating and important iron containing minerals. In nature, simple life forms such as bacteria and more evolved species such as birds use magnetite crystals as magneto receptors to orient themselves in the Earth's magnetic field (Gould 2011). Magnetite is also widely used commercially as a pigment for paints and construction, as an aggregate for high density concrete, and in many other forms for diverse purposes (Hiergeist et al. 1999, Mayo et al. 2007). Away from ambient conditions, extreme temperatures or pressures have revealed the complex physics of this material.

The crystal structure of magnetite is an inverse spinel type with tetrahedral (T) sites occupied by Fe^{3+} and octahedral (O) sites occupied by both Fe^{2+} and Fe^{3+}. The antiferromagnetic exchange between T- and O-sites align magnetic moments of iron along the [111] direction. Electron hopping between octahedra occupied by iron ions in different valence states determines the transport properties of magnetite. Magnetite is a half metal at ambient conditions with high polarization of charge carriers (Dedkov et al. 2002). The application of moderate pressures (<25 GPa) induces profound changes to its electronic properties (Morris and Williams 1997), leaving the crystal structure almost unaffected (Haavik et al. 2000), although some peculiarities were reported in a powder x-ray diffraction study (Rozenberg et al. 2007) . It is worth noting here, however, that powder x-ray diffraction analysis at high pressure of subtle features such as element coordination can give ambiguous and sometimes unrealistic results. This is mostly due to the small amount of sample which limits the signal quality, the limited resolution and 2θ range, as well as evolution of texture effects arising from uni-axial stress. Based on

existing information of the crystal structure of magnetite below 25 GPa, two possible scenarios have been heavily discussed in the literature to explain the high pressure behavior of magnetite.

The first hypothesis is a transition from the inverse type (IT) of spinel to the normal type (NT) at pressures 10-20 GPa (Pasternak et al. 2003). Analysis of powder x-ray diffraction data suggested a pressure-induced anomaly of the unit cell oxygen coordinate (u), indicating a decrease of the relative volumes of O-sites (V_O/V_{cell}) and an increase for T-sites (V_T/V_{cell}). The reported effect was extremely large: on average there was a ~10% volume change of O- and T- sites, which was interpreted to indicate that the large Fe^{2+} ion changed its position from the O- to the T-site due to compression inducing a redistribution of electronic charge.

The second hypothesis is a spin state transition of Fe^{2+} (O-sites) from high spin (HS) to intermediate spin (IS) (Ding et al. 2008). Combined x-ray magnetic circular dichroism and x-ray emission spectroscopy studies revealed a reduction of the net magnetic moment of magnetite. It was proposed that the competition between the crystal field splitting, Hund exchange integral and covalence effects induced the change of spin state.

The physics behind the HS-LS transition differs from the IT-NT model. It is important to note that these two scenarios of high-pressure behavior are incompatible, and that IT-NT and HS-IS transitions cannot occur within the same pressure range (10-20 GPa).

In order to seek a deeper insight into the complex physics of magnetite below 25 GPa, we performed a combined single crystal x-ray diffraction and Mössbauer study. The different crystallographic environments and valence states of iron in magnetite constrain the assignment of absorption features of the Mössbauer spectra. Thus before fitting the Mössbauer spectra, we obtained accurate information on the crystal structure of magnetite and directly tested the IT-NT model. The results of the single crystal study enabled an unambiguous fitting of Mössbauer data (powder samples). Mössbauer parameters obtained in the experiment allowed a rigorous testing of the HS-IS model through tracking of pressure-induced changes of electronic structure, crystallographic site valence states (isomer shift), distortions of the O- and T-sites (quadrupole splitting), and magnetic moments of iron atoms in different crystallographic sites (hyperfine magnetic field).

5.2.3 Experimental methods

The magnetite powders for the Mössbauer experiment were prepared in a gas mixing furnace from 99.99% Fe_2O_3 enriched with ^{57}Fe (>90%). The hematite starting material was compressed into pellets, heated for 12 hours at 1200 °C in a CO/CO_2 mixture ($\log(p_{O2})$=-6.4) and subsequently quenched. Based on the results of Mössbauer and x-ray powder diffraction experiments, we confirmed that the prepared material contained single phase magnetite. No traces of other iron oxides were found. The deviation from non stoichoimetric composition ($Fe3O_{4-\delta}$) for the powder material was estimated to be $0.0001<\delta<0.001$ based on the preparation conditions (Aragón et al. 1985). For the single crystal x-ray diffraction experiments we selected several small chips of natural magnetite (~3x10x20 μm) originating from the Bijiki iron formation, upper peninsula of Michigan, U.S.A. The analysis of impurities (Appendix 1) of the natural sample was done using Jeol JXA-8200 electron microprobe equipped with five wavelength dispersive spectrometers. An accelerating voltage of 15 kV and a beam current of 15 nA

were employed. The beam size was 1-2 μm.

The natural single crystal samples are expected to have a lower degree of stoichoimetry (higher δ values) than the synthesized powder material used in this work (Shepherd et al. 1985). Nevertheless, we believe that it is valid to use the single crystal structural data of magnetite to interpret the Mössbauer data of the powder material. Our reasoning comes from the observation of the behavior of the material in the vicinity of the Verwey transition (VT). On one hand, VT in magnetite can be affected by a deviation of δ from zero. For example for a material with δ>0.0036, the VT changes from first to second order (Kakol and Honig 1989). On the other hand, the high pressure resistivity data provide evidence that the driving force for the VT remains the same for different values of δ, and that the difference of VT critical pressures is small (1-4 GPa, measured in a highly nonhydrostatic pressure medium)(Môri et al. 2002). In this work we employ a significantly more hydrostatic pressure medium (Ne), and we believe that the difference between high pressure transitions at ambient temperature of magnetite with low and high degrees of stoichoimety should be negligible.

High pressure Mössbauer experiments were conducted using modified Merrill-Bassett diamond anvil cells (DACs). For single crystal x-ray diffraction experiments we used a different DAC (60° diffraction cone opening) equipped with two Boehler-Almax diamonds. The diamond culet size was 300 μm. The samples were loaded into 150 μm holes drilled in 30-40 μm preindented rhenium gaskets along with ruby chips for pressure calibration (Mao et al. 1986). Ne was used as a pressure transmitting medium for all experiments.

The 57Fe Mössbauer spectra were collected at Bayerisches Geoinstitut, Bayreuth, Germany. Spectra were obtained at room temperature in transmission mode on a constant acceleration Mössbauer spectrometer using a nominal 370 MBq ^{57}Co high specific activity source in a 12 μm Rh matrix (point source). The velocity scale was calibrated relative to 25 μm thick α Fe foil. Collection time for each spectrum varied from 24 to 30 h. Mössbauer absorption varied from 7 to 9%, depending on the sample loading. The spectra were fitted using the full transmission integral procedure implemented in the commercially available fitting program NORMOS written by R.A. Brand (distributed by Wissenschaftliche Elektronik GmbH, Germany)(Brand 1990).

Single crystal x-ray diffraction data were collected at room temperature using a MAR555 flat panel detector at ID09a, European Synchrotron Radiation Facility, Grenoble. We used 60° ω scans with a 0.5° step at 0.41520 Å wavelength. Oxford Diffraction Crysalis (Crysalis RED 2006) and JANA2006 (Petricek et al. 2006) software were used for data analysis and refinement of the lattice parameter and crystal structure of magnetite. Typical values of the R-factor were 3-7% (JANA2006). The data on pressure induced variation of crystallographic parameters can be found in Appendix 1.

5.2.4 Results and discussion

We collected single crystal diffraction at pressures from 0 to 21 GPa. Our data on unit cell volumes (Fig. 5.2.1) are in good agreement with previous powder diffraction experiments
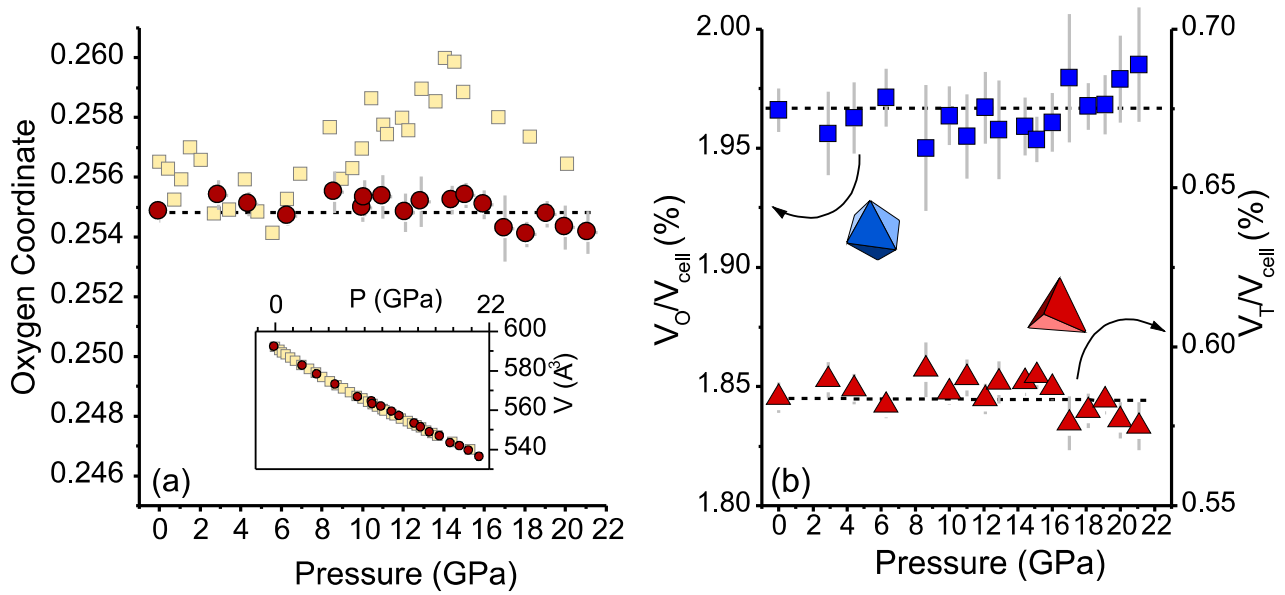
Fig. 5.2.1:
Pressure dependence of the magnetite (a) unit cell oxygen coordinate u and (b) ratios of specific crystallographic site volumes (T- V_T, and O- V_O) to volume of the unit cell (V_{cell}). The circles in (a) represent current data; and squares – data from Rozenberg et al. 2007. The inset in (a) shows the unit cell volume as a function of pressure. The triangles and squares in (b) mark T- and O-sites respectively. Dashed lines are guides to eyes.

(Rozenberg et al. 2007). However, we find a different pressure induced behavior of the u parameter from that reported previously (Fig. 5.2.1). Our single crystal diffraction data provide unambiguous evidence that the value of u remains essentially constant within experimental uncertainty at all studied pressures. This observation proves that there is no change in the relative volumes of T- and O-sites (Fig. 5.2.1). Thus, we conclude that there is no IT-NT transition in single-crystal magnetite at pressures of 10-21 GPa.

In the case of the HS-IS transition model the following considerations apply. Fe^{2+} occupies only O-sites and has a larger ionic radius in the high spin state than in the intermediate spin state. However, due to charge hopping between the O-sites the volume effect could be small. It is therefore possible that we are not able to resolve changes of this magnitude in the single crystal x-ray diffraction experiment. To more accurately investigate the possibility of a HS-IS transition, we have approached this problem independently using Mössbauer spectroscopy as described below.

The Mössbauer spectrum of magnetite consists of two subspectra at ambient conditions. One corresponds to $Fe^{2.5+}$ in O-sites while the second corresponds to Fe^{3+} in T-sites. The observation of $Fe^{2.5+}$ is due to the mean lifetime of the excited ^{57}Fe nucleus ($\sim 10^{-7}$ s) being much longer than charge fluctuation between the Fe^{2+} and Fe^{3+} ions ($< 10^{-16}$ s)(García et al. 2000). Consequently O-site Fe^{2+} and Fe^{3+} should be indistinguishable in Mössbauer absorption spectra.

Based on our single crystal x-ray diffraction studies we fitted Mössbauer absorption spectra using the inverse spinel-type structure model. Because overlapping peaks do not enable a unique set of hyperfine parameters to be obtained from an unconstrained fit of the data, we applied constraints based on results from the single crystal structural data. We fixed the area ratio between O- and T- subspectra to be 2:1, which is justified since we used the full transmission integral to fit the data, which corrects for distortion of the areas due to thickness effects. We assumed zero quadrupole splitting of the T-sites (no

Fig. 5.2.2:

Mössbauer spectra of magnetite at different pressures: (1) 0 GPa, (2) 4.2 GPa, (3) 12.2 GPa, (4) 16.3 GPa, (5) 19.19 GPa, (6) 20.7 GPa, (7) 24.9 GPa. Fitting was performed using the full transmission integral procedure.
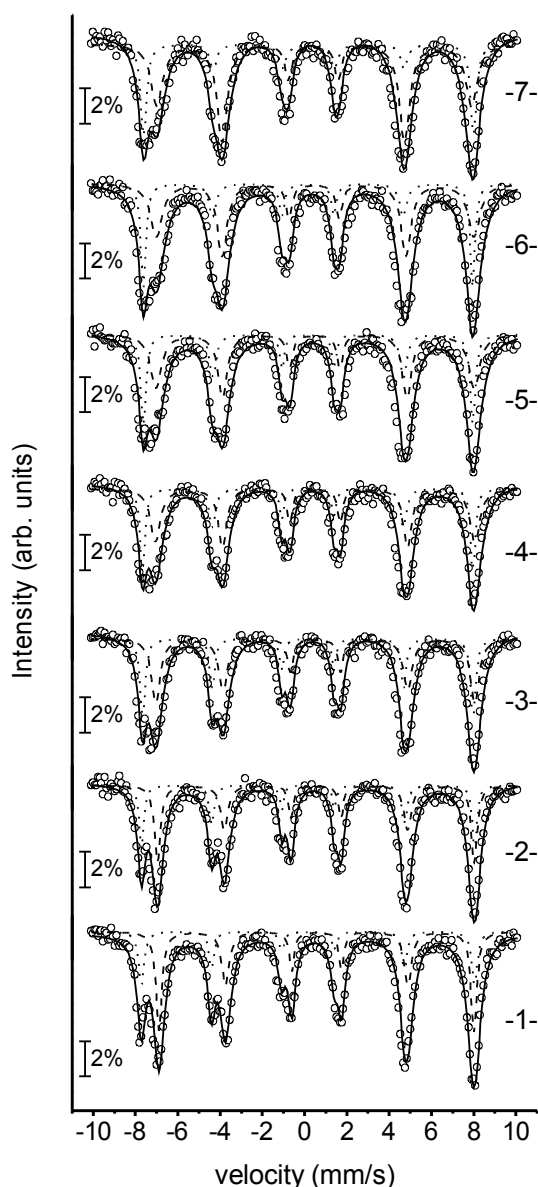
63
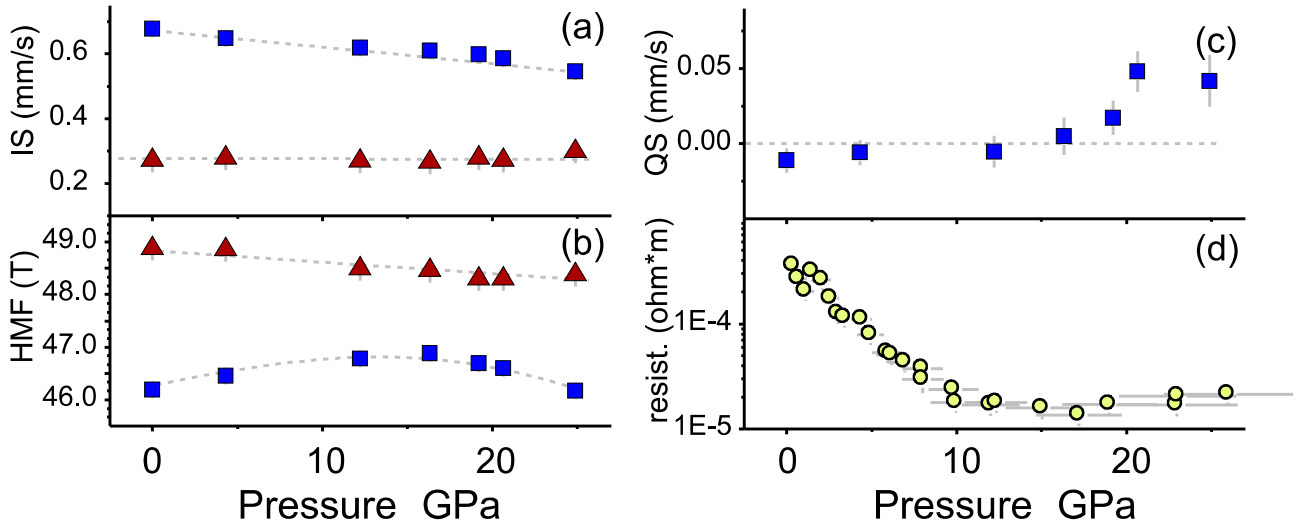
Fig. 5.2.3:
Pressure dependencies of (a) IS - isomer shift; (b) HMF - hyperfine magnetic field; (c) QS - quadrupole splitting; (d) bulk resistivity (Morris and Williams 1997). The O- and T-sites are marked by squares and triangles, respectively. The lines are guides for the eye.

electrical field gradient) based on the cubic environment of the site and the absence of charge hopping from O- to T-sites (T-sites are not observed to participate in charge transfer at ambient conditions, and according to theoretical studies, T-sites do not affect conductivity up to 20 GPa (Friák et al. 2007). On the other hand, the iron ions at the O-sites act as electron donors to the conductivity band; thus we allowed distortions of the O-site and hence non zero values of quadrupole splitting. The results of the fitting Mössbauer absorption spectra are shown on Fig. 5.2.2.

The pressure dependence of the parameters derived from the fits, namely isomer shift (IS), quadrupole splitting (QS) and the hyperfine magnetic field (HMF), for different crystallographic sites are shown in Fig. 5.2.3. Our data on hyperfine magnetic splitting and isomer shift are in good agreement with data reported by (Kobayashi et al. 2006), although we do not see an additional O-site component. This discrepancy can be related to the more hydrostatic conditions in our experiments due to the Ne pressure transmitting medium.

Before advancing to more detailed analysis, we address the question of the HS-IS transition in magnetite (Ding et al. 2008). The isomer shift data do not support presence of this transition. We consider the following simple reasoning. In the case of a spin state transition in Fe^{2+} ions, the charge distribution on the iron nucleus would become more spherical ($t_{2g}^{4}e_{g}^{2} \rightarrow t_{2g}^{5}e_{g}^{1}$), and the slope of isomer shift would change significantly, reflecting the higher polarization of s- electrons. No such changes are observed in the isomer shift data. In addition, it is important to add that the transport properties of magnetite are controlled by the t_{2g} electron minority band. In the case of a HS-IS transition, an additional electron is effectively added to the conduction band ($t_{2g}^{3}\uparrow t_{2g}^{1}\downarrow e_{g}^{2}\uparrow \rightarrow t_{2g}^{3}\uparrow t_{2g}^{1+1=2}\downarrow e_{g}^{1}\uparrow$); thus the resistivity of the material should drop significantly. There is no experimental observation of any electrical resistivity anomaly of magnetite in the pressure range of interest,10-20 GPa (Morris and Williams 1997, Ovsyannikov et al. 2008). We therefore conclude that there is no HS-IS transition in magnetite at pressures of 10-20 GPa.

Based on the current data and information available in the literature, we suggest the following model for the high-pressure behavior of magnetite. At ambient conditions magnetite is a half metal, and the O-site $t_{2g}\downarrow$ minority band electrons are responsible for conductivity. However, the polarization of charge carriers is less than 100%; thus the majority spin electrons $t_{2g}\uparrow$ also participate in charge transport. Pressure induces changes in the electronic and magnetic properties of magnetite.

First, pressure enhanced hybridization of charge carriers induces a drop of resistivity (Morris and Williams 1997). Analysis of isomer shift pressure dependence provides insight into the different roles of the T- and O-sites on the transport properties. By definition, the value of the isomer shift is related to the density of s- electrons at the nucleus; however shielding by d- and p- electrons also affects this value. For example, an increased hybridization of d- electrons with the conduction band would result in a larger density of s- electrons at the nucleus; hence the isomer shift would decrease. While the T-site isomer shift is almost constant at the pressures of our experiment, the value for O-site isomer shift constantly decreases with pressure. Thus at the pressures of this study, only O-sites provide charge carriers.

The higher the pressure, the greater is the number of $3d$ electrons that become delocalized. At some critical pressure, delocalization of electrons leads to distortions of the crystal lattice, which is strongly coupled to the electronic and magnetic properties of magnetite. Thus, the resistivity of the material will be significantly affected by electronic or crystal structure distortions. According to experimental data (Morris and Williams 1997) the resistivity decreases and then probably saturates at pressures below 25 GPa. Our single crystal study showed that structural distortions are small and cannot be resolved by x-ray diffraction data, but we can detect them through the quadrupole splitting (QS) Mössbauer parameter. QS is very sensitive and is nearly zero for the O-site at pressures below 15 GPa, but its value slightly increases at higher pressures. Based on the combined evidence above, we suggest that at 15 GPa the delocalization of $3d$ electrons could lead to dynamical distortions of the structure (dynamic Jahn-Teller effect). However, the explanation could be more complex, since there are three contributions to QS: effects of bonding and nonbonding electrons as well as the effect of lattice distortions (Dickson and Berry 2005).

We can extract further information from the high pressure behavior of hyperfine magnetic fields (HMF) of T- and O-sites. In the case of iron ions, the total hyperfine magnetic field can be written as:

$$\text{HMF} = B_c + B_{orb} + B_{dip},$$

where the terms are as follows: B_c – contact interaction (describes polarization of s- electrons by unpaired 3d electrons), B_{orb} – magnetic field produced at the nucleus by orbital motion of unpaired $3d$ electrons, B_{dip} – hyperfine interaction produced by dipolar field of the spins of $3d$ electrons. The major contribution to the total hyperfine field is the contact interaction (B_c). By definition, B_c is a function of the effective value of the magnetic spin ($<S>$) multiplied by a parameter describing the polarization of the s- electrons (k)(Dickson and Berry 2005).

T- and O- sites show different pressure dependences of HMF. There is a gradual decrease of HMF for the T-site. For Fe^{3+} in the T-site, the spherical charge distribution results in zero contribution from the B_{orb} and B_{dip} terms. Thus, we argue that the pressure induced decrease of HMF (T-sites) is related to the decrease of the effective value of the magnetic spin/magnetic moment ($<S>$) at the T-site. Additionally,

compression could induce weakening of the magnetic interaction between T-/O-sites.

The analysis of hyperfine magnetic interactions for the O-sites is challenging, as we expect non-zero values of B_{orb} and B_{dip} at higher hybridization or non zero values of quadrupole splitting. The magnetic moment on the O-site also decreases with pressure (Klotz et al. 2008). This observation is important because O-sites are occupied by Fe^{2+} ions ($3d^6$; $3t_{2g}\uparrow+2e_g\uparrow -1t_{2g}\downarrow=4\uparrow$) as well Fe^{3+} ($3d^5$; $3t_{2g}\uparrow+2e_g\uparrow=5\uparrow$). We believe that both majority- and minority-spins are hybridized, otherwise the magnetic moment on the O-site would increase with pressure. At low pressures the distortions of O-sites are small, and the t2g energy levels are degenerate. Thus $t_{2g}\uparrow$ electrons are equally delocalized until at some critical pressure (P_c), the spin polarization of the charge carriers will become zero and will then change sign with compression.

At pressures higher than P_c the magnetic moment of O-sites will suddenly decrease, because the effective number of spin-up states ($\uparrow$) will exceed the number of those with spin down ($\downarrow$). A recent XMCD study by Baudelet et al. 2010 has shown that the total magnetization of magnetite starts to decrease at pressures considerably higher than 15 GPa. Comparing the experimental observations, we conclude that at 15 GPa there is a change of charge carrier polarization.

In summary, the effective magnetic moment of the O-site decreases with pressure as a consequence of the weaker magnetic interaction between T- and O-sites and the ongoing hybridization. At first glance, the behavior of the O-site HMF appears to contradict our model below 15 GPa, because we observe an increase of HMF with compression (Fig. 5.2.3). However this observation can be easily explained by pressure-induced changes of the contact field (B_c), the major component of HMF.

As mentioned above, Bc is a function of $<S>\cdot k$. For the O-sites, higher polarization of s- electrons (k) implies a lower number of d- electrons in the $3d$ shell and hence a lower value of the isomer shift. Thus in a first order approximation, if paired t_{2g} electrons are first hydridized, the magnetic moment of the O-site will not decrease; however the polarization of s- electrons at the iron nucleus will increase considerably.

Next, if the increase in k overcompensates the decrease of $<S>$, there will be a positive change of B_c. We can neglect the $B_{orb}+B_{dip}$ contributions at pressures below 15 GPa (small quadroupole interaction at the O-site; small value of B_{orb}). Thus, HMF at O-sites will increase with compression below some critical pressure near 15 GPa. At higher pressures, the polarization of charge carriers changes, and we argue that the behavior of B_c and HMF is dominated by decreasing $<S>$. The total HMF of O-site then decreases at pressures above 15 GPa.

Although we cannot separate the contributions of t_{2g} and e_g electrons, the non-zero quadroupole splitting at O-sites at pressures higher than 15 GPa is evidence for small distortions from cubic symmetry. In this case e_g electrons should be more separated from t_{2g} electrons by a potential energy barrier and should contribute much less to the conductivity.

In conclusion, we have shown that there is no IT-NT spinel transition in magnetite at pressures up to 21 GPa. We argue that there is also no HS-IS transition in magnetite in the same pressure range. Based on the analysis of our Mössbauer data and data available in the literature, we propose a consistent model of the delocalization of $3d$ electrons. Within the framework of this model we distinguish two

regions: one below 15 GPa and the other above. We suggest that below 15 GPa the hybridization of majority spin electrons slowly increases with pressure. At 15 GPa the spin polarization of charge carriers becomes zero and slowly changes sign with further compression, resulting in a decrease of the magnetic moment at the O-site and a decrease in the bulk magnetization of magnetite.

5.2.5 Acknowledgments

5.2.6 Appendix 1

Table 5.2.1: Impurity element fractions in mole% determined by microprobe on natural single crystal of magnetite (locality Bijiki iron formation, upper peninsula of Michigan, U.S.A)

Elements									
Na	**Si**	**Ti**	**Ni**	**Fe**	**Al**	**Mg**	**Co**	**Cr**	**Mn**
0.02(1)%	0.08(1)%	0.19(4)%	0.01(1)%	99.22(20)%	0.40(4)%	0.04(2)%	0.00(0)%	0.03(1)%	0.02(5)%

Table 5.2.2: Lattice and crystallographic parameters, volume and R-factors of the data evaluation determined on natural single crystal of magnetite at 300K.

P, GPa	a, Å	V, Å^3	u	R_{int}, %	R_1, %
0.0001	8.394(3)	591.5(6)	0.2549(4)	6.9	4.2
2.9(1)	8.350(3)	582.1(6)	0.2554(5)	4.3	4.3
4.4(1)	8.328(3)	577.6(6)	0.2551(4)	3.4	3.4
6.3(1)	8.304(3)	572.5(6)	0.2547(3)	3.5	3.5
8.6(1)	8.272(3)	566.1(6)	0.2555(7)	6.6	6.6
10.0(1)	8.261(3)	563.8(6)	0.2550(5)	5.2	5.2
11.0(1)	8.249(3)	561.3(6)	0.2553(7)	5.7	4.5
12.1(1)	8.236(3)	558.7(6)	0.2554(6)	5.0	4.3
12.9(1)	8.225(3)	556.4(6)	0.2554(8)	5.3	4.4
14.4(1)	8.207(3)	552.7(6)	0.2552(5)	3.5	3.6
15.1(1)	8.198(3)	550.9(6)	0.2554(4)	3.4	3.3
16.0(1)	8.184(3)	548.1(6)	0.2551(6)	3.7	3.9
17.0(1)	8.174(4)	546.2(8)	0.2543(11)	8.4	7.4
18.1(1)	8.158(3)	543.0(6)	0.2547(4)	4.6	3.9
19.1(1)	8.149(3)	541.1(6)	0.2548(4)	4.7	3.7
20.0(1)	8.138(3)	539.0(6)	0.2543(7)	5.2	6.0
21.1(1)	8.125(3)	536.4(6)	0.2542(10)	5.9	5.6

The fractional coordinates of Fe[1] and Fe[2] are (0.5 0.5 0.5) and (0.125 0.125 0.125). The R factors R_1 and R_{int} are defined as $R_1 = \Sigma||F_O|-|F_C||/\Sigma|F_O|$ and $R_{int} = \Sigma|F_O^2 - F_O^2(mean)|/\Sigma F_O^2$, where F_O and F_C are the observed and the calculated intensities, respectively. The number of observed unique reflections of the sample loaded to the diamond anvil cell 28-35 in high pressure experiment (depending on loading and pressure).

5.3. Effect of composition and pressure on phase transitions in Fe$_x$O at low temperature.

K. Glazyrin[1], L. Dubrovinsky[1], S. Klotz[2], M. Uhlarz[3], J. Wosnitza[3], Th. Hansen,[4] N. Dubrovinskaia[5]

[1]*Bayerisches Geoinstitut, Universität Bayreuth, D-95447 Bayreuth, Germany,* [2]*IMPMC, Université P&M Curie, 4 Place Jusssieu, F-75252 Paris, France,* [3]*Helmholtz-Zentrum Dresden-Rossendorf, Institut Hochfeld-Magnetlabor Dresden, D-01314 Dresden, Germany,* [4]*Institut Laue-Langevin, F-38042 Grenoble Cedex 9, France,* [5]*Materialphysik und Technologie, Lehrstuhl für Kristallographie, Physikalisches Institut, Universität Bayreuth, D-95440 Bayreuth, Germany*

5.3.1 Abstract

We report the results of high-resolution neutron powder diffraction studies of Fe$_x$O (x = 0.925, 0.94) in the vicinity of the low-temperature antiferromagnetic transition and at pressures up to 8 GPa. Our analysis shows that the P-T phase diagram of Fe$_x$O is strongly affected by the composition and defect structure of the material. We observe the divergence of critical temperatures of magnetic and structural transitions. In contrast to the stoichiometric antiferromagnet MnO, we find no correlation between the magnitude of the magnetic moment of iron and the degree of the rhombohedral distortion in Fe$_x$O. We suggest that the defect structure of antiferromagnetic Fe$_x$O significantly influences the temperature of the structural transition.

5.3.2 Main text

At ambient conditions, Fe$_x$O (x < 1, mineral name wüstite) is a non-stoichiometric iron oxide with a cubic rock-salt (B1) structure. It is generally accepted that upon cooling paramagnetic Fe$_x$O, similar to other Mott insulators of the charge-transfer type (such as MnO, CoO, and NiO), undergoes an antiferromagnetic transition (Gebhard 2010). At the transition, the magnetic moments of iron become aligned parallel to the [111] direction (Roth 1958). The structure is believed to become rhombohedral at the same temperature, probably as a result of magnetostriction (Kanamori 1957). Being a good example of strongly correlated systems with a complex defect structure, Fe$_x$O has attracted great attention (Koch and Cohen 1969, Akimitsu et al. 1983, Ding et al. 2005b). Although it has been shown that its composition has a significant effect on the magnetic properties of the material (Akimitsu et al. 1983) at ambient pressure, the influence of both pressure and composition on its structure and magnetic properties has not been studied in detail. Moreover, recent Mössbauer spectroscopy, x-ray diffraction, and limited neutron-diffraction studies have shown that there is a divergence in the critical temperatures of the magnetic and structural transitions in Fe$_{0.92}$O (Kantor et al. 2005). Neutron diffraction is one of the few methods which allow simultaneous monitoring of structural and magnetic transitions in the material. We performed high resolution neutron powder diffraction studies of Fe$_x$O (x = 0.925, 0.94) in order to unravel the role of pressure, temperature, and composition on the magnetic and structural properties of the material close to the antiferromagnetic transition. The samples together with the

quasihydrostatic pressure medium (methanol/ethanol mixture) were loaded into Paris-Edinburgh press. Additional information on the sample preparation and experimental setup can be found in the Section 5.3.3. The compression sequence was 0, 4, and 6.8 GPa for $Fe_{0.94}O$, and 4.2, 8, and 0 GPa for $Fe_{0.925}O$, respectively. Here and below, the pressure value of 0 GPa indicates ambient pressure, and the uncertainty in the pressure estimate lies within 0.3 GPa. The data at 0 GPa for $Fe_{0.925}O$ were obtained to investigate how the abrupt pressure decrease (pressure-quench from high to ambient pressure at low temperatures) affects the material properties. In addition, we compare the data obtained upon quenching with those collected for the pristine material with similar composition ($Fe_{0.92}O$) at 0 GPa (Kantor et al. 2005). The neutron-diffraction patterns were analyzed using the Fullprof software package (Rodríguez-Carvajal 1993).

Our first task was to determine the P-T phase diagram of the magnetic and structural transitions manifested in the diffraction patterns through the appearance of magnetic peaks and the splitting of some of the structural diffraction lines, correspondingly. We will use the symbol T_S for the temperature of the structural transition, and T_N (the Néel temperature) for the temperature of the antiferromagnetic ordering.

In order to obtain reliable values of T_S and T_N for both of the studied compounds, we tracked the intensity of the strongest magnetic peak and the variation of the cell parameters. After fitting the whole set of data (before and after the expected structural transition) using the rhombohedral unit cell in the hexagonal setting, we found that the c/a ratio in the hexagonal setting is a sensitive parameter to detect the emergence of the structural transition at T_S (Fig. 5.3.1). At this temperature the slope of c/a suddenly changes, although the effect becomes blurry with pressure. We could not determine the temperature of the structural transition for $Fe_{0.925}O$ at 0 GPa, after quenching from 8 GPa, because upon cooling even to 110 K it remains cubic (see Section 5.3.3).

We used Fullprof (Rodríguez-Carvajal 1993) to extract the temperature-dependent magnetic moments at different pressures in order to evaluate T_N (Fig. 5.3.2). Due to experimental time constraints we could not collect neutron powder diffraction data to determine the value of T_N for $Fe_{0.925}O$ prior to the high-pressure treatment. However, we obtained T_N at ambient pressure from a separate magnetization measurement (see Section 5.3.3). The extracted value, $T_N = (200\pm5)$ K, is in good agreement with the result of specific-heat measurements (Grønvold et al. 1993) and with the data for iron oxide of a similar composition, $Fe_{0.92}O$, reported earlier (Kantor et al. 2005). In addition, we suggest that the pressure-quench of $Fe_{0.925}O$ from 8 GPa has little effect on T_N (Fig. 5.3.2).

The analysis of the temperature dependences of c/a (or the cell volume) and of the magnetic moments at the iron sites reveals no correlation between these parameters. Consequently, the magnetic order appears independently from the structural transition. As a possible cause for the structural transition we may consider a strong influence of the defect structure. We suggest that at ambient pressure and temperatures between T_S and T_N the long-range symmetry of Fe_xO remains cubic, while the short-range order may be different. Possibly, the application of pressure induces some distortion of the cubic structure prior to T_S, as the c/a ratio deviates from the exact value of (Fig. 5.3.1). A supplementary high-resolution x-ray
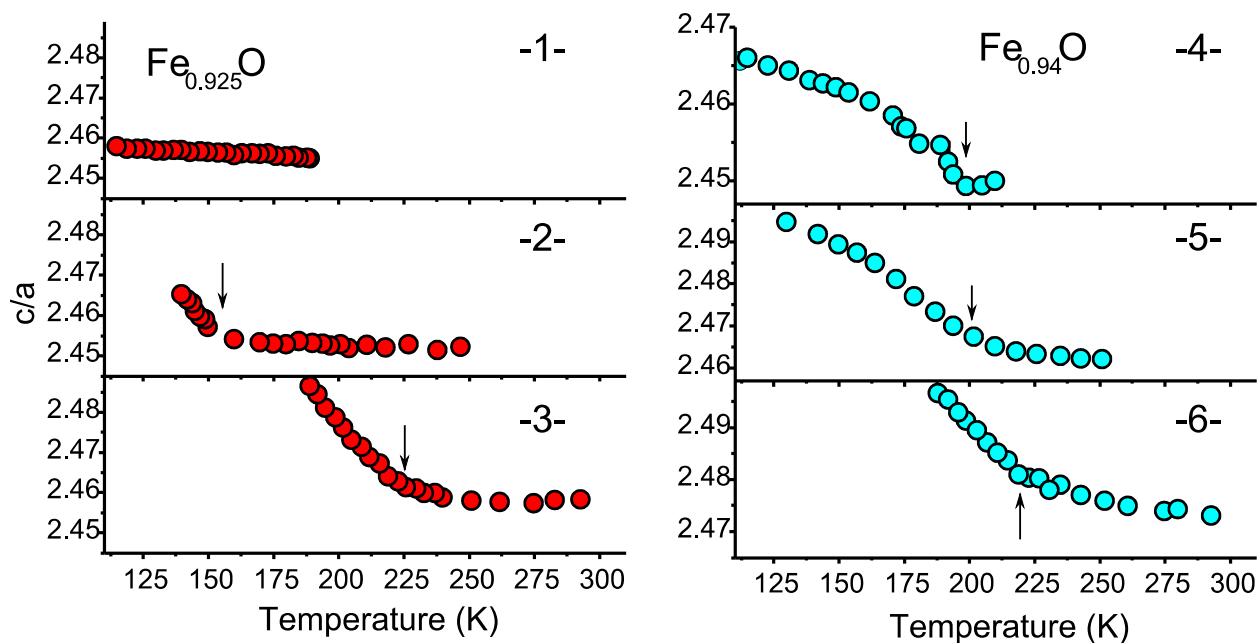
Fig. 5.3.1:

The ratio of the hexagonal lattice parameters *c/a* of $Fe_{0.925}O$ (left) and $Fe_{0.94}O$ (right) as a function of temperature at various pressures: (1) 0 GPa, (2) 4.2 GPa, (3) 8 GPa, (4) 0 GPa, (5) 4 GPa, (6) 6.8 GPa. Arrows indicate T_S. Error bars are comparable with the symbol size.
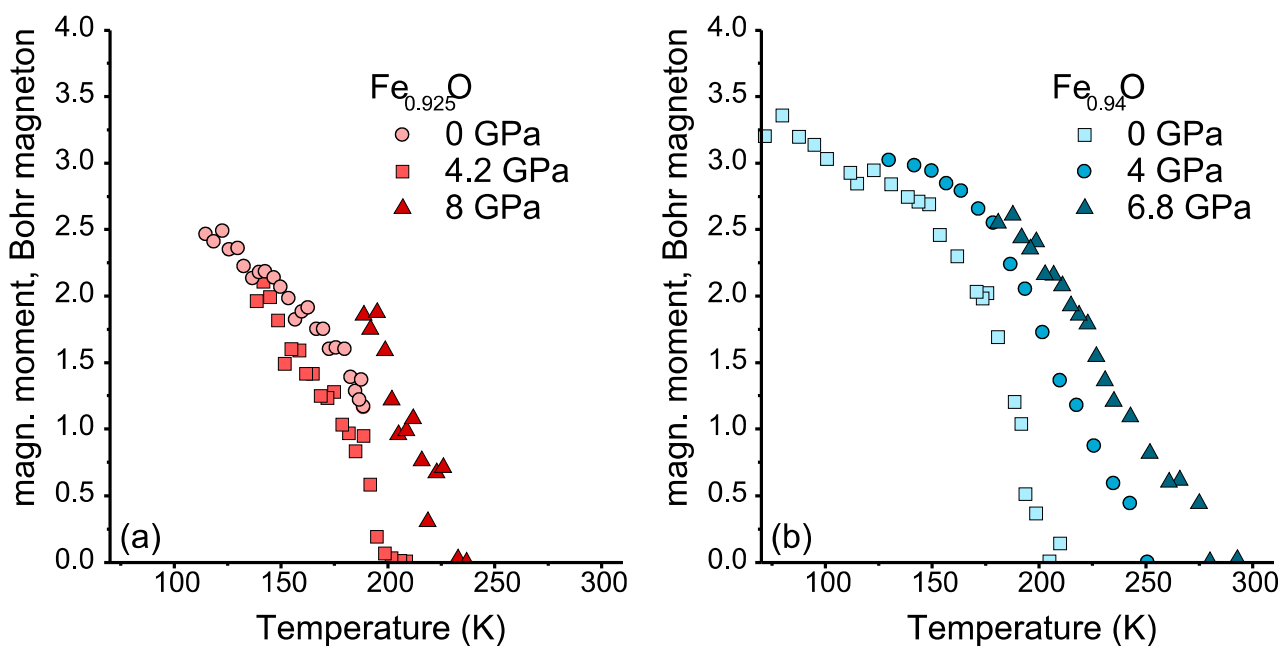
Fig. 5.3.2:

Evolution of the magnetic moment in (a) $Fe_{0.925}O$ and (b) $Fe_{0.94}O$ with temperature.

Effect of composition and pressure on phase transitions in FexO at low temperature.
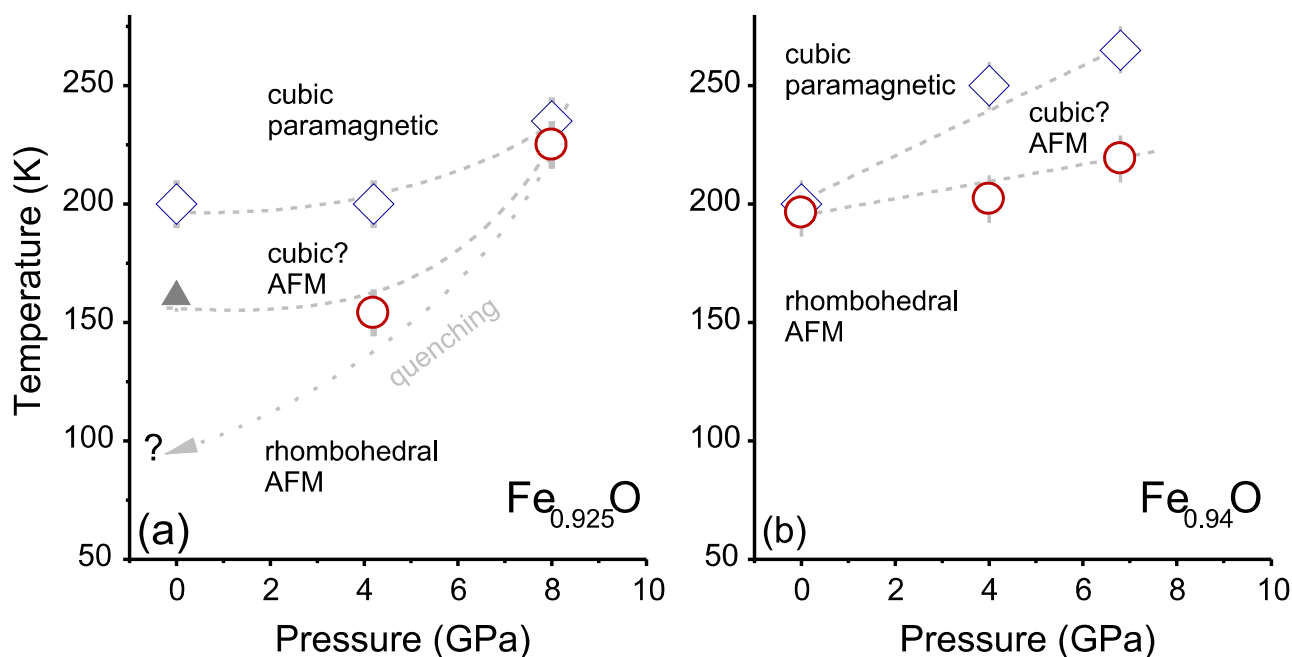
Fig. 5.3.3:
The P-T phase diagrams of (a) $Fe_{0.925}O$ and (b) $Fe_{0.94}O$. Diamonds and circles designate T_N and T_S, respectively. The grey triangle in the graph (a) marks the T_S reported earlier (Kantor et al. 2005). Lines are guides for the eyes. The dotted arrow denotes the quenching from high pressure.

diffraction experiment is necessary to test this hypothesis.

Fig. 5.3.3 summarizes our observations on the magnetic and structural phase transitions of $Fe_{0.925}O$ and $Fe_{0.94}O$. Both materials demonstrate a strongly different behavior, that obviously is related to the difference in their composition and, consequently, to different defect concentrations. It was suggested that the cubic magnetically ordered Fe_xO has a peculiar magnetic structure (Kantor et al. 2004). However, this hypothesis cannot explain the different evolution of the iron magnetic moments and the rhombohedral distortion.

It is known that defects in Fe_xO form clusters which influence the magnetic properties of the material and participate in magnetic ordering (Battle and Cheetham 1979). Both $Fe_{0.925}O$ and $Fe_{0.94}O$ contain defect clusters of the same kind (Akimitsu et al. 1983), while their concentration is different. We suggest that at low temperature and low pressure the material with larger defect concentration should more easily adapt to magnetic ordering by distorting individual clusters while overall preserving the (long-range) cubic symmetry. On the other hand, the presence of defects introduces some distortion of the structure of "as-prepared" Fe_xO samples making them "less ideal" in comparison with stoichometric FeO. The effect of magnetostriction induced by magnetic interactions should be less pronounced and softened by the defect-containing structure. We assume that the cubic magnetic phase should not exist in magnetically ordered Fe_xO in the absence of defects (i.e., for x = 1).

The effect induced by defects depends on their concentration and becomes less pronounced at higher pressures (e.g. in $Fe_{0.925}O$ at 8 GPa, Fig. 5.3.3). It may relate to the long-range order-disorder transition observed in cubic $Fe_{0.93}O$ at 14 GPa and 300 K on compression in He pressure transmitting medium (Ding et al. 2005a).

71

There are two types of defects in Fe_xO. At ambient pressure, it is energetically favorable for the cubic lattice to move Fe ions from octahedral sites to interstitial tetrahedral sites (Koch and Cohen 1969, Battle and Cheetham 1979). Four vacancies (for the Fe octahedral sites) enclose an interstitial site (see Section 5.3.3). The easiest way to produce a disordered state of the defect structure is to move interstitial iron ions to one of the randomly chosen neighboring vacant sites, thus, making the crystal structure "more ideal". The "effective concentration" of defects becomes smaller and provides a smaller difference between T_S and T_N. Note, that although the high-pressure disordered defect structure (DDS) is quenchable to ambient conditions for $Fe_{0.93}O$ (Ding et al. 2005a), there are no evidences that the DDS is also quenchable at low temperatures. Quenching the $Fe_{0.925}O$ sample from 8 GPa to 0 GPa results in a very significant decrease of T_S to below 110 K. This value is much lower than $T_S = (160\pm5)$ K reported for a pristine material with similar composition, $Fe_{0.92}O$ (Kantor et al. 2005). In case of $Fe_{0.925}O$, we suggest that a new defect structure is formed after quenching, different from the high-pressure DDS and the as-prepared one.

In conclusion, we have shown that the P-T phase diagram of Fe_xO in the vicinity of the antiferromagnetic transition is strongly influenced by the composition and coupled to the defect structure of the material. Compression changes the critical temperatures of the structural and magnetic transitions in different ways and probably stabilizes new types of defect structures that may be related to the long-range disordered defect structure (Ding et al. 2005a).

5.3.3 Supplementary material

5.3.3.1. Sample preparation

The samples were prepared in a gas mixing furnace by reduction of commercially available Fe_2O_3 (99.999% purity). To obtain desired compositions, CO/CO_2 gas mixtures were used (Darken and Gurry 1945). After heating samples for 24h, we quenched them in water to avoid precipitation of magnetite. The phase purity of the prepared material was tested using the x-ray diffraction and Mössbauer spectroscopy. The samples contained a single phase of wüstite. We estimated the composition using a previously reported relation between the composition and the lattice constants (McCammon and Liu 1984). The lattice parameters of 4.2983(10) and 4.3056(10) Å for the two different samples correspond to $Fe_{0.925}O$ and $Fe_{0.94}O$, respectively. Some iron was added initially to the $Fe_{0.94}O$ as a marker for powder diffraction measurements.

Samples along with a 4:1 deuterated methanol-ethanol mixture, used as a pressure transmitting medium, were loaded into the sample chamber of the Paris-Edinburgh press mounted in a cryostat (Klotz et al. 2005) At 300 K, the liquid (methanol-ethanol mixture) provides satisfactory hydrostatic conditions in the pressure range under investigation here (0-8 GPa). The data were collected at the D20 high intensity diffractometer at the Institute Laue Langevin, Grenoble (France) using the wavelength $\lambda=1.36$Å and an oscillating radial collimator to avoid a background signal from the cryostat. All pressure changes were carried out at ambient temperature where the pressure transmitting medium is known to be fluid. Data were then collected upon cooling at a rate of 0.126(1) K/min under constant load. The pressure values cited here were determined from the known equations of state of wüstite for different compositions (Kantor et al. 2008). The uncertainty of temperature determination was 5 K.

5.3.3.2. Neutron diffraction data

Collected neutron diffraction spectra were analyzed using the Fullprof (Rodríguez-Carvajal 1993) software with a minimal set of variable parameters, namely, the lattice parameters, the overall temperature factor (B_{iso}), the shape parameter U, the Lorentzian isotropic strain parameter X, and the value of the magnetic moment at iron sites. Fitting the data for the paramagnetic phase was accomplished using both cubic and rhombohedral (in hexagonal setting) models. The structure of the antiferromagnetic phase, ordered along the [111] direction, was fit only to the rhombohedral model. Fig. 5.3.4 shows an example of the Fullprof plot of the diffraction data of $Fe_{0.925}O$ (at 140 K and 4 GPa) after the Rietveld refinement.

For several sets of data collected for different compositions and P-T conditions, we observed the divergence of T_S (temperature of structural transition) and T_N (temperature of magnetic transition), which can clearly be seen in the grey color 2θ vs T maps for $Fe_{0.925}O$ (Fig. 5.3.5). At 8 GPa we see the rhombohedral splitting almost coinciding in temperature with the onset of the magnetic transition, while at 4.2 GPa T_N and T_S are obviously different. The separation of T_N and T_S becomes even more pronounced after quenching from high to ambient pressure, when we observe strong magnetic signal below 198 K, however there is no sign of the structural transition at temperatures down to 110 K.
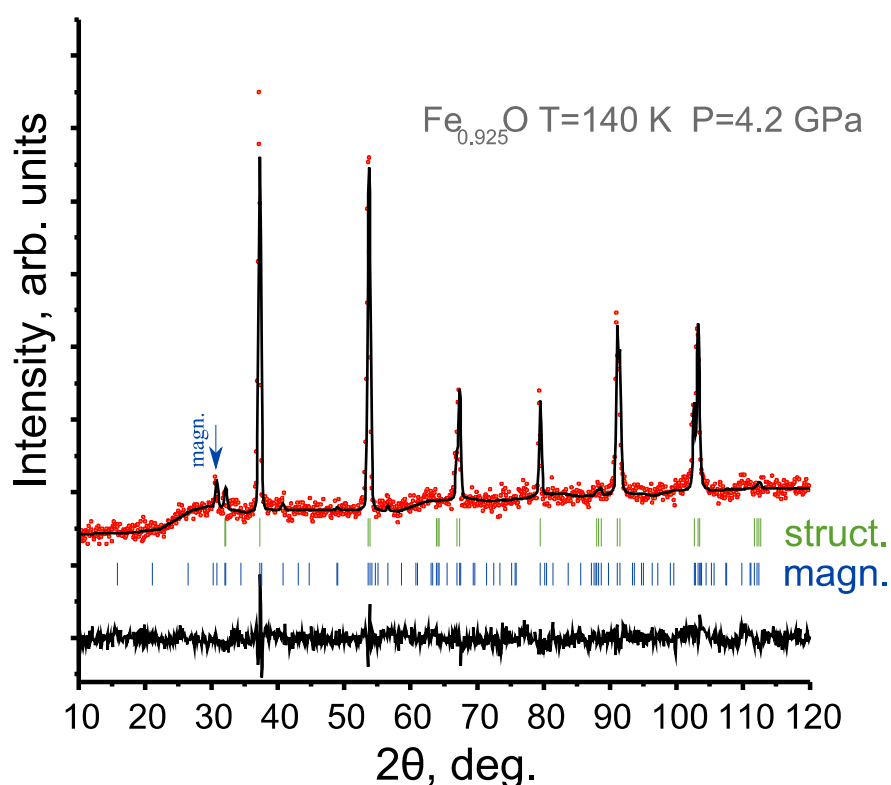
Fig. 5.3.4:
The Fullprof plot of the neutron powder diffraction data of $Fe_{0.925}O$ at 4.2 GPa and 140 K (red dots). The simulated diffraction data based on the crystallographic model is shown as a solid line. The tickmarks represent structural (upper tickmarks) and magnetic (lower tickmarks) contributions in the diffraction pattern. The arrow marks the strongest magnetic peak.
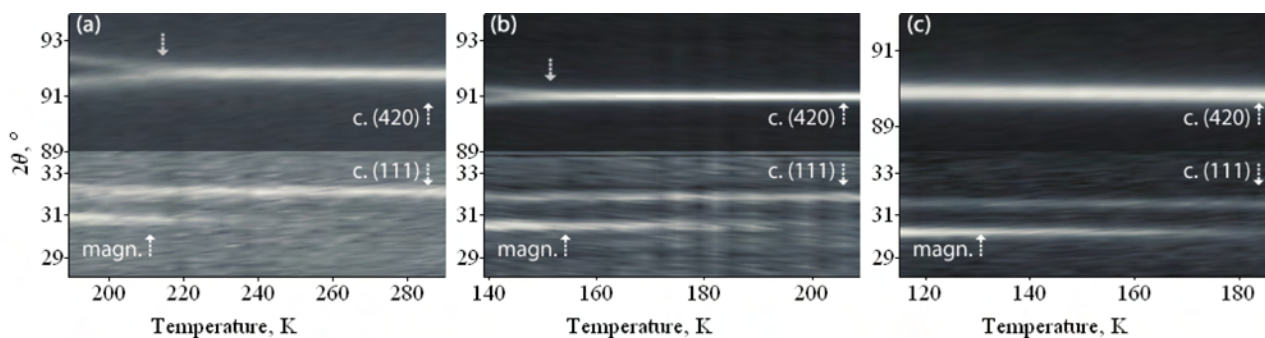
Fig. 5.3.5:

Grey color maps prepared based on $Fe_{0.925}O$ diffraction patterns for selected 2θ regions at different pressures: (a) 8 GPa, (b) 4.2 GPa, (c) 0 GPa. Lattice plane indices are given for the cubic structure. Magnetic reflection is marked additionally.

5.3.3.3. Magnetic measurments

The antiferromagnetic transition temperature of $Fe_{0.925}O$ (on "as prepared" sample, prior to compression) was measured in MPMS SQUID magnetometer (Quantum Design) at Forschungszentrum Dresden Rozendorf. The estimated temperature was $T_N = 200 \pm 5$ K (Fig. 5.3.6).
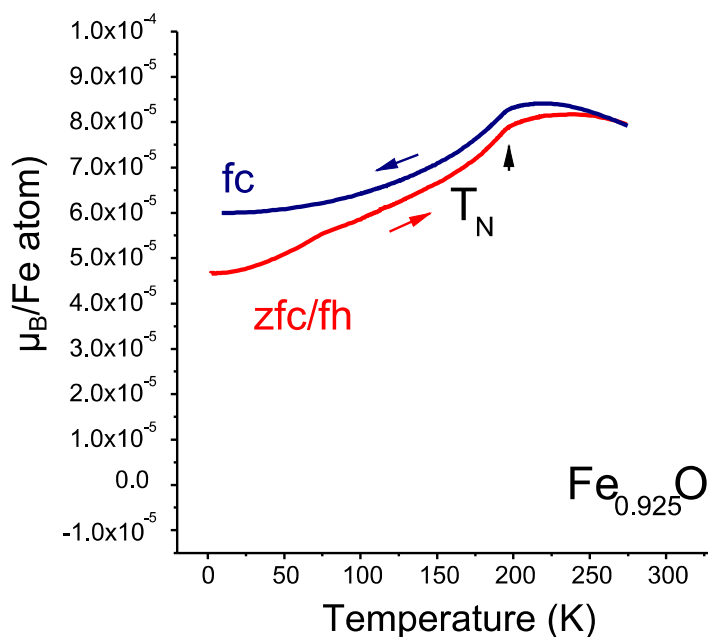
Fig. 5.3.6:

The results of the magnetization measurements on "as prepared" $Fe_{0.925}O$. Red curve – heating in the magnetic field (fh - 50 oe) after zero field cooling (zfc). Blue curve – cooling in the magnetic field (fc-50 oe) which followed field heating.

5.3.3.4. Defects in Fe_xO structure

Cubic structure of Fe_xO contains two major types of primitive defects (Fig. 5.3.7)(Battle and Cheetham 1979). (1) An interstitial Fe ion in a tetrahedral environment created by oxygen (blue sphere and (2) four octahedral vacant sites (red crosses) forming a tetrahedron filled with the interstitial Fe atom (red crosses).

In case of the order-disorder transition under high pressure, the blue atom occupies one of the empty neighboring octahedral sites. Upon release of pressure the blue atom may return back to the interstitial site.
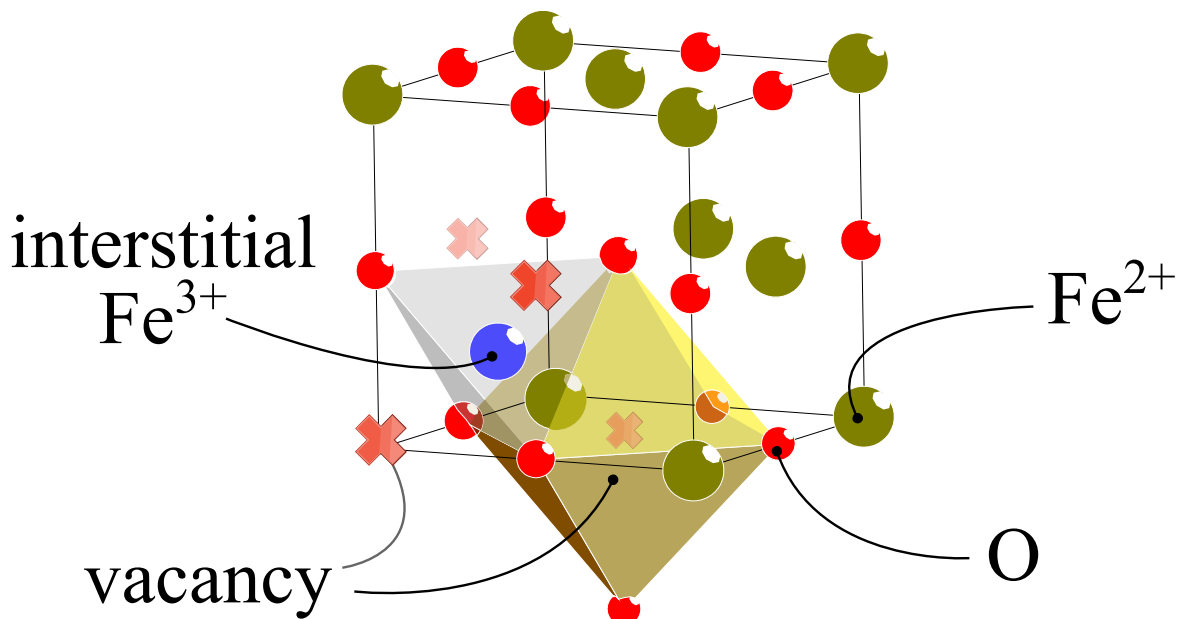
Fig. 5.3.7:
Structure of cubic Fe_xO with defects (Battle and Cheetham 1979). Red spheres mark oxygen, greenish spheres - iron in octahedral sites. Blue sphere is an interstitial Fe atom, red crosses – vacancies surrounding it.

5.4. Correlation effects in iron under extreme conditions.

L.V. Pourovskii[1,2], K. Glazyrin[3], O. Narygina[4], C. McCammon[3], L. Dubrovinky[3], B. Hewener[5], V. Schünemann[5], J. Wolny[5], K. Muffler[5], A. Chumakov[6], Vitali B. Prakapenka[7], F. Tasnádi[8], M. Ekholm[2], S. I. Simak[8], T. Miyake[9], M. Aichhorn[10], V. Vildosola[11], A. V. Ruban[12], M. I. Katsnelson[13], I. A. Abrikosov[8]

[1]Swedish e-science Research Centre (SeRC), Department of Physics, Chemistry and Biology (IFM), Linköping University, Linköping, Sweden, [2]Center de Physique Theorique, Ecole Polytechnique, 91128 Palaiseau Cedex, France, [3]Bayerisches Geoinstitut, Universität Bayreuth, Bayreuth, Germany, [4]School of Physics and Astronomy, University of Edinburgh, Edinburgh, UK, [5]Technische Universität Kaiserslautern, Kaiserslautern, Germany, [6]ESRF, F-38043 Grenoble Cedex, France, [7]GeoSoilEnviroCARS, University of Chicago, Argonne National Laboratory, Argonne, IL 60439, USA, [8]Department of Physics, Chemistry and Biology (IFM), Linköping University, Linköping, Sweden, [9]Nanosystem Research Institute, AIST, Tsukuba 305-8568, Japan, [10]Institute of theoretical and computational physics, TU Graz, 8010 Graz, Austria, [11]Departamento de Física Juan José Giambiagi, Facultad de Ciencias Exactas y Naturales, Universidad de Buenos Aires, 1428 Buenos Aires, Argentina, [12]Department of Materials Science and Engineering, Royal Institute of Technology, SE-10044, Stockholm, Sweden, [13]Radboud University Nijmegen, Institute for Molecules and Materials, 6525 AJ, Nijmegen, Netherlands

Submitted to Nature Communications

5.4.1 Abstract

We demonstrate that electronic correlations play a prominent role in determining electronic, elastic, and magnetic properties of iron at both moderate and high pressures and temperatures. Our *ab initio* simulations within the dynamical mean-field theory predict the existence of an electronic topological transition in the *hcp* phase of iron at pressures of about 30-40 GPa, leading to anomalies in the Debye sound velocity, lattice parameters *c/a* ratio and Mössbauer central shift that are indeed observed in our experiments. We also present evidences for the importance of iron magnetism in the Earth core. We demonstrate that all three likely crystal structures of iron and iron-rich alloys in the Earth inner core have sufficiently high magnetic susceptibility to stabilize the geodynamo. The strongest effect is observed in the body-centered cubic (*bcc*) phase, where a local magnetic moment of 1.5 μ_B is predicted to survive at 5800 K and 360 GPa.

5.4.2 Main text

Investigations of iron and its alloys at high pressure attract much attention due to their unusual behavior including superconductivity in the high pressure hexagonal close packed (*hcp*) phase (Shimizu et al. 2001), as well as due to their importance for the structure of the Earth inner core. While the structural properties of iron at ambient and moderate pressures are well known from experiment, its electronic and magnetic properties, as well as its crystal structure at extreme conditions remain under intense debate. The ground state of Fe at ambient conditions, *bcc* α phase, is ferromagnetic with spin magnetic moment well reproduced by electronic structure calculations based on the local (spin-)density

approximation, L(S)DA, for exchange and correlation effects. However, the accurate description of its electronic structure as observed, for example, in angular-resolved photoemission spectroscopy already requires proper treatment of the many-electron effects (Sánchez-Barriga et al. 2009). γ- Fe (face-centered cubic, *fcc*) is stabilized by elevated temperature, while ε- Fe (*hcp*) is stable at pressure above ~12 GPa. Their magnetic ground states are still debated (see Supporting Material, Section 5.4.3.2.3). All three of these phases, namely, *hcp*, *fcc*, and *bcc*, have been suggested as possible crystal structures of iron or its alloys in the Earth inner core (Lin et al. 2002a, Dubrovinsky et al. 2007, Mikhaylushkin et al. 2007, Tateno et al. 2010).

Theoretical simulations of iron at high pressures and temperatures, ranging from studies of the Earth's core structure to modeling the geodynamo, generally rely on a picture of non-magnetic wide-band metal with insignificant local correlations. Indeed under compression the overlap between localized states increases and so does the bandwidth W, while the local Coulomb repulsion U between those states is screened more efficiently. The reduction of U/W ratio is used to rationalize the absence of electronic correlations beyond the LDA at high-pressure conditions. The increase of the *d*-band width also results in the corresponding drop of the density of states at the Fermi energy leading to disappearance of the driving force for magnetism according to the Stoner criterion. Besides, even at the ambient pressure but at very high temperature $T \gg T_C$ (T_C is the Curie temperature, which is 1043 K in Fe) local magnetic moments are expected to be suppressed due to one-electron Stoner-type excitations. Thus, when extremely high pressure and temperature are simultaneously applied, disappearance of the local magnetic moment seems to be inevitable. Due to these considerations iron at the inner Earth core conditions (IECC) has been modeled as non-magnetic within LDA-based approaches. The results of recent works of Sola et al. (Sola and Alfè 2009, Sola et al. 2009), who applied fixed-node-approximation quantum Monte Carlo techniques to compute the equation of state and the melting temperature of *hcp* Fe at extreme conditions, are in good agreement with previous LDA-based simulations, thus strengthen the above argument, at least in the case of the hcp phase.

So, are electronic correlations important at high pressures, and can they lead to qualitatively new phenomena? To address this question we investigate the impact of correlations on the electronic structure, magnetic properties and thermodynamic stability of the *bcc*, *fcc* and *hcp* iron phases at moderate and high pressure. We employ a state-of-art fully self-consistent technique (Aichhorn et al. 2009) combining full-potential linear augmented plain-wave (LAPW) band structure method with the dynamical mean-field theory (DMFT) treatment of the on-site Coulomb repulsion between Fe *3d* states (see Section 5.4.3.2.1). The DMFT quantum impurity problem has been solved using the exact continuous-time strong-coupling Quantum Monte-Carlo method (Werner et al. 2006). A combination of LDA and DMFT has been applied earlier to study thermodynamic stability (Leonov et al. 2011) and to describe magnetic properties (Lichtenstein et al. 2001) of paramagnetic *bcc* Fe at ambient pressure, which justifies the choice of the method for this work.

We start with an investigation of the electronic structure of the *hcp* ε-phase at moderate pressures in the range 12-70 GPa, where reliable experimental work can be conducted. Note that despite the controversy on the magnetic ground state of *hcp* Fe, there is a consensus that the magnetic ordering temperature is well below room temperature (RT), such that experiments at RT must be compared to simulations for paramagnetic ε- Fe (Section 5.4.3.2.3).
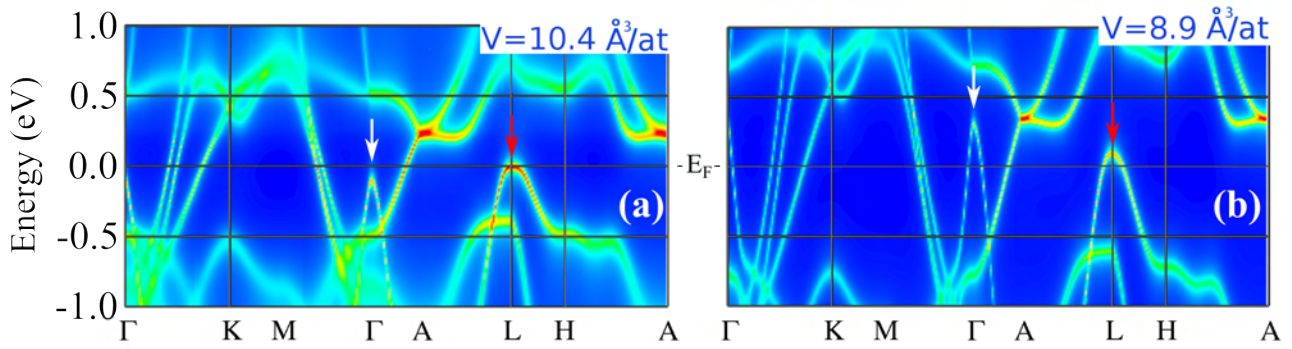
Fig. 5.4.1:
The LDA+DMFT *k*-resolved spectral function of hcp Fe at volumes of (a) 10.4 Å³/at and (b) 8.9 Å³/at corresponding to pressures of 15.4 and 69 GPa, respectively. Arrows indicate effect of pressure on featured electronic bands in the vicinity of the Fermi surface.

The LDA+DMFT *k*-resolved spectral functions for two different volumes are shown in Fig. 5.4.1. The *hcp* phase is predicted to be weakly correlated, with the average mass enhancement decreasing from 1.43 at 16 GPa to 1.25 at 69 GPa indicating a reduced correlation strength at smaller volumes. Sharp bands in the vicinity of the Fermi level and a noticeable shift of bands toward E_F compared to the LDA picture (see Section 5.4.3.2.5) are the usual features of a Fermi liquid. Most interestingly, the hole pockets at the Γ and L points visible at smaller volume are pushed below E_F at V=10.4 Å³/at. Hence, we predict *hcp* Fe to undergo an electronic topological transition (Lifshitz 1960) (ETT, see Section 5.4.3.2.4) under applied pressure due to the appearance of hole pockets at the Γ and L high-symmetry points. The actual ETT due to appearance of the pocket at Γ is predicted to take place at P~30 GPa. The observed ETT is absent in the LDA calculations (Section 5.4.3.2.5), it appears only upon inclusion of correlation effects!

Experimental detection of a pressure-induced ETT is not a trivial task. For instance, the most general tool to study electronic structure of solids - the angular-resolved photoemission cannot be applied at high-pressure. However, a ETT is expected to lead to a square root shape peculiarities of the sound velocity (Section 5.4.3.2.4). Our experimental measurements of the Debye sound velocity (see Section 5.4.3.1 for technical details), together with the analysis of the available literature data (Fig. 5.4.2) indeed confirm this prediction. Moreover, in hcp metals ETTs may also be detected in the ratio of lattice parameters *c/a* in the vicinity of the transition (Section 5.4.3.2.4). We measured the lattice parameters of *hcp*- Fe in a diamond anvil cell (DAC) on decompression from ⎯65 GPa in quasi-hydrostatic Ne pressure transmitting medium at ambient temperature (see Section 5.4.3.1) and found a profound and strong anomaly in *c/a* at about 40 GPa (Fig. 5.4.3), in agreement with our theoretical predictions of the ETT. Similar anomalous behavior of *c/a* has been reported (Ono et al. 2010) at about 50 GPa based on limited number of rather scatter data points collected in DAC experiments in non-hydrostatic (NaCl) pressure transmitting medium, but it was erroneously attributed to magnetic transition in *hcp*- Fe (see Section 5.4.3.2.3).

Mössbauer spectroscopy can also be a powerful method to detect ETT (Potzel et al. 1995). We performed Mössbauer experiments on pure Fe and $Fe_{0.9}Ni_{0.1}$ up to 60 GPa in the DAC loaded with He as a quasihydrostatic pressure transmitting medium, and observed a strong peculiarity of the central shift
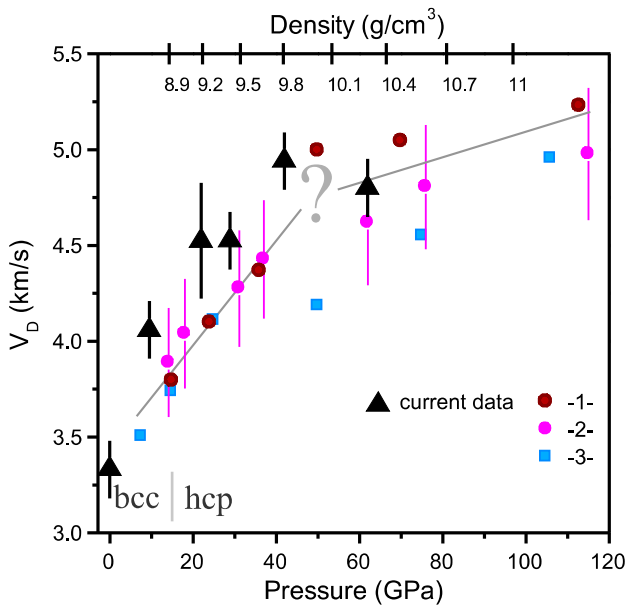
Fig. 5.4.2:

Debye sound velocity for pure Fe and Fe-Ni alloys as a function of pressure. Black solid triangles indicate our $Fe_{0.9}Ni_{0.1}$ data. We compare it with data on pure Fe measured by (-1-) NIS (Mao et al. 2001), and (-2-) impulsive stimulated light scattering measurements (Crowhurst et al. 2005). The blue symbols (-3-) correspond to $Fe_{0.92}Ni_{0.08}$ data points measured by NIS (Lin et al. 2003b). Dashed lines are the eye guides.
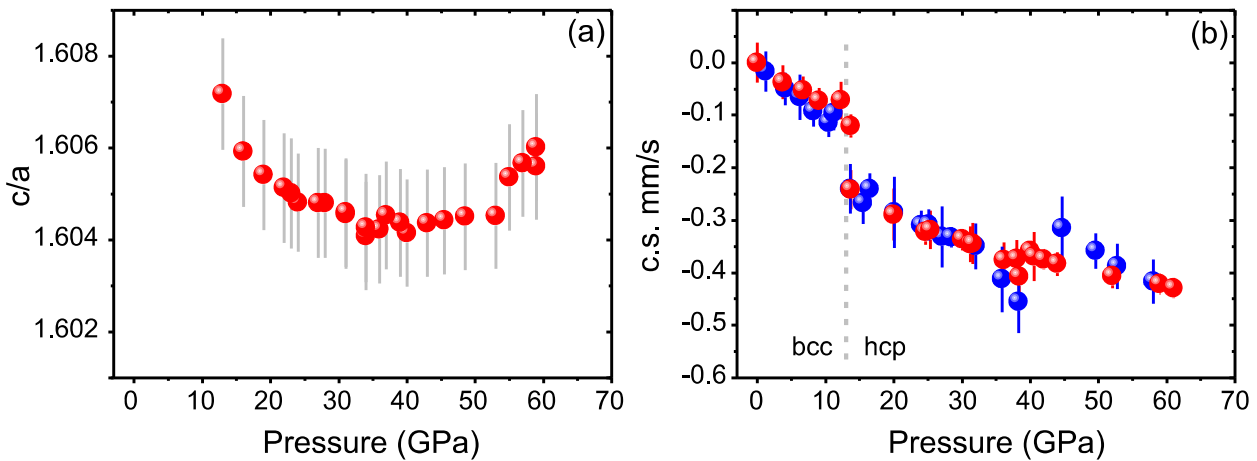
Fig. 5.4.3:

Pressure induced variation of (a) *hcp* phase c/a lattice parameters ratio and (b) Mössbauer central shift determined for pure iron (red circles), and $Fe_{0.9}Ni_{0.1}$ (blue circles). Central shift of materials is given relative to *bcc* iron measured at ambient conditions. Dashed line indicates transition of *bcc* phases of iron and iron-nickel alloy to *hcp* phase.

(c.s.) at 40-45 GPa (Fig. 5.4.3), which, from our theoretical calculations, cannot be explained by changes of the electron density at the nuclei - isomer shift (the main constituent of the central shift, see Section 5.4.3.2.6). But the ETT, which is predicted in our LDA+DMFT calculations to occur in the same pressure range, is expected to lead to a peculiarity of the second-order Doppler shift (another important constituent of the central shift, see Section 5.4.3.2.4). Thus, the ETT provides a convincing explanation of the experimentally observed peculiarities of the sound velocity, *c/a* ratio and central shift at 40-45 GPa.

Having established the predictive power of our theoretical approach and importance of correlation effects in Fe at moderate compression, we extend our study to the inner Earth core conditions (IECC)

and applied the LDA+DMFT theory to the *bcc*, *fcc* and *hcp* Fe at volume of 7.05 Å^3/at (corresponding to pressure ~360 GPa) and temperatures up to 5800 K. The on-site Coulomb interaction for all three phases at this volume has been calculated by means of the constraint random-phase approximation (cRPA) technique (Miyake et al. 2009) (see Section 5.4.3.2.7).

We have evaluated the correction to the electronic free energy ΔF_{el} due to the many body effects (Section 5.4.3.2.2). Within error bars the magnitude of ΔF_{el} is the same for *bcc* and *hcp* Fe (-1022±34 meV/at and -1032±43 meV/at, respectively), which are suggested as stable phases of iron (Vocadlo et al. 2003) and iron-based alloys at IECC (Lin et al. 2002a, Dubrovinsky et al. 2007). The magnitude of ΔF_{el} is substantially smaller (-895±31 meV) in the case of *fcc* Fe, showing that the many-body correction is strongly structure-dependent. This might affect the shape of the electronic free energy "landscape" and, consequently, the forces arising due to a lattice distortion in a given phase. Therefore, our calculations demonstrate that many-body effects should be considered for a proper description of thermodynamic, elastic and vibrational properties of iron at IECC.

To underline the significance of correlation effects we show in Fig. 5.4.4 the calculated ***k***-resolved spectral function *A(**k**,E)*, inverse quasiparticle lifetime Γ and uniform magnetic susceptibility χ for all phases. These quantities are expected to exhibit the typical Fermi-liquid properties in good metals at
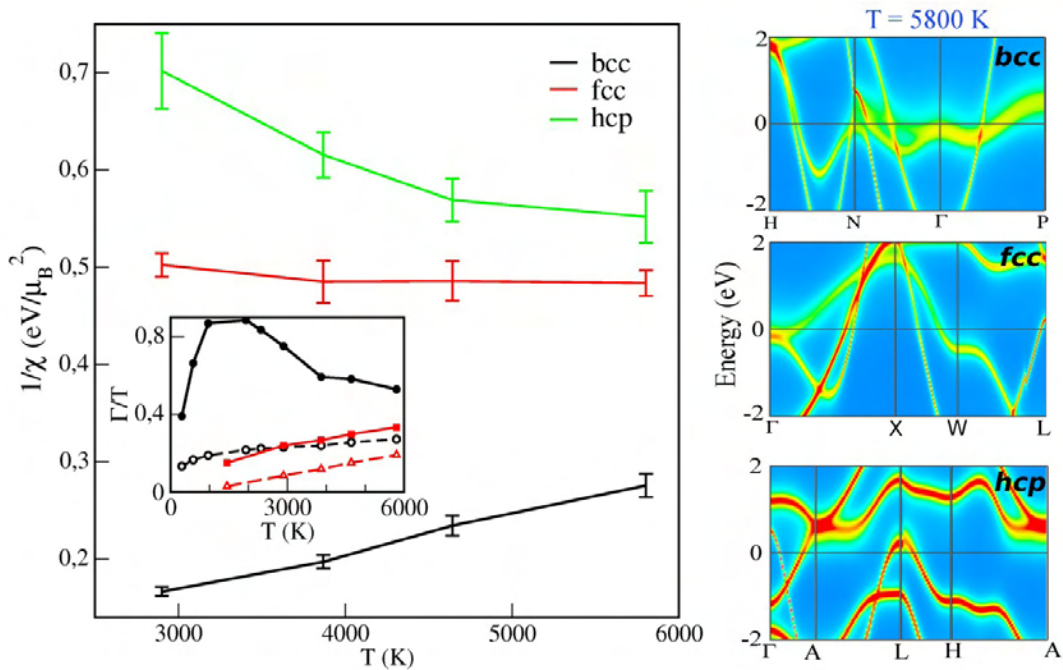
Fig. 5.4.4:
Left panel: the inverse of uniform magnetic susceptibility in paramagnetic state versus temperature. Inset: the inverse quasiparticle life-time Γ divided by temperature vs. temperature for *bcc* (in black) and *fcc* (in red). The solid/dashed curves are for e_g and t2g states, respectively. Right panel: the LDA+DMFT k-resolved spectral function A(k,E) for all three phases. The color scale is the same for all phases and the magnitude of *A(**k**,E)* increases from dark blue through green and yellow to red.

ambient conditions, namely, a temperature-independent Pauli susceptibility, a large quasiparticle lifetime at low energies (leading to well-defined quasiparticle "bands" in $A(\boldsymbol{k},E)$) with inverse quadratic temperature dependence.

From Fig. 5.4.4 one can clearly see that quasiparticle states remain sharp and well defined in *fcc* and *hcp* Fe, while in *bcc* Fe the low-energy e_g "band" is strongly broaden indicating destruction of quasipariticle states. In *fcc* and *hcp* Fe the ratio of the inverse quasiparticle life-time Γ to temperature T increases linearly with T as expected for a Fermi liquid (see inset in the left panel of Fig. 5.4.4). In contrast, Γ is significantly larger in *bcc* Fe, in particular, for e_g states and its temperature dependence follows the T^2 law only up to T=1000 K. Therefore, one may conclude that while *fcc* and *hcp* Fe have a typical metallic behavior, the *bcc* phase is clearly in non-Fermi liquid incoherent "bad metal" state, which cannot be consistently described within the LDA-based framework.

The application of the LDA+DMFT theory has the most important consequences for the understanding of magnetic properties of Fe at the Earth's core conditions. In particular, all three phases of Fe show significant uniform magnetic susceptibility, Fig. 5.4.4. At temperature T=5800 K we calculated χ (in SI units) and the results are $1.7 \cdot 10^{-4}$, $2.0 \cdot 10^{-4}$, and $3.5 \cdot 10^{-4}$ for *hcp*, *fcc*, and *bcc* Fe, respectively. Interestingly, the uniform magnetic susceptibility in the *fcc* and *hcp* phases is weakly temperature-depended (Fig. 5.4.4). On the contrary, the temperature evolution of χ^{-1} in bcc Fe is well fitted by a Curie-Weiss law corresponding to the moment of 1.5 μ_B explicitly showing that local magnetic moments survive in this phase at the IECC.

High bulk susceptibility of the inner core observed in our calculations is still not considered in current models of the Earth core dynamics and geodynamo (Aubert et al. 2009). An inner core with a paramagnetic susceptibility in the range $10^{-3} - 10^{-4}$ SI units, and with a paramagnetic relaxation time acting slower than field changes coming from the outer core, could also attenuate short frequency fluctuations and become an important factor stabilizing the geodynamo (Clement and Stixrude 1995, Gilder and Glen 1998), just as an electrically conducting inner core could stabilize the geodynamo because the inner core would have a magnetic diffusion constant independent of the outer core (Hollerbach and Jones 1993). The strongest effect is predicted for *bcc* Fe, one of the likely crystal structure of iron and iron-rich alloys in the Earth inner core (Lin et al. 2002a, Belonoshko et al. 2003, Vocadlo et al. 2003, Dubrovinsky et al. 2007).

5.4.3 Supporting Online Material

5.4.3.1. Experimental details

For the preparation of the iron sample we used enriched ^{57}Fe of 99.99% purity. The $Fe_{0.9}Ni_{0.1}$ samples were prepared by mixing appropriate amounts of ^{57}Fe enriched iron and nickel powder of 99.999% purity. The mixture was compressed to 2 GPa in a piston-cylinder apparatus, heated above the melting point and subsequently quenched.

To achieve high pressures in different experiments we used two types of diamond anvil cells: one conventional for Mössbauer experiment, with He gas for quasihydrostatic conditions loaded into a chamber of Re gasket, and another specifically developed in Bayerisches Geoinstitut for nuclear

resonant inelastic x-ray scattering (NRIXS). Special types of new cells slits make it possible to measure nuclear forward scattering (NFS) or X-Ray diffraction patterns at the same time as NRIXS, and, due to specific geometry of NRIXS cells, Be was chosen as a material for the gaskets. We used LiF as pressure medium for the NRIXS cells. In both experiments we used diamonds with 250 μm culet size and small ruby chips to measure pressure inside gaskets chambers. The prepared gaskets chambers were 60μm·20μm and 100μm·30μm (diameter·height) for NRIXS and Mössbauer experiments correspondingly.

NRINX studies were carried at the beam line ID18 (ESRF, Grenoble), the details of experiment are described in (Lübbers et al. 2000) and the references therein. NRIXS data analysis was performed using programs available at ESRF (DOS-2.1, written by Viktor Kohn), the calculation procedure is described in Sturhahn and the references therein.

To extract partial density of states for iron (PDOS) using NRINX we employed the following procedure. First, we collected dependencies of absorption of the sample enriched with ^{57}Fe on the energy of incident radiation (NIS spectra Fig. 5.4.5). After extracting elastic contribution to the NIS spectra, we used DOS-2.1 software to extract PDOS. Next, we calculated Debye sound velocities (VD) using the relation (Hu et al. 2003):

$$\rho \, V_D = \frac{4 \cdot \pi \cdot \tilde{m}}{h^3} \lim_{E \to 0} \left(\frac{E^2}{D(E)} \right)$$

where ρ is density of the material; $\tilde{m}$ is the mass of the nuclear resonant isotope (^{57}Fe); h is the Plank constant; $D(E)$ is the iron PDOS and E is energy. We determined the equation of state for the *hcp* phase of $Fe_{0.9}Ni_{0.1}$ (the variation of ρ with pressure) and the bulk modulus in a separate synchrotron x-ray diffraction experiment on the beam lines ID27 (ESRF, Grenoble) and at IDD-13 (APS, Argonne). The parameters derived from a fit to the Birch-Murnaghan equation of state are: bulk modulus K=159(3) GPa, K'=4.78(9) and V0=6.77(1) cm^3/mol.

^{57}Fe Mössbauer spectra (MS, Fig. 5.4.5) were recorded at room temperature in the transmission mode on a constant acceleration Mössbauer spectrometer using a nominal 370 MBq ^{57}Co high specific activity source in a 12 μm Rh matrix (point source). The velocity scale was calibrated relative to 25 μm α-Fe foil. Mössbauer spectra were fitted to Lorentzian lineshapes using the commercially available fitting program NORMOS written by R.A. Brand (distributed by Wissenschaftliche Elektronik GmbH, Germany). Collection time for each spectrum varied from 24 to 48 h.

In our experiments the *bcc* ε- phase transforms to the *hcp* ε-phase at 10-13 GPa, in good agreement with literature data (Cort et al. 1982, Mathon et al. 2004). The central shift in ε-Fe and ε-$Fe_{0.9}Ni_{0.1}$ gradually decreases with pressure, up to 40 45 GPa. In this pressure range we observe an abrupt increase of the central shift by -0.15 mm/s in $Fe_{0.9}Ni_{0.1}$ and smaller - 0.05 mm/s in pure iron (Fig. 5.4.3). Upon further compression to 60 GPa we see no sign of further irregular behavior. The discontinuity is reversible on decompression and was observed in several independent DAC loadings. We notice that x-ray diffraction measurements have not revealed any structural transformation in the pressure range 13-60 GPa in both *hcp* Fe and $Fe_{0.9}Ni_{0.1}$ (Mao et al. 1990, Yoo et al. 1995, Dubrovinsky et al. 2007).
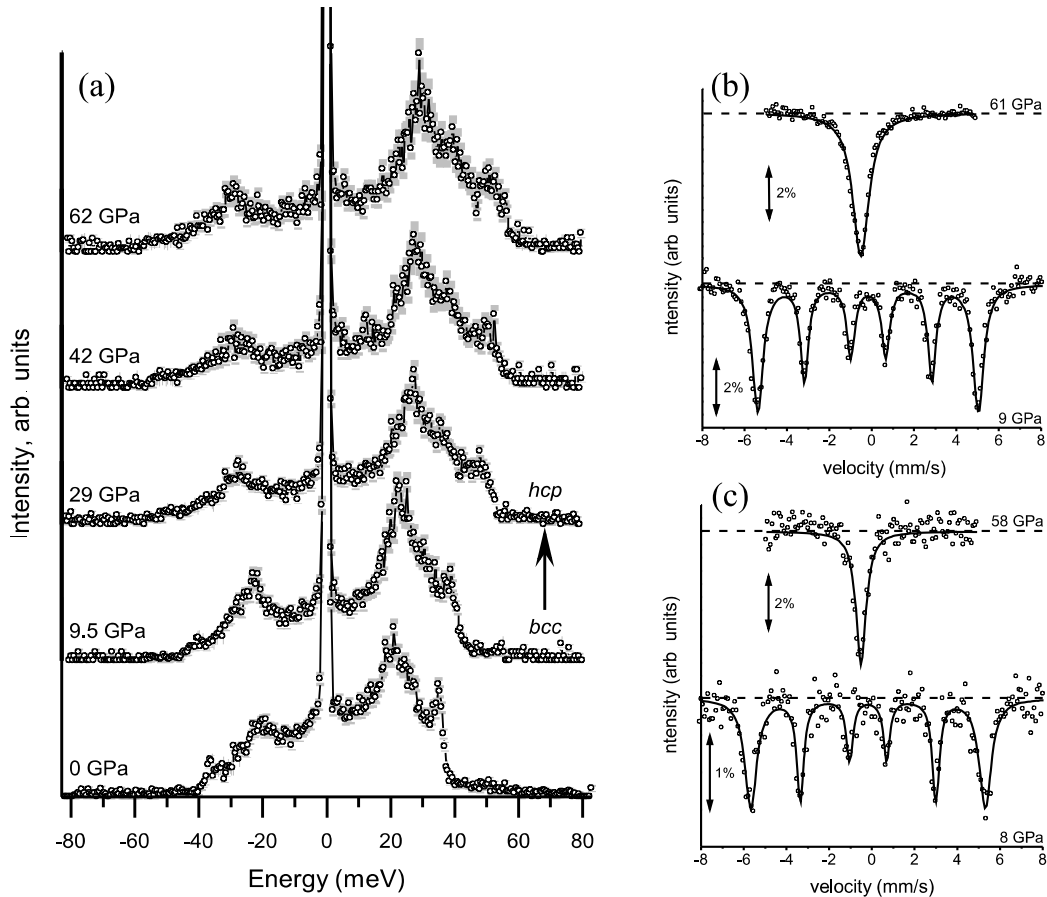
Fig. 5.4.5:

Left panel – $Fe_{0.9}Ni_{0.1}$ NIS spectra at different pressures. Right Panel - Representative Mössbauer spectra of (b) pure Fe and (c) $Fe_{0.9}Ni_{0.1}$ samples at different pressure. Solid lines represent model fits.

5.4.3.2. Theoretical calculations

5.4.3.2.1. Local-density approximation+dynamical mean-field theory (LDA+DMFT) approach

Our LDA+DMFT calculations have been performed with a full-potential fully-self consistent implementation (Aichhorn et al. 2009, 2011) combining the dynamical-mean-field-theory (Georges et al. 1996, Anisimov et al. 1997, Lichtenstein and Katsnelson 1998)and a highly precise full-potential linear augmented plane wave (FLAPW) electronic structure technique (Blaha et al. 2002) . The DMFT quantum impurity problem was solved by continuous-time quantum Monte Carlo (CTQMC) (Werner et al. 2006) method. At the beginning of each LDA+DMFT iteration the eigenvalues and eigenvectors of the Kohn-Sham problem were obtained by the FLAPW code. Wannier-like functions for the Fe-*3d* shell were then constructed by projecting local orbitals onto a set of FLAPW Bloch states located within a chosen energy window. We then introduced local Coulomb interaction acting between those Wannier orbitals and solved the resulting many-body problem within the DMFT framework. After completing the DMFT cycle we calculated the resulting density matrix in the Bloch states basis, which was then used to

recalculate the charge density and update the Kohn-Sham potential at the next iteration.

We have employed the density-density form of the local Coulomb interaction in the spherical approximation, in which case the interaction matrix is fully specified by the parameters U and J. In our simulations of *bcc*, *fcc* and *hcp* Fe at the Earth inner core conditions (EICC) these parameters were computed as described in Section 5.4.3.2.7. Calculations of *hcp* Fe in the moderate pressure range (up to 70 GPa) were performed with U=3.4 eV and J=0.9 eV. The quantum impurity problem has been solved with 3 and 2 millions CTQMC sweeps in high-temperatures and room temperature calculations, respectively. All iron phases under consideration are metals with a rather uniform occupancy of the orbitals within the Fe *3d* shell. Therefore, we employed the around mean-field form (Czyzdotyk and Sawatzky 1994) for the double-counting correction term.

In order to compute the magnetic susceptibility in uniform fields we performed LDA+DMFT simulations with KS eigenstates split by the magnetic field term $-H \cdot \mu_B \cdot \sigma_Z$ where the external magnetic field $H = 0.005$ eV/μ_B. This field resulted in appearance of a small magnetic moment M of order 0.01-0.1 μ_B, then the magnetic susceptibility was computed as $\chi = M/H$.

The CTQMC solver computes the Green's function on the imaginary-time axis so an analytic continuation is needed in order to obtain results on the real axis. For that we use a stochastic version of the Maximum Entropy method (Beach 2004) with which we calculate the retarded lattice Green's function, $G_{vv}(k, \omega^+)$, where v labels all the Bloch bands considered. We finally obtain the spectral function as follows: $A(k,\omega) = -\frac{1}{\pi} \cdot \text{Im}[\sum_v G_{vv}(k,\omega^+)]$

5.4.3.2.2. Calculation of electronic free energy within LDA+DMFT

The direct calculations of the electronic free energy is a difficult task as it requires the knowledge of the interaction energy functional Φ, which is defined within DMFT as the sum of all two-vertex-irreducible diagrams constructed from the local interaction and local Green's function (Kotliar et al. 2006). This quantity cannot be directly extracted from CTQMC calculations.

Therefore, we have used a coupling constant integration approach (Nozières 1997) to obtain the DMFT correction to the free energy. We define the free energy F_λ corresponding to a given value of the coupling:

$$F_\lambda = -\frac{1}{\beta} \cdot \ln[Tr(e^{-\beta \cdot (H_0 + \lambda \cdot H_1)})] \quad (1)$$

where H_0 is the one-electron (LDA) part of the Hamiltonian, the interacting part of the Hamiltonian H_1 equal to the difference between the on-site Coulomb interaction term and double-counting correction, H_{int}-E_{dc}, the coupling constant $\lambda=[0:1]$. Hence, the derivative of (1) over the coupling strength reads

$$\frac{\partial F_\lambda}{\partial \lambda} = \frac{1}{\lambda} \langle \lambda \cdot H_1 \rangle$$

and by integrating this over λ we obtain the many-body correction to the electronic free energy:

$$\Delta F = F - F_0 = \int_0^1 \frac{1}{\lambda} \langle \lambda \cdot H_1 \rangle d\lambda \quad (2)$$

In derivation of Eq. (2) we neglected the λ dependence of the one-electron part, and, hence, the charge density renormalization due to many-body effects. However, we verified that the difference in the total energies obtained with and without the charge density self-consistency is small, and the correction to the total energy due to the charge density self-consistency is within our error bars.

In order to obtain ΔF we have computed $\langle \lambda \cdot H_1 \rangle_\lambda$ for a discrete set of values of λ ranging from 0 to the full interaction strength. For $\lambda=0$ we calculated $\frac{\langle \lambda \cdot H_1 \rangle|_{\lambda=0}}{\lambda}$ analytically, as in this case it is equal to the Hartree-Fock approximation to $\langle H_{int} \rangle$ computed with the LDA density matrix minus the double-counting correction. The resulting value of $\frac{\langle \lambda \cdot (H_{int} - E_{dc}) \rangle|_{\lambda=0}}{\lambda}$ is very small. To obtain $\frac{\langle \lambda \cdot H_1 \rangle|_\lambda}{\lambda}$ for other values of λ we performed the corresponding LDA+DMFT simulations with the value of the local Coulomb interaction scaled accordingly. Then we integrated $\frac{\langle \lambda \cdot H_1 \rangle|_\lambda}{\lambda}$ (see Fig. 5.4.6) over λ in order to obtain ΔF and its error bar.

The resulting many-body correction to the electronic free energy is displayed together with the corresponding correction to the total energy in Fig. 5.4.7. One may see that the entropic contribution (i.e. the difference between $\Delta F - \Delta E = -T\Delta S_{el}$) becomes much more significant at the higher temperature, and its contribution is almost twice higher in the case of *bcc* Fe compared to the *hcp* and *fcc* phases.
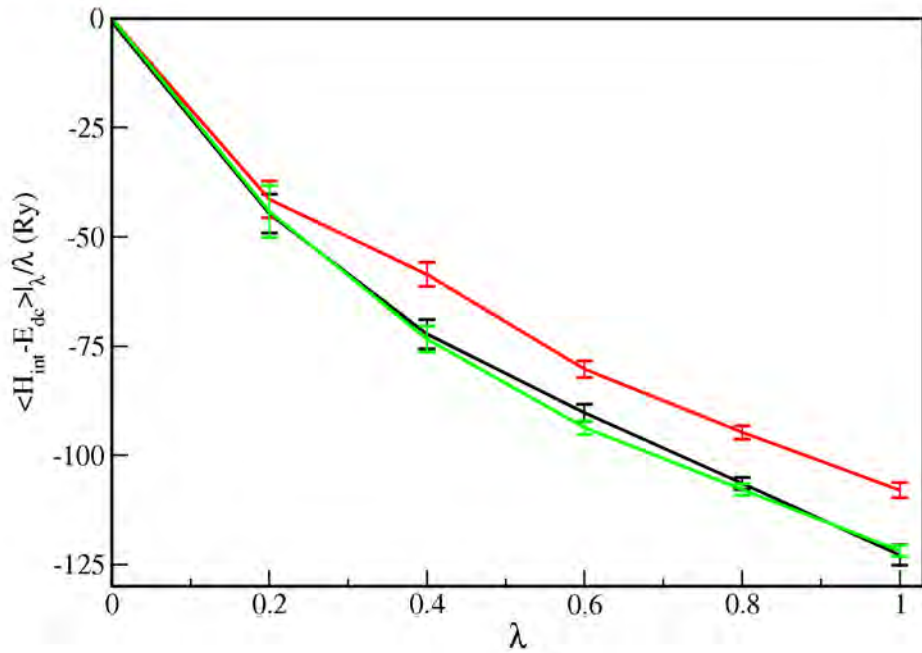
Fig. 5.4.6:

Evolution of as function of $\frac{\langle \lambda \cdot (H_{int} - E_{dc}) \rangle|_{\lambda=0}}{\lambda}$ for *bcc*, *fcc* and *hcp* Fe **(**the black, red, and green curves, respectively**)** at the temperature of 5800K.
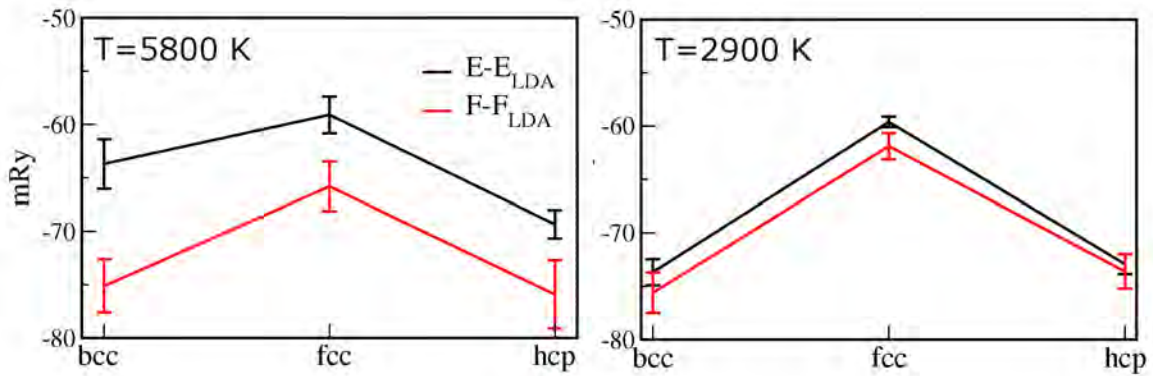
Fig. 5.4.7:

Many-body correction to the total (in black) and free (in red) energy for the three phases of Fe at the volume of 7.05 $Å^3$/at

5.4.3.2.3. Relevance of magnetic order for properties of *hcp* Fe

While it is well known that the *bcc* α- phases of Fe and $Fe_{0.9}Ni_{0.1}$ are ferromagnetic at ambient conditions, with high value of the magnetic order-disorder transition temperature, Curie temperature T_C, the *fcc* (γ-) phases of Fe and $Fe_{0.9}Ni_{0.1}$ are believed to have complex incommensurate magnetic ground states, which are still not reproduced by theory (Abrikosov et al. 2007). The ε- phases of Fe and $Fe_{0.9}Ni_{0.1}$ were believed to be nonmagnetic (Cort et al. 1982); however, recent theoretical work showed that a collinear antiferromagnetic state (AFM-II)(Steinle-Neumann et al. 1999b, 2004, Papandrew et al. 2006)or a more complex AFM state (Lizárraga et al. 2008) have lower energy than the nonmagnetic state. Computations on the AFM-II phase were performed to explain a second peak in the Raman spectra of ε- Fe (Merkel et al. 2000), and were also able to improve the agreement between calculated and measured equations of state (EOS) for *hcp* Fe (Steinle-Neumann et al. 1999b, 2004). Nevertheless, the AFM-II phase was not resolved in Mössbauer experiments. Moreover, also theoretical estimates of the magnetic order-disorder transition temperature of *hcp* Fe, the Néel temperature T_N, yield a maximum value of ~69 K for *hcp* Fe at the transition pressure (12 GPa), followed by its decrease with increasing pressure (Thakor et al. 2003). Although nickel atoms are predicted to result in an enhancement of magnetic moments on neighboring iron atoms, there is no evidence that ε- $Fe_{0.9}Ni_{0.1}$ is a static antiferromagnet down to 11 K at 21 GPa (Papandrew et al. 2006).

All this implies that a direct comparison between static zero temperature ab-initio calculations for AFM ε- Fe and room temperature experiments cannot be done straightforwardly. In particular, experiments on *c/a* ratio in *hcp* Fe (Ono et al. 2010) were conducted at ambient temperature, and therefore their interpretation of the observed peculiarity in terms of disappearance of ordered magnetic moments calculated for T=0 K is not correct. Because *hcp*-Fe is paramagnetic at room temperature, experimentally, as well as theoretically, its electronic structure and ground state properties should be simulated by paramagnetic (not to be confused with non-magnetic) calculations. The DMFT theory provides us with a natural description of the paramagnetic state, and explains the observed peculiarity in terms of the Electron Topological Transition, see Section 5.4.3.2.4 below.

5.4.3.2.4. **Electron Topological Transition and Fermi surface topology of** *hcp* **Fe**

By the Electron Topological Transition (ETT) (Lifshitz 1960) one understands a change of the Fermi surface topology in a system upon a variation of an external parameter, such as pressure or composition, which results in a singularity of the electron density of states at the Fermi energy - $N(E_F)$ as function of the external parameters. Here we present a brief review of the effects of ETT on lattice properties of metals (for more details, see Ref. (Katsnelson et al. 1994)).

For clarity, let us start the discussion within the one-electron approximation. A formal generalization of the theory to the many-electron case relevant for this work will be briefly discussed below (Katsnelson and Trefilov 2000). In the former case, the single-electron contribution to the electron total energy (E_{tot}) is $E_{se} = \sum_{\lambda}^{occ} \varepsilon_{\lambda}$, where the sum of the single-particle energies is taken over all occupied states $\varepsilon_{\lambda} < \varepsilon_F$, . The elastic moduli $C_{ii} = \frac{1}{V_0} \frac{\partial^2 E_{tot}}{\partial u_i^2}$, where V_0 and u_i are volume per elementary cell and corresponding deformation, respectively, is calculated at the condition of constant particle number at deformation and contains the contribution $\delta C_{ii} = -\frac{1}{V_0} \sum_{\lambda} (\frac{\partial \zeta_{\lambda}}{\partial u_i})^2 \cdot \delta(\zeta_{\lambda})$ ($\zeta_{\lambda} = \varepsilon_{\lambda} - \varepsilon_F$) which is singular near the ETT. This singular contribution has the same singularity as $-N(\varepsilon_F)$; it was studied in detail using alkali and alkaline earth metals under pressure as examples (Vaks et al. 1991, 1989). This means, in particular, that the peculiarity in the Debye sound velocity $\Delta V_D \sim -\delta N(\varepsilon_F)$, where $\delta N(\varepsilon_F)$ is the change in the density of states (DOS) at the Fermi level due to ETT. In case of an appearance of new hole pockets below the critical volume VETT the change in DOS $\delta N(\varepsilon_F) \sim (V_{ETT} - V)^{1/2}$, hence the one-electron theory predicts the square root down shape of the peculiarity. Our DMFT calculations show that in case of *hcp*-Fe at moderate compression one should use the Fermi-liquid theory of ETT (Katsnelson and Trefilov 2000). In this case many-electron effects make the singularity of the thermodynamic potential Ω at ETT to be *two-sided*. Still the leading term in $\Delta V_D \sim (V_{ETT} - V)^{1/2}$, while the peculiarity on the other side of the transition is one power weaker, and it should not be possible to distinguish it experimentally.

The Debye temperature θ_D has also singularity as $-N(\varepsilon_F)$, and lattice heat capacity at low temperatures $T << \theta_D$ has the same singularity as the electron heat capacity. Thermal expansion coefficient proportional to derivative of θ_D with respect to deformations has at these temperatures stronger singularity, like $\frac{\partial N(\varepsilon_F)}{\partial \varepsilon_F}$, that is, divergent at the point of ETT (Souvatzis et al. 2007). It is important to stress, however, that the Debye model is qualitatively incorrect in the situation of ETT. The point is that strong anomalies of the phonon spectra in harmonic approximation happens in a relatively small part of the Brillouin zone near the **Γ** point and average phonon frequency over the whole Brillouin zone, which is relevant for thermodynamics at T≈θ_D is weaker, by a factor $\varepsilon_F - \varepsilon_c$, ε_c being the Van Hove singularity energy (Vaks et al. 1991). However, if we take into account quasiharmonic and anharmonic effects, that is, temperature dependence of phonon frequencies due to thermal expansion and due to phonon-phonon interactions, the singularity enhance, again, and become like $N(\varepsilon_F)$ in average phonon frequencies and like $\frac{\partial N(\varepsilon_F)}{\partial \varepsilon_F}$ in the elastic moduli (Vaks and Trefilov 1991).

87

For *hcp* metals ETTs have been associated with the anomalies in the ratio of lattice parameters *c/a* in the vicinity of the transition (Meenakshi et al. 1992, Novikov et al. 1997, Li and Tse 2000, Kechin 2001). If we discuss dependence of lattice constants on the parameters they are less singular than C_{ii} since they are related with the first derivatives of the thermodynamic potential (and C_{ii} - with the second ones). This means that the anomaly in *c/a* ratio at zero temperature should be hardly visible but at finite (and high enough) temperatures it is proportional to $N(\varepsilon_F)$, via the anomaly of the thermal expansion coefficient. The same is correct for the second-order Doppler shift of the Mössbauer spectra related with the heat capacity and, thus, with average phonon frequencies over the Brillouin zone.

5.4.3.2.5. Fermi surface topology of *hcp* Fe: LDA vs. DMFT

Theoretical calculations of the volume-dependent electronic structure and the Fermi surface of pure *hcp* Fe were also carried out in the framework of density functional theory (Hohenberg and Kohn 1964) using both the Perdew-Wang local density approximation (PW-LDA) (Wang and Perdew 1991) and the Perdew-Brucke-Ernzerhof generalized gradient approximation (PBE-GGA) (Perdew et al. 1996) for the exchange-correlation energy and one-electron potential. For the Fermi surface calculations we employed the Full-Potential Local-Orbital minimum-basis code FPLO-08 (Koepernik and Eschrig 1999) with the built-in local basis set of Fe (*1s2s2p*)/(*3s3p4s5s3d4d4p*) in (core)/(valence) notation. The (14·14·14) tetrahedron mesh of the first Brillouin zone (Blöchl et al. 1994) has provided convergence. The resulted energy-volume curves were compared with those obtained by Exact Muffin Tin Orbital (EMTO) method (Kumar and Anderson 1995, Vitos et al. 2001) (EMTO was used for isomer shift calculations) and good agreement was found. For the LDA band structure calculations, we have employed the linear augmented plane wave (FLAPW) electronic structure technique as implemented in the Wien2k code (Blaha et al. 2002). We have used the same setup within Wien2k for both LDA and LDA+DMFT (see Section 5.4.3.2.1) with a 560 k-points mesh in the irreducible part of the *hcp* Brillouin zone. The calculated band structures have shown negligible effect on the electronic structure approach used and the approximation (LDA or GGA) employed for the exchange and correlations. In the left panel of Fig. 5.4.8 we display the resulting LDA- band structure for the volumes of 8.9 and 10.4 Å³/at. One may notice that the change of volume induces no qualitative modifications in the LDA band structure of *hcp* Fe. The Fermi surface calculated within FPLO-08 PW-LDA is displayed in Fig. 5.4.9. Again, one observes no topological transitions induced by the volume change.

The results show that the ETT is absent in the LDA calculations, it appears only upon inclusion of the correlation effects in our DMFT simulations (Fig. 5.4.1 and the right panel in Fig. 5.4.8) and is due to an upwards shift of the Fe *3d* band with increasing strength of correlations. Simple arguments can be given to demonstrate that within LDA and for metallic systems the overall shift of a band due to an on-site Coulomb interaction is underestimated for a more-than half-filled shell (the case of the Fe *3d* shell). The magnitude of this LDA error grows with increasing strength of correlations. Hence, a larger DMFT correction is expected for larger volumes. The formally *3d* bands forming the pockets have a substantial *4p* character and experience a smaller upward shift compared to other *3d* states leading to their disappearance with increasing volume.
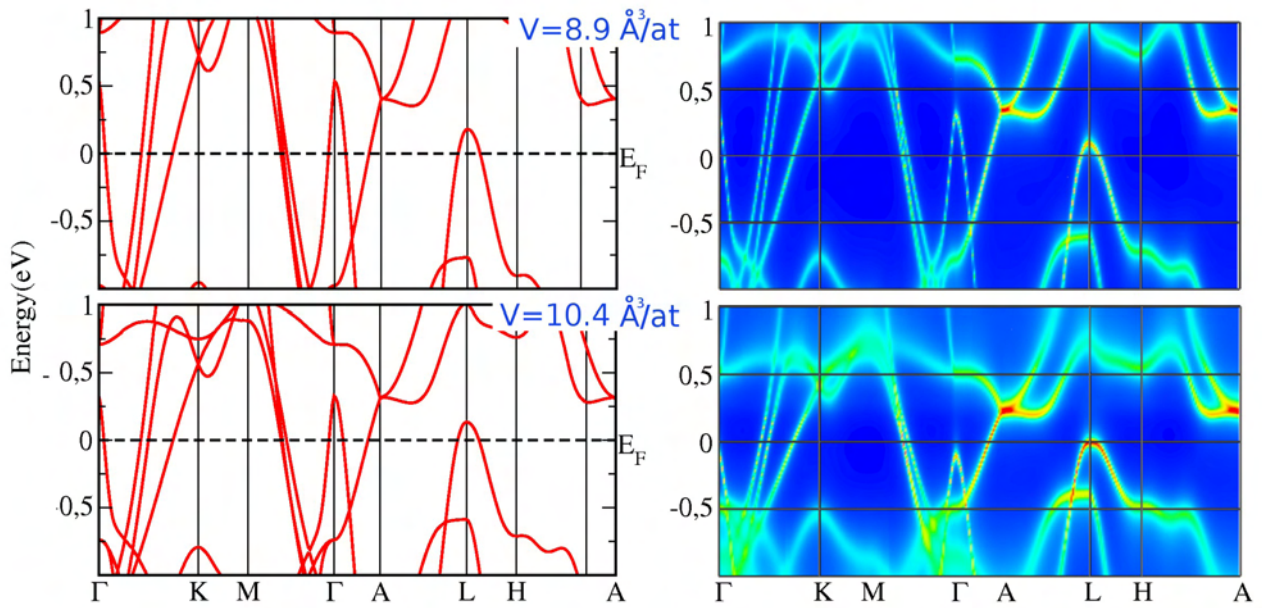
Fig. 5.4.8:

The LDA band structure (left panel) and LDA+DMFT k-resolved spectral function (right panel) of *hcp* Fe at volumes of 8.9 Å^3/at (top row) and 10.4 Å^3/at (bottom row).
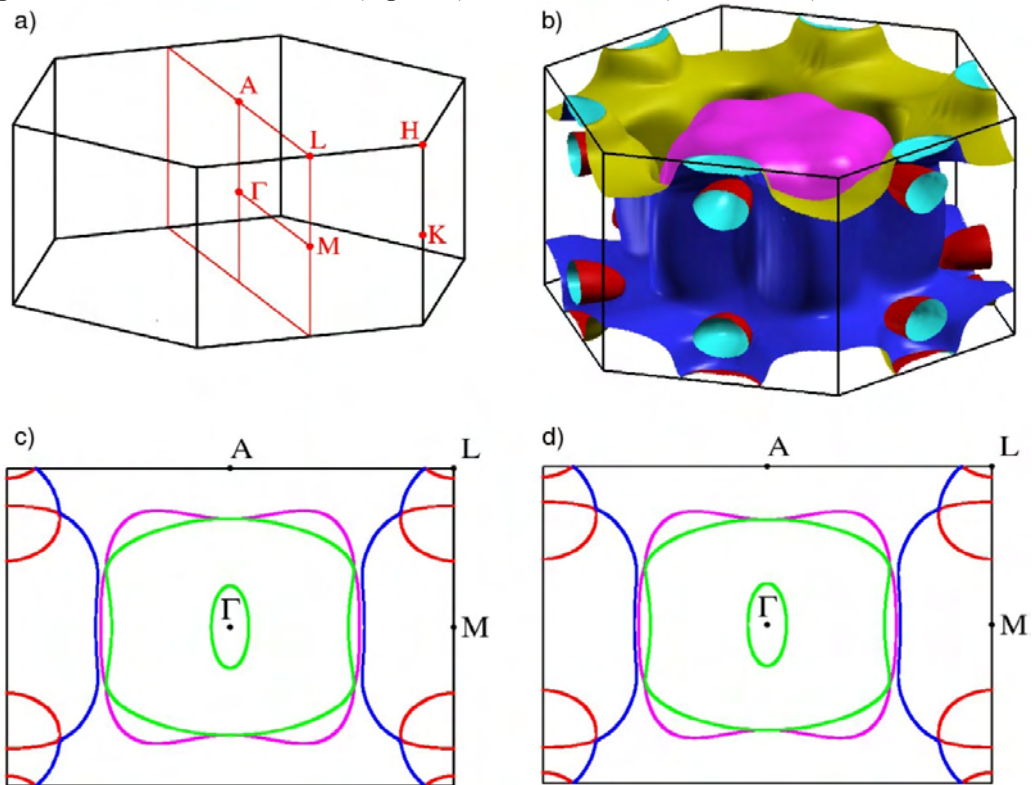
Fig. 5.4.9:

a) Hexagonal high symmetry **k**-points in the first Brillouin zone. b) The *hcp* Fe Fermi surface (FS) sheets. FS cross section at unit cell volumes 9.3 Å^3/at (c) and 9.9 Å^3/at (d) indicate that within the one-electron approximation there are no changes in the FS topology within the volume interval of interest for this study.

5.4.3.2.6. Isomer shifts calculations in Fe

The Mössbauer centre shift of the absorption line, ΔE^C, is composed of two contributions:

$$\Delta E^C = \delta^{IS} + \delta^{SOD},$$

called isomer shift (IS) and second-order Doppler shift (SOD), respectively. The latter is a relativistic Doppler shift of photon frequency due to the relative velocity (*v*) of a source and an absorber. Due to thermal motion of the ions, the corresponding shift of the absorption line E_γ depends on *v* to second order as: $\delta^{SOD} = \frac{\langle v^2 \rangle}{2 \cdot c^2} \cdot E_\gamma$, where *c* is the speed of light. The isomer shift, which is due to the different chemical environments of the source and the absorber, can in turn be calculated as $\delta^{IS} = -\alpha \cdot [\rho_a(0) - \rho_s(0)]$, where $\rho_a(0)$ and $\rho_s(0)$ are the electron densities at the nucleus in the absorber and the source materials, respectively, and α is an empirical nuclear calibration constant. We assigned it the value 0.27 a_0^3 mm/s, which is within the common range reported in the literature (Williamson et al. 1972, Moyzis and Drickamer 1968, Akai et al. 1986). We evaluated $\rho_a(0)$ and $\rho_s(0)$ from *ab initio* calculations, based on local density approximation (LDA) and local density approximation + dynamical mean- field theory (LDA+DMFT).

The pure LDA calculations were performed using two different computational methods: exact muffin-tin orbitals (EMTOs) (Vitos et al. 2001) and FPLAPW (Blaha et al. 2002). In EMTO calculations, we treated *3d* and *4d* electron states as valence, and the core states were recalculated in each iteration of the self-consistency cycle. The number of ***k***-points in the numerical integrals over the Brillouin zone was converged with respect to the total energy to within 0.1 meV/atom. In FPLAPW calculations, electronic states were separated into core- and valence-states at -6.0 Ry. The ***k***-points were chosen from a mesh of 10 000 points in the Brillouin zone, and we set the $R_{MT} \cdot K_{max}$ parameter to 8.0.

In DMFT+LDA calculations, the FPLAPW method was used for the LDA part, as described in Section 5.4.3.2.1. We used the experimental lattice constants at the corresponding pressures, which gives a highly accurate description of electronic structure at fixed volume (Ruban and Abrikosov 2008). The source system was taken to be body-centered cubic (*bcc*) Fe at ambient pressure, in order to emulate the experimental set-up.

Since only *s*-orbitals have finite probability density at the origin, it is reasonable to assume that δ^{IS} depends mainly on the difference in the *s*-electron charge density at the absorber and emitter nuclei. In the electronic structure computational methods employed in this work, the nucleus is assumed to be point-like and to be situated at the origin. As the *s*-electron wave function diverges in this limit, we have modeled the nucleus as a uniformly charged sphere of radius R_n ($R_n = C \cdot A^{1/3}$) for an isotope of atomic mass *A*, and *C* = 1.25 fm (Fernbach 1958). Rather than using the value $\rho = \rho(r = R_n)$, we take the average density, $\langle \rho \rangle = \frac{4 \cdot \pi}{V_n} \int_{R_0}^{R_n} \rho(r) \cdot r^2 dr$, evaluated from the radial point R_0, which is chosen to lie very close to the origin.

We have performed calculations assuming a paramagnetic state (see Section 5.4.3.2.3 for the discussion). For the LSDA calculations it was simulated by means of disordered local moments (DLM) (Gyorffy et al. 1985). The DLM state was treated using the coherent potential approximation (CPA) within the EMTO framework (Vitos et al. 2001). The magnitudes of the local moments were fixed to 0

(corresponding to non-magnetic calculations), 0.5, 1.0, and 1.5 µB in the entire volume range. We also used values determined self-consistently as a function of volume using the method developed recently (Ruban et al. 2007), which includes longitudinal spin fluctuations in a single-site mean-field approximation. Within the longitudinal spin fluctuation theory only the so-called on-site longitudinal spin fluctuation energy, *E(m)*, is calculated by a constrained DFT approach with electronic excitations at temperature T. Then, the average value of the magnetic moment, *<m>*, is determined using the corresponding partition function, Z_m, assuming that there is full coupling of the transverse and longitudinal degrees of freedom: $\langle m \rangle = \frac{1}{Z_m} \int m^3 \cdot e^{\frac{-E(m)}{k_B \cdot T}} dm \; ; Z_m = \int m^2 \cdot e^{\frac{-E(m)}{k_B T}}$. The resulting average magnetic moments are shown in Fig. 5.4.10 as a function of volume at 300 K.

Fig. 5.4.11 shows the calculated isomer shift as a function of unit cell volume in Fe, which is also compared to experimental measurements of the central shift. Using LDA, the trends of the obtained isomer shift follows the experimental central shift, and the shift due to *bcc-hcp* transition is also seen. However, the anomaly observed in the experimental central shift around the unit cell volume of 65 a.u.^{3} / atom is not seen in the calculated isomer shift, regardless of the assumed magnetic state.

Within the LDA+DMFT technique we obtain a slight offset with respect to the LDA data. This offset is far greater than the statistical fluctuations of the isomer shift during the computational iterations, which are indicated by errorbars in Fig. 5.4.11. The error bars correspond to +/- 2 standard deviations of the obtained isomer shift during the final ten iterations. In any case, the central shift anomaly is not seen in this case either. Therefore, it should be attributed to the peculiarity of the second-order Doppler shift (Potzel et al. 1995).
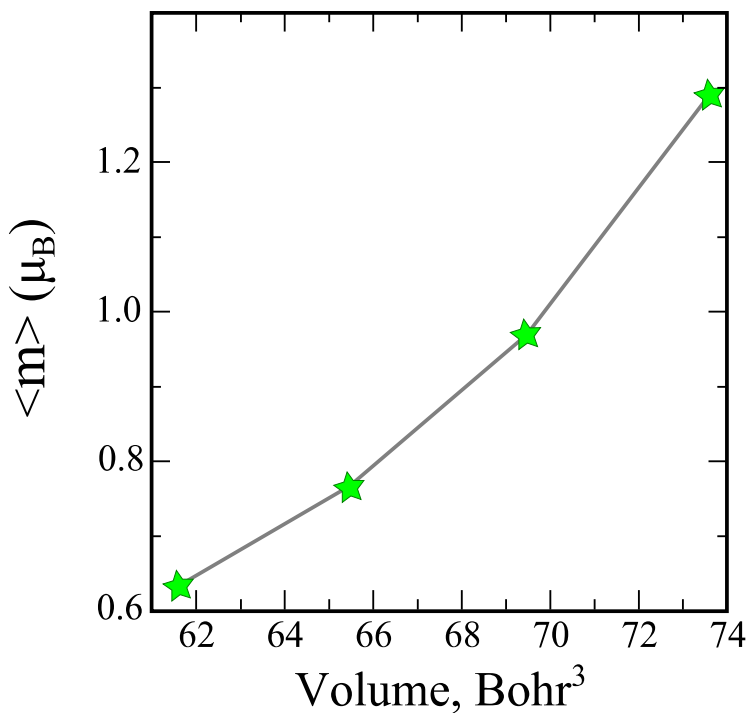
Fig. 5.4.10:

Average magnetic moments in the paramagnetic state of *hcp* Fe at T=300K as a function of volume per atom (in Bohr^3), as calculated by means of the longitudinal spin fluctuation theory.
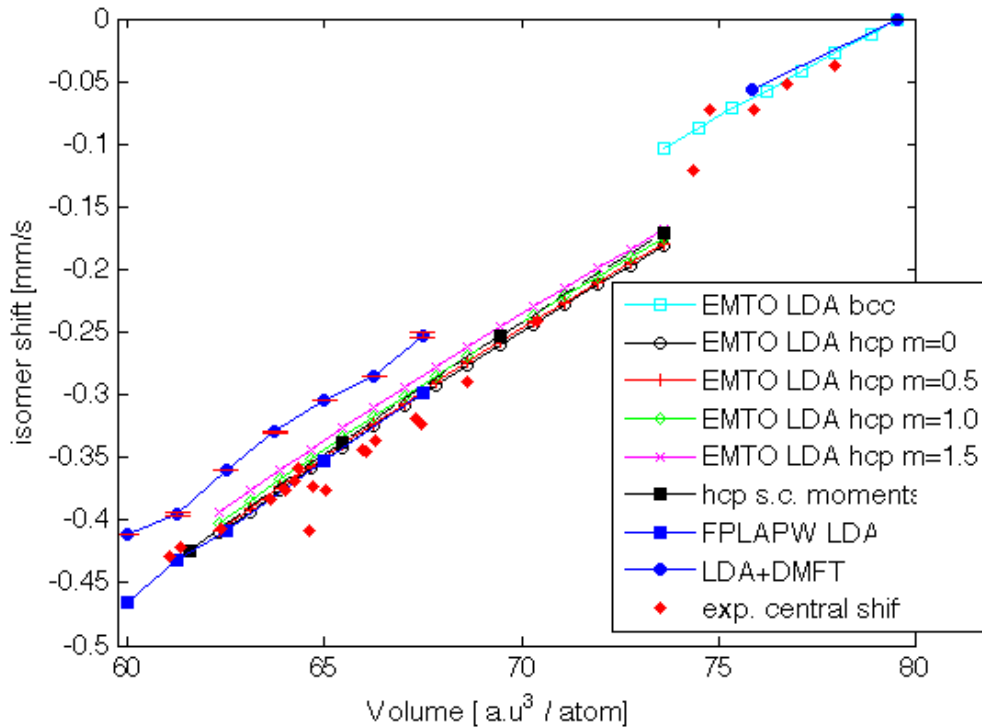
Fig. 5.4.11:

Calculated Mössbauer isomer shifts in Fe obtained within different approximations as a function of volume, compared to experimental measurements of the central shift (red solid diamonds). Results for the *bcc* phase (open cyan squares) are shown as obtained using the EMTO-LDA method. Calculations for the *hcp* phase include a non-magnetic state within the LDA based on the EMTO (open black circles) and FPLAPW methods (blue solid squares), as well as paramagnetic states based on the EMTO method with local magnetic moments 0.5 μB (red plus-signs), 1.0 μB (green open diamonds), and 1.5 μB (pink crosses) and self-consistent moments (Fig. 5.4.10) obtained by spin-fluctuation theory (black squares). We also present results obtained using the LDA+DMFT method (blue filled circles). The error bars correspond to +/- 2 standard deviations of the obtained isomer shift in the LDA+DMFT iterations. All shifts are relative to a reference point (filled cyan, red dot) which was recalculated within all above methods for a correct evaluation of the shifts.

5.4.3.2.7. Effective electron interaction parameters

The strength of electron repulsion is evaluated in the constrained random-phase-approximation (cRPA) method (Aryasetiawan et al. 2004, Miyake and Aryasetiawan 2008). The electronic structure is obtained by the full-potential LMTO method (Methfessel et al. 2000) in the framework of density functional theory within the local density approximation. A *spdf+spd* basis and 8·8·8 *k*-mesh are used. From the obtained electronic structure, the partially screened Coulomb interaction $Wr(\mathbf{r},\mathbf{r'})$ is computed in the cRPA, where *d-d* screening channels are excluded to avoid double counting of screening effects. The *d-d* screening is defined by the disentangled band structure (Georges et al. 1996) using the maximally localized Wannier function (MLWF) (Marzari and Vanderbilt 1997). The Coulomb (*U*) and

exchange (J) interaction matrices are obtained as matrix elements of Wr($\mathbf{r},\mathbf{r'}$) in the MLWF basis. The matrices are then spherically averaged through the Slater integrals (Miyake et al. 2009).

The calculated Coulomb interaction matrices are well approximated by a spherically-symmetric form with the parameter U (or the Slater parameter F_0) equal to 3.15, 3.04, and 3.37 eV and the Hund's rule coupling J equal to 0.9, 0.9 and 0.93 eV for *bcc, fcc,* and *hcp* phases, respectively.

5.5. Portable laser-heating system for diamond anvil cells.

L. Dubrovinsky,[a] K. Glazyrin,[a] C. McCammon,[a] O. Narygina,[a] E. Greenberg,[a] S. Übelhack,[a] A. I. Chumakov,[b] S. Pascarelli,[b] V. Prakapenka,[c] J. Bock[d] and N. Dubrovinskaia[e]

[a]*Bayerisches Geoinstitut, Universität Bayreuth, Bayreuth, Germany,* [b]*European Synchrotron Radiation Facility, Grenoble, France,* [c]*GeoCARS, University of Chicago, USA,* [d]*Precitek KG, Germany, and* [e]*Universität Heidelberg, Heidelberg, Germany.*

5.5.1 Abstract

The diamond anvil cell (DAC) technique coupled with laser heating has become the most successful method for studying materials in the multimegabar pressure range at high temperatures. However, so far all DAC laser-heating systems have been stationary: they are linked either to certain equipment or to a beamline. Here, a portable laser-heating system for DACs has been developed which can be moved between various analytical facilities, including transfer from in-house to a synchrotron or between synchrotron beamlines. Application of the system is demonstrated in an example of nuclear inelastic scattering measurements of ferropericlase $(Mg_{0.88}Fe_{0.12})O$ and h.c.p.-$Fe_{0.9}Ni_{0.1}$ alloy, and x-ray absorption near-edge spectroscopy of $(Mg_{0.85}Fe_{0.15})SiO_3$ majorite at high pressures and temperatures. Our results indicate that sound velocities of h.c.p.-$Fe_{0.9}Ni_{0.1}$ at pressures up to 50 GPa and high temperatures do not follow a linear relation with density.

5.5.2 Introduction

The diamond anvil cell (DAC) technique initiated in the late 1950s provides opportunities for high-pressure researchers with Mössbauer, infrared and Raman spectroscopy, resistivity measurements, x-ray diffraction and inelastic scattering (Eremets 1996). During the last few decades the DAC technique has become the most successful method of pressure generation capable of working in the multimegabar pressure range (Duffy 2005, Dubrovinsky et al. 2007, Dewaele et al. 2007). However, there are still a number of problems related to high-temperature experiments in DACs. There are two major methods of heating in DACs: laser and electrical (Eremets 1996, Dubrovinskaia and Dubrovinsky 2005). Electrical heating is very efficient at temperatures below #1000 K at pressures over 250 GPa, but laser-heating experiments become very demanding if higher temperatures are required (Dubrovinskaia and Dubrovinsky 2005). Laser-heating techniques cover a wide P–T field: P > 200 GPa, T = 1300–5000 K (Hirose 2006, Dewaele et al. 2007, Dubrovinsky et al. 2007). The sample preparation for laser-heating experiments is relatively easy and there is practically no risk to the diamonds owing to heating. There are numerous DAC laser-heating facilities in geo-, material-, physics- and chemistry-oriented laboratories (including the Bavarian Geoinstitute), and there are a number of examples of successful coupling of an *in situ* laser-heating system with synchrotron radiation facilities, including specialized beamlines at the third-generation synchrotrons: European Synchrotron Radiation Facility (ESRF), Advanced Photon Source (APS) and SPring-8 (Shen et al. 2001, Hirose 2006, Schultz et al. 2005, Prakapenka et al. 2008). However, so far all existing DAC laser-heating systems are stationary: they are

linked either to certain equipment (an optical or Raman spectrometer, for example) or to a beamline. Studies of various physical properties and chemical reactions at high pressures and temperatures in DACs require mobility of the laser-heating system; for example, the ability to move laser-heating equipment (preferably together with the same DAC, at the same pressure) between different analytical facilities, including transfer from in-house to a synchrotron or between synchrotron beamlines. Here we report on the design, mode of operation and some examples of application of a portable laser-heating system for DACs.

5.5.3 Design of a portable laser-heating system for DACs

The system consists of two major components: the source of laser light and the universal laser-heating head (UniHead) (Fig. 5.5.1 and Fig. 5.5.2). As a laser source we tested two SPI Lasers UK models, a G3 (30 W fiber-coupled pulse laser, weight 9 kg, excitation wavelength 1064 nm) and a SPI100 modulated high-power fiber laser (100 W, weight 40 kg, excitation wavelength 1064 nm). The 30 W pulse laser was used only to verify (successfully) that all optical components (see below) could sustain high-peak power up to 300 W at 50 kHz repetition rate; all results presented in this paper were obtained using the SPI100 laser.
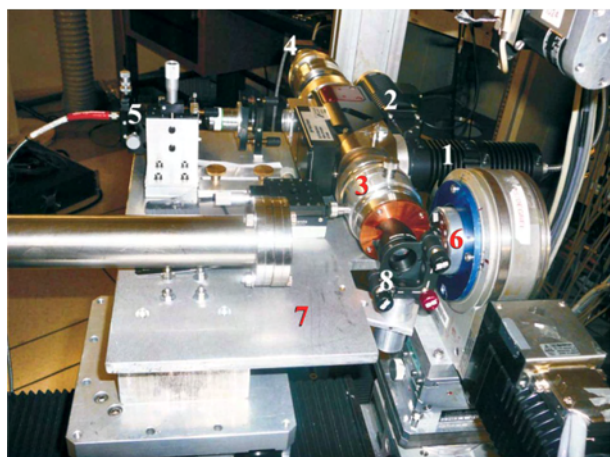
(a)

Fig. 5.5.1:

The universal laser-heating head (UniHead) mounted at beamline ID24 (a) for x-ray absorption near-edge spectroscopy measurements and at beamline ID18 (b) at ESRF (Grenoble, France) (inset in upper left corner) for nuclear inelastic scattering experiments in a large side opening DAC (inset in bottom left corner). **1**, connector for the SPI100 fibre laser; **2**, illumination unit; **3**, lenses unit for focusing of the incoming laser light; **4**, digital video camera; **5**, module for spectroscopic measurements; **6**, DAC mounted inside the holder; **7**, mounting plate; **8**, holder for a carbon laser mirror.
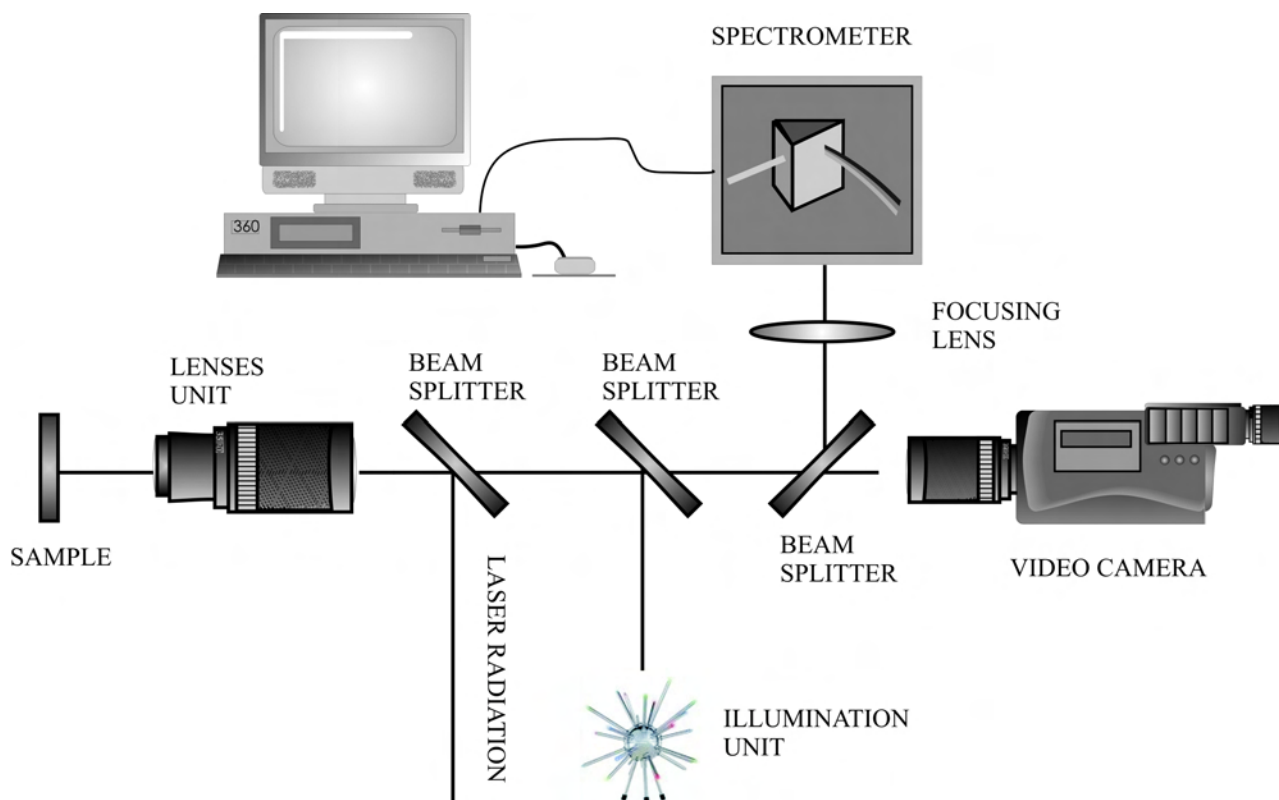
Fig. 5.5.2:

Schematic diagram of optical components of the UniHead.

The UniHead is based on the finite cutting laser head produced by Precitec KG (Germany) (weight ~4.5 kg). Originally the FCS (fine cutting system) was developed for three-dimensional cutting, cutting of filigree contours for the medicine industry, and applications in the fine mechanics and watch industry. It could work with a maximum laser power of 500 W for wavelengths of 1030–1090 nm (Nd:YAG, disc and fiber optical lasers).

The functions of the UniHead in the portable laser-heating system are to focus incoming laser light onto the sample within the DAC, to provide illumination by white light for observation of the sample in the DAC, and to give access for optical spectroscopic measurements (multiwavelength spectroradiometry, ruby fluorescence measurements, Raman spectroscopy etc.).

For focusing of the 1064 nm laser radiation, the UniHead employs a bending mirror (which also acts as a beam splitter transparent for light within the 400–900 nm wavelength range) and a set of lenses with a 80 mm working distance. The position of the mirror and the lenses can be adjusted in order to achieve an optimum (circular) beam shape and its centring with respect to the optical axis of the instrument. With a beam diameter of ~3 mm produced by the SPI100 laser, the distribution of intensity has a Gaussian shape with a half width at half-maximum of ~30 mm and a focus depth of ~10 mm at the focal position, whereas if the ~2 beam expander is used the beam size increases to ~60 mm and the focus depth is ~3–4 mm. Note that, although we did not conduct actual tests with laser-beam shapers (Prakapenka et al. 2008), it appears to be a straightforward strategy if one would like to modify the laser-beam intensity profile delivered by the UniHead.

Illumination of the sample is achieved owing to a built-in halogen 50 W lamp. Through the lens, the diffuser and the beam splitter it delivers a homogeneous light stream to the sample.

For observation of the sample in the DAC and for the process of laser-heating we use a high-resolution GigE uEye (SUXGA, 2048x1536) digital camera. The software of the digital camera makes it possible to enlarge a part of the observed area, and to mark and to trace a certain position in the image, which is very useful for alignment of the system.

The module for spectroscopic measurements exploits the optical access window used in the original (industrially produced FCS by Precitec KG) system for control of cutting processes (Fig. 5.5.1 and 5.5.2). The module includes two *x50* objectives separated by a pinhole in confocal configuration (Fig. 5.5.3). With a pinhole of 50 μm in diameter the observation area reduces to about 5 μm, which is several times smaller than the size of a laser beam spot. One of the objectives is mounted on a small three-dimensional stage and coupled with an optical fiber. The second objective is mounted on a small two-dimensional tilt-stage for alignment purposes. One end of the laboratory-grade splitter optical fiber assembly (Ocean Optics) is connected to a small solid-state 100 mW 532 nm laser (used for exciting ruby fluorescence), and the other is attached to the Ocean Optics QE65000 spectrometer (which is primarily used for measurements of the thermal radiation emitted by a laser-heated sample, but also could be used either for ruby fluorescence measurements, or for Raman spectroscopy in a laser-heated cell).
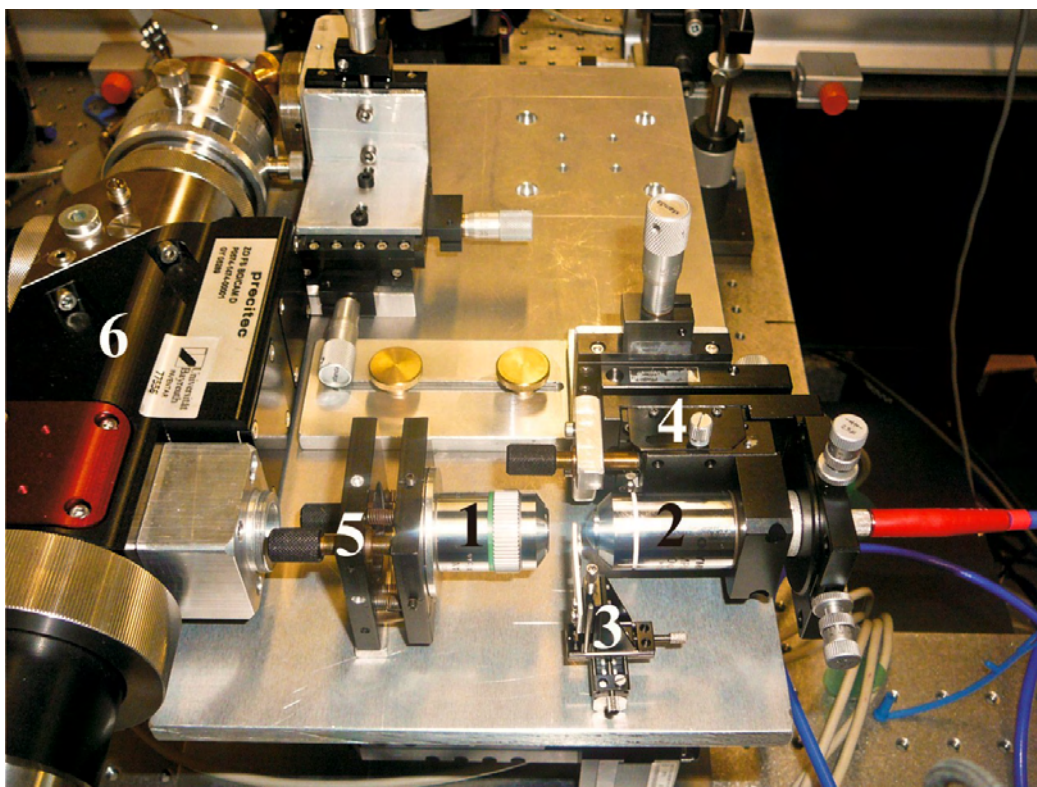
Fig. 5.5.3:

Module for spectroscopic measurements attached to the UniHead (6), where 1 and 2 are *x50* objectives mounted on 3D- (4) and 2D- tilt (5) stages. Pinhole is mounted on a miniature 3D stage (3).

5.5.4 Mode of operation

Owing to the modular construction, the portable laser-heating system can be used in different modifications for heating a sample in an alone-standing DAC or in a cell coupled directly to the UniHead with 'normal' (optical axes of the DAC and the UniHead coincide) or 'perpendicular' (90° between optical axes of the DAC and the UniHead; Fig. 5.5.2 and 5.5.4) geometries, with or without a spectroscopic or radiospectrometric module. However, the first step in the work with any modifications of the system is the alignment of the laser position in the DAC. The SPI100 laser is equipped with a low power (1 mW) red (735 nm) guide laser. It greatly simplifies the primary location of the heated area, but owing to construction peculiarities of optical fibers and optics the beam size of the guide laser at the focal point is ~500 μm in diameter. For precise location of the heated spot we use a metal foil (mostly Pt) or a polished block of pyrophyllite ('pipestone'). A laser power as low as 1–2 W is usually sufficient to form a bright glowing spot. A focusing lens incorporated into the UniHead in front of the digital camera (Fig. 5.5.2) should be adjusted until a clear and sharp image of a heated spot appears on the computer screen and then the centre of the spot is marked using a special software option.

In order to align the spectrometer, one of the ends of the splitter optical fiber assemblage is attached to the visible (in our experiments 532 nm) diode laser and its spot is focused and placed exactly at the position of the center of the heated area using the adjustment screws of objectives of the module for spectroscopic measurements (Fig. 5.5.3).
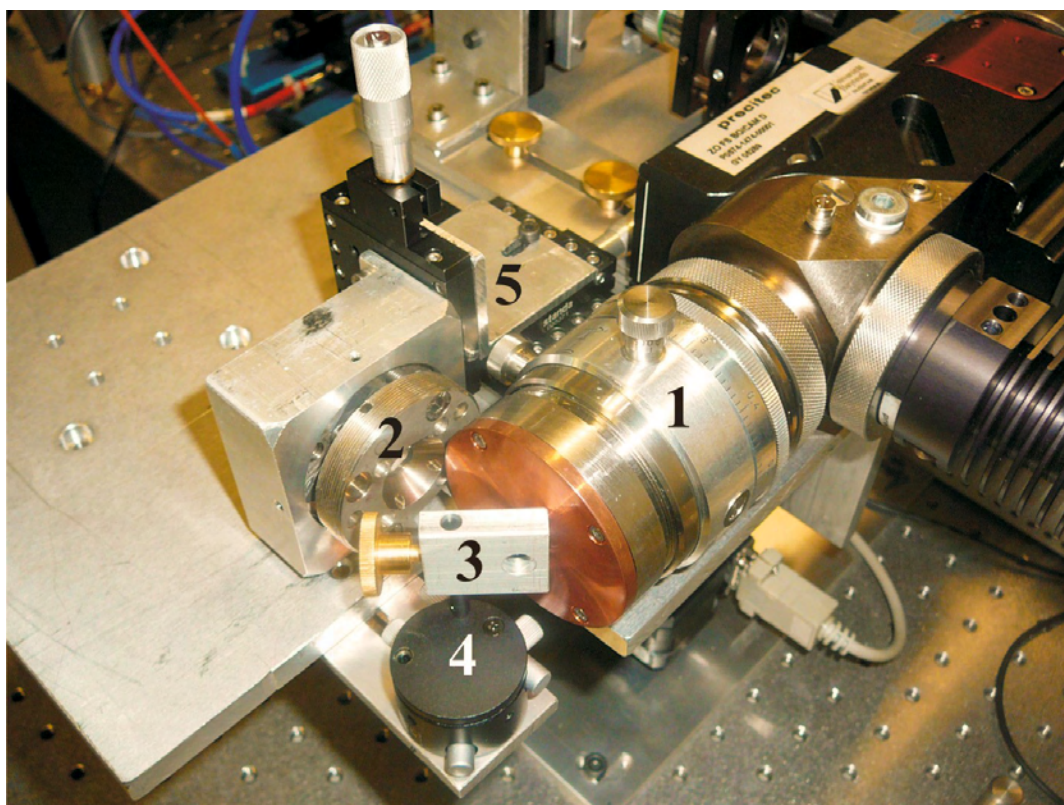
Fig. 5.5.4:

The UniHead (1) and DAC (2) in "perpendicular" (90° between optical axes of the DAC and UniHead) geometry mounted on an aluminum plate. (3 – the holder for a diamond laser mirror; 4-the rotary stage; 5 – the 3D mechanical stage for DAC positioning).

For the case of the normal configuration no further alignment is necessary. For the perpendicular geometry (Fig. 5.5.2 and 5.5.4) a glassy carbon or diamond mirror (Diamond Material, 10 mm diameter, 0.3 mm thick, Pt coated) should be adjusted by a miniature three-dimensional rotary stage (Edmund Scientific) until the shape of the heated spot becomes ideally circular.

It is important to underline that the assembly from components and the full alignment of the portable laser heating system is rather simple and can be done even by an inexperienced user within one hour.

5.5.5 Examples of application of the portable laser-heating system

The portable laser-heating system has been successfully used at the Bayerisches Geoinstitut in-house for routine experiments with DACs for samples annealing, melting experiments, Raman spectroscopy in laser-heated DACs, measurements of electrical resistance in DACs at high pressures and temperatures etc.

The clearest test of portability of our system was an experiment performed at beamline ID18 (Rüffer & Chumakov, 1996) at the ESRF. The whole system was transferred from Germany to France in a car, and then mounted and aligned in a hutch of beamline ID18 during about 2 h.

The experiments were performed during the hybrid and the 16-bunch modes of the storage-ring operation. The beam was focused to about 4 μm·20 μm using a Kirkpatrick–Baez mirror, and a MAR CCD detector was installed on the beamline to enable collection of x-ray diffraction data at the same pressure–temperature conditions as the nuclear inelastic scattering (NIS) and nuclear forward scattering (NFS) spectra. For NIS data collection the DAC was oriented with the gasket horizontal to the beam (i.e. both the beam and the incoherent signal passed through the gasket; Fig. 5.5.1), while NFS data were collected in either horizontal or vertical geometry of the DAC (or both). The procedure of data collection and analysis has been described in previous publications (Chumakov et al. 1996, Chumakov and Sturhahn 1999, McCammon et al. 2008).

The NIS of geophysically and geochemically important materials, i.e. the iron–nickel alloy $Fe_{0.9}Ni_{0.1}$, ferropericlase $(Mg_{0.875}Mg_{0.125})O$ and silicate perovskite $(Mg_{0.88}Fe_{0.12})SiO_3$, were studied at pressures over 100 GPa and temperatures up to 2000 K. A detailed description of observations and analysis of the results will be published elsewhere, while here our goal is to illustrate the performance of the new portable laser heating system.

Fig. 5.5.5 shows an example of the energy dependence of NIS spectra of $Mg_{0.88}Fe_{0.12}O$ ferropericlase at 37 (2) GPa and different temperatures. The material was compressed in a specially designed cell (Fig. 5.5.1, inset) in a Be gasket, and the pressure was determined by ruby fluorescence and/or the ferropericlase thermal equation of state (Fei et al. 2007b). The UniHead has a 50 mm distance between the end of optical components and the focal plane of the laser allowing a DAC with a large (37 mm) opening in the gasket plane (the distance between the end of the DAC and the sample is 47 mm) to be used. There is a remarkable increase in relative intensities of the Stokes and anti-Stokes parts of the NIS spectra (Fig. 5.5.5) at high temperature. Note that NIS measurements are time consuming and the
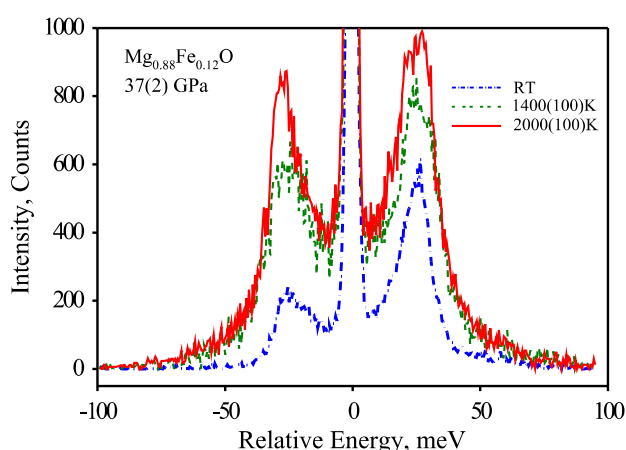
Fig. 5.5.5:

Nuclear inelastic scattering spectra of ferropericlase $(Mg_{0.88}Fe_{0.12})O$ at 37(2) GPa and different temperatures at the ID18 beam line at ESRF (Grenoble, France) in a laser-heated diamond anvil cell. Temperatures are derived from analysis of the intensities of the Stock and anti-Stocks parts of the spectra.
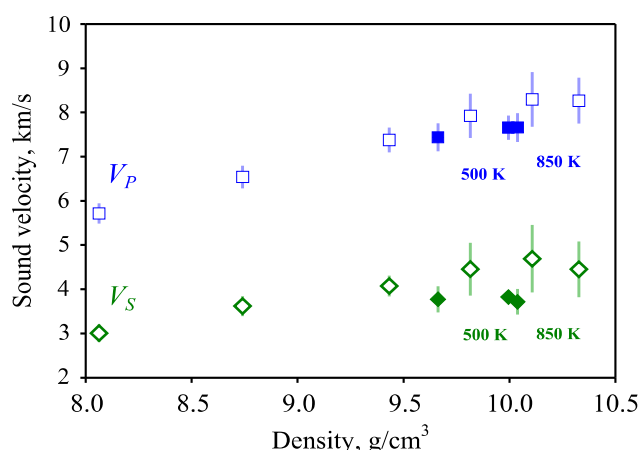
Fig. 5.5.6:

Experimental results of aggregate compressional VP and shear VS sound velocities of h.c.p.-$Fe_{0.9}Ni_{0.1}$ alloy at high pressures and ambient (empty symbols) and high (solid symbols) temperatures. Temperatures are given next to solid symbols.

portable laser-heating system allowed temperatures of the order of 2000 K to be maintained for two hours continuously.

Measurements of the energy dependency of NIS spectra of $Fe_{0.9}Ni_{0.1}$ alloy allowed us to extract information on changes of the sound velocities at high pressures and elevated temperatures. Combined with x-ray diffraction studies of the thermal equation of state (Dubrovinsky et al. 2007), this information is essential to model the dependence of the sound velocity as a function of density (Lin et al., 2005). According to Birch's law, the sound velocities of materials are linearly scaled with density, and this approximation is widely applied by the geophysical community for extrapolation of the results of experiments at ambient temperature and middle (a few dozens of GPa) pressure range to conditions of deep Earth interiors. However, it was demonstrated that the behavior of h.c.p.-Fe at high temperatures significantly deviates from Birch's law (Lin et al. 2005b). Fig. 5.5.6 shows that sound velocities of h.c.p.-$Fe_{0.9}Ni_{0.1}$ alloy decrease substantially with increasing temperature under moderately high pressures and, as in the case of h.c.p.-Fe, do not follow a linear relation with the density, thus confirming previous results.

At the energy-dispersive x-ray absorption spectroscopy beamline ID24 at the ESRF the portable laser-heating system was used for Fe K-edge XANES of $(Mg_{0.85}Fe_{0.15})SiO_3$ majorite at high pressure and temperature. For in situ high pressure micro-XANES measurements in the DAC we used diamonds with 250 μm culet size and ~1.5 mm thickness. For pressure calibration and evaluation of the pressure gradient we used small ruby chips that were loaded into the cell along with the sample. We noted that strong ~7 keV x-ray radiation is sufficient to excite ruby fluorescence and we were able to measure the
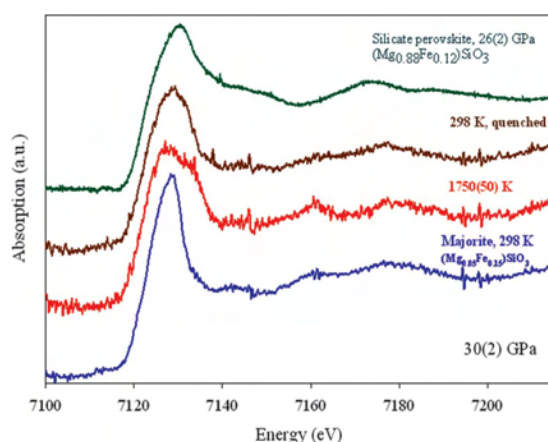
Fig. 5.5.7:

XANES spectra of $(Mg_{0.85}Fe_{0.15})SiO_3$ majorite at 30 (2) GPa before, during and after laser-heating. Upper spectra are from $(Mg_{0.88}Fe_{0.12})SiO_3$ silicate perovskite collected at ambient temperature at 26 (2) GPa (Narygina et al., 2009).

pressure using the spectroscopic module of UniHead. Temperatures were measured spectro-radiometrically during data collection.

The beam was focused horizontally using a curved polychromator Si(111) crystal in Bragg geometry and vertically with a bent Si mirror placed at 2.8 mrad with respect to the direct beam (Narygina et al. 2009). The Bragg diffraction peaks arising from the diamond anvils were removed from the energy range of interest by changing the orientation of the DAC and following in real time the intensity of the transmitted beam on a two-dimensional detector. The measured XANES spectra were analyzed using the VIPER program. The flat part of the pre-edge region of the spectrum was fitted to the Victoreen function ($F = a + b \cdot E^{-3}$, where E is the absorption energy, and *a* and *b* are fit parameters) and this baseline was extended over the entire energy region. The postedge jump in x-ray absorption was then normalized to unity.

In experiments at beamline ID24 we employed UniHead in the perpendicular geometry (Fig. 5.5.1 and 5.5.2) with a carbon mirror. Glassy carbon used as a substrate for silver coating does not introduce any structure into XANES spectra, but the thickness of the mirror appears to be critical for success of the experiment; with a 2 mm-thick mirror we were not able to collect any spectra, while with a mirror of thickness 0.9 mm the quality of the spectra are acceptable (Fig. 5.5.7) and we could clearly observe a transition from $(Mg_{0.85}Fe_{0.15})SiO_3$ majorite to silicate perovskite at 30 (2) GPa and 1750 (50) K.

5.5.6 Conclusions

We have developed a portable laser-heating system which consists of two major components: the fiber laser and the universal laser-heating head (UniHead). The main components of the system are industrially produced, which makes its duplication to be a rather straightforward task. The modular construction of the portable laser-heating system allows its application in different modifications: for heating a sample in an alone-standing DAC or in a cell attached and moved together with the UniHead with normal (optical axes of the DAC and UniHead coincide) or perpendicular (90° between optical axes of the DAC and UniHead) geometries, with or without a spectroscopic module. The system has been tested for in-house routine experiments with laser-heated DACs (samples annealing, melting experiments, Raman spectroscopy in laser-heated DACs etc.) as well as for *in situ* high pressure high-temperature NIS and NFS studies at ESRF.

References

Abrikosov, I. A., A. E. Kissavos, F. Liot, B. Alling, S. I. Simak, O. Peil, and A. V. Ruban (2007), Competition between magnetic structures in the Fe rich fcc FeNi alloys, *Phys. Rev. B*, 76, 014434, doi:10.1103/PhysRevB.76.014434.

Agnor, C. (1999), On the Character and Consequences of Large Impacts in the Late Stage of Terrestrial Planet Formation, *Icarus*, 142, 219-237, doi:10.1006/icar.1999.6201.

Aichhorn, M., L. Pourovskii, and A. Georges (2011), Importance of electronic correlations for structural and magnetic properties of the iron pnictide superconductor LaFeAsO, *arXiv/1104.4361*, 1-7.

Aichhorn, M., L. Pourovskii, V. Vildosola, M. Ferrero, O. Parcollet, T. Miyake, A. Georges, and S. Biermann (2009), Dynamical mean-field theory within an augmented plane-wave framework: Assessing electronic correlations in the iron pnictide LaFeAsO, *Phys. Rev. B*, 80, 085101, doi:10.1103/PhysRevB.80.085101.

Akai, H., S. Blügel, R. Zeller, and P. H. Dederichs (1986), Isomer Shifts and Their Relation to Charge Transfer in Dilute Fe Alloys, *Phys. Rev. Lett.*, 56, 2407, doi:10.1103/PhysRevLett.56.2407.

Akimitsu, M., T. Mizoguchi, J. Akimitsu, and S. Furomoto (1983), Magnetic structure and magnetic properties of non-stoichiometric $Fe_{1-x}O$, *Journal of Physics and Chemistry of Solids*, 44, 497-505, doi:10.1016/0022-3697(83)90037-9.

Allègre, C. J., J.-P. Poirier, E. Humler, and A. W. Hofmann (1995), The chemical composition of the Earth, *Earth and Planetary Science Letters*, 134, 515-526, doi:10.1016/0012-821X(95)00123-T.

Anisimov, V. I., A. I. Poteryaev, M. A. Korotin, A. O. Anokhin, and G. Kotliar (1997), First-principles calculations of the electronic structure and spectra of strongly correlated systems: dynamical mean-field theory, *J. Phys.: Condens. Matter*, 9, 7359-7367, doi:10.1088/0953-8984/9/35/010.

Antonangeli, D., J. Siebert, C. M. Aracne, D. L. Farber, A. Bosak, M. Hoesch, M. Krisch, F. J. Ryerson, G. Fiquet, and J. Badro (2011), Spin Crossover in Ferropericlase at High Pressure: A Seismologically Transparent Transition?, *Science*, 331, 64-67, doi:10.1126/science.1198429.

Aryasetiawan, F., M. Imada, A. Georges, G. Kotliar, S. Biermann, and A. I. Lichtenstein (2004), Frequency-dependent local interactions and low-energy effective models from electronic structure calculations, *Phys. Rev. B*, 70, 195104, doi:10.1103/PhysRevB.70.195104.

Aubert, J., S. Labrosse, and C. Poitou (2009), Modelling the palaeo-evolution of the geodynamo, *Geophysical Journal International*, 179, 1414-1428, doi:10.1111/j.1365-246X.2009.04361.x.

Badro, J., G. Fiquet, F. Guyot, J.-P. Rueff, V. V. Struzhkin, G. Vankó, and G. Monaco (2003), Iron

References

Partitioning in Earth's Mantle: Toward a Deep Lower Mantle Discontinuity, *Science*, 300, 789-791, doi:10.1126/science.1081311.

Bassett, W., and M. Weathers (1986), Temperature measurement in laser heated diamond anvil cells, *Physica B+C*, 139-140, 900-902, doi:10.1016/0378-4363(86)90724-2.

Battle, P. D., and A. K. Cheetham (1979), The magnetic structure of non-stoichiometric ferrous oxide, *J. Phys. C: Solid State Phys.*, 12, 337-345, doi:10.1088/0022-3719/12/2/021.

Baudelet, F., S. Pascarelli, O. Mathon, J.-P. Itié, A. Polian, and J.-C. Chervin (2010), Absence of abrupt pressure-induced magnetic transitions in magnetite, *Phys. Rev. B*, 82, doi:10.1103/PhysRevB.82.140412.

Beach, K. S. D. (2004), Identifying the maximum entropy method as a special limit of stochastic analytic continuation, *cond-mat/0403055*.

Belonoshko, A. B., R. Ahuja, and B. Johansson (2003), Stability of the body-centred-cubic phase of iron in the Earth's inner core, *Nature*, 424, 1032-1034, doi:10.1038/nature01954.

Bertka, C., and Y. Fei (1998), Density profile of an SNC model Martian interior and the moment-of-inertia factor of Mars, *Earth and Planetary Science Letters*, 157, 79-88, doi:10.1016/S0012-821X(98)00030-2.

Besson, J., R. Nelmes, G. Hamel, J. Loveday, G. Weill, and S. Hull (1992), Neutron powder diffraction above 10 GPa, *Physica B: Condensed Matter*, 180-181, 907-910, doi:10.1016/0921-4526(92)90505-M.

Bina, C. R., and G. Helffrich (1994), Phase transition Clapeyron slopes and transition zone seismic discontinuity topography, *J. Geophys. Res.*, 99, 15853-15860, doi:10.1029/94JB00462.

Birch, F. (1952), Elasticity And Constitution Of The Earth's Interior, *J. Geophys. Res.*, 57, 227-286, doi:10.1029/JZ057i002p00227.

Blaha, P., K. Schwarz, G. Madsen, D. Kvasnicka, and J. Luitz (2002), *WIEN2k, An augmented Plane Wave + Local Orbitals Program for Calculating Crystal Properties*, Techn. Universitat Wien, Wien, Austria.

Blakely, R. J., T. M. Brocher, and R. E. Wells (2005), Subduction-zone magnetic anomalies and implications for hydrated forearc mantle, *Geol*, 33, 445, doi:10.1130/G21447.1.

Blöchl, P. E., O. Jepsen, and O. K. Andersen (1994), Improved tetrahedron method for Brillouin-zone integrations, *Phys. Rev. B*, 49, 16223, doi:10.1103/PhysRevB.49.16223.

Bocian, A., C. L. Bull, H. Hamidov, J. S. Loveday, R. J. Nelmes, and K. V. Kamenev (2010), Gas loading apparatus for the Paris-Edinburgh press, *Rev. Sci. Instrum.*, 81, 093904, doi:10.1063/1.3480555.

Boehler, R. (1993), Temperatures in the Earth's core from melting-point measurements of iron at high static pressures, *Nature*, 363, 534-536, doi:10.1038/363534a0.

References

Boehler, R., and K. De Hantsetters (2004), New anvil designs in diamond-cells, *International Journal of High Pressure Research*, 24, 391-396, doi:10.1080/08957950412331323924.

Boehler, R., H. G. Musshoff, R. Ditz, G. Aquilanti, and A. Trapananti (2009), Portable laser-heating stand for synchrotron applications, *Rev. Sci. Instrum.*, 80, 045103, doi:10.1063/1.3115183.

Bouvier, A., and M. Wadhwa (2010), The age of the Solar System redefined by the oldest Pb–Pb age of a meteoritic inclusion, *Nature Geoscience*, 3, 637-641, doi:10.1038/ngeo941.

Bragg, W. L. (1913), The structure of some crystals as indicated bytheir diffraction of X rays., *Proceedings of the Royal Society (London)*, A89, 248-277.

Brand, R. A. (1990), *NORMOS programs, version 1990. The NORMOS program is available from Wissel GmbH, D-82319 Starnberg, Germany.*

Burns, R. (2005), *Mineralogical applications of crystal field theory*, 2nd ed., Cambridge University Press, Cambridge.

Cameron, A. G. W. (1973), Abundances of the elements in the solar system, *Space Sci Rev*, 15, doi:10.1007/BF00172440.

Catalli, K., S.-H. Shim, V. Prakapenka, J. Zhao, W. Sturhahn, P. Chow, Y. Xiao, H. Liu, H. Cynn, and W. J. Evans (2010), Spin state of ferric iron in $MgSiO_3$ perovskite and its effect on elastic properties, *Earth and Planetary Science Letters*, 289, 68-75, doi:10.1016/j.epsl.2009.10.029.

Chen, Y.-L., and D.-P. Yang (2007), *Mössbauer effect in lattice dynamics : experimental techniques and applications*, Wiley-VCH ;;John Wiley distributor], Weinheim ;[Chichester.

Chervin, J. C., B. Canny, J. M. Besson, and P. Pruzan (1995), A diamond anvil cell for IR microspectroscopy, *Rev. Sci. Instrum.*, 66, 2595, doi:10.1063/1.1145594.

Chumakov, A. I., R. Rüffer, A. Q. R. Baron, H. Grünsteudel, and H. F. Grünsteudel (1996), Temperature dependence of nuclear inelastic absorption of synchrotron radiation in alpha -^{57}Fe, *Phys. Rev. B*, 54, R9596, doi:10.1103/PhysRevB.54.R9596.

Chumakov, A. I., and W. Sturhahn (1999), Experimental aspects of inelastic nuclear resonance scattering, *Hyperfine Interactions*, 123-124, 781-808, doi:10.1023/A:1017052730094.

Clement, B. M., and L. Stixrude (1995), Inner core anisotropy, anomalies in the time-averaged paleomagnetic field, and polarity transition paths, *Earth and Planetary Science Letters*, 130, 75-85, doi:16/0012-821X(94)00264-Y.

Cort, G., R. D. Taylor, and J. O. Willis (1982), Search for magnetism in hcp ε-Fe, *J. Appl. Phys.*, 53, 2064, doi:10.1063/1.330745.

Crowhurst, J. C., A. F. Goncharov, and J. M. Zaug (2005), Direct measurements of the elastic properties of iron and cobalt to 120 GPa—implications for the composition of earth's core, in *Advances in High-Pressure Technology for Geophysical Applications*, pp. 3-23, Elsevier.

References

Crysalis RED (2006), *Oxford Diffraction CrysAlis RED*, Crysalis, Oxford Diffraction Ltd.

Czyzdotyk, M. T., and G. A. Sawatzky (1994), Local-density functional and on-site correlations: The electronic structure of La_2CuO_4 and $LaCuO_3$, *Phys. Rev. B*, 49, 14211, doi:10.1103/PhysRevB.49.14211.

Darken, L. S., and R. W. Gurry (1945), The System Iron-Oxygen. I. The Wüstite Field and Related Equilibria, *Journal of the American Chemical Society*, 67, 1398-1412, doi:10.1021/ja01224a050.

Dedkov, Y., U. Rüdiger, and G. Güntherodt (2002), Evidence for the half-metallic ferromagnetic state of Fe_3O_4 by spin-resolved photoelectron spectroscopy, *Phys. Rev. B*, 65, doi:10.1103/PhysRevB.65.064417.

Dewaele, A., M. Mezouar, N. Guignot, and P. Loubeyre (2007), Melting of lead under high pressure studied using second-scale time-resolved x-ray diffraction, *Phys. Rev. B*, 76, 144106, doi:10.1103/PhysRevB.76.144106.

Dickson, D., and F. J. Berry (Eds.) (2005), *Mössbauer spectroscopy*, Digitally print. 1. paperb., Cambridge Univ. Press, Cambridge, UK.

Ding, Y., D. Haskel, S. Ovchinnikov, Y.-C. Tseng, Y. Orlov, J. Lang, and H.-K. Mao (2008), Novel Pressure-Induced Magnetic Transition in Magnetite (Fe_3O_4), *Phys. Rev. Lett.*, 100, doi:10.1103/PhysRevLett.100.045508.

Ding, Y., H. Liu, M. Somayazulu, Y. Meng, J. Xu, C. Prewitt, R. Hemley, and H.-K. Mao (2005a), Zone-axis x-ray diffraction of single-crystal $Fe_{1-x}O$ under pressure, *Phys. Rev. B*, 72, doi:10.1103/PhysRevB.72.174109.

Ding, Y. et al. (2005b), Variable pressure-temperature neutron diffraction of wüstite ($Fe_{1-x}O$): Absence of long-range magnetic order to 20 GPa, *Appl. Phys. Lett.*, 86, 052505, doi:10.1063/1.1852075.

Dobson, D. P., and J. P. Brodholt (2005), Subducted banded iron formations as a source of ultralow-velocity zones at the core–mantle boundary, *Nature*, 434, 371-374, doi:10.1038/nature03430.

Dobson, D. P., and S. D. Jacobsen (2004), The flux growth of magnesium silicate perovskite single crystals, *American Mineralogist*, 89, 807-811.

Dreibus, G., and H. Wanke (1987), Volatiles on Earth and Mars: A comparison, *Icarus*, 71, 225-240, doi:10.1016/0019-1035(87)90148-5.

Dubrovinskaia, N., and L. Dubrovinsky (2003), Whole-cell heater for the diamond anvil cell, *Rev. Sci. Instrum.*, 74, 3433, doi:10.1063/1.1578151.

Dubrovinskaia, N., and L. Dubrovinsky (2005), Internal and external electrical heating in diamond anvil cells, in *Advances in High-Pressure Technology for Geophysical Applications*, edited by J. Chen, Y. Wang, T. S. Duffy, G. Shen, and L. F. Dobrzhinetskaya, pp. 487-501, Elsevier,

References

Amsterdam.

Dubrovinsky, L. S., N. A. Dubrovinskaia, C. McCammon, G. K. Rozenberg, R. Ahuja, J. M. Osorio-Guillen, V. Dmitriev, H.-P. Weber, T. L. Bihan, and B. Johansson (2003), The structure of the metallic high-pressure Fe_3O_4 polymorph: experimental and theoretical study, *J. Phys.: Condens. Matter*, 15, 7697-7706, doi:10.1088/0953-8984/15/45/009.

Dubrovinsky, L. et al. (2010a), Single-crystal X-ray diffraction at megabar pressures and temperatures of thousands of degrees, *High Pressure Research*, 30, 620-633, doi:10.1080/08957959.2010.534092.

Dubrovinsky, L. et al. (2007), Body-Centered Cubic Iron-Nickel Alloy in Earth's Core, *Science*, 316, 1880-1883, doi:10.1126/science.1142105.

Dubrovinsky, L. et al. (2009), Portable laser-heating system for diamond anvil cells, *Journal of Synchrotron Radiation*, 16, 737-741, doi:10.1107/S0909049509039065.

Dubrovinsky, L., J.-F. Lin, and N. Dubrovinskaia (2010b), Mineral Physics of Earth Core: Iron Alloys at Extreme Condition, in *High-Pressure Crystallography*, vol. 0, edited by E. Boldyreva and P. Dera, pp. 35-41, Springer Netherlands, Dordrecht.

Duffy, T. S. (2005), Synchrotron facilities and the study of the Earth's deep interior, *Rep. Prog. Phys.*, 68, 1811-1859, doi:10.1088/0034-4885/68/8/R03.

Dziewonski, A., and D. L. Anderson (1981), Preliminary reference Earth model, *Physics of The Earth and Planetary Interiors*, 25, 297-356, doi:10.1016/0031-9201(81)90046-7.

Eremets, M. I. (1996), *High Pressure Experimental Methods*, Oxford University Press, USA.

Farrugia, L. J. (1999), WinGX suite for small-molecule single-crystal crystallography, *Journal of Applied Crystallography*, 32, 837-838, doi:10.1107/S0021889899006020.

Fegley, B. J. (2007), Venus, in *Treatise on Geochemistry*, edited by A. M. Davis, pp. 487-507, Elsevier.

Fei, Y., D. J. Frost, H.-K. Mao, C. T. Prewitt, and D. Häusermann (1999), In situ structure determination of the high-pressure phase of Fe_3O_4, *american Mineralogist*, 84, 203-206.

Fei, Y., A. Ricolleau, M. Frank, K. Mibe, G. Shen, and V. Prakapenka (2007a), High-Pressure Geoscience Special Feature: Toward an internally consistent pressure scale, *Proceedings of the National Academy of Sciences*, 104, 9182-9186, doi:10.1073/pnas.0609013104.

Fei, Y., L. Zhang, A. Corgne, H. Watson, A. Ricolleau, Y. Meng, and V. Prakapenka (2007b), Spin transition and equations of state of (Mg, Fe)O solid solutions, *Geophys. Res. Lett.*, 34, doi:10.1029/2007GL030712.

Fei, Y., L. Zhang, A. Corgne, H. Watson, A. Ricolleau, Y. Meng, and V. Prakapenka (2007c), Spin transition and equations of state of (Mg, Fe)O solid solutions, *Geophys. Res. Lett.*, 34, doi:10.1029/2007GL030712.

References

Fernbach, S. (1958), Nuclear Radii as Determined by Scattering of Neutrons, *Rev. Mod. Phys.*, 30, 414, doi:10.1103/RevModPhys.30.414.

Fiquet, G., F. Guyot, and J. Badro (2008), The Earth's Lower Mantle and Core, *Elements*, 4, 177-182, doi:10.2113/GSELEMENTS.4.3.177.

Forman, R. A., G. J. Piermarini, J. D. Barnett, and S. Block (1972), Pressure Measurement Made by the Utilization of Ruby Sharp-Line Luminescence, *Science*, 176, 284-285, doi:10.1126/science.176.4032.284.

Friák, M., A. Schindlmayr, and M. Scheffler (2007), *Ab initio* study of the half-metal to metal transition in strained magnetite, *New J. Phys.*, 9, 5-5, doi:10.1088/1367-2630/9/1/005.

Friedrich, W., P. Knipping, and M. Laue (1912), Interferenz-Erscheinungen bei Röntgenstrahlen, *Sitzungberichte der mathematischephysikalischen Klasse der Königlichen Bayerischen Akademie derWissenschaften zu München*, 303-322.

Frost, D. J. (2008), The Upper Mantle and Transition Zone, *Elements*, 4, 171-176, doi:10.2113/GSELEMENTS.4.3.171.

García, J., G. Subías, M. Proietti, H. Renevier, Y. Joly, J. Hodeau, J. Blasco, M. Sánchez, and J. Bérar (2000), Resonant "Forbidden" Reflections in Magnetite, *Phys. Rev. Lett.*, 85, 578-581, doi:10.1103/PhysRevLett.85.578.

Garg, A. B., V. Vijayakumar, and B. K. Godwal (2004), Electrical resistance measurements in a diamond anvil cell to 40 GPa on ytterbium, *Rev. Sci. Instrum.*, 75, 2475, doi:10.1063/1.1763255.

Gebhard, F. (2010), *The Mott Metal-Insulator Transition: Models and Methods*, 1st ed. Softcover of orig. ed. 1997 ed., Springer Berlin Heidelberg.

Georges, A., G. Kotliar, W. Krauth, and M. J. Rozenberg (1996), Dynamical mean-field theory of strongly correlated fermion systems and the limit of infinite dimensions, *Rev. Mod. Phys.*, 68, 13, doi:10.1103/RevModPhys.68.13.

Gilder, S., and J. Glen (1998), Magnetic Properties of Hexagonal Closed-Packed Iron Deduced from Direct Observations in a Diamond Anvil Cell, *Science*, 279, 72 -74, doi:10.1126/science.279.5347.72.

Goettel, K. A. (1988), *Mercury*, edited by F. Vilas, C. R. Chapman, and M. S. Matthews, University of Arizona Press.

Goncharov, A. F., B. D. Haugen, V. V. Struzhkin, P. Beck, and S. D. Jacobsen (2008), Radiative conductivity in the Earth's lower mantle, *Nature*, 456, 231-234, doi:10.1038/nature07412.

Gonser, U. (1975), *Mössbauer Spectroscopy*, 1st ed., Springer.

Goodman, J. (2000), Secular Instability and Planetesimal Formation in the Dust Layer, *Icarus*, 148, 537-549, doi:10.1006/icar.2000.6467.

References

Gould, J. L. (2011), Animal Navigation: Longitude at Last, *Current Biology*, 21, R225-R227, doi:10.1016/j.cub.2011.01.063.

Grønvold, F., S. Stølen, P. Tolmach, and E. F. J. Westrum (1993), Heat capacities of the wüstites $Fe_{0.9379}O$ and $Fe_{0.9254}O$ at temperatures T from 5 K to 350 K. Thermodynamics of the reactions: $xFe(s) + (1/4)Fe_3O_4(s) = Fe_{0.7500}+xO(s) = Fe_{1-y}O(s)$ at T ≈ 850 K, and properties of $Fe_{1-y}O(s)$ to T = 1000 K. Thermodynamics of formation of wüstite, *The Journal of Chemical Thermodynamics*, 25, 1089-1117, doi:10.1006/jcht.1993.1107.

Gyorffy, B. L., A. J. Pindor, J. Staunton, G. M. Stocks, and H. Winter (1985), A first-principles theory of ferromagnetic phase transitions in metals, *J. Phys. F: Met. Phys.*, 15, 1337-1386, doi:10.1088/0305-4608/15/6/018.

Haase, J., S. K. Goh, T. Meissner, P. L. Alireza, and D. Rybicki (2009), High sensitivity nuclear magnetic resonance probe for anvil cell pressure experiments, *Rev. Sci. Instrum.*, 80, 073905, doi:10.1063/1.3183504.

Haavik, C., S. Stølen, H. Fjellvåg, M. Hanfland, and D. Häusermann (2000), Equation of state of magnetite and its high-pressure modification: Thermodynamics of the Fe-O system at high pressure, *American Mineralogist*, 85, 514-523.

Hammersley, A. P. (1997), Fit2D. An introduction and overview., *ESRF Internal Report*, ESRF97HA02T (unpublished).

Hammersley, A. P. (1998), FIT2D V9.129 Reference Manual V3.1,

Hansen, T. C., P. F. Henry, H. E. Fischer, J. Torregrossa, and P. Convert (2008), The D20 instrument at the ILL: a versatile high-intensity two-axis neutron diffractometer, *Meas. Sci. Technol.*, 19, 034001, doi:10.1088/0957-0233/19/3/034001.

Hart, S., and A. Zindler (1986), In search of a bulk-Earth composition, *Chemical Geology*, 57, 247-267, doi:10.1016/0009-2541(86)90053-7.

Hastings, J., D. Siddons, U. van Bürck, R. Hollatz, and U. Bergmann (1991), Mössbauer spectroscopy using synchrotron radiation, *Phys. Rev. Lett.*, 66, 770-773, doi:10.1103/PhysRevLett.66.770.

Hiergeist, R., W. Andrä, N. Buske, R. Hergt, I. Hilger, U. Richter, and W. Kaiser (1999), Application of magnetite ferrofluids for hyperthermia, *Journal of Magnetism and Magnetic Materials*, 201, 420-422, doi:10.1016/S0304-8853(99)00145-6.

Hirose, K. (2006), Postperovskite phase transition and its geophysical implications, *Rev. Geophys.*, 44, doi:10.1029/2005RG000186.

Hohenberg, P., and W. Kohn (1964), Inhomogeneous Electron Gas, *Phys. Rev.*, 136, B864, doi:10.1103/PhysRev.136.B864.

Hollerbach, R., and C. A. Jones (1993), Influence of the Earth's inner core on geomagnetic fluctuations and reversals, *Nature*, 365, 541-543, doi:10.1038/365541a0.

References

Horuichi, H., E. Ito, and D. J. Weidner (1987), Perovskite-type $MgSiO_3$: Single-crystal X-ray diffraction study, *Am. Min.*, 72, 357-360.

Hsu, H., P. Blaha, M. Cococcioni, and R. Wentzcovitch (2011), Spin-State Crossover and Hyperfine Interactions of Ferric Iron in $MgSiO_3$ Perovskite, *Phys. Rev. Lett.*, 106, doi:10.1103/PhysRevLett.106.118501.

Hu, M. Y., W. Sturhahn, T. S. Toellner, P. D. Mannheim, E. D. Brown, J. Zhao, and E. E. Alp (2003), Measuring velocity of sound with nuclear resonant inelastic x-ray scattering, *Phys. Rev. B*, 67, 094304, doi:10.1103/PhysRevB.67.094304.

Huang, E., and W. A. Bassett (1986), Rapid Determination of Fe_3O_4 Phase Diagram by Synchrotron Radiation, *J. Geophys. Res.*, 91, 4697-4703, doi:10.1029/JB091iB05p04697.

Huang, E., W. A. Bassett, and M. S. Weathers (1988), Phase Relationships in Fe-Ni Alloys at High Pressures and Temperatures, *J. Geophys. Res.*, 93, 7741-7746, doi:10.1029/JB093iB07p07741.

Iota, V., J.-H. P. Klepeis, C.-S. Yoo, J. Lang, D. Haskel, and G. Srajer (2007), Electronic structure and magnetism in compressed 3d transition metals, *Appl. Phys. Lett.*, 90, 042505, doi:10.1063/1.2434184.

Irifune, T., T. Shinmei, C. A. McCammon, N. Miyajima, D. C. Rubie, and D. J. Frost (2009), Iron Partitioning and Density Changes of Pyrolite in Earth's Lower Mantle, *Science*, 327, 193-195, doi:10.1126/science.1181443.

Jackson, I., and S. M. Ridgen (2000), *Composition and Temperature of the Earth's Mantle: SeismologicalModels Interpreted through Experimental Studies of Earth Materials in "The Earth's mantle : composition, structure, and evolution,"* 1st ed., edited by I. Jackson, Cambridge University Press, Cambridge, UK.

Jackson, J. M., W. Sturhahn, G. Shen, J. Zhao, M. Y. Hu, D. Errandonea, J. D. Bass, and Y. Fei (2005), A synchrotron Mossbauer spectroscopy study of $(Mg,Fe)SiO_3$ perovskite up to 120 GPa, *American Mineralogist*, 90, 199-205, doi:10.2138/am.2005.1633.

Jacobsen, S. D., J.-F. Lin, R. J. Angel, G. Shen, V. B. Prakapenka, P. Dera, H.-K. Mao, and R. J. Hemley (2005), Single-crystal synchrotron X-ray diffraction study of wüstite and magnesiowüstite at lower-mantle pressures, *J. Synchrotron Rad.*, 12, 577-583, doi:10.1107/S0909049505022326.

Jagoutz, E., H. Palme, H. Baddenhausen, K. Blum, M. Cendales, G. Dreibus, B. Spettel, V. Lorenz, and H. Wänke (1979), *The abundances of major, minor and traceelements in the earth's mantle as derived from primitive ultramafic nodules in "Proceedings of the Tenth Lunar and Planetary Science Conference, Houston, Texas, March 19-23, 1979,"* Pergamon Press, New York.

Jamieson, J. C., and A. W. Lawson (1962), X-Ray Diffraction Studies in the 100 Kilobar Pressure Range, *J. Appl. Phys.*, 33, 776, doi:10.1063/1.1777167.

Jephcoat, A., and P. Olson (1987), Is the inner core of the Earth pure iron?, *Nature*, 325, 332-335, doi:10.1038/325332a0.

Jones, J. H., and M. J. Drake (1986), Geochemical constraints on core formation in the Earth, *Nature*, 322, 221-228, doi:10.1038/322221a0.

Kakol, Z., and J. M. Honig (1989), The variation of Verwey transition temperature with oxygen stoichiometry in magnetite, *Solid State Communications*, 70, 967-969, doi:10.1016/0038-1098(89)90638-8.

Kanamori, J. (1957), Theory of the Magnetic Properties of Ferrous and Cobaltous Oxides, I, *Prog. Theor. Phys.*, 17, 177-196, doi:10.1143/PTP.17.177.

Kantor, A., L. Dubrovinsky, N. Dubrovinskaia, I. Kantor, and I. Goncharenko (2005), Phase transitions in MnO and FeO at low temperatures: A neutron powder diffraction study, *Journal of Alloys and Compounds*, 402, 42-45, doi:10.1016/j.jallcom.2005.04.155.

Kantor, A., S. Jacobsen, I. Kantor, L. Dubrovinsky, C. McCammon, H. Reichmann, and I. Goncharenko (2004), Pressure-Induced Magnetization in FeO: Evidence from Elasticity and Mössbauer Spectroscopy, *Phys. Rev. Lett.*, 93, doi:10.1103/PhysRevLett.93.215502.

Kantor, A., I. Kantor, A. Kurnosov, L. Dubrovinsky, M. Krisch, A. Bossak, and S. Jacobsen (2008), Anelasticity of Fe_xO at high pressure, *Appl. Phys. Lett.*, 93, 034106, doi:10.1063/1.2952274.

Kantor, I. Y., A. P. Kantor, L. S. Dubrovinsky, and C. A. McCammon (2007), High-pressure phase transformations in the system FeO-MgO, in *Special Paper 421: Advances in High-Pressure Mineralogy*, vol. 421, pp. 47-55, Geological Society of America.

Katsnelson, M. I., and A. V. Trefilov (2000), Fermi-liquid theory of electronic topological transitions and screening anomalies in metals, *Phys. Rev. B*, 61, 1643, doi:10.1103/PhysRevB.61.1643.

Katsnelson, M. I., I. I. Naumov, and A. V. Trefilov (1994), Singularities of the electronic structure and pre-martensitic anomalies of lattice properties in β-phases of metals and alloys, *GPHT*, 49, 143-191, doi:10.1080/01411599408201172.

Kechin, V. V. (2001), Electronic topological transitions in Zn under compression, *Phys. Rev. B*, 63, 045119, doi:10.1103/PhysRevB.63.045119.

Keppler, H., L. S. Dubrovinsky, O. Narygina, and I. Kantor (2008), Optical Absorption and Radiative Thermal Conductivity of Silicate Perovskite to 125 Gigapascals, *Science*, 322, 1529-1532, doi:10.1126/science.1164609.

Kimura, K., R. Lewis, and E. Anders (1974), Distribution of gold and rhenium between nickel-iron and silicate melts: implications for the abundance of siderophile elements on the Earth and Moon, *Geochimica et Cosmochimica Acta*, 38, 683-701, doi:10.1016/0016-7037(74)90144-6.

Klotz, S., J. C. Chervin, P. Munsch, and G. Le Marchand (2009), Hydrostatic limits of 11 pressure transmitting media, *Journal of Physics D: Applied Physics*, 42, 075413, doi:10.1088/0022-

3727/42/7/075413.

Klotz, S., G. Steinle-Neumann, T. Strässle, J. Philippe, T. Hansen, and M. Wenzel (2008), Magnetism and the Verwey transition in Fe_3O_4 under pressure, *Phys. Rev. B*, 77, doi:10.1103/PhysRevB.77.012411.

Klotz, S., T. Strässle, G. Rousse, G. Hamel, and V. Pomjakushin (2005), Angle-dispersive neutron diffraction under high pressure to 10GPa, *Appl. Phys. Lett.*, 86, 031917, doi:10.1063/1.1855419.

Kobayashi, H., I. Isogai, T. Kamimura, N. Hamada, H. Onodera, S. Todo, and N. Môri (2006), Structural properties of magnetite under high pressure studied by Mössbauer spectroscopy, *Phys. Rev. B*, 73, doi:10.1103/PhysRevB.73.104110.

Koch, F., and J. B. Cohen (1969), The defect structure of $Fe_{1-x}O$, *Acta Crystallogr B Struct Crystallogr Cryst Chem*, 25, 275-287, doi:10.1107/S0567740869002111.

Koepernik, K., and H. Eschrig (1999), Full-potential nonorthogonal local-orbital minimum-basis band-structure scheme, *Phys. Rev. B*, 59, 1743, doi:10.1103/PhysRevB.59.1743.

Komabayashi, T., Y. Fei, Y. Meng, and V. Prakapenka (2009), In-situ X-ray diffraction measurements of the γ-ε transition boundary of iron in an internally-heated diamond anvil cell, *Earth and Planetary Science Letters*, 282, 252-257, doi:10.1016/j.epsl.2009.03.025.

Komabayashi, T., K. Hirose, Y. Nagaya, E. Sugimura, and A. Ohishi (2010), High-temperature compression of ferropericlase and the effect of temperature on iron spin transition, *Earth and Planetary Science Letters*, 297, 691-699, doi:16/j.epsl.2010.07.025.

Kotliar, G., S. Y. Savrasov, K. Haule, V. S. Oudovenko, O. Parcollet, and C. A. Marianetti (2006), Electronic structure calculations with dynamical mean-field theory, *Rev. Mod. Phys.*, 78, 865, doi:10.1103/RevModPhys.78.865.

Kubo, A. (2000), Post-garnet transitions in the system $Mg_4Si_4O_{12}$–$Mg_3Al_2Si_3O_{12}$ up to 28 GPa: phase relations of garnet, ilmenite and perovskite, *Physics of The Earth and Planetary Interiors*, 121, 85-102, doi:10.1016/S0031-9201(00)00162-X.

Kumar, V., and O. K. Anderson (1995), *Lectures on Methods of Electronic Structure Calculations: Proceedings of the Miniworkshop on "Methods of Electronic Structure Calculations" and Work*, World Scientific Pub Co Inc.

Kurnosov, A., I. Kantor, T. Boffa-Bolaran, S. Lindhardt, L. Dubrovinsky, A. Kuznetsov, and B. H. Zehnder (2008), A novel gas-loading system for mechanically closing of various types of diamond anvil cells, *Review of Scientific Instruments*, 79, 045110, doi:10.1063/1.2902506.

Labrosse, S., J. W. Hernlund, and N. Coltice (2007), A crystallizing dense magma ocean at the base of the Earth's mantle, *Nature*, 450, 866-869, doi:10.1038/nature06355.

Larson, A. C., and R. B. Von Dreele (2000), General Structure Analysis System (GSAS), *Los Alamos National Laboratory Report*, LAUR 86-748, 1-224.

References

Lauterbach, S., C. A. McCammon, P. van Aken, F. Langenhorst, and F. Seifert (2000), Mössbauer and ELNES spectroscopy of (Mg,Fe)(Si,Al)O_3 perovskite: a highly oxidised component of the lower mantle, *Contrib Mineral Petrol*, 138, 17-26, doi:10.1007/PL00007658.

Lay, T., J. Hernlund, and B. A. Buffett (2008), Core–mantle boundary heat flow, *Nature Geoscience*, 1, 25-32, doi:10.1038/ngeo.2007.44.

Leonov, I., A. Poteryaev, V. Anisimov, and D. Vollhardt (2011), Electronic Correlations at the α-γ Structural Phase Transition in Paramagnetic Iron, *Phys. Rev. Lett.*, 106, doi:10.1103/PhysRevLett.106.106405.

Lewis, J. (2004), *Physics and chemistry of the solar system*, 2nd ed., Elsevier Academic Press, Amsterdam, Boston.

Li, Z., and J. S. Tse (2000), Phonon Anomaly in High-Pressure Zn, *Phys. Rev. Lett.*, 85, 5130, doi:10.1103/PhysRevLett.85.5130.

Lichtenstein, A. I., and M. I. Katsnelson (1998), Ab initio calculations of quasiparticle band structure in correlated systems: LDA++ approach, *Phys. Rev. B*, 57, 6884, doi:10.1103/PhysRevB.57.6884.

Lichtenstein, A. I., M. I. Katsnelson, and G. Kotliar (2001), Finite-Temperature Magnetism of Transition Metals: An ab initio Dynamical Mean-Field Theory, *Phys. Rev. Lett.*, 87, 067205, doi:10.1103/PhysRevLett.87.067205.

Lifshitz, I. M. (1960), Anomalies of Electronic Characteristics of a Metal in the High-pressure Region, *Soviet phys. JETP*, 11, 1130.

Lin, J. F., V. V. Struzhkin, W. Sturhahn, E. Huang, J. Zhao, Y. M. Hu, E. E. Alp, H.-K. Mao, N. Boctor, and R. J. Hemley (2003a), Sound velocities of iron-nickel and iron-silicon alloys at high pressures, *Geophys. Res. Lett.*, 30, doi:10.1029/2003GL018405.

Lin, J.-F., A. Gavriliuk, V. Struzhkin, S. Jacobsen, W. Sturhahn, M. Hu, P. Chow, and C.-S. Yoo (2006), Pressure-induced electronic spin transition of iron in magnesiowustite-(Mg,Fe)O, *Phys. Rev. B*, 73, doi:10.1103/PhysRevB.73.113107.

Lin, J.-F., D. L. Heinz, A. J. Campbell, J. M. Devine, and G. Shen (2002a), Iron-Silicon Alloy in Earth's Core?, *Science*, 295, 313 -315, doi:10.1126/science.1066932.

Lin, J.-F., L. Heinz, A. J. Campbell, J. M. Devine, W. L. Mao, and G. Shen (2002b), Iron-Nickel alloy in the Earth's core, *Geophys. Res. Lett.*, 29, doi:10.1029/2002GL015089.

Lin, J.-F., V. Struzhkin, H.-K. Mao, R. Hemley, P. Chow, M. Hu, and J. Li (2004), Magnetic transition in compressed Fe_3C from x-ray emission spectroscopy, *Phys. Rev. B*, 70, doi:10.1103/PhysRevB.70.212405.

Lin, J.-F., V. V. Struzhkin, S. D. Jacobsen, M. Y. Hu, P. Chow, J. Kung, H. Liu, H.-K. Mao, and R. J. Hemley (2005a), Spin transition of iron in magnesiowüstite in the Earth's lower mantle, *Nature*, 436, 377-380, doi:10.1038/nature03825.

References

Lin, J. F., V. V. Struzhkin, W. Sturhahn, E. Huang, J. Zhao, M. Y. Hu, E. E. Alp, H. K. Mao, B. Nabil, and R. J. Hemley (2003b), Sound velocities of iron-nickel and iron-silicon alloys at high pressures, *Geophys. Res. Lett.*, 30, doi:10.1029/2003GL018405.

Lin, J. F., W. Sturhahn, J. Zhao, G. Shen, H.-K. Mao, and R. J. Hemley (2005b), Sound Velocities of Hot Dense Iron: Birch's Law Revisited, *Science*, 308, 1892 -1894, doi:10.1126/science.1111724.

Lin, J.-F. et al. (2008), Intermediate-spin ferrous iron in lowermost mantle post-perovskite and perovskite, *Nature Geoscience*, 1, 688-691, doi:10.1038/ngeo310.

Lizárraga, R., L. Nordström, O. Eriksson, and J. Wills (2008), Noncollinear magnetism in the high-pressure hcp phase of iron, *Phys. Rev. B*, 78, 064410, doi:10.1103/PhysRevB.78.064410.

Lübbers, R., H. F. Grünsteudel, A. I. Chumakov, and G. Wortmann (2000), Density of Phonon States in Iron at High Pressure, *Science*, 287, 1250 -1253.

Lundin, S., K. Catalli, J. Santillán, S.-H. Shim, V. B. Prakapenka, M. Kunz, and Y. Meng (2008), Effect of Fe on the equation of state of mantle silicate perovskite over 1 Mbar, *Physics of the Earth and Planetary Interiors*, 168, 97-102, doi:16/j.pepi.2008.05.002.

Lyubutin, I. S., A. G. Gavriliuk, K. V. Frolov, J. F. Lin, and I. A. Troyan (2010), High-spin-low-spin transition in magnesiowüstite $(Mg_{0.75},Fe_{0.25})O$ at high pressures under hydrostatic conditions, *Jetp Lett.*, 90, 617-622, doi:10.1134/S0021364009210061.

Manga, M., and R. Jeanloz (1996), Implications of a metal-bearing chemical boundary layer in D″ for mantle dynamics, *Geophys. Res. Lett.*, 23, 3091, doi:10.1029/96GL03021.

Mao, H. K. et al. (2001), Phonon Density of States of Iron up to 153 Gigapascals, *Science*, 292, 914-916, doi:10.1126/science.1057670.

Mao, H.-K., T. Takahashi, W. A. Bassett, G. L. Kinsland, and L. Merrill (1974), Isothermal Compression of Magnetite to 320 kbar and Pressure-Induced Phase Transformation, *J. Geophys. Res.*, 79, 1165-1170, doi:10.1029/JB079i008p01165.

Mao, H.-K., Y. Wu, L. C. Chen, J. F. Shu, and A. P. Jephcoat (1990), Static Compression of Iron to 300 GPa and $Fe_{0.8}Ni_{0.2}$ alloy to 260 GPa: Implications for Composition of the Core, *J. Geophys. Res.*, 95, 21737-21742, doi:10.1029/JB095iB13p21737.

Mao, H. K., J. Xu, and P. M. Bell (1986), Calibration of the Ruby Pressure Gauge to 800 kbar Under Quasi-Hydrostatic Conditions, *J. Geophys. Res.*, 91, 4673-4676, doi:10.1029/JB091iB05p04673.

Mao, W. L., G. Shen, V. B. Prakapenka, Y. Meng, A. J. Campbell, D. L. Heinz, J. Shu, R. J. Hemley, and H.-K. Mao (2004), Ferromagnesian postperovskite silicates in the D'' layer of the Earth, *Proceedings of the National Academy of Sciences*, 101, 15867-15869, doi:10.1073/pnas.0407135101.

Marzari, N., and D. Vanderbilt (1997), Maximally localized generalized Wannier functions for

composite energy bands, *Phys. Rev. B*, 56, 12847, doi:10.1103/PhysRevB.56.12847.

Mathon, O., F. Baudelet, J. Itié, A. Polian, M. d' Astuto, J. Chervin, and S. Pascarelli (2004), Dynamics of the Magnetic and Structural α-ε Phase Transition in Iron, *Phys. Rev. Lett.*, 93, doi:10.1103/PhysRevLett.93.255503.

Mayo, J. T., C. Yavuz, S. Yean, L. Cong, H. Shipley, W. Yu, J. Falkner, A. Kan, M. Tomson, and V. L. Colvin (2007), The effect of nanocrystalline magnetite size on arsenic removal, *Sci. Technol. Adv. Mater.*, 8, 71-75, doi:10.1016/j.stam.2006.10.005.

McCammon, C. (2005), GEOCHEMISTRY: The Paradox of Mantle Redox, *Science*, 308, 807-808, doi:10.1126/science.1110532.

McCammon, C. A., and L.-G. Liu (1984), The effects of pressure and temperature on nonstoichiometric wüstite, Fe_xO: The iron-rich phase boundary, *Physics and Chemistry of Minerals*, 10, 106-113, doi:10.1007/BF00309644.

McCammon, C. A., D. C. Rubie, C. R. Ross, F. Seifert, and H. S. C. O'Neill (1992), Mössbauer spectra of $^{57}Fe_{0.05}Mg_{0.95}SiO_3$ perovskite at 80 and 298 K, *Am. Min.*, 77, 894-897.

McCammon, C., I. Kantor, O. Narygina, J. Rouquette, U. Ponkratz, I. Sergueev, M. Mezouar, V. Prakapenka, and L. Dubrovinsky (2008), Stable intermediate-spin ferrous iron in lower-mantle perovskite, *Nature Geoscience*, 1, 684-687, doi:10.1038/ngeo309.

McDonough, W., and S.-S. Sun (1995), The composition of the Earth, *Chemical Geology*, 120, 223-253, doi:10.1016/0009-2541(94)00140-4.

McSween, H. Y. J., and J. R. Huss (2010), *Cosmochemistry*, Cambridge University Press, Cambridge, New York.

Meenakshi, S., V. Vijayakumar, B. K. Godwal, and S. K. Sikka (1992), Distorted hcp structure of zinc under pressure, *Phys. Rev. B*, 46, 14359, doi:10.1103/PhysRevB.46.14359.

Meng, Y., G. Shen, and H.-K. Mao (2006), Double-sided laser heating system at HPCAT for *in situ* x-ray diffraction at high pressures and high temperatures, *J. Phys.: Condens. Matter*, 18, S1097-S1103, doi:10.1088/0953-8984/18/25/S17.

Merkel, S., A. F. Goncharov, H.-K. Mao, P. Gillet, and R. J. Hemley (2000), Raman Spectroscopy of Iron to 152 Gigapascals: Implications for Earth's Inner Core, *Science*, 288, 1626 -1629, doi:10.1126/science.288.5471.1626.

Merrill, L., and W. A. Bassett (1974), Miniature diamond anvil pressure cell for single crystal x-ray diffraction studies, *Rev. Sci. Instrum.*, 45, 290, doi:10.1063/1.1686607.

Methfessel, M., M. Schilfgaarde, and R. A. Casali (2000), A Full-Potential LMTO Method Based on Smooth Hankel Functions, in *Electronic Structure and Physical Properies of Solids*, vol. 535, edited by H. Dreyssé, pp. 114-147, Springer Berlin Heidelberg, Berlin, Heidelberg.

Mikhaylushkin, A. S., S. I. Simak, L. Dubrovinsky, N. Dubrovinskaia, B. Johansson, and I. A. Abrikosov (2007), Pure Iron Compressed and Heated to Extreme Conditions, *Phys. Rev.*

References

Lett., 99, 165505, doi:10.1103/PhysRevLett.99.165505.

Mito, M., M. Hitaka, T. Kawae, K. Takeda, T. Kitai, and N. Toyoshima (2001), Development of Miniature Diamond Anvil Cell for the Superconducting Quantum Interference Device Magnetometer, *Jpn. J. Appl. Phys.*, 40, 6641-6644, doi:10.1143/JJAP.40.6641.

Miyake, T., and F. Aryasetiawan (2008), Screened Coulomb interaction in the maximally localized Wannier basis, *Phys. Rev. B*, 77, 085122, doi:10.1103/PhysRevB.77.085122.

Miyake, T., F. Aryasetiawan, and M. Imada (2009), Ab initio procedure for constructing effective models of correlated materials with entangled band structure, *Phys. Rev. B*, 80, 155134, doi:10.1103/PhysRevB.80.155134.

Moore, R. O., and J. J. Gurney (1985), Pyroxene solid solution in garnets included in diamond, *Nature*, 318, 553-555, doi:10.1038/318553a0.

Morard, G. et al. (2007), Optimization of Paris-Edinburgh press cell assemblies for in situ monochromatic X-ray diffraction and X-ray absorption, *High Pressure Res.*, 27, 223-233, doi:10.1080/08957950601183553.

Morgan, J. W., and E. Anders (1980), Chemical Composition of Earth, Venus, and Mercury, *Proceedings of the National Academy of Sciences*, 77, 6973-6977, doi:10.1073/pnas.77.12.6973.

Morgan, J. W. (1986), Ultramafic Xenoliths: Clues to Earth's Late Accretionary History, *J. Geophys. Res.*, 91, 12375-12387, doi:10.1029/JB091iB12p12375.

Môri, N., S. Todo, N. Takeshita, T. Mori, and Y. Akishige (2002), Metallization of magnetite at high pressures, *Physica B: Condensed Matter*, 312-313, 686-690, doi:16/S0921-4526(01)01525-3.

Morris, E. R., and Q. Williams (1997), Electrical resistivity of Fe_3O_4 to 48 GPa: Compression-induced changes in electron hopping at mantle pressures, *J. Geophys. Res.*, 102, 18139-18148, doi:10.1029/97JB00024.

Mosenfelder, J. L., P. D. Asimow, D. J. Frost, D. C. Rubie, and T. J. Ahrens (2009), The $MgSiO_3$ system at high pressure: Thermodynamic properties of perovskite, postperovskite, and melt from global inversion of shock and static compression data., *J. Geophys. Res.*, 114, doi:10.1029/2008JB005900.

Mössbauer, R. L. (1958), Kernresonanzfluoreszenz von Gammastrahlung in Ir[191], *Z. Physik*, 151, 124-143, doi:10.1007/BF01344210.

Moyzis, J. A., and H. G. Drickamer (1968), Effect of Pressure on the Isomer Shift of Fe[57] in the bcc Phase, *Phys. Rev.*, 171, 389, doi:10.1103/PhysRev.171.389.

Murakami, M., K. Hirose, K. Kawamura, N. Sata, and Y. Ohishi (2004), Post-Perovskite Phase Transition in $MgSiO_3$, *Science*, 304, 855-858, doi:10.1126/science.1095932.

<center>**References**</center>

Murthy, V. R. (1991), Early Differentiation of the Earth and the Problem of Mantle Siderophile Elements: A New Approach, *Science*, 253, 303-306, doi:10.1126/science.253.5017.303.

Narygina, O., L. S. Dubrovinsky, H. Samuel, C. A. McCammon, I. Y. Kantor, K. Glazyrin, S. Pascarelli, G. Aquilanti, and V. B. Prakapenka (2011), Chemically homogeneous spin transition zone in Earth's lower mantle, *Physics of the Earth and Planetary Interiors*, 185, 107-111, doi:16/j.pepi.2011.02.004.

Narygina, O., M. Mattesini, I. Kantor, S. Pascarelli, X. Wu, G. Aquilanti, C. McCammon, and L. Dubrovinsky (2009), High-pressure experimental and computational XANES studies of $(Mg,Fe)(Si,Al)O_3$ perovskite and $(Mg,Fe)O$ ferropericlase as in the Earth's lower mantle, *Phys. Rev. B*, 79, 174115, doi:10.1103/PhysRevB.79.174115.

Nimmo, F. (2007), *Energetics of the Core in "Treatise on Geophysics,"* Elsevier.

Nimmo, F., and D. Alfè (2007), *Advances in earth science from earthquakes to global warming*, edited by P. Sammonds, Imperial College Press, Distributed by World Scientific Pub., London, Hackensack NJ.

Novikov, D. L., A. J. Freeman, N. E. Christensen, A. Svane, and C. O. Rodriguez (1997), LDA simulations of pressure-induced anomalies in c/a and electric-field gradients for Zn and Cd, *Phys. Rev. B*, 56, 7206, doi:10.1103/PhysRevB.56.7206.

Nozières, P. (1997), *Theory Of Interacting Fermi Systems*, Westview Press.

O'Neill, H. S. C., and H. Palme (2000), *Composition of the Silicate Earth: Implications for Accretion and CoreFormation in "The Earth's mantle : composition, structure, and evolution,"* 1st ed., edited by I. Jackson, Cambridge University Press, Cambridge [u.a.].

Oed, A. (1988), Position-sensitive detector with microstrip anode for electron multiplication with gases, *Nuclear Instruments and Methods in Physics Research Section A: Accelerators, Spectrometers, Detectors and Associated Equipment*, 263, 351-359, doi:10.1016/0168-9002(88)90970-9.

Ono, S., and T. Kikegawa (2006), High-pressure study of FeS, between 20 and 120 GPa, using synchrotron X-ray powder diffraction, *American Mineralogist*, 91, 1941-1944, doi:10.2138/am.2006.2347.

Ono, S., T. Kikegawa, N. Hirao, and K. Mibe (2010), High-pressure magnetic transition in hcp-Fe, *American Mineralogist*, 95, 880-883, doi:10.2138/am.2010.3430.

Ovsyannikov, S. V., V. V. Shchennikov, S. Todo, and Y. Uwatoko (2008), A new crossover in Fe_3O_4 magnetite under pressure near 6 GPa: modification to "ideal" inverse cubic spinel?, *J. Phys.: Condens. Matter*, 20, 172201, doi:10.1088/0953-8984/20/17/172201.

Palme, H., and K. Nickel (1985), Ca/Al ratio and composition of the Earth's upper mantle, *Geochimica et Cosmochimica Acta*, 49, 2123-2132, doi:10.1016/0016-7037(85)90070-5.

Palme, H., and A. Jones (2003), *Treatise on Geochemistry*, Elsevier Academic Press, Oxford.

<center>116</center>

References

Papandrew, A. B., M. S. Lucas, R. Stevens, I. Halevy, B. Fultz, M. Y. Hu, P. Chow, R. E. Cohen, and M. Somayazulu (2006), Absence of Magnetism in hcp Iron-Nickel at 11 K, *Phys. Rev. Lett.*, 97, 087202, doi:10.1103/PhysRevLett.97.087202.

Pasternak, M. P., W. M. Xu, G. K. Rozenberg, R. D. Taylor, and R. Jeanloz (2003), Pressure-induced coordination crossover in magnetite; the breakdown of the Verwey-Mott localization hypothesis, *Journal of Magnetism and Magnetic Materials*, 265, L107-L112, doi:16/S0304-8853(03)00549-3.

Pasternak, M., R. Taylor, R. Jeanloz, X. Li, J. Nguyen, and C. McCammon (1997), High Pressure Collapse of Magnetism in $Fe_{0.94}O$: Mössbauer Spectroscopy Beyond 100 GPa, *Phys. Rev. Lett.*, 79, 5046-5049, doi:10.1103/PhysRevLett.79.5046.

Perdew, J. P., K. Burke, and M. Ernzerhof (1996), Generalized Gradient Approximation Made Simple, *Phys. Rev. Lett.*, 77, 3865, doi:10.1103/PhysRevLett.77.3865.

Petricek, V., M. Dusek, and L. Palatinus (2006), *JANA2006. The crystallographic computing system*, Institute of Physics, Praha, Czech Republic.

Potapkin, V., C. A. McCammon, L. Dubrovinsky, K. Glazyrin, G. V. Smirnov, S. L. Popov, A. I. Chumakov, and R. Rüffer (2011), Spin state of iron in lower mantle, *submitted*.

Potzel, W., M. Steiner, H. Karzel, W. Schiessl, M. Köfferlein, G. M. Kalvius, and P. Blaha (1995), Electronically Driven Soft Modes in Zinc Metal, *Phys. Rev. Lett.*, 74, 1139, doi:10.1103/PhysRevLett.74.1139.

Prakapenka, V. B., A. Kubo, A. Kuznetsov, A. Laskin, O. Shkurikhin, P. Dera, M. L. Rivers, and S. R. Sutton (2008), Advanced flat top laser heating system for high pressure research at GSECARS: application to the melting behavior of germanium, *High Pressure Res.*, 28, 225-235, doi:10.1080/08957950802050718.

Riner, M. A., C. R. Bina, M. S. Robinson, and S. J. Desch (2008), Internal structure of Mercury: Implications of a molten core, *J. Geophys. Res.*, 113, doi:10.1029/2007JE002993.

Ringwood, A. E. (1962), A Model for the Upper Mantle, *J. Geophys. Res.*, 67, 857-867, doi:10.1029/JZ067i002p00857.

Ringwood, A. E. (1979), *Origin of the earth and moon.*, Springer, New York.

Rodríguez-Carvajal, J. (1993), Recent advances in magnetic structure determination by neutron powder diffraction, *Physica B: Condensed Matter*, 192, 55-69, doi:10.1016/0921-4526(93)90108-I.

Röntgen, W. C. (1895), Über eine neue Art von Strahlen., *Sitzungberichte der Würzburger Physikalischen-Medizinishen Gesellschaft*, 132-141.

Roth, W. (1958), Magnetic Structures of MnO, FeO, CoO, and NiO, *Phys. Rev.*, 110, 1333-1341, doi:10.1103/PhysRev.110.1333.

Rozenberg, G., Y. Amiel, W. Xu, M. Pasternak, R. Jeanloz, M. Hanfland, and R. Taylor (2007),

Structural characterization of temperature- and pressure-induced inverse-normal spinel transformation in magnetite, *Phys. Rev. B*, 75, doi:10.1103/PhysRevB.75.020102.

Ruban, A. V., and I. A. Abrikosov (2008), Configurational thermodynamics of alloys from first principles: effective cluster interactions, *Rep. Prog. Phys.*, 71, 046501, doi:10.1088/0034-4885/71/4/046501.

Ruban, A. V., S. Khmelevskyi, P. Mohn, and B. Johansson (2007), Temperature-induced longitudinal spin fluctuations in Fe and Ni, *Phys. Rev. B*, 75, 054402, doi:10.1103/PhysRevB.75.054402.

Rubie, D. C., F. Nimmo, and H. J. Melosh (2007), *Treatise on Geophysics*, Elsevier.

Sánchez-Barriga, J. et al. (2009), Strength of Correlation Effects in the Electronic Structure of Iron, *Phys. Rev. Lett.*, 103, 267203, doi:10.1103/PhysRevLett.103.267203.

Saxena, S. K., L. S. Dubrovinsky, F. Tutti, and T. Le Bihan (1999), Equation of state of $MgSiO_3$ with the perovskite structure based on experimental measurement, *American Mineralogist*, 84, 226-232.

Schollenbruch, K., A. B. Woodland, D. J. Frost, and F. Langenhorst (2009), Detecting the spinel–post-spinel transition in Fe_3O_4 by *in situ* electrical resistivity measurements, *High Pressure Research*, 29, 520-524, doi:10.1080/08957950903392092.

Schollenbruch, K., A. B. Woodland, D. J. Frost, Y. Wang, T. Sanehira, and F. Langenhorst (2011), In situ determination of the spinel-post-spinel transition in Fe_3O_4 at high pressure and temperature by synchrotron X-ray diffraction, *American Mineralogist*, 96, 820-827, doi:10.2138/am.2011.3642.

Schultz, E. et al. (2005), Double-sided laser heating system for in situ high pressure-high temperature monochromatic x-ray diffraction at the esrf, *High Pressure Res.*, 25, 71-83, doi:10.1080/08957950500076031.

Sheldrick, G. M. (2008), A short history of SHELX, *Acta Crystallographica*, A64, 112-122, doi:10.1107/S010876730704393.

Shen, G., H.-K. Mao, R. J. Hemley, T. S. Duffy, and M. L. Rivers (1998), Melting and crystal structure of iron at high pressures and temperatures, *Geophys. Res. Lett.*, 25, 373, doi:10.1029/97GL03776.

Shen, G., M. L. Rivers, Y. Wang, and S. R. Sutton (2001), Laser heated diamond cell system at the Advanced Photon Source for in situ x-ray measurements at high pressure and temperature, *Rev. Sci. Instrum.*, 72, 1273, doi:10.1063/1.1343867.

Shepherd, J., J. Koenitzer, R. Aragón, C. Sandberg, and J. Honig (1985), Heat capacity studies on single crystal annealed Fe_3O_4, *Phys. Rev. B*, 31, 1107-1113, doi:10.1103/PhysRevB.31.1107.

Shimizu, K., T. Kimura, S. Furomoto, K. Takeda, K. Kontani, Y. Onuki, and K. Amaya (2001), Superconductivity in the non-magnetic state of iron under pressure, *Nature*, 412, 316-318,

doi:10.1038/35085536.

Sohl, F., and G. Schubert (2007), *Interior Structure, Composition, and Mineralogy of the Terrestrial Planets in "Treatise on Geophysics,"* edited by G. Schubert, Elsevier.

Sola, E., and D. Alfè (2009), Melting of Iron under Earth's Core Conditions from Diffusion Monte Carlo Free Energy Calculations, *Phys. Rev. Lett.*, 103, 078501, doi:10.1103/PhysRevLett.103.078501.

Sola, E., J. P. Brodholt, and D. Alfè (2009), Equation of state of hexagonal closed packed iron under Earth's core conditions from quantum Monte Carlo calculations, *Phys. Rev. B*, 79, 024107, doi:10.1103/PhysRevB.79.024107.

Solomatov, V. (2007), *Treatise on Geophysics*, Elsevier.

Souvatzis, P., O. Eriksson, and M. I. Katsnelson (2007), Anomalous Thermal Expansion in alpha -Titanium, *Phys. Rev. Lett.*, 99, 015901, doi:10.1103/PhysRevLett.99.015901.

Speziale, S. (2005), Iron spin transition in Earth's mantle, *Proceedings of the National Academy of Sciences*, 102, 17918-17922, doi:10.1073/pnas.0508919102.

Stackhouse, S., J. Brodholt, and G. Price (2007), Electronic spin transitions in iron-bearing $MgSiO_3$ perovskite, *Earth and Planetary Science Letters*, 253, 282-290, doi:10.1016/j.epsl.2006.10.035.

Steinle-Neumann, G., R. E. Cohen, and L. Stixrude (2004), Magnetism in iron as a function of pressure, *J. Phys.: Condens. Matter*, 16, S1109-S1119, doi:10.1088/0953-8984/16/14/020.

Steinle-Neumann, G., L. Stixrude, and R. Cohen (1999a), First-principles elastic constants for the hcp transition metals Fe, Co, and Re at high pressure, *Phys. Rev. B*, 60, 791-799, doi:10.1103/PhysRevB.60.791.

Steinle-Neumann, G., L. Stixrude, and R. E. Cohen (1999b), First-principles elastic constants for the hcp transition metals Fe, Co, and Re at high pressure, *Phys. Rev. B*, 60, 791, doi:10.1103/PhysRevB.60.791.

Stixrude, L., and C. Lithgow-Bertelloni (2005a), Mineralogy and elasticity of the oceanic upper mantle: Origin of the low-velocity zone, *J. Geophys. Res.*, 110, doi:10.1029/2004JB002965.

Stixrude, L., and C. Lithgow-Bertelloni (2005b), Thermodynamics of mantle minerals - I. Physical properties, *Geophysical Journal International*, 162, 610-632, doi:10.1111/j.1365-246X.2005.02642.x.

Sturhahn, W., J. M. Jackson, and J.-F. Lin (2005), The spin state of iron in minerals of Earth's lower mantle, *Geophys. Res. Lett.*, 32, doi:10.1029/2005GL022802.

Sugahara, M., A. Yoshiasa, Y. Komatsu, T. Yamanaka, N. Bolfan-Casanova, A. Nakatsuka, S. Sasaki, and M. Tanaka (2006), Reinvestigation of the $MgSiO_3$ perovskite structure at high pressure, *American Mineralogist*, 91, 533-536, doi:10.2138/am.2006.1980.

References

Sweeney, J. S., and D. L. Heinz (1993), Thermal analysis in the laser-heated diamond anvil cell, *PAGEOPH*, 141, 497-507, doi:10.1007/BF00998342.

Tateno, S., K. Hirose, Y. Ohishi, and Y. Tatsumi (2010), The Structure of Iron in Earth's Inner Core, *Science*, 330, 359-361, doi:10.1126/science.1194662.

Thakor, V., J. B. Staunton, J. Poulter, S. Ostanin, B. Ginatempo, and E. Bruno (2003), Ab initio calculations of incommensurate antiferromagnetic spin fluctuations in hcp iron under pressure, *Phys. Rev. B*, 67, 180405, doi:10.1103/PhysRevB.67.180405.

Thorne, M. S., and E. J. Garnero (2004), Inferences on ultralow-velocity zone structure from a global analysis of SPdKS waves, *J. Geophys. Res.*, 109, doi:10.1029/2004JB003010.

Tonks, B. W. (1992), Core formation by giant impacts, *Icarus*, 100, 326-346, doi:10.1016/0019-1035(92)90104-F.

Truran, J. W., and A. J. Heger (2005), *Origin of the Elements in "Meteorites, comets, and planets,"* 1st ed., edited by A. Davis, Elsevier, Amsterdam ;;Boston.

Urakawa, S., K. Someya, H. Terasaki, T. Katsura, S. Yokoshi, K. Funakoshi, W. Utsumi, Y. Katayama, Y. Sueda, and T. Irifuna (2004), Phase relationships and equations of state for FeS at high pressures and temperatures and implications for the internal structure of Mars, *Physics of The Earth and Planetary Interiors*, 143-144, 469-479, doi:10.1016/j.pepi.2003.12.015.

Vaks, V. G., and A. V. Trefilov (1991), Anomalies of phonon spectra and anharmonic effects in metals and alloys due to proximity of the Fermi level to singular points of band structure, *J. Phys.: Condens. Matter*, 3, 1389-1408, doi:10.1088/0953-8984/3/11/003.

Vaks, V. G., M. I. Katsnelson, A. I. Likhtenstein, G. V. Peschanskikh, and A. V. Trefilov (1991), Pre-transition softening and anomalous pressure dependence of shear constants in alkali and alkaline-earth metals due to band-structure effects, *J. Phys.: Condens. Matter*, 3, 1409-1428, doi:10.1088/0953-8984/3/11/004.

Vaks, V. G., M. I. Katsnelson, V. G. Koreshkov, A. I. Likhtenstein, O. E. Parfenov, V. F. Skok, V. A. Sukhoparov, A. V. Trefilov, and A. A. Chernyshov (1989), An experimental and theoretical study of martensitic phase transitions in Li and Na under pressure, *J. Phys.: Condens. Matter*, 1, 5319, doi:10.1088/0953-8984/1/32/001.

Varlamov, A. A., V. S. Egorov, and A. V. Pantsulaya (1989), Kinetic properties of metals near electronic topological transitions ($2^1/_2$-order transitions), *Advances in Physics*, 38, 469-564, doi:10.1080/00018738900101132.

Verwey, E. J. W. (1939), Electronic Conduction of Magnetite (Fe_3O_4) and its Transition Point at Low Temperatures, *Nature*, 144, 327-328, doi:10.1038/144327b0.

Vitos, L., I. A. Abrikosov, and B. Johansson (2001), Anisotropic Lattice Distortions in Random Alloys from First-Principles Theory, *Phys. Rev. Lett.*, 87, 156401, doi:10.1103/PhysRevLett.87.156401.

References

Vocadlo, L., D. Alfe, M. J. Gillan, I. G. Wood, J. P. Brodholt, and G. D. Price (2003), Possible thermal and chemical stabilization of body-centred-cubic iron in the Earth's core, *Nature*, 424, 536-539, doi:10.1038/nature01829.

Wang, Y., and J. P. Perdew (1991), Correlation hole of the spin-polarized electron gas, with exact small-wave-vector and high-density scaling, *Phys. Rev. B*, 44, 13298, doi:10.1103/PhysRevB.44.13298.

Wänke, H., G. Dreibus, and E. Jagoutz (1984), *Mantle chemistry and accretion history of the Earth in "Archaean geochemistry : the origin and evolution of the Archaean continental crust,"* edited by A. Kröner, Springer-Verlag, Berlin, New York.

Weir, C. E., E. R. Lippincott, A. V. Valkenburg, and E. N. Bunting (1959), Infrared Studies in the 1- to 15-Micron Region to 30,000 Atmospheres, *J. Res. Natl. Bur. Stand*, 63A, 55-62.

Werner, P., A. Comanac, L. de' Medici, M. Troyer, and A. Millis (2006), Continuous-Time Solver for Quantum Impurity Models, *Phys. Rev. Lett.*, 97, doi:10.1103/PhysRevLett.97.076405.

Wicks, J. K., J. M. Jackson, and W. Sturhahn (2010), Very low sound velocities in iron-rich (Mg,Fe)O: Implications for the core-mantle boundary region, *Geophys. Res. Lett.*, 37, doi:10.1029/2010GL043689.

Williams, Q., J. Revenaugh, and E. Garnero (1998), A Correlation Between Ultra-Low Basal Velocities in the Mantle and Hot Spots, *Nature*, 281, 546-549, doi:10.1126/science.281.5376.546.

Williamson, D. L., S. Bukshpan, and R. Ingalls (1972), Search for Magnetic Ordering in hcp Iron, *Phys. Rev. B*, 6, 4194, doi:10.1103/PhysRevB.6.4194.

Wolfram Research, Inc. (2008), *Mathematica*, Mathematica, Wolfram Research, Inc., Champaign, Illinois.

Woolfson, M. (2000), The origin and evolution of the solar system, *Astronomy and Geophysics*, 41, 1.12-1.19, doi:10.1046/j.1468-4004.2000.00012.x.

Xu, Y., C. McCammon, and B. T. Poe (1998), The Effect of Alumina on the Electrical Conductivity of Silicate Perovskite, *Science*, 282, 922-924, doi:10.1126/science.282.5390.922.

Yamazaki, D. et al. (2010), Phase boundary between perovskite and post-perovskite structures in $MnGeO_3$ determined by in situ X-ray diffraction measurements using sintered diamond anvils, *American Mineralogist*, 96, 89-92, doi:10.2138/am.2011.3499.

Yoo, C. S., J. Akella, A. J. Campbell, H. K. Mao, and R. J. Hemley (1995), Phase Diagram of Iron by in Situ X-ray Diffraction: Implications for Earth's Core, *Science*, 270, 1473 -1475, doi:10.1126/science.270.5241.1473.

Zhai, S., and E. Ito (2011), Recent advances of high-pressure generation in a multianvil apparatus using sintered diamond anvils, *Geoscience Frontiers*, 2, 101-106, doi:10.1016/j.gsf.2010.09.005.

References

Zhang, F., and A. Oganov (2006), Valence state and spin transitions of iron in Earth's mantle silicates, *Earth and Planetary Science Letters*, 249, 436-443, doi:10.1016/j.epsl.2006.07.023.

Zuber, M. T. et al. (2007), The Geophysics of Mercury: Current Status and Anticipated Insights from the MESSENGER Mission, *Space Science Reviews*, 131, 105-132, doi:10.1007/s11214-007-9265-4.

Erklärung

Hiermit versichere ich, die vorliegende Arbeit selbstständig verfasst und keine anderen als die von mir angegebenen Quellen und Hilfsmittel benutzt zu haben.

Ferner erkläre ich, dass ich nicht anderweitig versucht habe, mit oder ohne Erfolg, eine Dissertation einzureichen und auch keine gleichartige Doktorprüfung an einer anderen Hochschule endgültig nicht bestanden habe.

Konstantin Glazyrin

Bayreuth, August 2011